Dental pulp stem cells adhesion, growth and differentiation on porous silicon scaffolds

Pierre-Yves Collart Dutilleul

Pierre-Yves Collart Dutilleul. Dental pulp stem cells adhesion, growth and differentiation on porous silicon scaffolds. Human health and pathology. Université Montpellier I, 2013. English. NNT : 2013MON12203 . tel-03362569

HAL Id: tel-03362569
https://theses.hal.science/tel-03362569v1
Submitted on 1 Oct 2021

THÈSE

Pour obtenir le grade de Docteur

Délivré par L'UNIVERSITE MONTPELLIER 1

Préparée au sein de l'école doctorale :
Sciences Chimiques et Biologiques pour la Santé

Et de l'unité de recherche :
Laboratoire Biosanté Nanoscience EA 4203

Spécialité : BIOLOGIE SANTE

Présentée par Pierre-Yves COLLART DUTILLEUL

Dental Pulp Stem Cells adhesion, growth and differentiation on porous silicon scaffolds

Soutenue le 17 Décembre 2013 devant le jury composé de

M. Frédéric CUISINIER	Professeur, Université Montpellier 1	Co-Directeur
Mme Frédérique CUNIN	Chargé de Recherches CNRS, ICG Montpellier	Examinateur
Mme Dominique DEVILLE de PERIERE	Professeur, Université Montpellier 1	Directeur de Thèse
Mme Csilla GERGELY	Professeur, Université Montpellier 2	Examinateur
M. Philippe KEMOUN	Maitre de Conférence, Université de Toulouse	Examinateur
M. Guy LADAM	Maitre de Conférence, Université de Rouen	Rapporteur
M. Raùl J MARTIN-PALMA	Professeur, Université de Madrid	Rapporteur

Pierre-Yves COLLART DUTILLEUL

Laboratoire Biosanté Nanoscience EA 4203
545, Av Pr. J-L Viala
34193 MONTPELLIER Cedex 5

Adhésion, croissance et différenciation de cellules souches pulpaires sur silicium poreux

Dental pulp stem cells growth and osteodifferentiation on porous silicon scaffolds

Mots Clés :

Ingénierie Tissulaire
Cellules Souches Mésenchymateuses
Silicium Poreux
Adhésion cellulaire
Différenciation cellulaire

Key Words:

Tissue Engineering
Mesenchymal Stem Cells
Porous Silicon
Cell Adhesion
Cell Differentiation

Résumé en français:

Le silicium poreux est un biomatériau prometteur pour l'ingénierie tissulaire car il est non toxique et biorésorbable. Des modifications de surface permettent de controler sa vitesse de dégradation et peuvent favoriser l'adhésion cellulaire. Les cellules souches de la pulpe dentaire (DPSC) sont des cellules souches mésenchymateuses retrouvées dans la pulpe dentaire, à l'intérieur des dents, et constituent une source accessible de cellules souches. Regrouper les capacités de prolifération et différenciation des DPSC avec les propriétés morphologiques et biochimiques du pSi représente une approche intéressante pour des applications thérapeutiques de médecine régénératrice. Dans cette thèse, nous avons étudié le comportement de DPSC humaines sur des supports de pSi, avec des pores variant de quelques nanomètres à plusieurs centaines de nanomètres. Nous avons travaillé sur différentes fonctionalisations chimiques afin d'optimiser l'adhésion cellulaire et de stabiliser le matériau: oxydation thermique, silanisation et hydrosilylation. L'adhésion, la prolifération et la différenciation osseuse ont été évaluées par microscopie à fluorescence, microscopie électronique à balayage, activité enzymatique, tests de prolifération (activité mitotique), immunofluorescence et spectroscopie FTIR. Le pSi avec des pores de 30 à 40 nm de diamètre s'est révélé être le plus approprié pour l'adhésion, la prolifération cellulaire et la différenciation ostéoblastique. De plus, la structure nanométrique et le relargage d'acide silicique par le pSi a démontré un effet positif sur l'induction osseuse et la formation d'une matrice minéralisée. Le pSi est donc apparu comme un matériau prometteur pour l'adhésion de cellules souches mésenchymateuses, que ce soit pour une transplantation immédiate *in vivo* ou pour expansion et différenciation *in vitro*.

Abstract in english:

Porous silicon (pSi) is a promising biomaterial for tissue engineering as it is both non-toxic and bioresorbable. Moreover, surface modification can offer control over the degradation rate of pSi and can also promote cell adhesion. Dental pulp stem cells (DPSC) are mesenchymal stem cells found within the teeth and constitute a readily source of stem cells. Coupling the good proliferation and differentiation capacities of DPSC with the textural and chemical properties of the pSi substrates provides an interesting approach for therapeutic use. In this thesis, the behavior of human DPSC is analyzed on pSi substrates presenting pore of various sizes, from few to hundreds nanometers. We investigated different chemical surface treatments, in order to enhance cell adhesion and stabilize the material: thermal oxidation, silanization and hydrosilylation. DPSC adhesion, proliferation and further osteodifferentiation were followed for up to 3 weeks by fluorescence microscopy, scanning electron microscopy (SEM), enzymatic activity assay, BrdU assay for mitotic activity, immunostaining and FTIR spectroscopy. Porous Silicon with pore size ranging from 30 to 40 nm was found to offer the best adhesion, the fastest growth rate for DPSC and the highest osteoinductive effect. Moreover, the pSi nanostructure and the release of silicic acid had a positive effect on precursor cells osteodifferentiation and mineralized matrix formation. Porous silicon appeared to be an appropriate biomaterial for mesenchymal stem cells adhesion and immediate *in vivo* transplantation, or for long term *in vitro* culture, for stem cells proliferation and differentiation.

Table of contents

Acknowledgements

Madame le Professeur Dominique Deville de Périère,
« Respectueux et reconnaissant envers mes Maîtres, je rendrai à leurs enfants l'instruction que j'ai reçue de leurs pères ». Vous avez été présente durant tout mon cursus, dès mon arrivée à l'Université Montpellier 1. Je vous remercie de l'honneur que vous m'avez fait en acceptant la direction de cette thèse, et vous assure de mon respect et ma reconnaissance.

Monsieur le Professeur Frédéric Cuisinier,
Mon parcours scientifique, dans son intégralité, s'est fait grâce à vous. Je vous suis autant redevable que reconnaissant. L'apprentissage à vos côtés restera un élément fondateur de ma vie professionnelle. Merci.

Madame le Docteur Frédérique Cunin,
Je vous remercie pour votre encadrement, votre soutien et votre patience durant ma thèse. Vous m'avez fait découvrir tout un monde dont j'ignorais jusqu'à l'existence. J'espère de tout cœur avoir l'opportunité de poursuivre cette collaboration.

Madame le Professeur Csilla Gergely,
Je ne saurais exprimer suffisamment ma reconnaissance en quelques mots. Votre présence a été primordiale dans l'avancement de mon travail scientifique. Et votre profonde humanité a été un soutien permanent, tant professionnel que personnel. Merci.

Monsieur le Docteur Philippe Kémoun,
Votre présence dans ce jury est très importante pour moi. Vous avez été, et demeurez pour moi, la personne de référence en ce qui concerne les cellules souches dentaires. Merci pour votre disponibilité et votre bienveillance durant ces années de thèse.

Professor Raùl Martìn Palma,
This is a great pleasure and honor for me to have you in my thesis jury. Your expertise in the field of porous silicon and its biological applications are of prime interest for me. I thank you for evaluating my work.

Monsieur le Docteur Guy Ladam,
Je vous suis tout particulièrement reconnaissant d'avoir accepté d'être rapporteur de cette thèse, alors que vous étiez déjà en charge d'un autre rapport. Vous m'avez déjà été présenté comme un modèle à suivre.

Professor Nico Voelcker,
The four months spent in your lab have been a very good experience for me. Thank you for your disponibility in building and following research projects. We still have some works in progress. I wish I could work in your team again.

Monsieur le Docteur Jean-Olivier Durand,
Depuis le début de mon projet de thèse, vous avez été là. Je vous remercie pour votre présence discrète et votre expertise reconnue qui ont accompagné mes travaux. Vous avez contribué au point central de ma thèse, à savoir l'approche multidisciplinaire.

Remerciements personnels / Personal thanks

Emeline Collart Dutilleul : Tu es si précieuse et formidable. J'ai bien fait de t'épouser !
A ma famille : mes chers parents, frères et belles-sœurs, sœur et beau-frère, et mes admirables et abondants neveux et nièces.
« Pour toi, reste attaché à tout ce que tu as appris et reçu avec une entière conviction. Tu sais de qui tu l'as appris »

Au laboratoire BioSanté et Nanoscience EA 4203, et ses collaborateurs du LCC-GES :
Nous avons partagé 5 années de vie, tant professionnelle que personnelle. Sous la bienveillante supervision de Frédéric et Csilla, avec la modération de Bernard Levallois, l'expertise de Marta Martin et Thierry Cloitre, et l'encadrement de Hélène, Elodie, Catherine et Alban. Une pensée sincère pour mes co-thésards : Hamideh et Ivan. Et mes chaleureuses salutations à tout l'équipe : Marie-Alix, Amel, Farès, Satish (*brother from another mother*), Olivier Romieu, Chakib (pour nous, tu fait toujours partie de l'équipe), Wafa, Michel Fages, Jacques-Henri Torrès, Jean-Cédric, Bruno Jacquot, Matthieu, Yohan, Philippe et tous les autres, dont la présence est importante.
Quelques remerciements plus spécifiques à Marta qui est à la fois mon encadrante et mon amie et à Cyril, à Emilie Secret qui a fabriqué de si nombreux échantillons de pSi, à Pierre Jacquemart qui m'a toujours accueilli au bloc, à Franck Chaubron, Marion, Severine et Catherine pour la collaboration avec l'Institut Clinident BioPharma, et à Christophe Hirtz avec qui le contact est resté intact.
Warm greetings to the Voelcker laboratory, Mawson Institute, University of South Australia, with special thought to my dear friend Ruth Zoehrer, to Sandhya, Fran, Steve.
Je remercie également l'école doctorale CBS2 et surtout l'Asso cbs2, qui arrive à donner une belle dynamique à notre formation.

A mes chers amis, que je ne vais pas tous citer...
De la Pompignane : vous êtes précieux pour nous. La fraternité existe, vraiment!
De la bande à choco « j'allais me coucher, mais je me suis aperçu que je vous aimais trop »
De la fac... De toujours...
Quelques remerciements plus spécifiques à Anne et Robby qui ont relu et corrigé l'anglais de ce manuscrit, à Monsieur Alban Desoutter qui m'a soutenu jusqu'au 42e km, et aux bons amis.

List of abbreviations

ACP	Amorphous Calcium Phosphate
AFM	Atomic Force Microscopy
ALP	Alkaline Phosphatase
APTES	Aminopropyltriethoxysilane
BMP	Bone Morphogenic Protein
BrdU	BromodeoxyUridine
BSA	Bovine Serum Albumine
BSP	Bone Sialeprotein
CD	Cluster of Differentiation
DPSC	Dental Pulp Stem Cell
ECM	Extra Cellular Matrix
FACS	Fluorescence-Activated Cell Sorting
FDA	Fluorescein Diacetate
MEM	Minimum Essential Medium
MSC	Mesenchymal Stem Cell
OD	Optical Density
OCN	Osteocalcin
OM	Osteogenic Medium
PBS	Phosphate Buffer Saline
PI	Propidium Iodide
pNPP	para Nitrophenylphosphate
pSi	Porous Silicon
RGD	Arginine – Glycine – Aspartic Acid peptide
RNA	Ribonucleic Acid
SBF	Simulated Body Fluid
SCF	Stem Cell Factor
SEM	Scanning Electron Microscopy

Chapter 1 Porous Silicon Scaffolds for Stem Cells Culture and Bone Tissue Engineering

Numerous studies have been carried out to verify if stem cells could become a source of stable differentiated cells capable of inducing tissue formation, including mineralized hard tissue. Stem cells for hard tissue formation has considerably increased attention of researchers as these cells can be an interesting source of stable differentiated cells, able to induce bone formation ie secretion of an organic matrix and hydroxyapatite crystal growth. Stem cells of various origins are able to produce *in vitro* calcified nodules and to form a mineralized tissue after transplantation *in vivo*. The property to form mineralized tissue is found in normal calcification system and also in pathological conditions and involves many cell types (Huitema *et al.*, 2007). Supporting scaffolds for bone tissue engineering are often required to lead cell implantation, growth and differentiation (D'Aquino *et al.*, 2007; Graziano *et al.*, 2008). These scaffolds can be inductive or instructive to direct stem cells down specific lineage pathways and increase the therapeutic effect. Thus, directed stem cells have the potential for rapid bone regeneration and repair. Since the advent of tissue engineering, bone has received particular interest as it is one of the tissue with most regenerative abilities in the human body and because of it apparent simplicity.

Porous silicon (pSi) is a promising biomaterial for bone tissue engineering, as it is non-toxic, it is bioresorbable and it can be inductive for osteodifferentiation. It has the ability to degrade in aqueous solutions into non-toxic silicic acid and surface modifications offer control over the degradation rate of pSi (Low et al., 2006). Moreover, this tunable, biocompatible and resorbable material has been reported for the growth of hydroxyapatite, inferring the possible bone implantibility of the material (Cahnam, 1995).

1.1 Stem cells for bone tissue engineering

The first cell-based strategy for bone repair was autologous connective tissue progenitors from the iliac crest. This autograft procedure was accomplished without any *in vitro* manipulation, and was thus considered as part of the surgical procedure (Conolly *et al.*, 1991). However, bone graft is not always possible, as it injures the donor site, and the success of grafting is entirely dependent on the transfer of sufficient numbers of progenitor cells. In addition, this approach may be least applicable in situations where it is most needed, such as in the case of ageing or disease with a reduction of osteogenic progenitors. Stem cell therapy involves *in vitro* sorting and expansion, before cell grafting. Cells can be of autologous or allogenic origin. Autologous grafts offer the optimal compatibility, but require available cells from the patients. Therefore, allogenic grafts with cells from alternative allogenic source are of great interest, as they could provide “ready for use” products for bone treatments.

1.1.1 Adult, neonatal and embryonic stem cells

1.1.1.1 Adult mesenchymal stem cells: Bone Marrow, Adipose tissue and Dental Pulp-derived stem cells

It has been shown that plastic adherent human cells derived from bone marrow were able to differentiate into a number of mesenchymal cell types including osteoblasts, chondrocytes and adipocytes. These cells were called “mesenchymal stem cells (MSCs)” in reference to their high self-renewing properties, clonogenicity, and ability to form cartilage and bone (Figure 1.1). They were suggested to be responsible for the normal turnover and maintenance of adult mesenchymal tissues. These MSC have been defined to be plastic-adherent when maintained in standard culture conditions; they must express CD105, CD73 and CD90, and lack expression of CD45 and CD34 (hematopoietic markers) surface molecules; and they must also differentiate to osteoblasts, adipocytes and chondroblasts *in vitro* (Dominici *et al.*, 2006). MSC’s therapeutic potential has generated significant excitement in the field of regenerative medicine, as they can be found in various niches within human body. The ability of these cells to self-renew and differentiate into multiple tissues makes them an attractive cell source for cell-based regenerative therapies. MSCs have considerable potential for the treatment of musculoskeletal disorders owing to their expansion capacity, immunosuppressive properties and ability to differentiate into bone and cartilage (Ma, 2010).

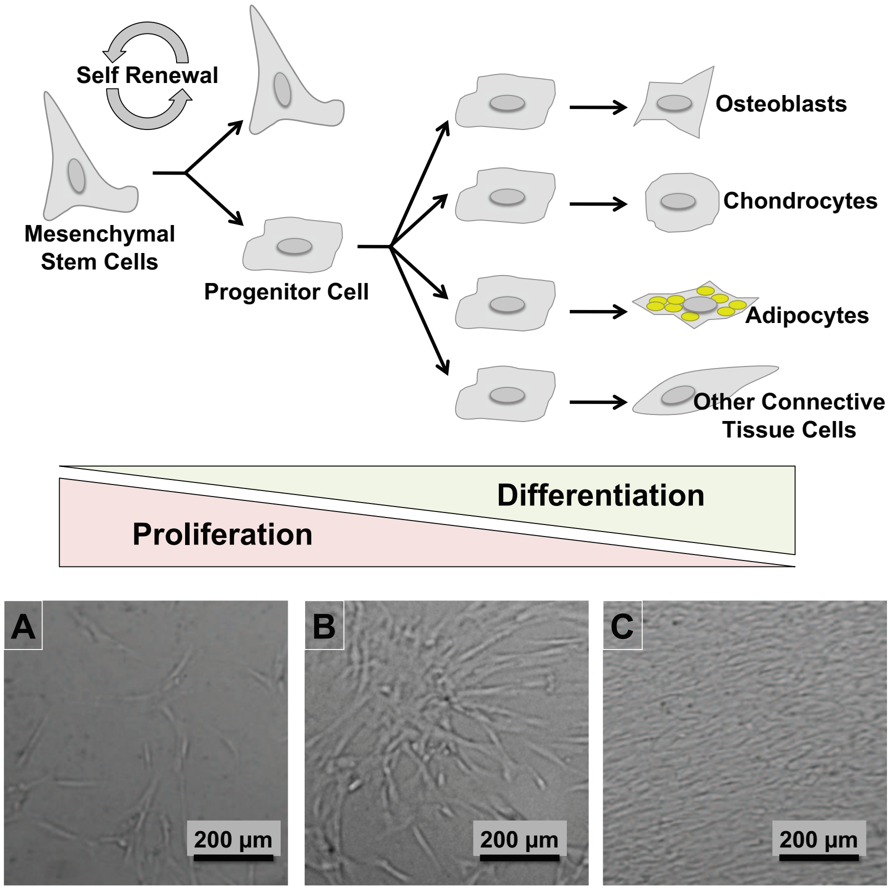

Figure 1.1: Proliferation and differentiation model of mesenchymal stem cells, illustrating their high self-renewing properties, clonogenicity, and ability to form various tissues, such as bone, cartilage, adipose tissue and other connective tissues. Images A, B and C present optical microscopy images of mesenchymal stem cells in vitro, proliferating (A) to form progenitor cells colonies (B) and starting to differentiate when reaching confluence (C).

The most studied source of adult MSCs has been the bone marrow, as it was recognized early that its stroma contained stem cells capable of forming bone and cartilage. Later, other sources of adult stem cells have been described, such as adipose tissue, dental pulp, skeletal muscle, umbilical cord blood and others (Marolt *et al.*, 2010).

1.1.1.1.1 Bone marrow mesenchymal stem cells (BMSCs)

BMSCs are commonly recovered from pure bone marrow aspirates and isolated according to their adherence and culture on tissue culture plastics. They can be also selected using specific cell surface markers, and then expanded in culture. The number of stem cells varies between different patients. Age and marrow aspiration volume influence also the number of isolated stem cells. BMSCs can, however, be expanded in vitro to large numbers and keep their osteogenic potential even in older patients (Bianco et al., 2001).

1.1.1.1.2 Adipose-derived stem cells (ADSCs)

Zuk *et al.* (2002) have been the first to describe and characterise ADSCs from human lipoaspirates. They showed that a multi-lineage stem cell population could be isolated from the stromo-vascular fraction of adipose tissue. These ADSCs are able to differentiate into osteoblasts, can be recovered from raw lipoaspirates consecutive through liposuction under anaesthesia, and represent an important niche of adult stem cells. They have been extensively studied in vitro for their ability to form various tissues, including bone-like tissue.

1.1.1.1.3 Dental pulp stem cells (DPSCs)

Stem cells within the dental pulp have been first described by Gronthos *et al.* (2000). They have then been studied and characterised as an adult stem-cell population that possesses the properties of high proliferative potential, the capacity of self-renewal and multi-lineage differentiation. Dental pulp can be easily collected from adult (DPSC) or deciduous teeth (stem cells from human exfoliated deciduous teeth) after dental extraction, when teeth have to be removed (Figure 1.2). The most frequent case is the collection of normal human third molar extracted for orthodontic reasons (Gronthos *et al.*, 2002).

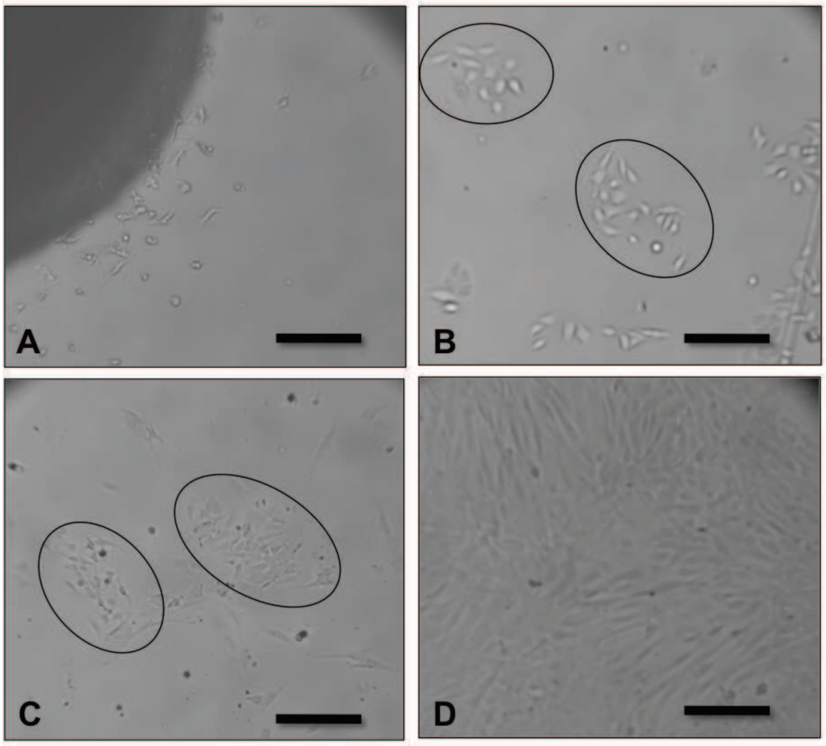

Figure 1.2: Human mesenchymal stem cells from dental pulp. A: Stem cells outgrow from pulp tissue explants. B, C, D: stem cells colonies formed after digestion and being plated in culture dishes. Colonies formed in 3 and 5 days (A and B respectively), cells reaching confluence after 10 days (D). Scale bar: 300µm. From Collart Dutilleul *et al.* (2014)

1.1.1.2 Embryonic stem cells (ESCs)

ESCs from rat or other animal origin are widely used in research. But for biomedical applications, ESCs have to be of human origin, which leads to technical and ethical issues. Human ESCs are harvested from pre-implanted embryos from the inner-cell mass before the first 2 weeks of development. These cells are obtained from extra embryos developed by in vitro fertilization techniques, or from embryos derived from voluntary interruption of pregnancy. They proliferate *in vitro* while maintaining an undifferentiated state and are capable of differentiating into many somatic cell types. Although they show great capacities for cell therapy and tissue engineering, these particular cells create a delicate ethical debate, as they induce destruction of human embryos.

1.1.1.3 Neonatal stem cells from the umbilical cord

Neonatal tissues constitute a stem cell source that can be accessed in a non-invasive and rapid manner during and just after birth. The main source is the umbilical cord, covered by an amniotic epithelium that protects a gelatinous matrix called "Wharton's jelly". Stem cells can be recovered during birth, *in utero* or *ex utero*, from both cord blood and cord matrix (Wharton's jelly) (Forraz and McGuckin, 2011). Cord blood can be collected using a collecting needle connected to an anticoagulant-containing bag. Wharton's jelly is obtained by collecting the whole umbilical cord. With the average umbilical cord measuring 50 cm, this source of MSCs might become more and more clinically relevant.

1.1.2 Stem cells osteodifferentiation and bone formation

Bone tissue is composed of matrix and cells: bone matrix is mainly built of type I collagen (90%), with non-collagenous proteins (such as osteocalcin, osteonectin, bone sialoproteins). These scarce non-collagenous proteins participate in matrix maturation and mineralization. Osteoblasts and osteoclasts are responsible for bone formation and bone resorption. With progenitor cells, they mediate the mechanism of bone remodelling. During bone formation phase, the osteoblasts are recruited from MSC in bone marrow, since osteoclasts are derived from haematopoietic cells. Thus, stem cell therapy for bone regeneration will focus on MSC for osteoblastic differentiation, since host cells will provide osteoclasts during vascularisation process.

1.1.2.1 Molecular control of osteogenesis

Bone repair consists in inflammation, intra membranous ossification, chondrogenesis, endochondral ossification and remodelling. Li *et al.* (2007) have described molecular events that regulate osteogenesis: they observed an upregulation of genes related to cell cycle and cell-to-cell signalling, confirming the fact that both cell division and communication are essential to initiate bone healing. MSCs proliferate and differentiate under the influence of a number of molecular pathways, but MAPK (mitogen-activated protein kinase) signalling plays a pivotal role in osteogenic induction. MAPK pathway is activated by a variety of growth factors such as FGF (fibroblast growth factors), PDGF (platelet derived growth factors), TGF-β (transforming growth factor beta), BMP (bone morphogenic proteins) and IGF (insulin-like growth factors). These extracellular signals activate a signalling cascade of MAP kinase inside the cell, resulting in cell proliferation and osteodifferentiation. Another pathway involved in osteodifferentiation is the Wnt signalling pathway: Wnt represents a family of secreted molecules that are involved in various aspects of cellular biology, including cell growth, differentiation and death. The binding of Wnt proteins permits the translocation of β-catenin into the nucleus, resulting in an enhanced expression and activity of the osteogenic promoter Runx2. Wnt signalling and Hedgehog signalling cooperate in controlling bone formation, especially at the early stage of osteoblast formation, initiating cellular differentiation. Cell−cell interactions are also required for activating some signalling cascade: Notch signalling and Ephrin signalling are the main cell-cell interaction pathways. Notch receptors and ligands are membrane proteins able to up-regulate bone related genes to favour the proliferation of immature osteoblasts, while limiting osteoblast maturation by inhibiting the Runx2 transactivation function. Ephrin ligands and receptors are also membrane proteins. They are constituted by two classes of ephrins: the B class ephrin ligands and receptors (EphB-Tyrosine Kinase receptor) induce osteogenic transcription factors, and inhibit osteoclast differentiation, leading to bone formation. EphrinA/EphA receptor interaction facilitates bone remodelling by suppressing osteoblast differentiation and activating osteoclast differentiation (Figure 1.3, next page).

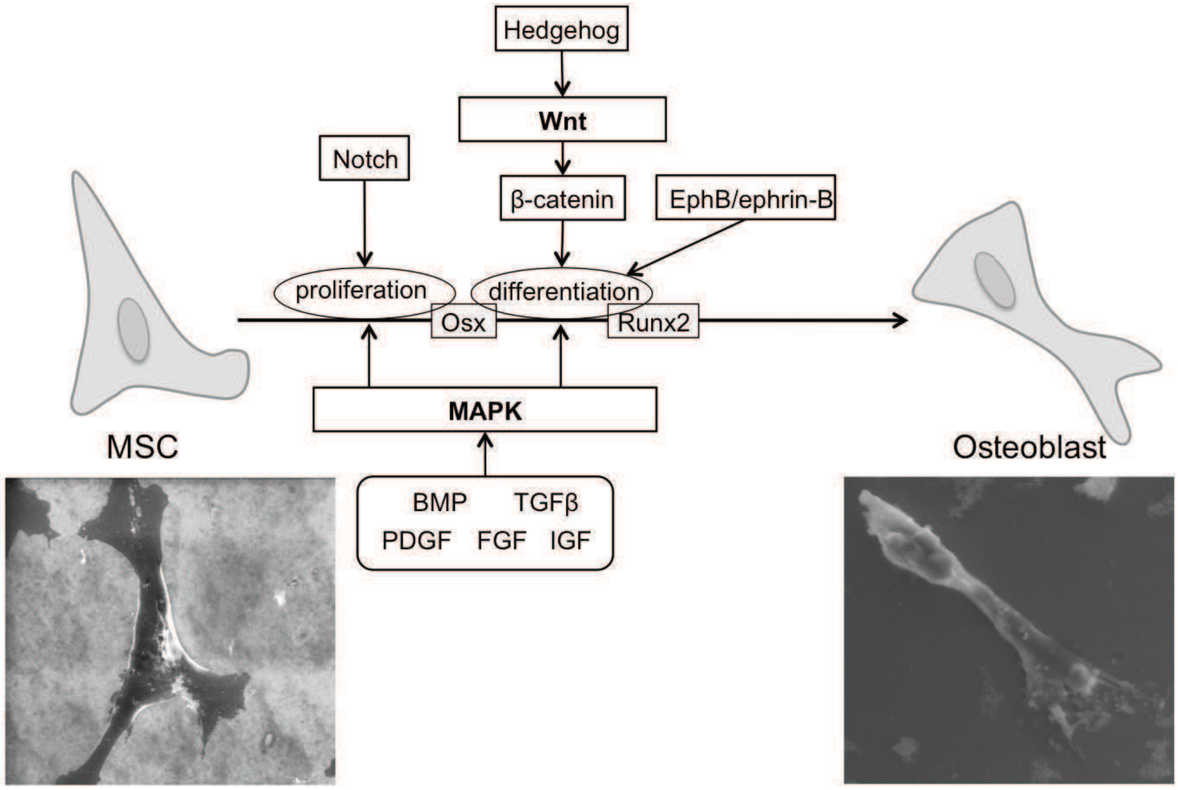

Figure 1.3: Schematic representation of the principal signalling networks and transcription factors regulating osteoblast differentiation and osteogenesis. Scanning electron microscopy of a mesenchymal stem cell (MSC, original magnification x2000) and of an osteoblast differentiated *in vitro* from MSC (original magnification x2000). BMP: bone morphogenic protein, TGFβ: transforming growth factor, PDGF: platelet derived growth factor, FGF: fibroblast growth factors, IGF: insulin-like growth factor, MAPK: mitogen-activated protein kinase. From Collart Dutilleul *et al.* (2014)

1.1.2.2 Osteoblastic differentiation *in vitro* and *in vivo*

MSCs are capable of osteodifferentiation in vitro under appropriate conditions. This differentiation is induced through addition of various molecules and chemicals, such as dexamethasone, ascorbic acid and β-glycerophosphate. Osteoblast-specific genes expression and proteins demonstrate this in vitro differentiation. However, in vitro assays have limitations and there is always a need to verify osteoblast differentiation potential in vivo. Thus, it has been shown that osteoprogenitor cells can only form bone tissue when transplanted in vivo, while MSCs can form both bone and bone microenvironment supporting haematopoesis in vivo. Moreover, MSCs demonstrate self-renewal and maintenance of stemness capacity during in vivo implantation (Arvidson *et al.*, 2011).

1.1.2.3 Stem cells potential for scaffold-based bone tissue engineering applications

ESCs and adult (or neonatal) MSCs are the main types of stem cells usable for scaffold-based tissue engineering. However, ESCs have a limited applicability to human cell therapy due to ethical concerns, but also immunological incompatibilities, potential for malignant tumor growth and insufficient understanding and control over differentiation. Thus, adult MSCs seem to be the cell type of choice for scaffold-based therapeutic applications. MSC delivery to the site of bone tissue defects requires scaffolds adapted to cell culture and activity in endogenous osteogenesis, including correct biochemical and mechanical stimuli.

1.2 Stem cells and mineralization process

Biomineralization is a general process by which inorganic calcium phosphate crystals are produced in biological environments. For bone formation, deposition of calcium phosphate salts occurs on an extracellular organic matrix by means of a heterogeneous nucleation process, which constitutes the first stage of hard tissue mineralization (Ngankan *et al.*, 2000).

1.2.1 Biomineralization process: Ions and nucleation sites

Bone biominerals are composed of complex structures, having precise architectural order over several length scales. They rely on their biological constituents for regulation of mineralization, forming an organic-inorganic hybrid structure. The formation mechanisms of biomineralization involving several possible pathways remain unclear. Biomineralization has been described to start with matrix vesicle-mediated mineral initiation. It also involves heterogeneous nucleation of mineral crystals with an important role played by non-collagenous glycoproteins that bind calcium and collagen.

Calcium phosphate crystals can be formed via stable pre-nucleation clusters, with aggregation into an amorphous precursor phase, then transformation of this phase into a crystal (Cölfen, 2010). Nudelman *et al.* (2010) demonstrated that collagen forms the structural matrix and has an active role in the mineralization of apatite for bone formation. Indeed, collagen fibrils have positively charged regions, and these nanosized regions can be used for mineral infiltration and charge-charge attractions. This initial mineral deposition leads to a dense network of pre-nucleation clusters, to transformation into amorphous calcium phosphate and to oriented crystalline hydroxyapatite inside the fibrils (Figure 1.4, next page). Even though the biomineralization process has been mainly studied with *in vitro* models (and *in vivo* bone formation may follow different rules), observations in small animals and tooth formation suggest that at least part of the mineralization mechanism of the collagen model is relevant for *in vivo* systems (Beniash *et al.*, 2009).

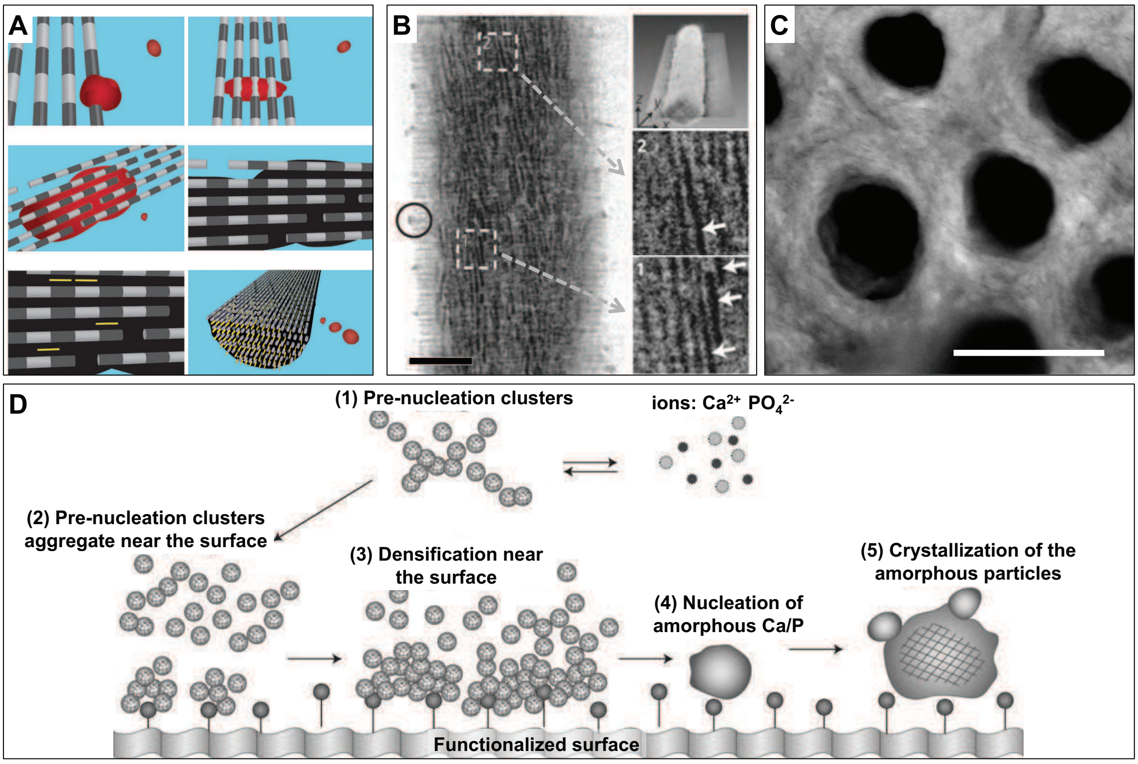

Figure 1.4: Schematic representation of biomineralization process, describing matrix vesicle-mediated mineral initiation. (A) Mineralization of a collagen fibril, with calcium phosphate mineral droplets (red) binding to collagen fibers and entering the fibrils. Once inside the collagen, the mineral in a liquid state diffuses through the interior of the fibril and solidifies into an amorphous phase (black). Finally, directed by the collagen, the amorphous mineral transforms into oriented apatite crystals (yellow). (B) Two-dimensional cryo TEM image of a mineralized collagen fiber. Crystals are visible on insets 1 and 2 (white arrows). Scale bar = 100 nm (C) SEM image of mineralized collagen fibers (dentin tissue from a human tooth). Scale bar = 2 μm. (D) Surface-directed mineralization of calcium phosphate. (1) Aggregates of pre-nucleation clusters are in equilibrium with ions in solution. (2) Pre-nucleation clusters approach and aggregate near the functionalized surface. (3) Further aggregation causes densification near the surface. (4) Nucleation of amorphous spherical particles occurs at the surface. (5) Crystallization occurs in the region of the amorphous particles directed by the surface. Adapted from Cölfen *et al.* (2010), Nudelman *et al.* (2010) and Collart Dutilleul *et al.* (2013)

1.2.2 Collagen and calcium-phosphate deposition during osteodifferentiation

Calcium and inorganic phosphate are the two main constituents of hydroxyapatite, the bone mineral that give mechanical resistance to the organic matrix. The Ca/P mass ratio in bone is 2.2, and the initial step of Ca-P crystal nucleation takes place within matrix vesicles that appears from the plasma membrane of osteogenic cells and migrates into the extracellular skeletal compartment. Phosphate accumulates inside these matrix vesicles by a transport system, followed by an influx of calcium ions. This process permits the formation of hydroxyapatite crystal, associated with organic matrix collagen fibrils. Collagen is synthesized and assembled by osteoprogenitors, following a classical pathway for a secreted protein. The collagen chains are synthesized as precursors, and undergo a series of maturation reaction such as glycosylation and hydroxylation in the endoplasmic reticulum and Golgi complex. They are then assembled to form a triple helix. After processing and assembly, this type I procollagen is secreted into the extracellular space, where it will mature and polymerize into normal fibrils. Thus, collagen, calcium and phosphate are provided to the extracellular space through osteoprogenitors. During osteodifferentiation MSCs will turn into progenitor cells, then osteoblasts, expressing type I collagen genes.

1.3 Porous silicon scaffolds

Porous silicon (pSi) is a nanostructured form of the chemical element silicon that has introduced nanoporous holes in its microstructure, rendering a large surface to volume ratio. It is a semiconductor material created by electrochemical techniques, having electrical conductivity to a degree between that of metal and that of glass (insulator). Porous silicon was accidentally discovered in the 50's as an undesired product of experimental methods for polishing and shaping silicon surfaces for use as semiconductors: under certain conditions the combination of acid etching and anodic current resulted in the formation of a thick black, red or brown film on the material's surface. This was regarded as a failure for the purposes of polishing until the 70's when a interests arose because the high surface area of porous silicon was found to be useful as a model of the crystalline silicon surface in spectroscopic studies and as a dielectric layer in capacitance-based chemical sensors (Sailor, 2011). In the 90's, pSi was evaluated as biomaterial, especially as bone implantable material: the huge surface area of silicon exposed by the pores relative to the volume, coupled with the covalently bonded hydrogen on the surface, renders pSi soluble in water and aqueous solutions (Cahnam, 1995).

1.3.1 Porous silicon fabrication and degradation

1.3.1.1 Fabrication

Porous silicon is generated by etching crystalline silicon in aqueous or non-aqueous electrolytes containing hydrofluoric acid (HF). Under appropriate electrochemical conditions, the silicon wafer doesn't dissolve uniformly but instead, fine holes appears, propagating primarily in the <100> (x;y;z) direction in the wafer. The most common method is through anodization with a platinum cathode and a silicon wafer anode, both immersed in a hydrofluoric acid electrolyte. A direct current, passed through the set-up, corrodes the anode wafer, producing a porous layer (Figure 1.5, next page). The pore diameter and depth can be controlled by HF concentration, with longer and narrower pores produced by concentrated HF solutions. Once the wafer is fully etched, the created pSi can be rinsed in ethanol then dried under nitrogen airflow. Pore width is classified into 3 sizes, according to the pore diameters: less than 2 nm as nanoporous, from 2 to 50 nm as mesoporous and larger than 50 nm as macroporous (Sailor, 2011).

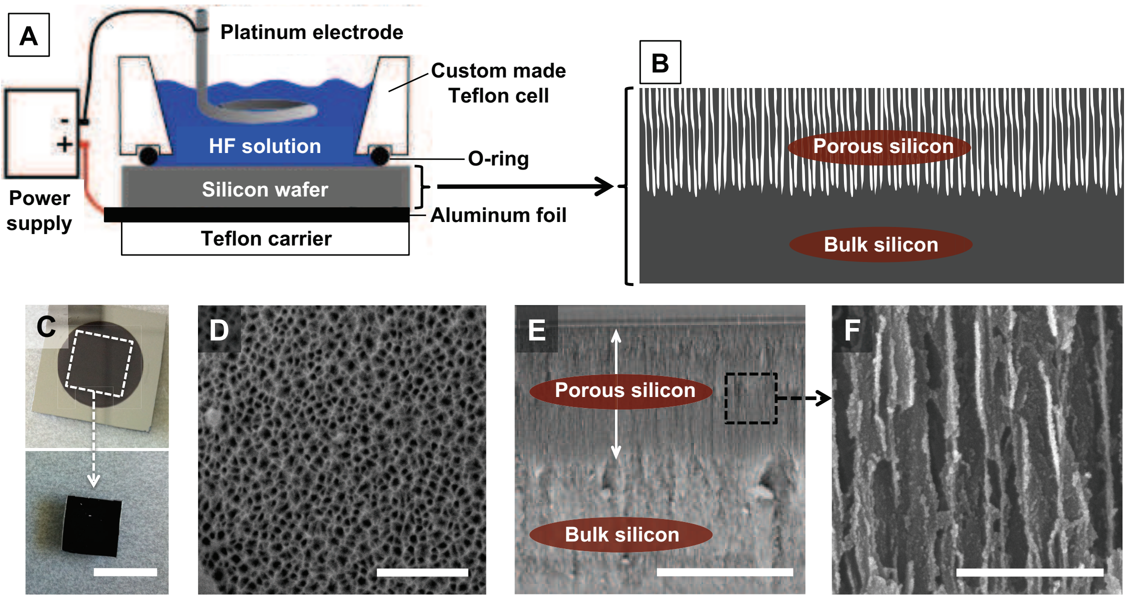

Figure 1.5: Schematic representation of an electrochemical set-up used to make porous silicon. (A) Schematic side view of the custom made set-up. Silicon is the anode and platinum electrode is the cathode. (B) Schematic side view of the silicon wafer after etching, with a superficial porous part (porous silicon) and an unetched part (bulk silicon). (C) Top view photograph of a freshly etched silicon wafer. The black area is the porous part while the mirror area is the unetched part. The etched area is round because of the O-ring in the set-up. Samples are cut in square to remove the unetched surfaces. Scale bar = 1 cm. (D) SEM image of pSi surface. Scale bar = 500 nm. (E) and (F) SEM images of pSi: cross section of the wafer. E: Scale bar = 10 µm. F: Scale bar = 300 nm. Adapted from Alvarez *et al.* (2009) and personal data.

1.3.1.2 Degradation in aqueous solutions

Due to the large surface area of Si-H on the surface and interior space of the material, pSi is soluble in water and aqueous solutions, dissolving along the mechanism:

$$Si + 4\ H_2O \longrightarrow Si(OH)_4 + 2\ H_2$$

Orthosilicic acid $Si(OH)_4$ is liberated from the surface of the decomposing pSi in addition to hydrogen gas. Silicic acid is the form of bioavailable silicon in human body, under physiological conditions. It is mainly found in foods rich in fiber and whole grains, with beer being one of the main sources of this element in the diet (González-Muñoz *et al.*, 2008).

Surface treatment resulting in accessible porosity with chemically stable inner surface is a key step to prevent rapid hydrolysis and degradation of the pSi in aqueous solutions. The most common and simple surface treatment is oxidation, which can be performed by either ozone, aging, thermal or chemical treatments and creates Si-OH bounds on the surface. Amine-terminated modifications as silanization with aminopropyl trimethoxysilane or triethoxysilane improve pSi chemical stability (Low *et al.*, 2006). Thermal hydrosilylation can also be used to graft chemical species, such as dodecene, undecenoic acid or oligoethylene glycol (Alvarez *et al.*, 2009).

1.3.1.3 Biological activity and biocompatibility

Silicon is an very abundant element, constituting the majority of mineral found on earth, as sand, quartz, agate, amethyst, rock crystal, flint, chalcedony, jasper and opal in combination with other elements. But despite this abundance, silicon is rarely found in biology, forming only 0.02% of the human body by weight. However, silicon plays an important role in connective tissue, such as bone and cartilage, for the formation of organic matrix (collagen and glycosaminoglycan). Silicon is a major ion of osteogenic cells and participates in the biochemistry of subcellular enzyme-containing structures, highlighting its metabolic role in connective tissue (Carlisle *et al.*, 1988).

Soluble silicic acid, the biologically active form of silicon, is mainly absorbed for man from silicic acid-containing drinking water, beverages made from phytoliths-containing plants (mainly beer) and some food (mainly banana and green bean). In western countries diet, beer and bananas form the main source of bioavailable silicon for men, while the main source for women are bananas and green beans (Jugdaohsingh *et al.*, 2002).

For biomedical applications, porous silicon biocompatibility and immunogenicity have already been demonstrated under different conditions (Ainslie *et al.*, 2008). Furthermore, pSi-based scaffolds have been investigated for orthopaedic (Whitehead *et al.*, 2008) and ophtalmic implants (Cheng *et al.*, 2008), for controlling the adhesion and proliferation of different cell types (Low *et al.*, 2006)(Alvarez *et al.*, 2009) (Torres-Costa *et al.*, 2012), and even as intravenously injectable particles for imaging tumors in vivo (Park *et al.*, 2009) or retina pressure actuators (Muñoz-Noval *et al.*, 2013).

1.3.2 Influence of pore size, nanoroughness and chemical surface treatment

To mimic the *in vivo* cell behavior for *in vitro* culture, one should consider scaffold chemistry, mechanical properties and architecture (Yang *et al.*, 2012). An extra-cellular matrix is composed of various proteins within a 3D network. Thus, a scaffold for tissue engineering should provide optimal mechanical properties and environment for cell culture. PSi can be designed to mimic the properties of bone tissue, and coatings can impart proper surface chemistry, adapting various pore size, porosity and nanoroughness. Indeed, nanotopography can affect protein adsorption, cytoskeletal arrangement, and cell adhesion and spreading.

1.3.2.1 Influence of pSi pore size on MSC adhesion

The effect of pore size and porosity on cell growth is of particular relevance, as it will direct the fabrication of a porous biomaterial. Additionally, its biocompatibility depends on its porosity and pore size. These pore dimensions can be precisely controlled and are highly tunable during pSi electrochemical anodization or etching. A variety of pore sizes can be produced: from micropores (< 2 nm), mesopores (2−50 nm) to macropores (> 50 nm) depending on the preparation conditions (Sailor, 2011). Although microscale topography modulates cellular behavior *in vitro*, it is important to consider that cells *in vivo* make contact with nanoscale as well as microscale topographical features. Even if cells are typically tens of microns in diameter, the dimension of subcellular structures tends to the nanometer scale. Furthermore, extracellular supporting tissues present an intricate network of cues at the nanoscale composed of a complex mixture of nanometer-size (5−200 nm) pits, pores, protrusions, and fibers (Biggs *et al.*, 2010). The main mean to evaluate the influence of pore size on MSCs adhesion and proliferation is the use of pSi gradients, allowing cells growth on surface with a pore range from few nanometers to few micrometers: this method involves electrochemical etching of crystalline Si in a hydrofluoric acid (HF) solution to fabricate pSi films displaying a gradient of pore sizes in an asymmetrical arrangement. The size range of these pores can be controlled by modifying the applied current and the HF (Collins et *al.*, 2012; Clements *et al.*, 2012). Different cell types respond differently to topographical features, such as nanoscale pores and studies demonstrated that MSCs show better attachment to pSi with pore size of 20–30 nm in diameter (Wang *et al.*, 2012). Pore size in this range is similar to the pore size of biological systems, such as pores in basement membranes, and corresponds to the size of biological pits, pores, protrusions and fibers (Figure 1.6). While producing pSi, pore depth can also vary. However, cells are not sensitive to changes in pore depth of the range observed with various type of pSi (Low *et al.*, 2006).

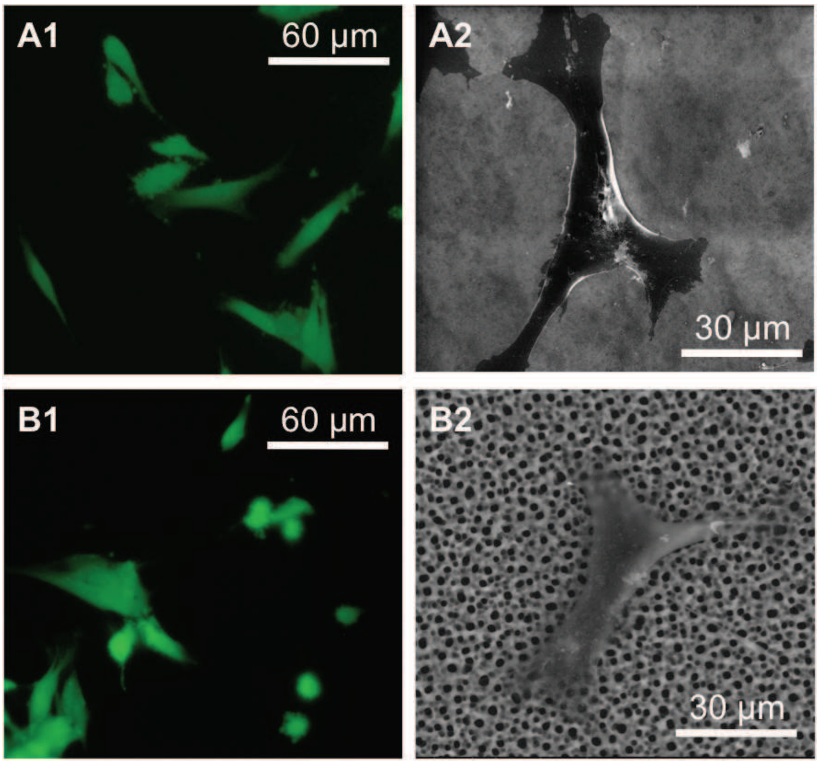

Figure 1.6: Epifluorescence microscopy and SEM of MSC culture on pSi, after 24H of culture. A: mean pore size = 30 nm. A1 and A2: epifluorescence microscopy and SEM, respectively. B: mean pore size = 1 µm. B1 and B2: epifluorescence microscopy and SEM, respectively. Cells present a better adhesion on pSi with small pore size, compared to pSi with large pores: cells recover a more physiological shape (A1) and spread more (A2) on 30nm-pSi, while cells are more bulging and spread less on 1 µm-pSi (B1 and B2). From Collart Dutilleul *et al.* (2014)

1.3.2.2 Optimal surface treatment and coating for cells adhesion

MSCs were shown to respond to both topographical and chemical characteristics. However, chemical surface treatment and grafting of proteins seem to have a higher impact than changes in pore size during short-term culture (Clements *et al.*, 2012). PSi surface treatment is necessary not only to improve cell adhesion, but firstly to permit accessible and stable pores: the inner walls of the porous matrix must be protected from an excessive degradation in the aqueous cell culture environment without eliciting any undesirable effects on the cells. Moreover, surface modification by turning pSi from hydrophobic to hydrophilic promotes cell adhesion and growth. The most common and simple treatment is oxidation, which can be done by ozone, aging, or thermal or chemical treatment. PSi biocompatibility has been extensively studied with various cell lines cultured on chemically modified pSi samples. Few studies have been done with primary MSC cultures to determine an optimal surface treatment (Hajj-Hassan *et al.*, 2011; Clements *et al.*, 2012). Moreover, it has been shown that stem cells growth can be modulated by factors mimicking extracellular matrix, such as amino or RGD residues. Cell behavior is influenced by changing the integrin and focal adhesion assembly, leading to changes in cytoskeletal organization and cell mechanical properties (Yim *et al.*, 2010). Thus, amine-terminated samples are expected to enhance MSC adhesion and proliferation as it does for other cell lines: silanisation with aminopropyl trimethoxysilane and triethoxysilane improves pSi stability and enhances cell adhesion in comparison to oxidized pSi. The chemistry greatly improves the stability of pSi in contact with cultured cells while allowing cell coverage levels comparable to standard culture preparations on tissue culture polystyrene (Low *et al.*, 2006). Thermal hydrosilylation is also used to graft chemical species to generate a stable substrate for cell adhesion and proliferation. Among these species are: dodecene, undecylenic acid and oligoethylene glycol (Alvarez *et al.*, 2009).

In addition to chemical surface treatment, a coating of proteins can be realized onto the pSi surface to mimic cell adhesion and relative responses in an *in vivo* condition with surface presenting biocompatible contact sites in a nanoscale dimension (topographic scale of adhesive proteins such as collagen fibers, laminine and fibronectin is present on the order of nanometers). The cell adhesion process depends upon cell surface receptors interacting with proteins belonging to the extracellular matrix. Several proteins have been considered for pSi coating: collagen, fetal calf serum and the tripeptide arginine-glycine-aspartate (RGD). Collagen is a component of the extracellular matrix and can be used to coat surfaces to stimulate cell adhesion, as well as foetal calf serum, which contains several cell adhesive proteins. Collagen and fetal calf serum have been successfully used to promote cell attachment and cell spreading (Low *et al.*, 2006). The tripeptide RGD is an integrin-binding domain present within many matrix proteins including fibronectin and vitronectin. Clements *et al.* (2012) showed that RGD immobilized on pSi is still a bioactive peptide and that cells adhere more when the concentration of RGD grafted increases.

Composite materials, such as poly(ε-caprolactone) / pSi, are also used for cell culture and tissue engineering. Highly porous scaffolds composed of mesoporous Si and commonly-used biopolymers, such as polycaprolactone, are electrically conductive composite materials exhibiting an interfacial behavior that promotes calcification and sustains the *in vitro* stability and proliferation of connective tissue cells in implant surfaces. Poly(ε-caprolactone) has been shown to have biocompatible and biodegradable character that is widely exploited in guided bone regeneration and drug delivery, and the resorbable pSi component sensitively accelerates the necessary calcification process. This type of composite presents a relevant material to orthopedic tissue engineering with tunable properties as mechanical strength, controlled release of molecules, and rate of resorption of the composite to the host surroundings (Coffer *et al.*, 2005). This pSi-containing polymer scaffold enhances calcification, can be considered nontoxic to cells, and support the proliferation, viability, attachment, and differentiation of bone precursor cells, suggesting that materials of this type of composition have potential merit as biomaterials (Whitehead *et al.*, 2008).

Another type of pSi membrane has also been described using porous nanocrystalline Si, which is a new type of Si nanomaterial, with potential applications in cell culture and tissue engineering. This pSi material is a 15 nm thick nanoporous membrane made with scalable Si manufacturing, permeable to small solutes. This nanoporous and ultrathin material can serve as a cell culture substrate, and is of interest to separate tissues during surgical grafting, such as bone tissue, bone substitute, periosteum or epithelium (Agrawal *et al.*, 2010).

1.3.2.3 Roughness and surface energy

Several molecular mechanisms by which cells perceive and respond to their surrounding environments have been studied, including integrin-ligand interactions, contact surface hydrophilicity and extracellular matrix topography and architecture. The *in vitro* control of the cellular environment is a challenge for manipulating both cell development and scaffold substitute function in the field of bioengineering. However, the differences existing between natural and experimental surface characteristics may confer some of the discrepancies reported between *in vivo* and *in vitro* results. Several approaches have been used to generate biomimetic *in vitro* environments. These experiments explore cell interaction either with the substrate's topography (physical domain) or with the substrate's chemical nature (chemical domain). The effects of nanotopographic features on cell behaviors have been investigated using a variety of nanoscale patterns, such as columns, sharp tips, pores and dots. Therefore, to biomimic cell adhesion and relative responses in an *in vivo* condition, cell adhesion surfaces are required to present biocompatible contact sites in a nanoscale dimension with periodicity matching with cell surface proteins. Nonetheless, the physical nature of the interactions between the cell and the surfaces in controlling specific cell behavior remains unclear. Several results suggest that nanometer-sized topographical biocompatible substrates potentially provide a distinct *in vitro* environment for cells, resembling the *in vivo* conditions (Yang *et al.*, 2010). However, the nanotopography plays a relevant role in the final wettability properties of surfaces, where hydrophobic surfaces prevent cell adhesion. PSi can be arranged with nanoscale patterns but freshly formed nanostructured pSi shows hydrophobic properties. Surface oxidation turns hydrophobic surfaces into hydrophilic: freshly etched pSi is hydrophobic and controlled ozone or thermal oxidation can drop the water contact angle to below 5°. This is attributed to the formation of a polar Si-OH capped surface after oxidation (Low *et al.*, 2006).

1.3.2.4 Influence of pore size, stiffness and surface treatment on osteodifferentiation

Cell attachment on pSi substrate has been extensively studied, but few studies evaluated the influence of topography on cell differentiation. Recently, Wang *et al.*

(2012) explored the influence of nanoscale surface topography on cell behavior. Using rat MSCs, they found that surface topography influences cell differentiation, but not proliferation. Osteogenesis was enhanced by porous topography with a ridge roughness lower than 10 nm with an increase in osteodifferentiation when pores size decreased. Thus, osteodifferentiation was comparable between flat Si and pSi with 100–200 nm, and was clearly enhanced when pore sizes decreased to 10–30 nm. This impact of pore size on osteodifferentiation is of high importance for the development of scaffold materials that can stimulate stem cell differentiation into osteoblasts in absence of chemical treatment without compromising material properties. Dalby *et al.* (2007) already demonstrated the use of nanoscale disorder to stimulate human MSCs to produce bone mineral *in vitro* in the absence of osteogenic supplements. Their approach had similar efficiency to that of cells cultured with osteogenic media. Nanocues, such as pSi pores, may prove to be important in tissue-specific stem cell differentiation. These findings are supported by various observations of chemical stimulation, chemical patterning and material hardness having roles in stem cell differentiation (Zemel *et al.*, 2010). The effect of surface treatment of pSi on stem cells has been investigated mainly for cell adhesion, however, several studies have shown that the immobilization of RGD on the substrate not only enhanced cell adhesion but also modulated the intercellular mechanisms of cell proliferation and differentiation (Hu *et al.*, 2003; Cavalcanti-Adam *et al.*, 2007; Lagunas *et al.*, 2011). Thus, RGD peptide coated surfaces enhance osteogenic differentiation when present in sufficient concentration (Frith *et al.*, 2011). At last, the mechanical properties of the underlying substratum have previously been shown to affect a number of cellular processes including locomotion, proliferation and differentiation. Microenvironments appear important in stem cell lineage specification, but can be difficult to control with pSi. MSCs are shown to specify lineage and commit to phenotypes with extreme sensitivity to tissue-level elasticity. Soft matrices that mimic brain are neurogenic, stiffer matrices that mimic muscle are myogenic, and comparatively rigid matrices that mimic collagenous bone, like pSi, prove to be osteogenic. After several weeks in culture, cells commit to the lineage specified by matrix elasticity (Engler *et al.*, 2006).

1.3.3 Growth factors delivery and Si effects on osteodifferentiation

Stem cells grown in biomaterials with bone growth factors constitute a source of transplantable material. Indeed, mesenchymal stem cells differentiation into elements of the skeleton can be enhanced by the addition of bone growth factors. PSi is a potential carrier scaffold to deliver growth factors to the site of defect, where regeneration is needed.

Moreover, controlled release of ionic products from PSi dissolution can stimulate and enhance bone-cell function: dissolved Si has been shown to enhance osteoblast differentiation (Gupta *et al.*, 2010).

1.3.3.1 Drug delivery devices for osteogenic induction

Tissue engineering combines precursor cells from the patient with scaffolding matrices and the stimulus of growth factors. Bone morphogenetic proteins (BMPs) are probably the most important growth factors in bone formation and healing. These cytokines have been extensively studied during recent decades and, nowadays, recombinant human BMPs (rhBMPs) are widely used in several tissue-engineering products that might serve for the complete regeneration of bone or cartilage. Current applications include rhBMPs loaded in delivery systems made of synthetic or natural polymers and the differentiation of transplanted stem cells from the patient with rhBMPs for later body implantation. Bone morphogenetic proteins have a strong effect on bone and cartilage growth during early skeletal formation, and thus have promising potential for clinical bone and cartilage repair, working as powerful bone-inducing components in diverse tissue-engineering products. PSi may also be used as carrier for the delivery of BMPs. BMP-2 and BMP-7 have received approval by the US Food and Drug Administration for specific clinical cases (Bessa *et al.*, 2008). Indeed pSi also exhibits a number of properties that make it an attractive material for controlled drug delivery applications. Its high surface area, coupled with the ability to control pore sizes allow pSi to be loaded with a range of bioactive species. Tunable properties of surface area, porous volume, and pore size allow controlling the amount and *in vivo* release rate of molecule payloads (Anglin *et al.*, 2008). By promoting osteogenic development of MSCs, the association of pSi and BMPs offer interesting perspective for bone reparation and regeneration.

1.3.3.2 Silicic acid and Si effects on bone formation

Since the discovery that bioactive ceramics bond to bone without fibrous encapsulation, many studies have focused on the mechanism of bioactivity *in vitro* and *in vivo*. These studies indicated that controlled dissolution of bioactive ceramics was of prime importance for stimulation of bone cell function and tissue regeneration (El-Gahnnam *et al.,* 2006). The main advantage of pSi over other biomaterials is its ability to degrade, in aqueous solutions, into non-toxic silicic acid [$Si(OH)_4$], which is the biologically significant form of Si that is in blood plasma. Silicic acid is vital for normal bone and connective tissue homeostasis. *In vivo*, pSi releases $Si(OH)_4$ with a negligible inflammatory response before being excreted in the urine (Popplewel *et al.*, 1998; Park *et al.*, 2009). The release of $Si(OH)_4$ due to the corrosion of pSi in plasma stimulates calcification and collagen growth, which could ideally accelerate new bone regeneration. Cell differentiation assays and ultrastructural measurements (TEM) have been carried out to explore the influence of Si on stem cell osteodifferentiation. It has been demonstrated that Si plays an important role in the expression of alkaline phosphatase, a specific biomarker for mesenchymal stem cell differentiation (Fan *et al.*, 2012). Osteocalcin (OCN) and bone sialoprotein (BSP) (non-collagenic proteins produced by osteoblast and involved in Ca-P crystal formation) are significantly more expressed by stem cells cultured in Si-rich medium, confirming that Si enhances stem cell differentiation into osteoblast and that Si may directly be involved in OCN and BSP-mediated mechanisms (Gupta *et al.*, 2010). Histological evaluation and histomorphometric quantification of none ingrowth and mineral apposition *in vivo* demonstrated the benefits to bone ingrowths and repair through incorporation of Si (Hing *et al.*, 2006). These results show that pSi, by its degradation, plays a significant role in both stem cell osteodifferentiation and mineralization (see Figure 1.7). If it is clear that the dissolution of pSi in the form of $Si(OH)_4$ is a powerful mechanistic force behind the nucleation and growth of calcium phosphate, it also seems that Si surfaces provide nucleation sites for the formation of apatite deposits. This conclusion is based on mechanistic observations concerning surfaces formed of CaO-rich silica, noting that Si in these materials are responsible for directing the formation of apatite deposits in simulated plasma. Si intermediates as a nucleation site in directing the formation of calcium phosphate spherulites and growth of apatite on the scaffold (Whitehead *et al.*, 2008). Bone cells attached onto the surface containing high Si content absorb significantly higher concentrations of calcium than cells attached onto the surface that contains low Si content. In conjunction with the absorption of high calcium concentration, attached bone marrow stem cells produce calcified nodules and mineralized extracellular matrix, indicating osteoblastic differentiation (El-Gahnnam *et al.,* 2006). Thus, the mechanism of bone mineralization at the interface with bioactive surfaces is mainly cell mediated: a Si-rich phase provides a guided cell adhesion and tissue growth *in vitro*. The addition of Si to a scaffold affects surface topography, dissolution-reprecipitation rates and the bone apposition process (Porter, 2006).

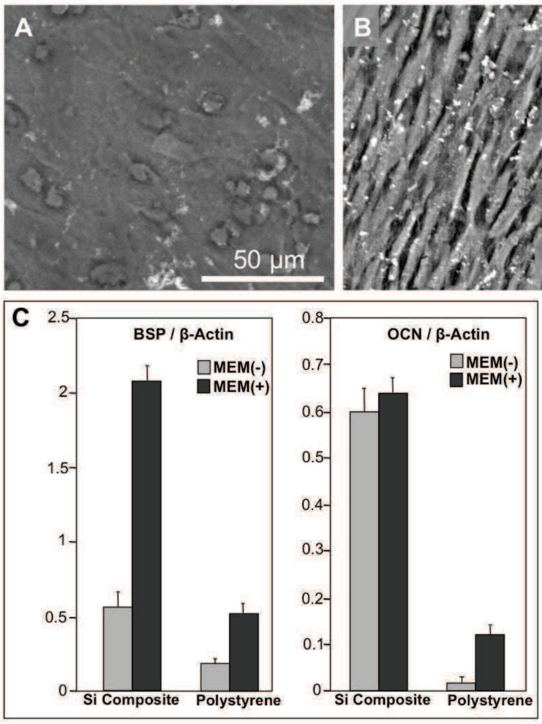

Figure 1.7: A and B: SEM of MSC osteodifferentiation and mineralized matrix deposits. A: on psi membrane (pore diameter = 30 nm); B: on culture plate. On pSi, osteoblast-like cells are embedded in a mineralized matrix, while cells are more clearly visible on polystyrene, with less extracellular matrix. C: quantity of mRNA bone sialoprotein (BSP) and osteocalcin (OCN) expressed by osteoblast-like cells on Si composite and on culture plate, after 2 days of culture in basal medium MEM(-) or in osteogenic medium MEM(+). Mean concentration of [Si] in culture medium containing Si composite is 6.5mg/l. Cells express more of osteogenic marker when cultured in the presence of [Si]. Adapted from Gupta *et al.* (2010) and Collart Dutilleul *et al.* (2014).

1.4 Objectives of the investigation and future trends

In tissue engineering, developing synthetic grafts with sufficient combined mechanical strength, bioactivity and biodegradability for bone–tissue regeneration applications therefore remains an important challenge. A material that combines high bioactivity and porous structure (for good tissue growth) with high levels of mechanical strength (for load-bearing applications) will improve clinical outcomes and enable a significantly wider application of restorative materials (Zreiqat *et al.*, 2010). Most materials currently used in medical implants are bioinert and, as such, do not interact with living systems. PSi has the property to be used as a scaffold, which could be well vascularized and integrated within the host skeleton, to stimulate the formation of new living bone. It provides a controlled biophysical and biochemical microenvironment, possibly directing the differentiation of stem cells into a specific lineage. Its porous, tunable and loadable structure allows cell adhesion and maintenance of cell function.

MSCs have a great potential for cell replacement, relying on their capacities to differentiate into several cell lineages, to modulate immune response and to secrete biological soluble factors. They have been assessed *in vivo* by direct transplantation to injured sites. However, new strategies involve the generation of an engineered construct combining biocompatible scaffolds with MSCs. Several pilot clinical trials are currently in process (http://www.clinicaltrials.gov). PSi has been extensively studied *in vitro* for its capacity to support various cell lines growth and differentiation. Its efficiency in bone tissue engineering has now to be confirmed in experimental research with primary human stem cells for potential *in vivo* and clinical applications.

The overall aim of the research presented here is to assess porous silicon as a potential bioactive scaffold, promoting both human stem cell adhesion and osteodifferentiation, for bone tissue engineering using primary human dental pulp stem cells (DPSC). A secondary aim is to further elucidate the influence of pore diameter (at the nanometer scale) on stem cells adhesion, proliferation and differentiation.

Therefore, the aims of this work can be presented as follow (each point outlines the themes for the following chapter):

- Development and optimization of human dental pulp stem cells recovery, in order to have an efficient and accessible source of primary human stem cells.
- Dental pulp stem cells adhesion and proliferation onto various porous silicon scaffolds, in order to determine the ideal porosity and functionalization of pSi.
- Dental pulp stem cells growth and osteodifferentiation on porous silicon scaffold, to study the inductive effects of pSi for osteodifferentiation, due to the silicic acid released during pSi degradation and due to its porous structure.
- Pore diameter influence on Dental Pulp Stem Cells Adhesion, Proliferation and Osteodifferentiation: use of porous silicon gradients to specifically determine an ideal pore diameter for DPSC use in bone tissue engineering.
- Dental pulp stem cells behavior on porous structure at the nanometer scale: atomic force microscopy assessment of DPSC spreading and filopodia formation on pSi scaffolds.

Chapter 2 Dental Pulp Stem Cells Recovery

2.1 Introduction

2.1.1 Dental pulp

Teeth are formed with two main parts: the crown and the root that can be defined with anatomic or clinical criteria. They are linked, by the periodontal ligament, to the supporting alveolar bone, which is composed of both compact and trabecular bone (Figure 2.1).

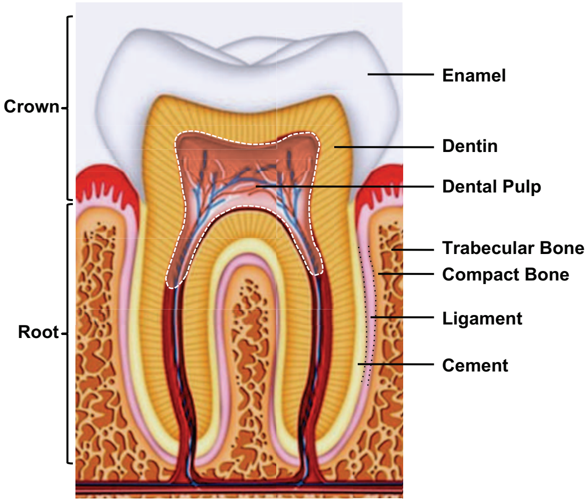

Figure 2.1: Schematic of a tooth, showing both internal structures and supporting ligament and bone. DPSC are recovered from the inner dental pulp. Adapted from the *National Library of Medicine, National Institute of Health* (http://www.nlm.nih.gov/medlineplus/ency/imagepages/1121.htm).

The crowns of human teeth consist of enamel, dentin, and dental pulp tissue. During tooth growth and development, ameloblasts form enamel and odontoblasts generate primary dentin. After tooth eruption, ameloblasts disappear from the surface of the enamel; consequently, enamel formation ceases to occur naturally *in vivo*. In contrast, odontoblasts, along the inner surface of the dentin inside the pulp chamber, continue to deposit dentin matrix to form secondary dentin throughout life. In addition to secondary dentin, odontoblasts can form tertiary (reparative) dentin in response to several stimuli, such as mechanical, chemical, and/or bacterial stimulation. Even when odontoblasts have been damaged, the reparative dentin can be formed in the dental pulp to protect against further disruption of the pulp tissue. This reparative dentinogenesis has been thought to be mediated by newly generated odontoblasts arising from dental pulp tissue. These findings have led to the speculation that odontogenic progenitor cells or stem cells may exist in dental pulp tissue (Sonoyama *et al.*, 2007). And in 2000, Dental Pulp Stem Cells have been, for the first time, clearly identified, isolated and characterized (Gronthos *et al.*, 2000). Thus, we can represent dental pulp as a soft connective tissue entrapped within the dental crown, and divided into four layers. The external layer is made up of odontoblasts producing dentin; the second layer is poor in cells and rich in collagen fibers; the third layer contains progenitor cells and undifferentiated cells, some of which are considered stem cells. From this layer, undifferentiated cells migrate to various districts where they can differentiate under different stimuli and make new differentiated cells and tissues. The innermost layer is the core of the pulp and comprises the vascular area and nerves (D'Aquino *et al.*, 2009).

2.1.2 Dental pulp stem cells (DPSC)

A stem cell is defined as a cell that has the ability to continuously divide to either replicate itself (self-renewing), or produce specialized cells that can differentiate into various other types of cells or tissues (multilineage differentiation). The microenvironment in which stem cells reside is called a stem cell niche and is composed of heterogeneous cell types, extracellular matrix (ECM) and soluble factors to support the maintenance and self-renewal of the stem cells. Dental pulp is a tissue enrich of adult mesenchymal stem cells: the Dental Pulp Stem Cells (DPSC). These adult stem cells may play an important role in regenerative medicine both for oral and non-oral pathologies thanks to their biological properties such as multipotency, high proliferation rate and accessibility. Beyond natural capacity of response to injury, dental pulp stem cells are attractive for their potential to differentiate, *in vitro*, into several cell types including odontoblasts, neural progenitors, chondrocytes, endotheliocytes, adipocytes, smooth muscle cells and osteoblasts (Yamada *et al.*, 2011).

Dental tissue from human third molar represents an easily accessible and often discarded source for MSC harvesting. The first type of dental stem cell was isolated from the human pulp tissue and termed dental pulp stem cells (DPSC) (Gronthos *et al.*, 2000). Subsequently, four more types of dental-MSC-like populations were identified: stem cells from exfoliated deciduous teeth (SHED) (Miura *et al.*, 2003), periodontal ligament stem cells (PDLSCs) (Seo *et al.*, 2004), stem cells from apical papilla (SCAP) (Sonoyama *et al.*, 2006), and dental follicle precursor cells (DFPCs) (Morsczeck *et al.*, 2005). Among them, all except SHED are from permanent teeth.

Stem cells that reside in dental pulp (DPSC) are a population of MSC, as they match the definition given by the Mesenchymal and Tissue Stem Cell Committee of the International Society for Cellular Therapy (Dominici *et al.*, 2006). This committee proposed minimal criteria to define human MSC: first, cells must be plastic-adherent when maintained in standard culture conditions; second, they must express some specific surface molecules such as CD105, CD73 and CD90, and lack expression of CD45, CD34, CD14, CD19 and HLA-DR surface molecules; third, they must differentiate to osteoblasts, adipocytes and chondroblasts *in vitro* (Figure 2.2, next page).

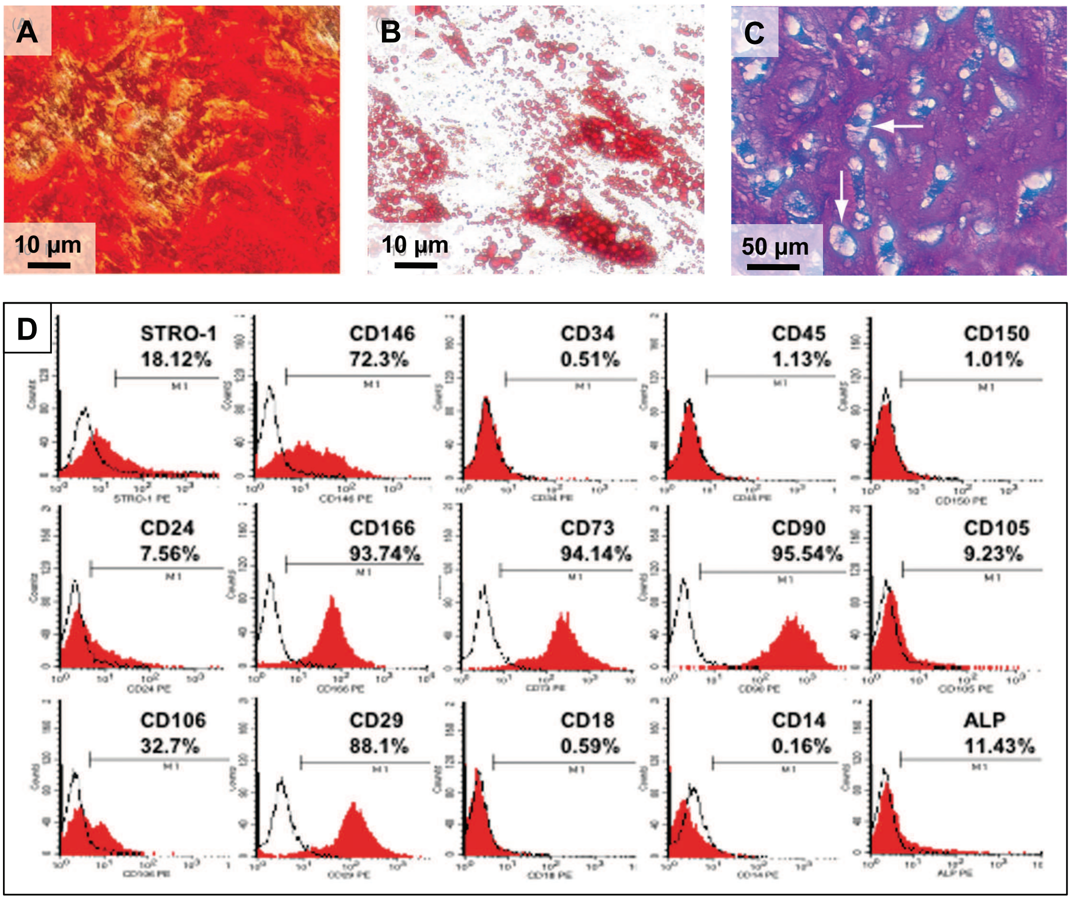

Figure 2.2: Minimal criteria to define MSC: differentiation assays and flow cytometry analysis. A-B: Optical microscopic images representing results of differentiation assays. (A) Alizarin Red S-stained monolayer of osteogenic MSC. (B) Oil Red O-stained monolayer of adipogenic MSC. (C) Sections of chondrogenic pellets stained with Toluidine Blue. (D) Flow Cytometry analysis of MSC for various cell surface markers. MSC are negative for CD34, CD45, CD150, CD18 and CD14. They are positive for the other markers, with various intensities. Adapted from Sonoyama *et al*. (2006 and 2007).

Characterization revealed that DPSC possessed osteogenic, chondrogenic and adipogenic differentiation capacities. In addition, DPSCs were also found to undergo myogenic and neurogenic differentiation capacities *in vitro*, expressing respective gene markers and exhibiting neuronal-like cell morphologies. The plasticity and multipotential capability of DPSC can be explained by the fact that dental pulp is made of both ectodermic and mesenchymal components, containing neural crest-derived cells (D'Aquino *et al*., 2009). Concerning cell surface molecules, markers that have been used for identifying MSC have also been investigated for DPSC: DPSC have been shown positive for various markers, such as STRO-1, CD13, CD24, CD29, CD44, CD73, CD90, CD105, CD106, CD146, Oct4, Nanog and β2 integrin, and negative for CD14, CD45 and HLA-DR. The persistence of negativity for CD45 demonstrates that these cells are not derived from a hematopoietic source, although they are of mesenchymal origin (D'Aquino *et al.*, 2007). Like all MSC, DPSC are also heterogeneous and the various markers listed here may be expressed differently by subpopulations of these stem cells (Huang *et al.*, 2009). In 2005, Laino and co-workers described a selected subpopulation of $CD34^+/CD45^-$ DPSC, which roughly represented 10% of dental pulp cells. These cells displayed a great capability of self-expanding and differentiating in pre-osteoblasts, able to self-maintain and renew for long time (Laino *et al.*, 2005). Although MSC were described to be CD34(-), it seems that a subpopulation of DPSC expressed this cell surface antigen described for the most primitive stromal, other than hematopoietic, stem cells, and gradually lost after lineage committed progenitors differentiation (Yoo *et al.*, 2013).

2.1.3 Potential applications of DPSC in regenerative medicine

Upon discovery of stem cells in the dental pulp, DPSC demonstrated their ability to regenerate a complex consisting of a mineralized matrix with odontoblasts and connective tissue containing blood vessels similar to that observed in normal human tooth (Gronthos *et al.*, 2000). Nowadays, the use of DPSC concerns the repair and regeneration of liver tissue, heart tissue, bone, central nervous system, eye, and holds great potential in the field of regenerative medicine (d'Aquino *et al.*, 2008) (Gronthos *et al.*, 2002). They even appear to have greater potential than the actual mesenchymal stem cells gold standard, the bone marrow-derived mesenchymal stem cells (Alge *et al.*, 2010).

2.1.3.1 Hepatic tissue regeneration

DPSC transplantation in injured hepatic tissue in rat leaded to liver primary function recovery, after hepatocytes restoration. In 2008, Ikeda and co-workers examined DPSC potential by the transplantation into a carbon tetrachloride (CCl4)-

treated liver injured rat, to determine whether these cells might be useful for cell-based therapy to treat liver diseases. The successful engraftment of the DPSC was demonstrated at 4 weeks after transplantation. They prevented the progression of liver fibrosis and contributed to the restoration of liver function, as assessed by the measurement of hepatic serum markers aspartate aminotransferase and alanine aminotransferase. Furthermore, the liver functions, observed by the levels of serum bilirubin and albumin, appeared to be improved following transplantation of DPSC (Ikeda *et al.*, 2008). These findings suggested that DPSC were one of the candidates for cell-based therapy to treat liver diseases and offered opportunities for developing therapies. These strategies of transplantation of DPSC could help halting malignant progression in hepatitis patients receiving antiviral treatment.

2.1.3.2 Myocardiac regeneration

DPSC, like bone marrow stem cells, can secrete vascular endothelial growth factor (VEGF) (Shi *et al.*, 2001) and stem cell factor (SCF, corresponding to the cell surface receptor CD117) (Gagari *et al.*, 2006). These factors have proangiogenic, antiapoptotic, and cardio protective actions (Tran-Hung *et al.*, 2006). Thus, in 2008, Gandia and co-workers investigated whether DPSC could be useful for cardiac repair, in a rat model of myocardial infarction. DPSC were injected intramyocardially in nude rats 7 days after induction of myocardial infarction by coronary artery ligation (Gandia *et al.*, 2008). At 4 weeks, DPSC-treated animals showed an improvement in cardiac function, observed by left ventricular wall thickness and reduction in infarct size (Figure 2.3, next page). Moreover, angiogenesis was increased compared to control animals. Thus, DPSC appeared to be a potential alternative therapeutics for cardiac repair after acute myocardial infarction.

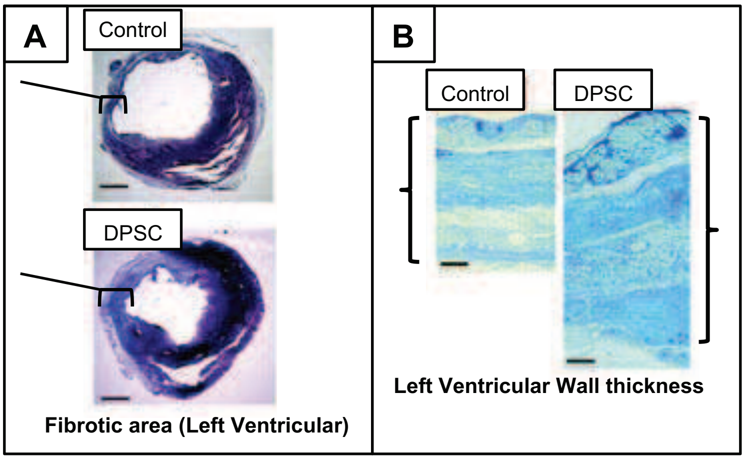

Figure 2.3: Effect of DPSC transplantation on infarct size. (A): Masson's trichrome-stained heart sections from infracted rats receiving either no cells (control) or DPSC. Arrows show the fibrotic area. (B): Thin sections and quantification of the Left Ventricular Wall thickness. Adapted from Gandia *et al.* (2008)

2.1.3.3 Bone reconstruction

Numerous *in vitro* and *in vivo* studies demonstrated DPSC capacities to produce mineralized bone tissue. The woven bone tissue produced *in vitro* could even be remodeled into lamellar bone when transplanted *in vivo* (Graziano *et al.*, 2008). A study on human subject was performed to assess the efficiency of DPSC to rebuild mandibular bone: DPSC seeded on a collagen sponge scaffold were grafted for bone tissue repair in patients requiring extraction of their third molars (wisdom teeth). Three months after autologous DPSC grafting, alveolar bone of patients had optimal vertical repair and complete restoration of periodontal tissue back to the second molars. Histological observations highlighted the complete regeneration of bone at the injury site one year after grafting (d'Aquino *et al.*, 2009). The stability and quality of the regenerated bone and vessel network was assessed 3 years after the grafting intervention: the regenerated tissue from the graft sites was composed of a fully compact bone with a higher matrix density than control human alveolar spongy bone from the same patient (Giuliani *et al.*, 2013).

2.1.3.4 Neural tissue regeneration

DPSC are thought to originate from migrating cranial neural crest cells. During embryonic development, these neural crest cells differentiate into a wide variety of cell types, including neurons of the peripheral nervous system. In 2008, Arthur and co-workers demonstrated that *ex vivo* expanded human adult DPSC responded to neuronal inductive conditions to form neuronal cells, and expressed neuronal specific markers, both *in vitro* and *in vivo* (Arthur *et al.*, 2008). Thus, adult human DPSC could provide a readily accessible source of stem cells for therapeutic applications in neurological pathologies. Several experiments with DPSC grafted in mice and rats assessed the regeneration of injured neural tissue (brain or spinal chord injuries) (Huang *et al.*, 2008) (Kiraly *et al.*, 2009) (Sakai *et al.*, 2012). These works showed up that tissue regeneration after DPSC graft was related to DPSC proliferation and differentiation, and to enhancement of local progenitor cells recruitment and maturation.

2.1.3.5 Eye reparation

Limbal stem cells reside in the eye, between the cornea and the sclera. They are responsible of constant renewal of the corneal epithelium and can promote its regeneration when injured. In case of partial or total limbal stem cell deficiency, a conjunctival epithelium invasion can occur, leading to a significant loss of visual acuity. DPSC have been shown able to rebuild the eye surface after total limbal stem cell deficiency in rabbits (Monteiro *et al.*, 2009). Thus, it is suggested that DPSC share similar characteristics with limbal stem cells and might be used as a potential alternative source of cells for corneal reconstruction.

2.1.4 Aims of the study

Important knowledge about the characteristics of bone marrow stem cells has permitted to isolate putative stem cell populations from the dental pulp of human third molars (DPSC) and deciduous teeth (stem cells from human exfoliated deciduous teeth; SHED), which exhibit properties similar to those of bone marrow stem cells. DPSC were found to reside in a specific perivascular microenvironment, where they were quiescent and maintained their basic stem cell characteristics, including a self-renewal capacity and undifferentiated status (Shi *et al.*, 2003). Various procedures for the isolation, purified preparation, expansion, and tissue regeneration potential of DPSC have been described.

The work presented in this chapter is about development and optimization of human dental pulp stem cells recovery, in order to have an efficient and accessible source of primary human stem cells. We aimed to establish a clear and efficient way to recover primary cultures of human DPSC. These cells can be collected from dental pulp by means of a non-invasive practice that can be performed in the adult during life and in the young after surgical extraction of wisdom teeth. We wanted to develop an access to this source of MSC, for potential autologous or allogenic therapeutic applications. And as DPSC can be cryopreserved and stored for long periods without losing their multipotential differentiation ability (Laino *et al.*, 2005), we studied cell stemness after storage in liquid nitrogen.

2.2 Materials and methods

2.2.1 Patients

2.2.1.1 Pre operative step

We developed our protocol at the public hospital in Montpellier, in accordance to the local ethical committee (Comité de Protection des Personnes, Montpellier hospital, France) (see statement, in french, in Appendix). Once the protocol was approved, we submitted it to a private clinic, where oral surgeons are working. In public hospital or in the private clinic, human impacted third molar extracted for orthodontic reasons were recovered from healthy patients (15-30 years of age). Patients were considered as “healthy” when they were not known to have any chronic or acute infection or pathology. Pregnant women were not included in the protocol. The pre operative step also evaluated the feasibility to recover intact impacted teeth, by radiographic evaluation (see Figure 2.4, next page). Written informed consent was obtained from all the patients or their parents, after a discussion in which the project was explained and patients had the opportunity to ask questions about the program and to freely accept or refuse. The document signed by the patients (or parents) is shown in

Appendix. Patients were also offered to receive information and results of the research program conducted with their teeth.

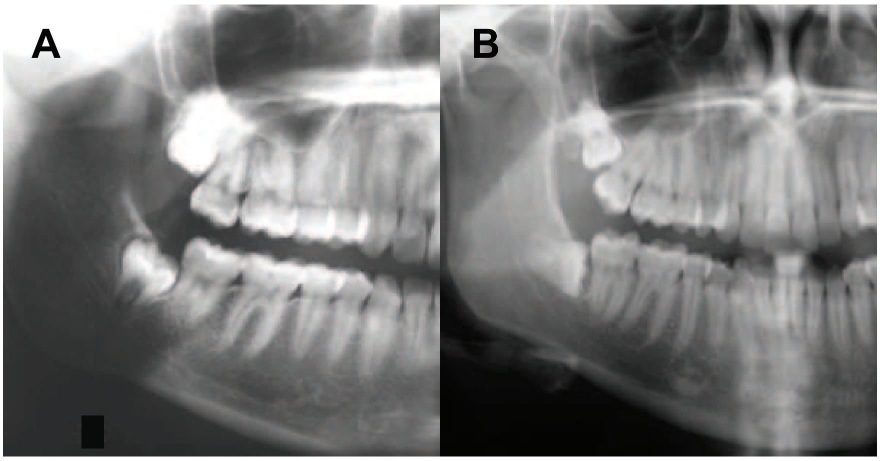

Figure 2.4: Orthopantomogram (panoramic radiograph) of impacted wisdom teeth, before extraction for orthodontic purpose. (A) Favorable case, where teeth will probably remain intact during dental extraction. (B) Unfavorable case, where wisdom teeth will probably have to be cut in several pieces by the dental surgeon during dental extraction. From Collart Dutilleul *et al.* (2012)

2.2.1.2 Per operative step

Tooth avulsions were realized under local or general anesthesia, in aseptic conditions, after local disinfection of the oral cavity. Teeth recovery didn't interfere with the dental surgeon treatment. Discarded wisdom teeth were collected in sterile tubes containing sterile culture medium, and stored in a refrigerated box (4°C) during transportation to the laboratory (Figure 2.5, next page).

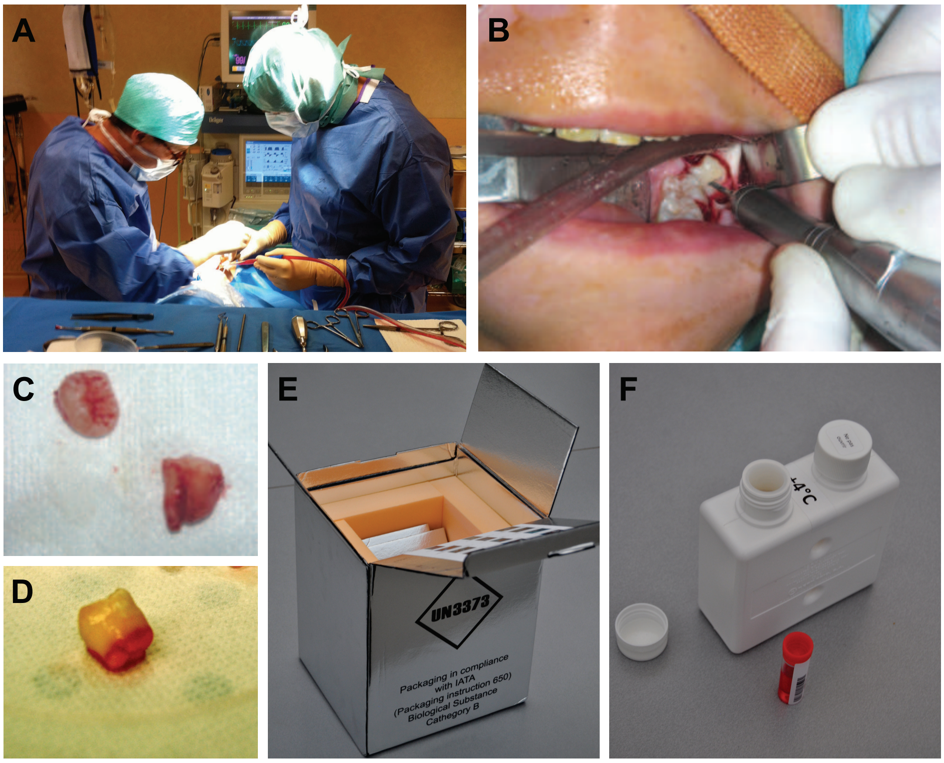

Figure 2.5: Wisdom teeth recovery procedure, in aseptic conditions. (A) Dental extraction under general anesthesia. (B) Wisdom tooth removal; the oral cavity has been disinfected here with povidone-iodine. (C) Dental crown separated from the root during extraction: the exposed dental pulp won't be used for stem cells recovery. (D) Discarded tooth used for pulp tissue extraction, then DPSC recovery. (E) Refrigerated transportation kit with (F) sterile tubes containing culture medium with antibiotics. Adapted from Collart Dutilleul *et al.* (2012)

2.2.1.3 Post operative step

After teeth collection, the refrigerated box was brought to the laboratory, where the dental pulp tissue was recovered, under sterile conditions. All the research work was then conducted. After 3 to 6 months, a short summary of the work was sent to the patients who asked for.

2.2.2 Cell extraction

Transport tubes were opened under a laminar flow hood. Teeth surfaces were cleaned using 2% chlorhexidine and cut around the cementum-enamel junction by using sterilized disc. The teeth were then broken into 2 pieces to reveal the pulp chamber. The pulp tissues were gently separated from the crown and root. The pulps were submitted to enzymatic digestion. This technique has been already widely described: extracellular matrix of the pulp tissue were digested in a solution of 3 mg/ml type I collagenase and 4 mg/ml dispase for 1 hour at 37°C. The solution was then filtered through 70 µm Falcon strainers and immersed in αMEM supplemented with 10% fetal bovine serum (FBS), 100 U/ml penicillin, 100 µg/ml streptomycin and placed in 75 ml flasks. Cells were incubated for 1 week at 37°C with 5% CO_2 (Gronthos *et al.*, 2002). For each dental pulp, the total number of extracted cells was evaluated by counting cells in a Glasstic® slide with grids, under optical microscopy. Cell viability was assessed by 0.4% Trypan Blue staining.

2.2.3 Cell sorting

Non-adherent cells were removed by a change of medium 24 h after cell seeding. The remaining cells were let in culture medium and followed for a week, to avoid them to reach confluence. Subconfluent cells were then either selected by Fluorescence-activated cell sorting (FACS) or directly analyzed by flow cytometry. Cell sorting by FACS was realized for the expression of cell surface markers CD146 and CD34 (see below).

2.2.4 Cell characterization

After 1 week, subconfluent cells were collected (after FACS or without sorting) and analyzed for minimal criteria to define human mesenchymal stem cells, such as adherence to plastic, clonogenicity, competence to proliferate, expression of specific cell surface antigens and ability to differentiate into osteoblasts, adipocytes and chondroblasts *in vitro* (Morsczeck *et al.*, 2005) (Dominici *et al.*, 2006).

2.2.4.1 Colony forming efficiency

To assess colony-forming efficiency (CFU-F, colony forming units fibroblast), dental pulp cells were seeded in a dilution of $5x10^4$ cells/well in 6-well cell culture plates, immediately after cell recovery. On day 7, all cultures were fixed with 4%

formaldehyde, and then stained with 0.1% toluidine blue. Aggregates of >50 cells were scored as colonies (Seo *et al.*, 2004).

2.2.4.2 Proliferation rate

The proliferation rate of sub-confluent cultures (first passage) of stem cells was assessed by bromodeoxyuridine incorporation for 24 h, with a Zymed Laboratories BrdU staining kit. BrdU was incorporated into proliferating cells (during S-phase of mitosis) and revealed using a highly sensitive streptavidin-biotin staining system (Morsczeck *et al.*, 2005).

2.2.4.3 Flow cytometry characterization

For flow cytometry, cells were dissociated from their substrate with 0.5 mM Accutase for 1 min. Cells were then resuspended in 1% BSA in PBS, counted and placed in flow cytometry tubes (10^5 cells per tube). The tubes were centrifuged at 1400 rpm for 10 min, the supernatant discarded, and 5 µL of antibody solutions were placed on the centrifuged cells. The antigen profiles of cultured DPSC were analyzed by detecting the expression of the cell surface markers CD90, CD146, CD117, CD34, STRO-1 and CD45 using flow cytometry and conjugated monoclonal antibodies, presented in Table 2.1.

- CD90 is a widely accepted marker for mesenchymal stem cells. This surface protein plays a role in cell-cell interaction events, including intracellular adhesion and cell recognition during development, and is considered an important stem cell marker (Kern *et al.*, 2006) (Mercati *et al.*, 2009).
- CD146 is a marker expressed in perivascular mesenchymal stem cells, also known as MCAM (Melanoma Cell Adhesion Molecule) or cell surface glycoprotein MUC18. Notably, CD146 is not expressed by bone marrow hematopoietic stem cells or their progenitors and has been linked to various cellular processes including cell adhesion, cytoskeletal reorganization, cell shape, migration, and proliferation through transmembrane signaling (Shi *et al.*, 2003). Several studies demonstrated that CD146 positive cells from connective tissue exhibited MSC potential (Kemoun *et al.*, 2011).

- CD117 is a receptor expressed on the surface of hematopoietic stem cells as well as other cell types. CD117, also known as c-Kit, is a tyrosine kinase receptor that binds to the Stem Cell Factor (SCF), forming a dimer that activates its intrinsic tyrosine kinase activity. Signaling through CD117 plays a role in cell survival, proliferation, and differentiation (Li *et al.*, 2003) (Fawzy El-Sayed *et al.*, 2012).
- CD34 is a marker selectively expressed by primitive myeloid and lymphoid progenitor. However, CD34 is not restricted to hematopoietic progenitors, but is expressed by vascular endothelial cells and in basement membrane structures (Simmons *et al*., 1991). CD34+ cells are normally found in the umbilical cord and bone marrow as hematopoietic cells, and can be primitive stromal stem cells (Gordon *et al.*, 2006).
- STRO-1 is a marker of pre-osteogenic, pre-chondrogenic or pre-adipogenic populations. Its expression is progressively lost during cell proliferation and differentiation. Thus, STRO-1 seems to be an early marker of mesenchymal stem cells, and is often used in combination with cell adhesion molecules (such as CD106 or CD146) to isolate purified bone marrow stem cell populations (Gronthos *et al.*, 2006).
- CD45 is a marker of hematopoietic cells, mainly myeloid progenitors. It is used in this study as a control to verify the stromal origin of dental pulp cells and the absence of hematopoietic precursor contamination (Bakopoulou *et al.*, 2011).

Antigen	Antibody	Conjugated	Supplier
CD90	Human anti CD 90	APC	Miltenyi Biotec
CD146	Human anti CD 146	FITC	Miltenyi Biotec
CD117	Human anti CD 117	APC	Miltenyi Biotec
CD34	Human anti CD 34	PE	Miltenyi Biotec
STRO-1	Mouse anti hSTRO-1	*unconjugated*	R&D Systems
CD45	Human anti CD 45	PerCP	Miltenyi Biotec
Secondary Ab	Mouse anti IgM	FITC	Miltenyi Biotec
Isotype APC	Mouse IgG2a	APC	Miltenyi Biotec
Isotype FITC	Mouse IgG2a	FITC	Miltenyi Biotec
Isotype PE	Mouse IgG2a	PE	Miltenyi Biotec
Isotype PerCP	Mouse IgG2a	PerCP	Miltenyi Biotec

Table 2.1: Antibodies for flow cytometry analysis

2.2.4.4 Differentiation assays

Recovered cells were controlled for multipotency with *in vitro* osteogenic, chondrogenic and adipogenic differentiation. For osteogenic and adipogenic differentiation, dental pulp cells were seeded at a density of 10^5 cells/cm^2 and maintained in αMEM supplemented with 10% FBS until confluence. Cells were then cultured in osteogenic medium (αMEM supplemented with 15% FBS, dexamethasone, L-ascorbate phosphate, and β-glycerophosphate) or in adipogenic medium (αMEM supplemented with 10% FBS, dexamethasone, insulin, and isobutylmethylxanthine) for 21 days, with medium changed twice a week. Control cultures were maintained without osteogenic or adipogenic supplements. To induce chondrogenic differentiation, cells were cultured for 21 days as pellets in a serum-free expansion medium containing dexamethasone, L-ascorbate phosphate, L-proline, sodium pyruvate, ITS-Premix, and TGF-β3. Control pellet cultures were maintained in basal medium (Kemoun *et al.*, 2007). The detailed differentiation media and supplements are presented in Table 2.2

Osteogenic medium	Adipogenic medium	Chondrogenic medium
αMEM	αMEM	αMEM
15% FBS	10% FBS	Serum free
10^{-8} M Dexamethasone	10^{-5} M Dexamethasone	10^{-7}M Dexamethasone
50 µg/mL L-Ascorbate Phosphate	50 µg/mL L-Ascorbate Phosphate	50 µg/mL L-Ascorbate Phosphate
5 mM β-Glycerophosphate	1 µg/mL Insulin	40 µg/mL L-Proline
1.8 mM Monopotassium Phosphate	0.5 mM Isobutylmethylxantine	100 µg/mL Sodium Pyruvate
		50 mg/mL ITS-Premix
		10 ng/mL TGF-β3

Table 2.2: Composition of the various differentiation media.

At the end of the 3 weeks of induced differentiation, cultures were fixed and assessed for mineralization by Alizarin Red staining, for adipogenic differentiation by Red O Oil staining and for chondrogenic differentiation by Alcian blue staining of thin section.

2.2.5 Use and conservation

Recovered primary DPSC were either used directly for various experiments (cell interactions with porous silicon scaffolds) or cryopreserved in liquid nitrogen. For storage, 10^6 cells were resuspended in 10% dimethylsulfoxide (DMSO) in FBS in a cryotube and frozen in liquid nitrogen. Storage was prolonged for up to 1 year. At the end of the storage period, cells were quickly thawed in a water bath at 37°C, then added to 10 ml of αMEM supplemented with 10% FBS. Cells were centrifuged at 1,400 rpm for 10 min, the supernatant was removed and fresh medium was added to the tube. Cells were then placed in T-75 flasks and cultured at 37°C in a 5% CO_2 humid atmosphere.

2.3 <u>Results</u>

2.3.1 Cells recovery

The pulp tissue enzymatic digestion permitted to extract an important amount of cells. This quantity was mainly depending on the tooth formation: the more immature the tooth, the bigger the pulp tissue available. We worked only with discarded wisdom teeth, extracted for orthodontic reasons, mainly impacted immature teeth, with a number of recovered cells varying between $5x10^5$ to $1.5x10^6$: for all the evaluated teeth, we found an average amount of 1,068,301 ± 501,722 cells per pulp (mean value ± standard error of the mean).

2.3.2 Cells characterization

2.3.2.1 Adherence, clonogenicity and proliferation

We removed all non-adherent cells by changing the culture medium after 24 h. We found the presence of a clonogenic cell population from the dental pulp tissue, and cells within each colony were characterized by a typical fibroblast-like morphology (Figure 2.6). The frequency of colony-forming cells derived from dental pulp tissue was of 20 to 65 colonies for $5x10^4$ cells plated in 6-well plates. The number of proliferating cells, assessed for recovered dental cell cultures after 7 days, was of 63% BrdU-positive cells (62.8 ± 12.3 %).

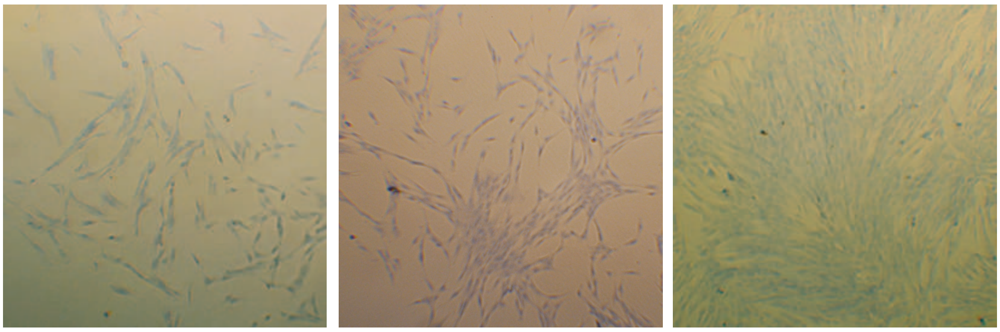

Figure 2.6: Optical microscopic images of DPSC stained with Toluidine Blue. Left picture: cells with typical fibroblast morphology. Central picture: colonies of DPSC, forming aggregates (CFU). Right pictures: DPSC reaching confluence.

2.3.2.2 Differentiation assays

Recovered DPSC were tested for their ability to differentiate into osteoblast, chondrocyte and adipocyte. After 3 weeks of *in vitro* differentiation assays, DPSC cultures formed calcium deposits in osteogenic medium (stained with Red Alizarin), lipid droplets in adipogenic medium (stained with Red O Oil) and proteoglycans in chondrogenic medium (stained with Alcian Blue) (see Figure 2.7, next page).

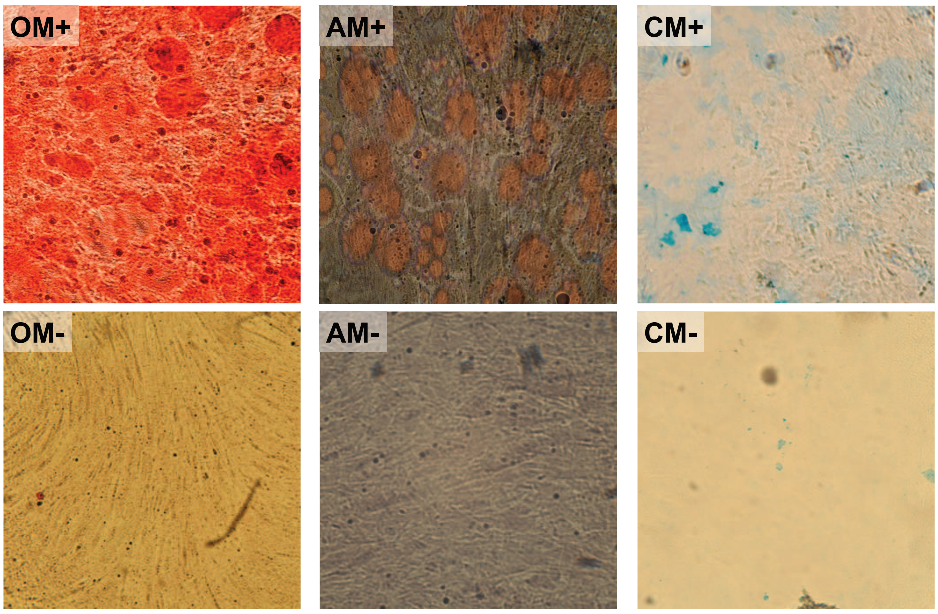

Figure 2.7: Optical microscopic images of differentiation assays: (OM+) & (OM-): Alizarin Red S staining of DPSC cultures after 21 days in osteogenic medium (OM+) or in basal medium (OM-). (AM+) & (AM-): Red-O-oil staining of DPSC cultures after 21 days in adipogenic medium (AM+) or in basal medium (AM-). (CM+) & (CM-): Alcian Blue staining of DPSC cultured ad pellet during 21 days in chondrogenic medium (CM+) or in basal medium (CM-).

2.3.2.3 Flow cytometry assays

Dental pulp cells were analyzed by flow cytometry for several cell surface markers, such as CD90, CD146, CD117, CD34, STRO-1 and CD45. This characterization was realized immediately after cells recovery (without *in vitro* expansion), after 24 h in culture medium (to remove non adherent cells), after 7 days in culture (subconfluent cells) and after cryopreservation (6-12 months in liquid nitrogen).

The first flow cytometry analysis was realized immediately after dental extraction, tooth opening, pulp tissue recovery and cells extraction. These assays showed a widely heterogeneous population, mainly CD90 positive with cells varying from high to low positivity. We found this cell population to be 36% CD117+, 11% CD34+ and 2% CD45+. No CD146+ cells were found within the recovered cells (Figure 2.8).

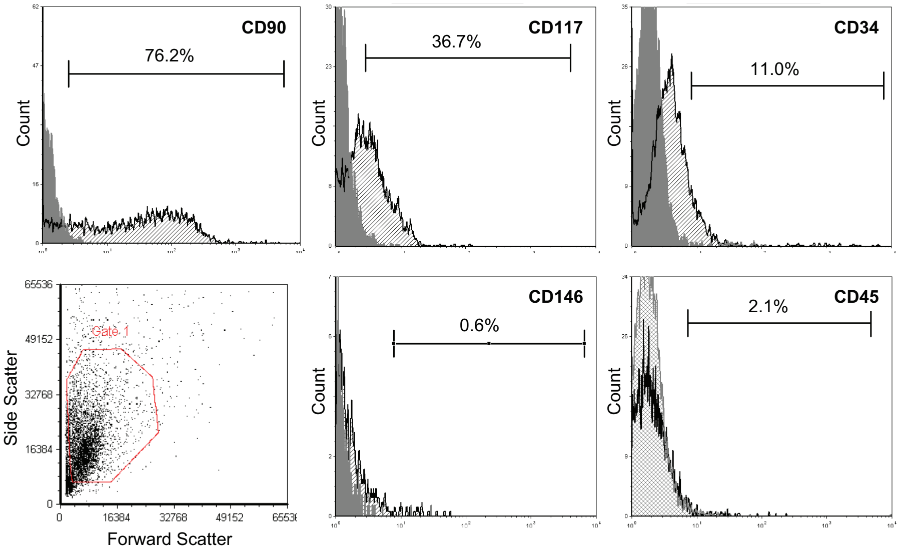

Figure 2.8: Representative flow cytometry analysis performed on cells immediately after their recovery, without *in vitro* step.

After 24 h in culture plates, cells were rinsed to remove any non-adherent cells, and analyzed by flow cytometry. Representative results are presented in Figure 2.9. Briefly, the cell population was more homogeneous than the first analysis. Almost all cells were CD90+, with a high positive population. Cells expressed 60% positivity for CD117, 8% positivity for STRO-1, and just few cells were CD146+. Concerning CD34 marker, a small population of highly CD34+ could be clearly distinguished. There were not any CD45+ cells, confirming the absence of hematopoietic origin of the cultured cells.

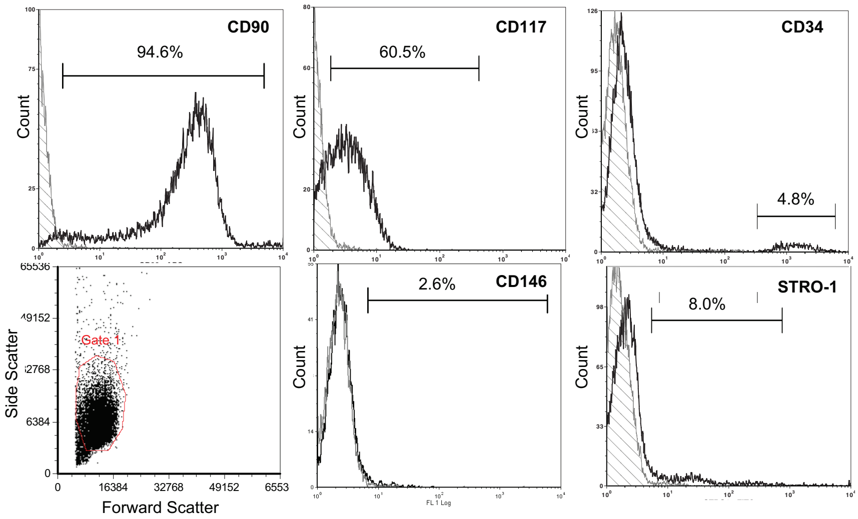

Figure 2.9: Flow cytometry performed on dental pulp cells after 24 h in culture *in vitro*, and rinsing to remove non-adherent cells.

After 7 days, dental pulp cells recovered from one tooth and placed in T75 flask were almost reaching confluence. We analyzed these subconfluent cells by flow cytometry, to follow variations in markers expression during *in vitro* expansion. All cells were CD90+, and partially CD117+. There were slightly less STRO-1+ cells (3 to 5 %, while 7 to 10% after 24 h). Few CD34+ cells were found, with percentage varying from 1 to 3% but the high positive CD34 populations (visible after 24 h) were not found. The main difference with cells after 24 h *in vitro* is the appearance of CD146 expression (not expressed after 24 h), with CD146+ cells representing 70 to 80% of the total cells (Figure 2.10).

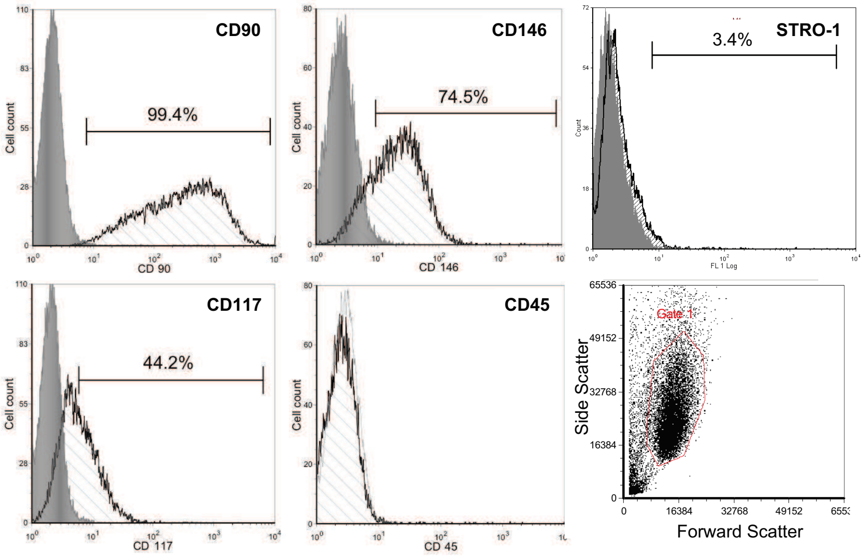

Figure 2.10: Flow cytometry performed on dental pulp cells after one week of *in vitro* expansion.

We assessed cell surface markers expression after cryopreservation. Dental pulp cells were put in cryotubes ($5x10^5$ to 10^6 per vial), frozen in liquid nitrogen, and thawed after 6 months to 1 year. Flow cytometry was performed 3 to 5 days after thawing, on subconfluent cells. The markers expressions were similar to the results obtained for subconfluent fresh cells (cultured for 7 days after tooth extraction), confirming the stability of markers expression during cryopreservation (Figure 2.11).

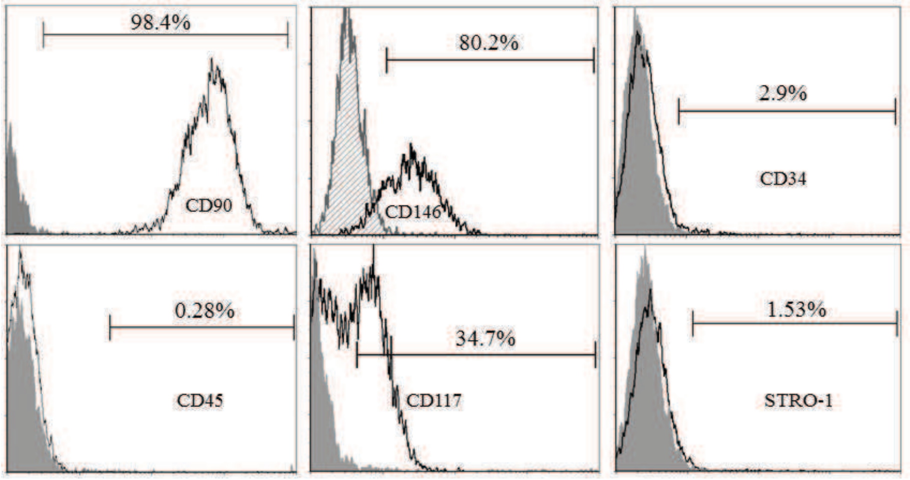

Figure 2.11: Flow cytometry performed on dental pulp cells after cryopreservation (1 year in liquid nitrogen). There was not any noticeable difference compared to flow cytometry preformed on fresh cells after 7 days in culture.

2.3.2.4 Fluorescence Activated Cell Sorting (FACS)

We found a distinguished high-positive CD34 population after 24 h and a clear CD146+ population after 7 days. Thus, after 3 days in culture, we characterized and sorted dental pulp cells by FACS for CD34 and CD146 positivity, and controlled for CD45 negativity. We obtained a pure population of CD34+/CD146+/CD45- stem cells. We kept this purified population in culture *in vitro* for 3 weeks (passage 3), controlling the expression of CD146 and CD34 positivity after passage 3. It appeared that these sorted DPSC kept their CD146 positivity for up to 3 weeks. However, the high positive CD34 population couldn't be kept in culture: the CD34+ cells expressed weakly this marker after 3 weeks in culture (Figure 2.12)

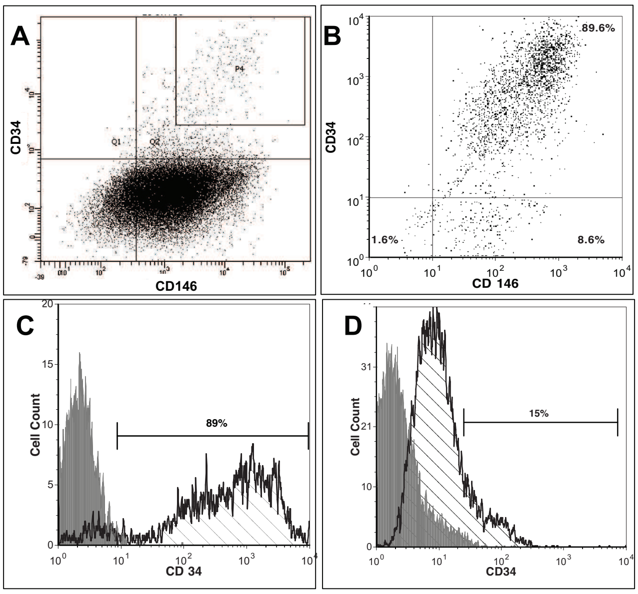

Figure 2.12: FACS of CD34+/CD146+ cells. (A) Total population analyzed for CD34 and CD146 positivity. Double positive cells were selected and sorted. (B) Cell analysis after sorting, showing the CD34+/CD146+ population. (C) Histogram of CD34 expression, after sorting. (D) CD34 expression after 3 weeks in culture (Passage 3).

2.4 Discussion

As already shown in numerous studies, several populations of stem cells have been isolated from different parts of the human tooth and all of them have been shown to have generic mesenchymal stem cell-like properties (Shi *et al.*, 2001) (Gronthos *et al.*, 2002) (Shi *et al.*, 2003) (Laino *et al.*, 2005) (Papaccio *et al.*, 2006) (d'Aquino *et al.*, 2007) (Graziano *et al.*, 2008) (d'Aquino *et al.*, 2009). We demonstrated here the presence of an accessible and reliable source of Dental Pulp Stem Cells (DPSC) within the dental pulp of discarded wisdom teeth. Indeed, following the criteria of the International Society for Cellular Therapy (Dominici *et al.*, 2006), we showed that we could recover mesenchymal stem cells from the dental pulp, even without cell sorting:

(1) We kept only plastic adherent cells by changing culture medium after 24 h.

(2) We confirmed the clonogenicity and proliferation capacities by counting CFU-F (fibroblast-like colony forming units) and measuring the rate of proliferative BrdU-positive cells. Our results were consistent with previous studies (Gronthos *et al.*, 2000) (Miura *et al.*, 2003) (Seo *et al.*, 2004) (Sonoyama *et al.*, 2006).

(3) We performed flow cytometry experiments on the recovered cells, from the immediate cells extraction until cells after cryopreservation. We confirmed the expression of CD90 and CD117 by the recovered cells. The expression of CD146 marker appeared after several days *in vitro*, when cells started to proliferate and migrate. The expression lack of CD45 showed that the recovered cells were not hematopoietic cells, but originated from the dental pulp.

(4) We followed cells differentiation *in vitro*, to confirm that the recovered cells were able to differentiate into osteoblasts, adipocytes and chondroblasts.

The overall purpose of our whole project was to develop an efficient complex composed of resorbable biomaterials (porous silicon) covered by stem cells, for bone tissue engineering. As it had been demonstrated that different cell lines had different adhesion and growth characteristics, we wanted to work with primary human stem cells, usable for therapeutic applications. The third molars appeared to be one of the most accessible source of dental stem cells, because their extraction could be currently performed for orthodontic purpose and, according to the french regulation, these extracted teeth were considered to be medical waste. Because the third molar is the last tooth to develop, it was often, when extracted, in an early stage of development. Thus, wisdom teeth yielded an optimum quantity of dental pulp tissue for the isolation of DPSC (Gandia *et al.*, 2008) (Atari *et al.*, 2012). Our aim was not to discover a new subpopulation of dental stem cells, but to work out an efficient technique to recover stem cells. Thus, we could proceed all experiments with fresh primary culture of human stem cells.

At the beginning of the study, we focused on the CD34+/CD146+ subpopulation because the characteristics of these adherent CD34+ cells were supposed to identify them as a separate putative stem/progenitor cell population (Gordon *et al.*, 2006), and because most of the cell population in our preliminary studies was found to express CD146 marker. In addition, CD34 has been showed as an epitope commonly expressed on human hematopoietic stem cells and on some primitive stromal stem cells from bone marrow (Garcia-Pacheco *et al.*, 2001) and it was demonstrated that the expression of CD146 in the dental pulp was restricted to blood vessel areas, localized in the perivascular region of the pulp tissue (Shi *et al.*, 2003). The expression of CD34 antigen contrasted with previous studies (Gronthos *et al.*, 2002) (Miura *et al.*, 2003) and with the general definition of MSC (Dominici *et al.*, 2006). However, the targeted CD34+/CD146+ population lacked expression of the hematopoietic cell marker CD45 suggesting a mesenchymal origin of these cells and the absence of hematopoietic precursor contamination. And this finding was in agreement with previously published studies that identified a CD117+/STRO-1+/CD34+/CD45- population inside the dental pulp (Laino *et al.*, 2006) (Bakopoulou *et al.*, 2011). We aimed to isolate and purify a primitive stem cells population from mesenchymal tissue, with the ability to proliferate and migrate. However, we could not maintain the purified CD34+/CD146+ population *in vitro.* Cultured cells kept their CD146 positivity for several weeks (as did cells without cell sorting), but lost high CD34 expression after passage 1 or passage 2. Even though it had been reported that DPSC could keep CD34 expression for up to 4 weeks, we didn’t manage to reproduce such results (d’Aquino *et al.*, 2007). For these reasons, we chose to conduct our tissue engineering experiments with non-purified DPSC, without cell sorting, following the minimal criteria for defining mesenchymal stem cells.

The dental pulp is, in many ways, one of the most interesting adult tissues for recovery, therapeutic use and storage of stem cells. The properties of DPSC have been demonstrated to be remarkable for their multipotency as well as their ability to proliferate after cryopreservation. Currently, stem cells that are most used in medicine are stem cells from bone marrow. Comparing the properties of DPSC to those of stem cells from the bone marrow, it seems that DPSC could be a new gold standard for the use of multipotent stem cells in regenerative medicine, for both autologous or allogenic use (Huang *et al.*, 2009) (Collart Dutilleul *et al.*, 2012).

Chapter 3 DPSC Adhesion and Proliferation on surface modified porous silicon scaffolds

3.1 Introduction

In regenerative medicine, tissue engineering applications are based on the development of biological substitutes that can restore, maintain or even improve tissue functions: tissue engineering combines cells and bioactive factors in a defined microenvironment created by a biomaterial scaffold. A key component for tissue engineering is the biomaterial scaffold that, ideally, should support cell attachment, proliferation and differentiation, and be biocompatible and biodegradable at a controlled rate (Wang *et al.*, 2006). Stem cell-based therapy often requires a scaffold to carry cells to the injured site. Porous silicon (pSi) appears to be a promising biomaterial for tissue engineering as it is both non-toxic and bioresorbable under physiological conditions, and it dissolves progressively into nontoxic silicic acid (Collart Dutilleul *et al.*, 2014). Its dissolution rate is dependent on the pore geometry and surface chemical properties, and these two factors influence cell adhesion (Low *et al.*, 2006) (Khung *et al.*, 2008). Moreover, this tunable, biocompatible, and resorbable material has been reported to favor the growth of hydroxyapatite, suggesting the possible bone implantability of the material (Canham, 1995). Its biocompatibility and immunogenicity has already been demonstrated under different conditions and it additionally offers useful photoluminescence properties (Ainslie *et al.*, 2008). Furthermore, pSi-based scaffolds have been investigated for orthopedic (Whitehead *et al.*, 2008) and ophthalmic implants (Cheng *et al.*, 2008), for controlling the adhesion and proliferation of different cell types (Low *et al.*, 2006)(Alvarez *et al.*, 2009) (Torres-Costa *et al.*, 2012), and even as intravenously injectable particles for imaging tumors in vivo (Park *et al.*, 2009) or retina pressure actuators (Muñoz-Noval *et al.*, 2013).

Surface treatment resulting in accessible porosity with chemically stable inner surface is a key step to prevent rapid hydrolysis and degradation of the porous matrix in aqueous environments, without eliciting any undesirable effects on the cells. Moreover, surface chemical modification by turning pSi from hydrophobic to hydrophilic promotes cell adhesion and growth (Low *et al.*, 2006) (Muñoz-Noval *et al.*, 2012). The most common and simple surface treatment is oxidation, which can be performed by either ozone, aging, thermal or chemical treatments. Amine-terminated modifications as silanization with aminopropyl trimethoxysilane or triethoxysilane improve pSi chemical stability and enhance cell adhesion in comparison to oxidized pSi (Low *et al.*, 2006). Thermal hydrosilylation was also used to graft chemical species to generate a substrate for cell adhesion and proliferation, such as dodecene, undecenoic acid or oligoethylene glycol (Alvarez *et al.*, 2009).

Substrate topography has been known for a long time to affect crucial cell functions, namely adhesion, proliferation, migration, and differentiation. Moreover, material surface morphology has strong effects on cell cytoskeleton and morphology (Dalby *et al.*, 2003). Furthermore cellular organization requires that a cell assess its relative location, taking in multiple cues from its microenvironment i.e. the extracellular matrix *in vivo*, and the supporting scaffold *in vitro* (Buxboim *et al.*, 2010). Cells respond to topographic surfaces in a wide variety of ways, which depend upon cell type, pore size, as well as the physicochemical properties of the substrate material. The effect of pore size and porosity of pSi on cell growth is of particular relevance. Indeed, its pore dimensions can be precisely controlled and are highly tunable during pSi electrochemical anodization. A variety of pore sizes can be produced: from micropores (< 2 nm), mesopores (2−50 nm) to macropores (> 50 nm) depending on the preparation conditions (Sailor, 2011). Although microscale topography modulates cellular behavior *in vitro*, it is important to consider that cells *in vivo* make contact with microscale as well as nanoscale topographical features. Diverse topographical features have been assessed for different cell types, at the micrometer and submicrometer scale, and some recent studies on pSi have focused specifically on pore geometry influence on cell adhesion and proliferation (Sapelkin *et al.*, 2006) (Khung *et al.*, 2008) (Wang *et al.*, 2012) (Clements *et al.*, 2012) (Gentile *et al.*, 2012). Pore geometry was clearly shown to affect the cellular response, but each cell type responded differently. Rat hippocampal neurons were observed to preferentially adhere on macroporous surfaces, with a pore size ranging between 50 and 100 nm, rather than on flat silicon surfaces (Sapelkin *et al.*, 2006). Neuroblastoma cells cultured over continuous porous gradient substrates were more likely to develop on surface topography with feature sizes of <20 nm, and substrates with an average pore size of a few hundreds of nanometers restricted cell adhesion and proliferation (Khung *et al.*, 2008). Primary human endothelial cells, mouse fibroblasts, mouse neuroblastoma cells, and human cortical neuron cell lines adhered and proliferated more on mesoporous silicon than on flat silicon, with a tendency to proliferate more on pSi with an average pore size of ≈5 nm, rather than ≈20 nm (Gentile *et al.*, 2012). It is of interest to note that this was, so far, the only study assessing human primary cells. Rat mesenchymal stem cells (rMSC) adhesion was enhanced as pore size decreased, with a maximum proliferation for an average pore size of ≈20 nm but responded more strongly to surface chemical changes during short-term culture (Clements *et al.*, 2012) and had a high proliferation rate also on flat silicon (Wang *et al.*, 2012).

Coupling the auspicious capacities of human adult mesenchymal stem cells (hMSC) with the unique properties of pSi substrates provides a promising approach for therapeutic application in regenerative medicine. Indeed, mesenchymal stem cells therapeutic potential has generated significant excitement in the field of regenerative medicine, as they can be found in various niches within human body. The ability of these cells to self-renew and differentiate into multiple tissues makes them an attractive cell source for cell-based regenerative therapies. MSCs have considerable potential for the treatment of musculoskeletal disorders owing to their expansion capacity, immunosuppressive properties and ability to differentiate into bone and cartilage (Ma, 2010). Adult stem cells constitute the source of differentiated cells for the regeneration of tissues that are diseased or injured. In adults, these cells are accessible from different origins, such as bone marrow, adipose tissue or dental pulp (Marolt *et al.*, 2010).

In the study presented in this chapter, we investigated for the first time the behavior of primary culture of hMSC on pSi scaffolds. Mesenchymal stem cells from the dental pulp, named Human Dental Pulp Stem Cells (DPSC) (Gronthos *et al.*, 2000), were studied for adhesion and proliferation on oxidized mesoporous and macroporous pSi substrates, presenting pore size of 10 ± 2 nm, 36 ± 4 nm and 1.0 ± 0.1 µm. We also evaluated the influence of pSi substrate surface modification with CO_2H, NH_2 or $NHCONHNH_2$ groups on the cell behavior. After characterization of the silicon substrates, cell adhesion and proliferation behavior were studied using fluorescence and electron microscopy, enzymatic proliferation assays and bromodeoxyuridine (BrdU) incorporation for the detection of proliferating cells.

3.2 Materials

3.2.1 Human Dental Pulp Stem Cells (hDPSC)

Human impacted third molar extracted for orthodontic reasons were recovered from healthy patients (15-18 years of age). Written informed consent was obtained from the parents of the patients. This protocol was approved by the local ethical committee (Comité de Protection des Personnes, Montpellier hospital, France). Tooth surfaces were cleaned using 2% chlorhexidine and cut around the cementum-enamel junction by using sterilized disc. The teeth were then broken into 2 pieces to reveal the pulp chamber. The pulp tissue was gently separated from the crown and root and then digested in a solution of 3 mg/mL collagenase type I and 4 mg/mL dispase for 1 hour at 37°C. The solution was then filtered through 70 µm Falcon strainers and immersed in αMEM supplemented with 10% fetal bovine serum (FBS), 100 U/mL penicillin, 100 µg/mL streptomycin and placed in 75 ml flasks. Cells were incubated for 1 week at 37°C with 5% CO2. Non-adherent cells were removed by a change of medium 24 h after cell seeding.

3.2.2 DPSC characterization

After 1 week, sub-confluent cells were collected and analyzed for minimal criteria to define human mesenchymal stem cells, such as adherence to plastic, expression of cell surface antigens and ability to differentiate into osteoblasts, adipocytes and chondroblasts *in vitro* (Dominici *et al.*, 2006). The antigen profiles of cultured DPSC were analyzed by detecting the expression of the cell surface markers CD90, CD146, CD117 and CD45 using flow cytometry. CD90 is a widely accepted marker for mesenchymal stem cells, CD146 is a marker expressed in perivascular mesenchymal stem cells, CD117 is the receptor of stem cell factor, and CD45 is a marker of hematopoietic cells, mainly myeloid progenitors (Coppe *et al.*, 2009)(Shi *et al.*, 2003). The latter has been used to demonstrate the absence of contamination by CD45+ hematopoietic progenitors. Cells were controlled for multipotency with *in vitro* osteogenic, adipogenic and chondrogenic differentiation following a previously described protocol (Kemoun *et al.*, 2007). Briefly, for osteogenic and adipogenic differentiation, dental pulp cells were seeded at a density of 105 cells/cm2 and maintained in αMEM supplemented with 10% FBS until confluence. Cells were then cultured in osteogenic medium (αMEM supplemented with 15% FBS, dexamethasone, L-ascorbate phosphate, and β-glycerophosphate) or in adipogenic medium (αMEM supplemented with 10% FBS, dexamethasone, insulin, and isobutylmethylxanthine) for 21 days. Control cultures were maintained without osteogenic or adipogenic supplements. To induce chondrogenic differentiation, cells were cultured for 21 days as pellets in a serum-free expansion medium containing dexamethasone, L-ascorbate phosphate, L-proline, sodium pyruvate, ITS-Premix, and TGF-β3. Control pellet cultures were maintained in basal medium.

3.2.3 Porous silicon scaffolds preparation

P++ type boron-doped crystalline silicon wafers with 0.0008 - 0.0012 Ωcm resistivity were obtained from Siltronix®. Wafers were etched in a custom-made Teflon cell at a constant current density of either 30 mA/cm^2 for 10 min or 300 mA/cm^2 for 2 min 15 s, in a hydrofluoric acid (HF) solution in ethanol (3:1 HF:ethanol solution, volume ratio). To create pSi with larger pores (1 µm), p-type <100> wafers with 7 - 21 Ωcm resistivity were etched at a constant current density of 4.5 mA/cm^2 for 10 min, in a 50% HF solution in dimethylformamide (DMF). Etched wafers were oxidized at 800°C for 1 hour. The wafers were cut into 0.5 cm^2 pieces. Some of the samples etched in a 300 mA/cm^2 current were also submitted to various chemical treatments: silanization with aminopropyltriethoxysilane (APTES) after thermal oxidation (as described above), hydrosilylation with undecenoic acid without pre-oxidation treatment, and hydrosilylation with semicarbazide without pre-oxidation treatment. PSi surface modifications with APTES, and with undecenoic acid were described elsewhere (Low *et al.*, 2006) (Alvarez *et al.*, 2009). The covalent attachment of the semicarbazide to hydrogen-terminated pSi surfaces by thermal hydrosilylation was realized according to recently published procedure using tert-Butyl-2[(allylamino)carbonyl]hydrazine carboxylate (Secret *et al.*, 2013). The removal of the protecting group yields a semicarbazide-terminated monolayer, (Coffinier *et al.*, 2005). For use in cell culture, the wafers were sterilized with 70% ethanol (volume ratio) for 10 min before drying under sterile airflow.

3.2.4 Surface characterization

The topography of the surface modified pSi samples was analyzed by environmental scanning electron microscopy (SEM) (Analytic FEI Quanta FEG 200) to determine the pore size, and by atomic force microscopy (AFM) (Asylum MFP-3D, Asylum Research, Santa Barbara, CA) to determine the surface roughness. For SEM, an acceleration voltage of 20.00 kV was used in a pressure of 0.5 Torr. For AFM, gold-coated silicon nitride rectangular cantilevers were used with a typical spring constant of 30 pN/nm-1, tip radius ~30 nm (BL-RC150 VB-C1: Bio- Lever A, Olympus Optical Co., Ltd., Tokyo, Japan). The spring constant for each cantilever was determined by thermal noise method within the supplied software. Height images were recorded in tapping mode in liquid at room temperature. Typically, 512 x 512 point scans were taken at a scan rate of 1 Hz per line.

Surface tension was determined using sessile drop contact angle measurements, using a custom-made set-up consisting of a syringe dispenser, a sample stage, a macro lens and a CCD camera. 5µl of MilliQ water was spotted onto the surface at room temperature. Images of the drop profiles were captured and ImageJ® software was used to measure contact angles on both sides of the droplet. A minimum of four replications was conducted for each sample surface.

3.2.5 Cell adhesion

DPSC attachment was monitored by fluorescence microscopy. Cells were seeded onto the surface of sterilized pSi at a cell density of $5x10^4$ cell/ml. Flat silicon (non etched silicon wafers) and glass coverslip were used as controls. Cells were incubated for 4h, 24h, 48h and 72h at 37°C with 5% CO2, in a humidified incubator, in ultra low adherence 24 well plates (Corning, NY, USA) which inhibit cell attachment on the tissue culture plate, allowing DPSC to attach only to the pSi. After the incubation time, the cells were fixed with 2.5% glutaraldehyde and stained with 50 µg/mL of 4,6-diamidino-2-phenylindole (DAPI) for 30 min before being washed with PBS to remove any non-adherent cells. Cells were observed under fluorescence microscopy at an excitation wavelength of 290 nm. Controls were cells cultured on glass coverslip and flat silicon, cut into 0.5 cm^2 squares. Cell counts were conducted at five different locations on the surface of each sample (four peripheral and one central) in areas of 1400 μm x 1050 μm.

3.2.6 Proliferation assays

Cell proliferation was first measured via quantification of acid phosphatase activity using paranitrophenylphosphate phosphatase test (pNPP) (Werner *et al.*, 2009). DPSC proliferation was assessed after 4 h, 24 h, 48 h and 72 h incubation. At the end of each experimental time, the cells were washed three times with PBS and lysed with 500 mL of acid phosphatase lysis buffer (0.1 M sodium acetate, 0.1% Triton X-100, pH 5.5), supplemented with 1 mg/mL of pNPP (Sigma-Aldrich). After 1 h incubation at 37 °C, the reaction was stopped by the addition of 10 μL of 1 N NaOH. The supernatant was removed, placed in a new 24 wells plate and the yellow colorimetric reaction was measured by a microtiter plate reader at 405 nm. All proliferation experiments were performed at least in triplicate and results were normalized according to the glass coverslip control at 72 h, for which 100% of proliferation was attributed.

The proliferation rate of DPSC on pSi was also assessed by bromodeoxyuridine (BrdU) incorporation for 24 h (Horner *et al.*, 2000). DPSC were seeded on the various pSi scaffolds at a density of 105 cells/ml in αMEM supplemented with 10% FBS with 1:100 diluted BrdU labeling (Invitrogen). After 24 h incubation at 37°C, samples were rinsed 3 times in PBS, fixed in 4% paraformaldehyde, rinsed again 3 times in PBS and put in 1.5M HCl (Sigma) for 30 min at room temperature to dissociate DNA strands. Samples were washed with PBS, incubated in PBS with 0.1% Triton X-100 and 1% BSA for 1 h at room temperature, then incubated with mouse anti-BrdU primary antibody (Miltenyi) overnight at 4°C. After immunostaining, cells were washed with PBS/1% BSA, incubated with FITC conjugated rabbit anti-mouse secondary antibody for 30 min and counterstained with 2μg/ml Hoechst 33342 (Sigma) for nucleus staining. Samples were observed under fluorescence microscopy at an excitation wavelength of 290 nm for nuclei (blue staining) and 490 nm for BrdU (green staining). All experiments were performed at least in triplicate and the number of BrdU-positive cells was expressed as a percentage of the total number of cells, counted at 5 different points per sample.

3.2.7 Cellular morphology and viability

Fluorescein diacetate (FDA) and propidium iodide (PI) staining was used to observe cell morphology and to distinguish viable and dead cells. FDA, which enters viable cells by energy-dependent endocytosis, yield a bright green color; while PI, which interacts with RNA and DNA of cells having disrupted cytoplasmic and nuclear membranes, produces a red color (Cao *et al.*, 2011). Living cells were stained with 25 µg/mL of fluorescein diacetate (FDA) and 20 µg/ml of propidium iodide (PI), and incubated for 3 min at 37°C. After staining, samples were washed with PBS before being observed under a Nikon TE2000-E microscope equipped with a Nikon digital camera at an excitation wavelengths of 480 nm for FDA and 630 nm for PI. Observations were conducted at five different locations on the surface of each sample (four peripheral and one central) at magnifications x20 and x40. All experiments were made in triplicate.

3.2.8 SEM evaluation of DPSC morphology and spreading

The cells were cultured on the various pSi scaffolds and control for 24 h under normal conditions, as described above. After 24 h incubation the cells were washed twice with PBS buffer and fixed with 2.5% glutaraldehyde for 1 h at room temperature. After washing the specimens were dehydrated in graded ethanol solutions from 50% to 100%, and in hexamethyldisilazane (HMDS, Ted Pella, USA). The samples were then sputter-coated with platinum. Scanning electron microscopy (SEM) was performed on an Analytic FEI Quanta FEG 200 microscope with an acceleration voltage of 15 kV in a pressure of 10^{-5} Torr. From the SEM images, two parameters for characterizing the cell morphology were considered: the cell area (in μm^2), defined as the area covered by the cell projected over the substrate and the cell circularity, defined as the ratio between the shorter and the longer axis of the cell (value between 0 for elongated cells and 1.00 for round cells). All experiments were made in triplicate.

3.2.9 Statistical analysis

All data were evaluated with a Shapiro-Wilk normality test. The cell attachment evaluations (cell counts) were plotted as mean ± standard error of the mean and statistical analyses were performed using a parametric Student t-test. The results of proliferation experiments with pNPP enzymatic assays were normalized according to the glass coverslip control at 72 h, for which 100% of proliferation was attributed. The data were plotted as mean ± standard error of the mean and statistical analyses were performed using a parametric Student t-test. The results of BrdU proliferation assay, cell surface area and cell circularity were analyzed with a non-parametric one-way Tukey ANOVA test (SigmaStats, SPSS Inc., Chicago, IL, USA). A p-value of <0.05 was considered to be significant.

3.3 Results

3.3.1 pSi samples

PSi substrates were generated from bulk boron-doped p-type silicon wafers via anodization (Sailor, 2011). Substrates with various pore sizes were obtained by modulating the etching conditions and the doping level of the silicon wafer. Figure 3.1 shows representative SEM and AFM images of the pSi substrates; distinct textural features are depicted when comparing the different pSi substrates. PSi substrates obtained from silicon wafers with a resistivity of 0.0008 - 0.0012 Ωcm by applying a constant current density of 30 mA/cm2 and 300 mA/cm2 had an average pore diameter of 10 ± 2 nm (pSi 10 nm) and 36 ± 4 nm (pSi 36 nm), respectively. The pSi layers produced from silicon wafers with 7 - 21 Ωcm resistivity, by applying a current density of 4.5 mA/cm2, had an average pore diameter of 1020 ±100 nm (pSi 1 µm). The pSi substrates were quite uniformly porosified. Topographic images of pSi were obtained using AFM, and the calculated statistical roughness (RMS) of the substrate were found at 1.9 ± 0.7 nm for “pSi 10 nm”, 7 ± 2 nm for “pSi 36 nm” and 54 ± 20 nm for “pSi 1 µm”.

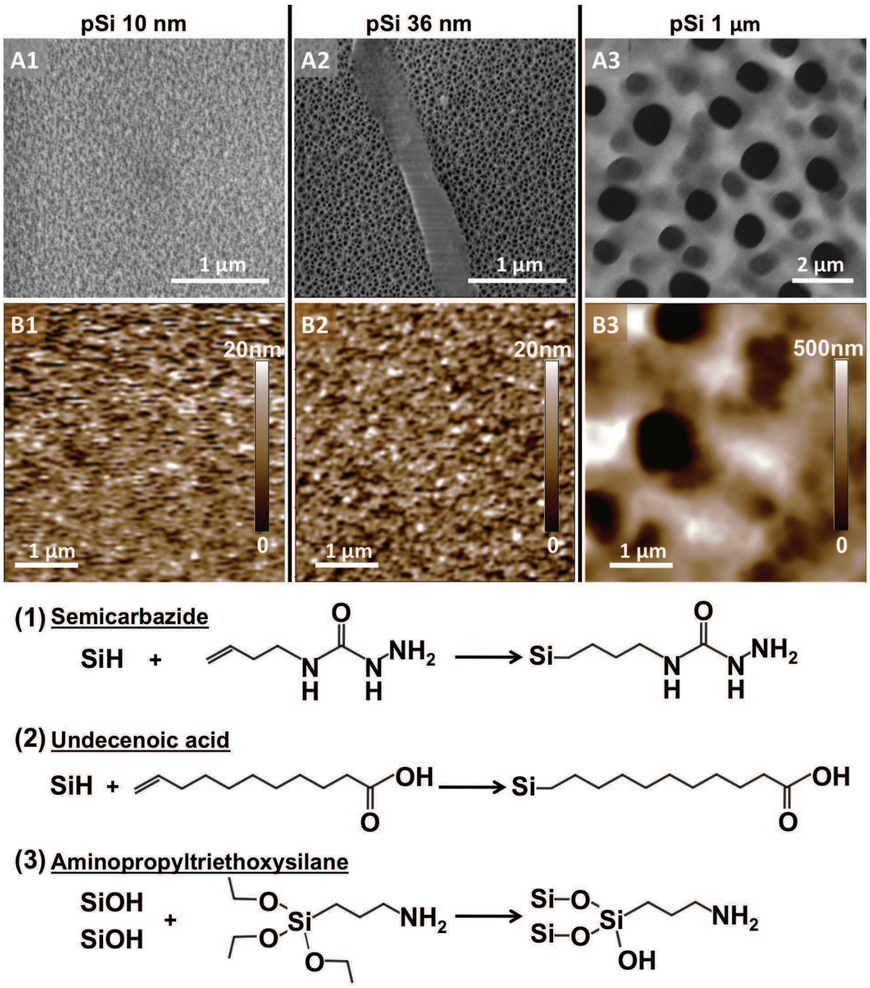

Figure 3.1: Characterization of the porous silicon scaffolds. Surface topography of the silicon substrates imaged with (A) scanning electron microscopy and (B) atomic force microscopy. Porous silicon with mean pore diameter of 10 ± 2 nm, 36 ± 4 nm and 1.0 ± 0.1 µm are shown as A1-B1, A2-B2 and A3-B3 respectively. Surface chemical treatments are presented as: (1) Non-oxidized pSi hydrosilylated with semicarbazide. (2) Non-oxidized pSi hydrosilylated with undecenoic acid. (3) Oxidized pSi silanized with APTES.

Surface chemical treatments realized on “pSi 36 nm” substrates are hydrosilylation with undecenoic acid or semicarbazide, and silanization (after thermal oxidation) with APTES. The reaction schemes of the chemical treatments are presented in Figure 3.1. The sample pSi 36 nm was chosen because it displayed the best results in term of cell adhesion, compared to pSi 10 nm and pSi 1 µm (Figure 3.2). Water contact angle measurements performed after surface functionalization revealed that all the substrates were hydrophilic (Table 3.1). Oxidized pSi hydrophilicity was attributed to the formation of a polar Si-OH capped surface after oxidation. By analyzing SEM micrographs, the surface porosities (ratio between total area of the pores and the area of the considered region of interest) were found to be as follows: 40 ± 4% for pSi 10nm, 45 ± 6% for pSi 36nm and 24 ± 4% for pSi 1μm.

	Flat Si	pSi 10 nm	pSi 36 nm	pSi 1 μm
Oxidized	26° ± 4	16° ± 2	15° ± 3	33° ± 5
Undecenoic acid			35° ± 5	
APTES			37° ± 6	
Semicarbazide			12° ± 3	

Table 3.1: Water contact angle of the various scaffolds (Flat Si and pSi)

3.3.2 Cell adhesion and growth

We examined DPSC attachment to various surface-modified pSi layers and compared the results with those of DPSC cultured on glass coverslips and on flat silicon wafers after a period of 4 h, 24 h, 48 h and 72 h. The results are shown in Figure 3.2.

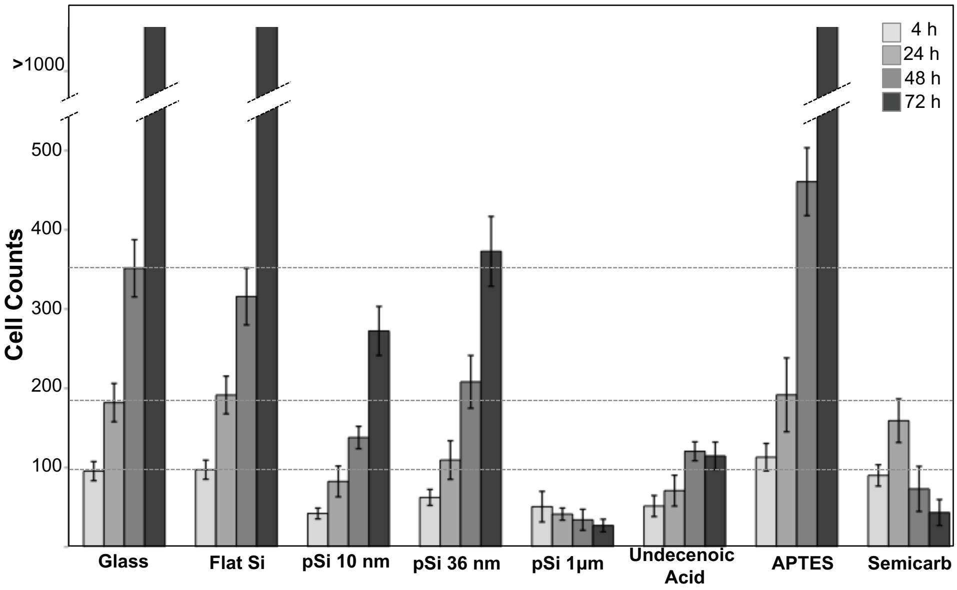

Figure 3.2: DPSC attached on various type of pSi, after 4h, 24h, 48h and 72h of incubation. Glass coverslip and (non-porous) flat silicon were used as controls. Cells were counted per 1400 µm x 1050 µm area, in five areas per samples. After 72 h, cells couldn't be counted on glass, flat Si and APTES as they reached confluence (protruding bars).

The experimental results show that initial cell adhesion and growth were very similar on glass coverslip, Flat Si, APTES-treated pSi and semicarbazide-treated pSi, after 4 h and 24 h. Initial cell adhesion on oxidized pSi (pSi 10nm, pSi 36nm and pSi 1µm) and undecenoic acid-treated pSi were significantly lower compared to glass coverslip ($p<0.001$, $p=0.003$, $p<0.001$, and $p<0.001$ respectively). However, DPSC started to proliferate on pSi 10 nm and pSi 36 nm after 24 h following the same growth pattern observed on glass coverslip, while the number of cells slightly decreased on pSi 1 µm and on undecenoic acid-treated pSi after 24h and 48 h respectively. After 48 h, the numbers of cells were similar on glass coverslip and on flat Si, significantly higher on APTES-treated pSi ($p<0.001$) and significantly lower on semicarbazide-treated pSi (p<0.001), pSi 10 nm (p<0.001) and pSi 36 nm (p<0.001). It is remarkable that there were significantly more cells on pSi 36 nm than on pSi 10 nm after 48 h and 72 h (p=0.006 and p=0.004, respectively), and that the number of cells on semicarbazide-treated pSi increased during 24 h and decreased abruptly after 48 h. After 72 h, DPSC reached confluence on glass coverslip, flat Si and APTES-treated pSi.

Cells were stained with the vital dye FDA to observe cell adherence and cytoplasmic spreading. The morphologies of DPSC on surface modified pSi at early attachment stage (after 4 h) are shown in Figure 3.3.

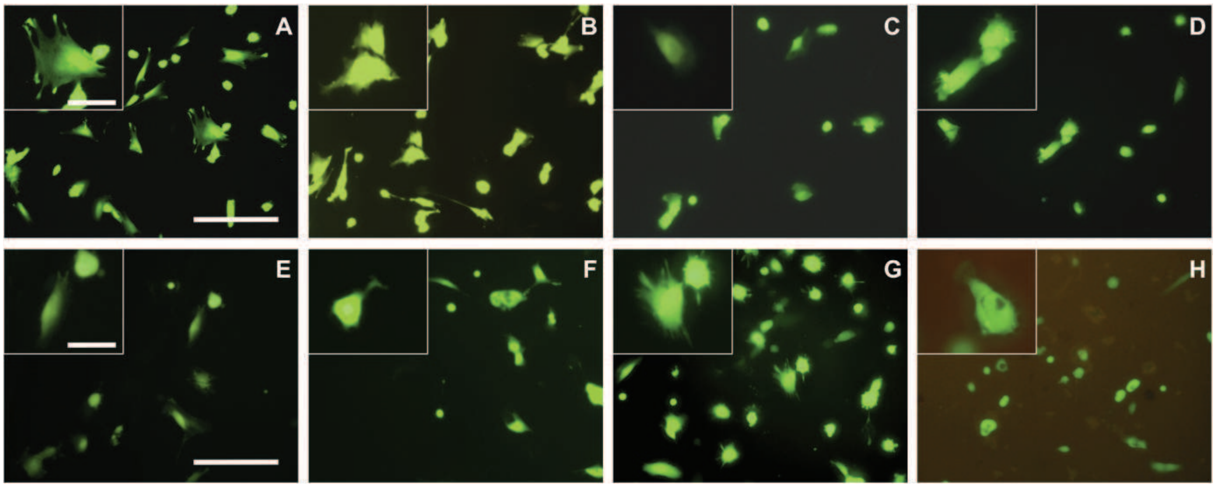

Figure 3.3: Fluorescence microscopy of DPSC on the various scaffolds after 4 h incubation. Cells are stained with vital FDA staining (cytoplasma: green staining). A: glass coverslip, B: Flat Si, C: pSi 10nm, D: pSi 36nm, E: pSi 1µm, F: undecenoic acid-treated pSi, G: APTES-treated pSi, H: semicarbazide-treated pSi. Main pictures: x20, scale bar = 100 µm. Inserts: magnification x40, scale bar = 40 µm.

From Figure 3.3 it is obvious that cells attached on all surfaces, with various shapes from normal fibroblastic morphology (Fig 3.3A, 3.3B and 3.3G) to less-spread cells with protrusions (Fig 3.3C and 3.3D), and even round cells (Fig 33.E, 3.3F and 3.3H). Fibroblastic morphologies were found mainly on glass coverslip, flat Si and APTES-treated pSi. Cells with protrusions were mainly found on pSi 10 nm and pSi 36 nm, while round cells with few protrusions were recovered on pSi 1 µm, undecenoic acid-treated pSi and semicarbazide-treated pSi. These results correlate well with the results on cell adhesion described from Figure 3.2.

3.3.3 Cell proliferation

DPSC proliferation over a 3-day-time period, assessed by acid phosphatase activity, was evaluated for the various pSi scaffolds, and compared to that of glass coverslip and Flat Si. In order to normalize the results, 100% cell enzymatic activity was attributed to the value found for glass coverslip after 72 h of cell incubation (Figure 3.4).

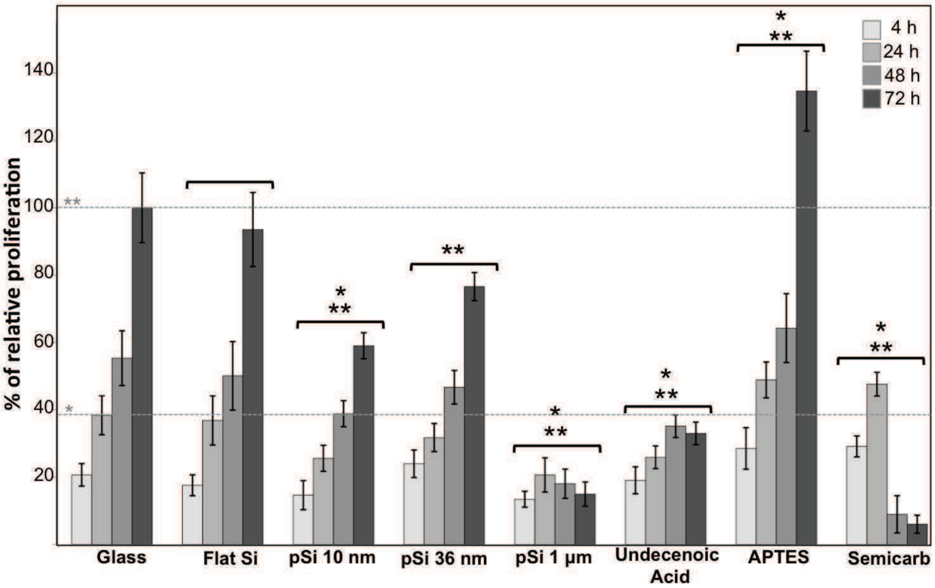

Figure 3.4: DPSC proliferation at 4 h, 24 h, 48 h and 72 h on various pSi surfaces, assessed by acid phosphatase activity determination. Glass coverslip and oxidized non-porous silicon (flat Si) were used as control. In order to normalize the results, 100% adhesion was attributed to cells attached on glass coverslip after 72 h of cell seeding. All experiments were performed in triplicate. Statistical significance was determined by using the Student's t test ($P < 0.05$) for comparison with glass coverslip: (*)Statistical difference at 24 h. (**)Statistical difference at 72 h.

The experiments show that DPSC clearly proliferated at all time points on glass coverslip, flat Si, pSi 10 nm, pSi 36 nm and APTES-treated pSi, while the proliferation was limited on pSi 1 µm and undecenoic acid-treated pSi. For semicarbazide-treated pSi, the proliferation rate was higher compared to glass coverslip until 24 h, and dropped dramatically after 48 h. After 24 h of incubation, the proliferation rate was equivalent on glass coverslip and on flat Si. At 24 h, APTES-treated pSi and semicarbazide-treated pSi improved DPSC proliferation of 27 % and 24 % (p=0.042 and p=0.039, respectively). The proliferation rate was lower on pSi 10 nm, pSi 1 µm and undecenoic acid-treated pSi (p=0.012, p=0.004 and p=0.011, respectively). On pSi 36 nm, this rate was slightly lower compared to glass coverslip and slightly higher compared to pSi 10 nm, but without statistical significance (p=0.106 and p=0.094, respectively). Interestingly, we found that, after 48 h and 72 h, the proliferation rate on pSi 36 nm was significantly higher than the rate on pSi 10 nm (p=0.006 at 48 h and p=0.003 at 72 h), revealing the tendency for DPSC to attach and proliferate more on pores of about 36 nm than on pores of about 10 nm. After 72 h of incubation, the proliferation rate was equivalent on flat Si and glass coverslip, higher for 34 % on APTES-treated (p=0.005), and lower on pSi 10 nm, and pSi 36 nm.

To confirm the proliferation capacities of DPSC on pSi, we investigated their mitotic activity just after cell seeding, by BrdU incorporation for 24 h. The percentages of BrdU positive cells, corresponding to mitotically active cells, are shown in Figure 3.5.

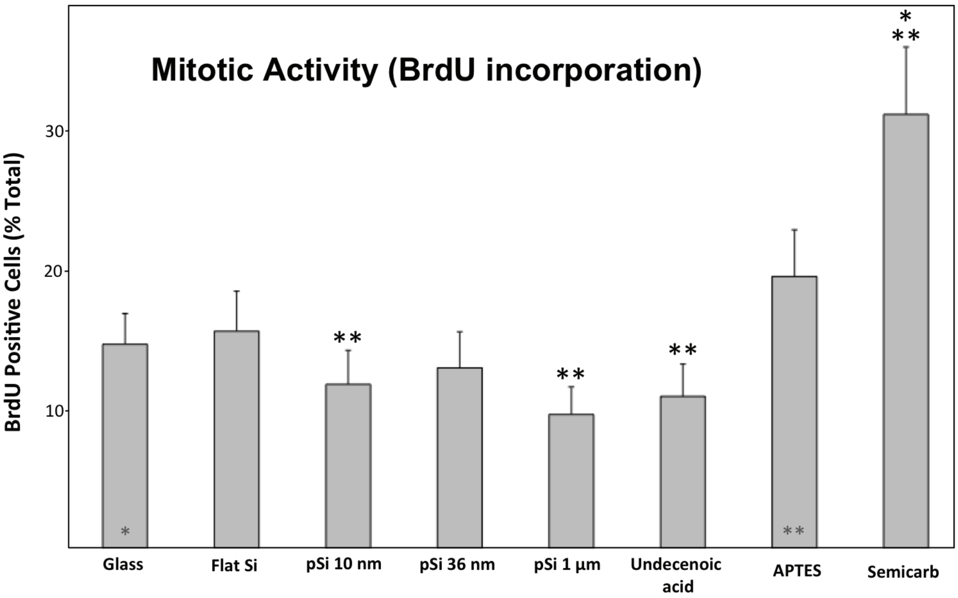

Figure 3.5: Number of BrdU-positive cells after 24 h of incubation, expressed as a percentage of the total number of DPSC counted on the various pSi surfaces. Glass coverslip and oxidized non-porous silicon (Flat Si) were used as controls. All experiments were performed in triplicate. Statistical significance was determined by one-way ANOVA Tukey test ($P < 0.05$): (*) Comparison with glass coverslip. (**) Comparison with APTES

The ratios of BrdU-positive cells were remarkably enhanced on semicarbazide-treated pSi (29.2 ± 6%) compared to glass coverslip (14.7 ± 4%, $p<0.001$), Flat Si (15.6 ± 6%, $p<0.001$) and APTES-treated pSi (19.5 ± 7%, $p=0.011$). The BrdU-positive cells rate was 14.7 ± 4% on glass coverslip. In comparison, this rate was similar on flat Si (15.6 ± 6%, $p=0.756$), slightly higher on APTES-treated pSi (19.5 ± 7%, $p=0.142$), and slightly lower on pSi 10 nm (11.8 ± 5%, $p=0.331$), on pSi 36 nm (13.0 ± 5%, $p=0.555$), on pSi 1 μm (9.6 ± 4%, $p=0.075$) and on undecenoic acid-treated pSi (10.9 ± 4%, $p=0.189$).

3.3.4 Cell morphology

SEM was employed to study the effects of porosity and chemical surface treatments on the morphology of single adhering cells, and to determine cell circularity and cell surface area. Figure 3.6 shows representative images of DPSC growing on the different pSi substrates, on glass coverslip and flat silicon as controls, after 24 h of incubation.

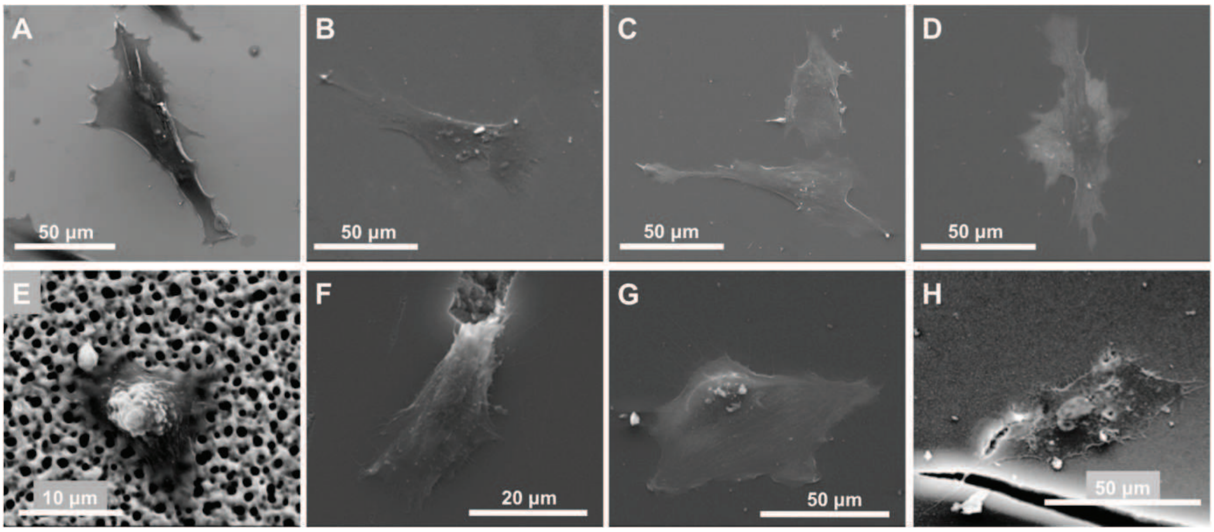

Figure 3.6: Scanning electron microscopy of DPSC after 24 h incubation. A: glass coverslip, B: flat Si, C: pSi 10nm, D: pSi 36nm, E: pSi 1μm, F: undecenoic acid-treated pSi, G: APTES-treated pSi, H: semicarbazide-treated pSi.

On pSi 10 nm and pSi 36 nm substrates, cells appeared elongated and well spread with the formation of long protrusions out of the cell membrane (Figure 3.6 C and 3.6D). The same shapes were recovered on both glass coverslip and flat Si, even though fewer protrusions were visible (Figure 3.6A and 3.6B). DPSC on APTES-treated and semicarbazide-treated pSi appeared less elongated, but well spread with many long protrusions (Figure 3.6G and 3.6H). Differently, on the pSi 1 µm and undecenoic acid-treated pSi substrates, cells appeared more rounded with a few short and squat protrusions (Figure 6E and 6F). Similar images are presented in Figure 3.7, showing cell protrusions at higher magnification, highlighting the relationship between cells and porous scaffolds at the nanometer scale.

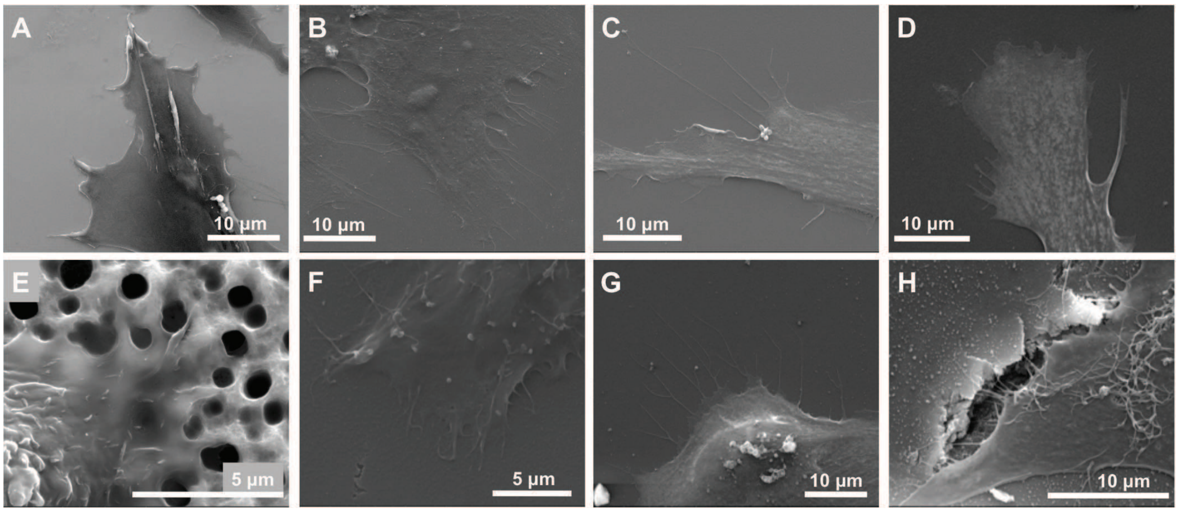

Figure 3.7: Scanning electron microscopy of DPSC after 24 h incubation at magnification x 8000 (image A, B, C D and G), x 15000 (image F and H) or x 30000 (image E). A: glass coverslip, B: flat Si, C: pSi 10nm, D: pSi 36nm, E: pSi 1µm, F: undecenoic acid-treated pSi, G: APTES-treated pSi, H: semicarbazide-treated pSi.

To gain a more quantitative understanding of cell surface adhesion, the cell surface area and circularity were determined on the different substrates (Figure 3.8).

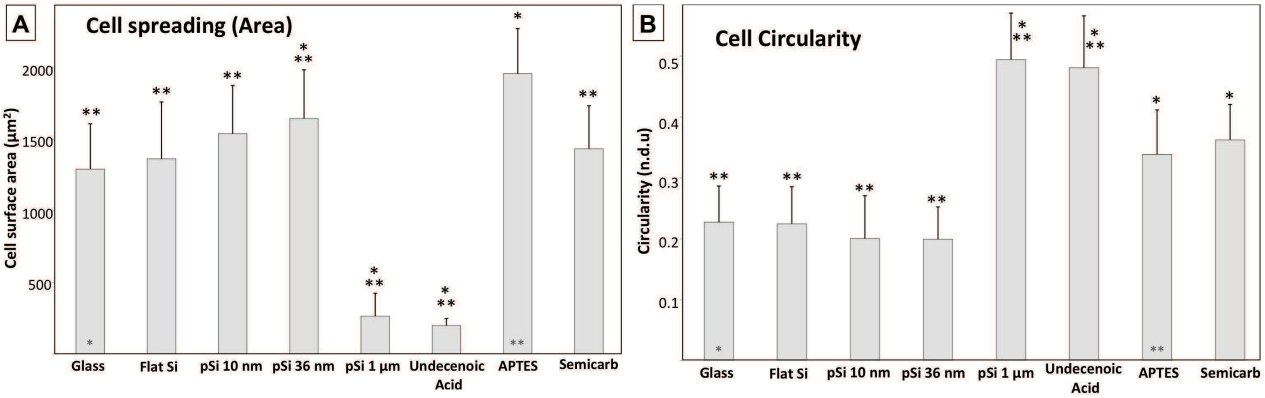

Figure 3.8: A: Mean cell surface area calculated from SEM images after 24 h (in µm2). B: Mean cell circularity, evaluated from the SEM images after 24 h. 0 represent a line and 1.0 a circle (non defined unit). Statistical significance was determined by one-way ANOVA Tukey test (P < 0.05): (*) Comparison with glass coverslip. (**) Comparison with APTES.

Compared to glass coverslip, the mean cell surface area was similar on flat Si, pSi 10 nm and semicarbazide-treated pSi; it was higher on pSi 36 nm (p=0.040) and APTES-treated pSi (p<0.001); and it was lower on pSi 1 µm (p<0.001) and undecenoic acid-treated pSi (p<0.001). APTES-treated pSi had a significantly higher cell surface area compared to all other surfaces (Figure 3.8A). It is interesting to note that, on all surfaces except pSi 1 µm and undecenoic acid-treated, DPSC were spread and covered a very large area (between 1290 ± 316 µm2 on glass coverslip and 1958 ± 314 µm2 on APTES-treated pSi), which is consistent with the mesenchymal stem cells characteristics (Krishna *et al.*, 2011). We also considered cell circularity which value varies between 0 (elongated cell) and 1.0 (perfect circle). Comparing directly circularity of cells on the various pSi substrates, morphology was found to vary significantly on 3 groups of substrates: DPSC had a similar circularity on glass coverslip (0.23 ± 0.06), flat Si (0.22 ± 0.06), pSi 10 nm (0.20 ± 0.07) and pSi 36 nm (0.20 ± 0.05). Cell circularity was similar on APTES-treated (0.34 ± 0.07) and semicarbazide-treated pSi (0.36 ± 0.06), and it was also similar on pSi 1 µm (0.49 ± 0.08) and undecenoic acid-treated pSi (0.48 ± 0.08) (Figure 3.8B).

3.3.5 Cell morphology after 72 hours

We followed cell growth for 72 h, until they reached confluence on the control surfaces (glass coverslip and flat Si). Cells were stained with the vital dye FDA to observe cell adherence and cytoplasmic spreading. The morphologies of DPSC on surface modified pSi after 72 h are shown in Figure 3.9.

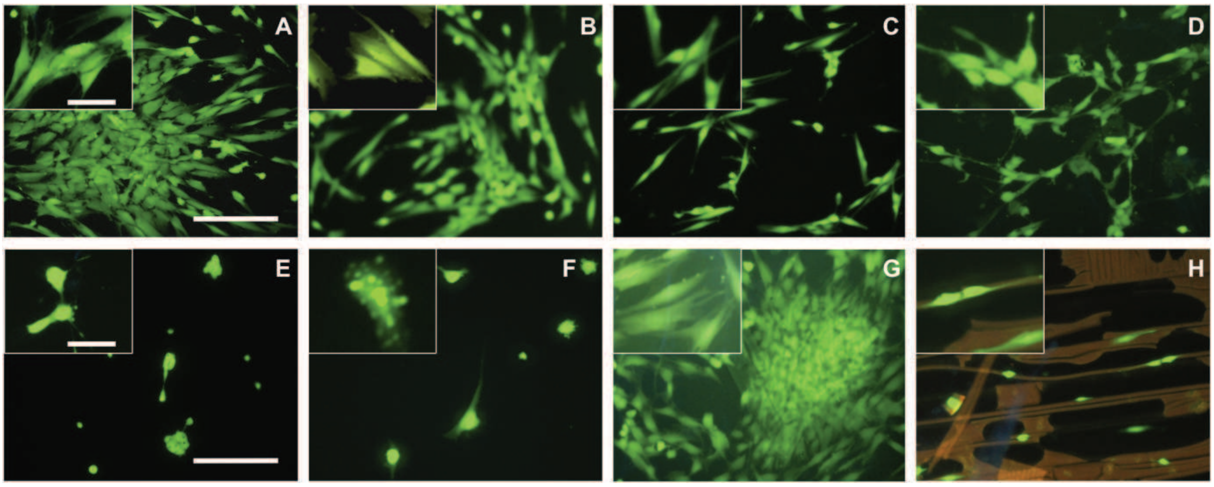

Figure 3.9: Fluorescence microscopy of DPSC after 72 h incubation. Cells are stained with vital FDA. A: glass coverslip, B: Flat Si, C: pSi 10 nm, D: pSi 36 nm, E: pSi 1 µm, F: undecenoic acid-treated pSi, G: APTES-treated pSi, H: semicarbazide-treated pSi. Main pictures: x20, scale bar = 100 µm. Inserts: x40, scale bar = 40 µm.

As expected according to results presented above, DPSC reached confluence on glass coverslip, flat Si and APTES-treated pSi, growing as clonogenic cell clusters (CFU-F: colony-forming units-fibroblastic) with a high proliferation rate. On pSi 10 nm and pSi 36 nm, DPSC were forming few CFU-F with a moderate proliferation rate, while DPSC were hardly growing on pSi 1 µm and undecenoic acid-treated pSi. The semicarbazide-treated pSi was clearly degraded, with DPSC attached only on the porous remaining substrate (Figure 3.9H), highlighting the fast resorbability of the pSi scaffold.

3.4 Discussion

The aim of this work was to elucidate the influence of pore morphology and chemical status of different pSi substrates on immediate human mesenchymal stem cell adhesion and on their proliferation rate. Therefore we compared the attachment, spreading, morphology and proliferation of DPSC seeded on different porous surfaces. Our major finding was that pore geometry and surface chemical surface modification strongly influenced the subsequent behavior of DPSC that adhered and proliferated on pSi substrates. It was previously observed that cells could sense nanoscopic features on pSi substrates down to just a few nanometers (≈ 5 nm) and reacted differently to distinctive nanotopographic cues (Gentile *et al.*, 2012) (Buxboim *et al.*, 2010) (Khung *et al.*, 2003).

Considering topographical influence, our results showed a higher adhesion and higher proliferation rate for DPSC on pSi substrates with typical pore sizes around 36 nm, as compared to the other pore sizes, at all the considered time points. In term of morphology and spreading, DPSC seemed to react in a similar way on pSi 10 nm and pSi 36 nm as on other substrates such as glass coverslips, and flat Si wafers, with a wider surface area on pSi 36 nm indicating an enhanced cell spreading. On pSi 1 µm, DPSC were not able to proliferate after adhesion and to cover the surface. Even if flat surfaces (glass and flat Si), used as controls in this work, allowed a better cell adhesion compared to porous surfaces, the same proliferation profile was obtained for simple oxidized pSi surface as for the flat surfaces, with the advantage for the porous surfaces to be bioresorbable (Figure 3.2 and 3.4). Recently, it has been demonstrated, for four distinct cell types (endothelial cells, mouse fibroblasts, mouse neuroblastoma cells, and human cortical neurons), a higher adhesion on pSi substrates with pore size of 10 nm, as compared to flat silicon or pSi with pore size of 20 nm (Gentile *et al.*, 2012). Our results clearly portrayed a different behavior for human mesenchymal stem cells and confirmed the fact that each cell line had different adhesion characteristics on various pSi surfaces at different time points (Low *et al.*, 2006). As mesenchymal cells, DPSC are involved in structural and fibrous tissues, and their preferential adhesion and proliferation on 36 nm pores could be related to the formation of focal adhesion complex: it has been shown that focal adhesions exhibited a complex multiscale architecture where nanoscopic, doughnut-shaped complexes (≈25 nm in diameter and spaced at ≈45 nm intervals) were distributed within the adhesion area (Patla *et al.*, 2010). More recently, it has been reported that a 34 nm lateral spacing of adhesion peptides increased the formation of mature focal adhesions point (Frith *et al.*, 2012). Thus, we hypothesize that DPSC, as other hMSC, have the ability to form mature focal adhesion on pSi with pores around 36 nm, explaining the differences observed in their attachment onto pSi 36 nm, pSi 10 nm and pSi 1 µm.

After investigating the pore size influence, pSi with 36 nm pores were used to investigate the influence of various surface chemical treatments, including silanization (after thermal oxidation) and hydrosilylation. Hydrosilylation with undecenoic acid offered a limited adhesion and proliferation rate. As already reported in previous works, with other cell types (Low *et al.*, 2006) (Alvarez *et al.*, 2010), we showed that silanization with APTES encouraged cell attachment, spreading and proliferation, with a significant number of DPSC attached to the pSi surface and a proliferation rate higher than on glass coverslip or flat Si. We also demonstrated here, for the first time, the efficiency of semicarbazide grafted by hydrosilylation for DPSC adhesion and early proliferation. Indeed, semicarbazide-treated pSi permitted cell adhesion, spreading and proliferation similar to those found on APTES-treated pSi, with an even higher rate of mitotically active cells after 24 h. These results are in accordance with studies showing that amine-capped surfaces promoted cell attachment (Faucheux *et al.*, 2004). However, after 48 h, semicarbazide-treated pSi degraded and only few cells remained attached on the surface. In contrast, thermal oxidation, by creating Si-OH bonds at the pSi surface, significantly stabilized pSi in aqueous solution and functionalization with APTES further reduced the rate of hydrolytic dissolution. Thus, the semicarbazide grafting approach on pSi appears not to be used for long-term cell culture in vitro, but offers promising perspectives for cell attraction and immediate transplantation *in vivo*, as stem cell therapy often requires a scaffold to carry stem cells to the injured site in the body.

We have investigated three different pore sizes and three different chemical treatments to evaluate the use of pSi scaffolds for the adhesion and proliferation of primary culture of human mesenchymal stem cells from the dental pulp. We have identified, for the first time, two efficient amino-grafted pSi scaffolds for human mesenchymal stem cells adhesion and growth, with optimized pore diameter, for *in vitro* proliferation (and further differentiation), with an interesting potential for *in vivo* transplantation.

DPSC on pSi 36 nm were observed to have a better adhesion and a faster growth compared to pSi with smaller (10 nm) or larger (1 µm) pore size, in particular after silanization with APTES. Hydrosilylation with semicarbazide led to a new chemical modification favoring cell adhesion and proliferation, especially mitosis after cell adhesion. As this modified pSi surface was stable for only 24 to 48 h, it appeared to be potentially usable for stem cells adhesion and immediate *in vivo* transplantation, while APTES-treated pSi was more suitable for long term *in vitr*o culture, for stem cells proliferation and differentiation.

More studies are on course to investigate: (1) the ability of APTES-treated pSi as scaffold for stem cells differentiation in different lineage, as pore size might also influence cell differentiation, (2) the optimization of surface stabilization with the semicarbazide treatment, (3) the efficiency of semicarbazide-treated pSi as an immediate cell carrier for *in vivo* transplantation. Further studies will also elucidate the role played by the porosity on focal adhesion formation, as well as the implication on the cytoskeleton organization.

Chapter 4 Osteodifferentiation and Mineralization process on pSi Scaffolds

4.1 Introduction

4.1.1 Scaffold-based bone tissue engineering

Synthetic biomaterials designed for bone repair are no longer considered effective if they are inert; they are now also expected to elicit a response from the body in order to favor their integration within the host bone (Campion *et al.*, 2013). Scaffold-based bone tissue engineering aims to regenerate bone defects, using osteogenic/progenitor cells and a bioresorbable scaffold to create a scaffold-cell hybrid. The combination of living cells, biologically active molecules and a structural scaffold to form a tissue-engineered construct to promote the regeneration of tissues is the most common concept underlying tissue engineering. The scaffold component is expected to support cell colonization, migration, growth and differentiation, so that it guides the development of the required tissue. In parallel with tissue formation, the scaffold may undergo degradation through the release of products that are either biocompatible or that can be excreted or subjected to metabolism (Hutmacher *et al.*, 2007). Porous silicon shows great promise as a biointerface material due to the ability to precisely adjust its textural features, and due to its ability to degrade into non-toxic silicic acid in aqueous solution. In this chapter, we present the growth of primary cultures of DPSC, plated at confluence, for up to 21 days in culture with or without osteogenic induction. Our aim was to culture DPSC onto pSi in order to generate a mineralized matrix, mimicking bone formation. We followed induced or spontaneous osteodifferentiation onto porous silicon scaffolds and assessed the influence of silicic acid release and porosity.

4.1.2 Calcium-Phosphate formation onto pSi

In vivo grafting of a biomaterial initiates various inflammatory reactions. Bio-inert materials are characterized by minimal corrosion and fibrous encapsulation in the surrounding tissues. On the contrary, pSi is considered to be bioactive as this biomaterial elicits physiological responses when implanted in living tissues (Canham *et al.*, 1997) (Low *et al.*, 2009) (Park *et al.*, 2009). For bone tissue engineering, the ability of pSi to form direct bond with bone and soft tissues could reduce the inflammation due to implant micro-movements and promote integration within the body (Canham *et al.*, 1997). An essential requirement for such tissue-bonding ability is that pSi could induce precipitation of calcium phosphate (CaP) on its surface. Hydroxyapatite growth is a function of both composition and textural properties such as surface area, pore dimensions, density and porosity (Campion *et al.*, 2013). Canham and co-workers demonstrated that it was possible to grow hydroxyapatite on pSi surfaces *in vitro* over periods of days to weeks. Without defining an optimum porous silicon structure, they showed that low porosity films could promote hydroxyapatite nucleation, whereas bulk silicon and macroporous silicon didn't grow any apatite nucleation (Canham *et al.*, 1995). Calcium-Phosphate deposits on pSi are shown in Figure 4.1. It was also reported that high porosity pSi structures (>70%) were rapidly corroded, thus preventing CaP nucleation, while low porosity films (<50%) were sufficiently stable to promote nucleation. Thus, both surface morphology and resorbability appeared to be two important factors to take in account for mineral Ca/P growth and further integration in the body.

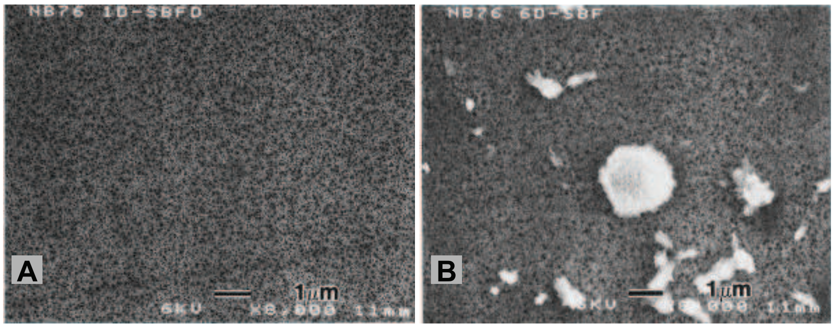

Figure 4.1: SEM images of porous silicon surfaces: (A) after 1 day in simulated body fluid (SBF) and (B) after 6 days in SBF. From Canham *et al.* (1997).

4.1.3 Mineralization process

Mineralization for bone and dentin takes place within an organized matrix of type I collagen fibers, and the crystalline phase consists of aggregates of individual nanocrystals of hydroxyapatite, oriented and located specifically by the collagen fibril structure (Veis *et al.*, 2003). More generally, simple biominerals are composed of complex structures, which often have precise architectural order over several length scales. This architecture contributes to their superior strength and toughness. These biominerals rely heavily on their biological constituents, such as biomacromolecules, for regulation of mineralization (Cölfen *et al.*, 2010). Even in the case of bone and teeth, the details of biomineralization remain unclear. Recent works demonstrated that calcium-phosphate biominerals were formed via stable pre-nucleation clusters, with aggregation into an amorphous precursor phase and, subsequently, transformation of this phase into a crystal (Cuisinier *et al.*, 1995) (Houllé *et al.*, 1997) (Dey *et al.*, 2010). These pre-nucleation clusters could be stabilized then turned into apatite with an active role of collagen, in the case of bone and tooth formation. These structures are mobile and negatively charged, while collagen fibrils exhibiting positively charged regions. The nanosized, positively charged regions can be used for mineral infiltration, leading to the deposition of a dense network of pre-nucleation clusters and their subsequent transformation into amorphous calcium phosphate and, finally, oriented crystalline hydroxyapatite inside the fibrils (Nudelman *et al.*, 2010). Thus, a disordered amorphous calcium phosphate phase (ACP) is the major mineral phase in the newly formed mineralized tissues, and this disordered amorphous phase is a precursor of mature crystalline hydroxyapatite (Cuisinier *et al.*, 1993) (Houllé *et al.*, 1998) (Mahamid *et al.*, 2008). Amorphous calcium phosphates (ACP) represent a unique class of calcium orthophosphate salts, in which there is no orientational ordering of the atomic positions. They are described as the first solid phases precipitated in aqueous solutions containing Ca^{2+} and PO_4^{3-} (Dorozhkin, 2010).

4.1.4 Silicon effect on osteodifferentiation

The dissolution behavior of implantable scaffolds in physiological solutions is of biological and clinical importance as biomaterials dissolution leads to graft resorption. This dissolution is responsible of the material bioactivity, and depends on the physicochemical properties, porosity, and matrix ultra structure. Biomaterials resorption *in vivo* and *in vitro* is mediated by both a cell and solution phenomenon. Cellular activity affects the dissolution reactions and the material degradation can, in turn, affect the cell function (Gupta *et al.*, 2010). Porous silicon, as a resorbable material, degrades in physiological solutions into silicic acid, the soluble form of silicon (Si). It was shown that silicon deficiency in animal led to abnormally shaped bones and defective cartilaginous tissue, with reversible effects when soluble Si was restored to the diet. This knowledge led to the suggestion that Si may play an important role in connective tissue metabolism (Carlisle *et al.*, 1972) (Schwarz *et al.*, 1972). Its main effect in bone and cartilage was thought to be on matrix synthesis rather than on mineralization, although its influence on calcification might be an indirect phenomenon through its effects on matrix components (Seaborn *et al.*, 1994). More recently, it was observed that human osteoblasts cultured in media treated with ionic dissolution products from bioactive glass exhibited significantly upregulated IGF-II gene expression and protein synthesis and dissolved Si (silicic acid, in physiological concentrations) was shown to increase type 1 collagen synthesis and enhance osteoblast differentiation (Reffitt *et al.*, 2003). However, the precise cellular mechanism by which silicon affected type 1 collagen synthesis was not elucidated. It was then shown that silicon-rich phases could provide a guided cell adhesion and tissue growth *in vitro*, and bone-cells attached to silicon-rich materials could absorb higher concentrations of calcium (El-Ghannam *et al.*, 2006). Another recent study investigated the effects of dissolved silicon on osteoblast differentiation *in vitro*. Through the investigation of osteocalcin and osteopontin expression, it was demonstrated that Si played an important role in enhancing bone-cell differentiation *in vitro* (Gupta *et al.*, 2010). This was confirmed by the significant role in the kinetics of mineralization and stromal cells differentiation played by resorbable porous silicon particles embedded in electrospun polycaprolactone. The presence of the pSi structures in such polycaprolactone composites could accelerate mesenchymal stem cell differentiation and the corresponding calcification process (Fan *et al.*, 2010).

4.1.5 Aims of the study

Taking in account that silicic acid could enhance osteoblastic differentiation and that Ca/P formation was influenced by surface chemical composition and morphology, we investigated the osteodifferentiation of DPSC onto pSi surface. We aimed to elucidate whether DPSC could attach, proliferate and differentiate on pSi scaffolds for up to 3 weeks, until producing a mineralized extra cellular matrix. We wanted to evaluate the impact of Si release on osteogenic differentiation and on mineralization. Finally, we focused on porous surface influence on Ca/P formation.

4.2 Materials

4.2.1 Human dental pulp stem cells

Human impacted third molar extracted for orthodontic reasons were recovered from healthy patients (15-30 years of age). Written informed consent was obtained from the patients or their parents. This protocol was approved by the local ethical committee (Comité de Protection des Personnes, Montpellier hospital). Tooth surfaces were cleaned using 0.12% chlorhexidine and cut around the cementum-enamel junction by using sterilized disc. The teeth were then broken into 2 pieces to reveal the pulp chamber. The pulp tissue was gently separated from the crown and root and then digested in a solution of 3 mg/ml type I collagenase and 4 mg/ml dispase for 1 hour at 37°C. The solution was then filtered through 70 μm Falcon strainers and immersed in αMEM supplemented with 10% fetal bovine serum (FBS), 100 U/ml penicillin, 100 μg/ml streptomycin and placed in 75 ml flasks. Cells were incubated for 1 week at 37°C with 5% CO_2. Non-adherent cells were removed by a change of medium 24 h after cell seeding. After 1 week, sub-confluent cells were collected and analyzed for minimal criteria to define human mesenchymal stem cells.

4.2.2 Flow cytometry assays

The antigen profiles of cultured DPSC were analyzed by detecting the expression of the cell surface markers CD90, CD146, CD117 and CD45 using flow cytometry. CD90 is a widely accepted marker for mesenchymal stem cells, CD146 is a marker expressed in perivascular mesenchymal stem cells, CD117 is the receptor of stem cell factor, and CD45 is a marker of hematopoietic cells, mainly myeloid progenitors. The latter has been used to demonstrate the absence of contamination by CD45+ hematopoietic progenitors. For cell surface antigen detection, DPSC were detached with accutase, then incubated with fluorescence-conjugated antibody or the isotype control IgG for 1 h at 4°C in PBS containing 1% BSA. Antibodies used were the following mouse anti-human antibodies: CD90-APC conjugated, CD45-PerCP conjugated, CD117-APC conjugated and CD146-FITC conjugated. Analysis of 15,000 events was performed in an Epics XL4C (Beckman-Coulter). Data were analyzed with the FCS Express software.

4.2.3 Cell differentiation assays

Cells were controlled for multipotency with *in vitro* osteogenic, adipogenic and chondrogenic differentiation assays, following protocols described in chapter 2. Briefly, for osteogenic and adipogenic differentiation, dental pulp cells were seeded at a density of 10^5 cells/cm^2 and maintained in αMEM supplemented with 10% FBS until confluence. Cells were then cultured in osteogenic medium (αMEM supplemented with 15% FBS, dexamethasone, L-ascorbate phosphate, and β-glycerophosphate) or in adipogenic medium (αMEM supplemented with 10% FBS, dexamethasone, insulin, and isobutylmethylxanthine) for 21 days. Control cultures were maintained without osteogenic or adipogenic supplements. To induce chondrogenic differentiation, cells were cultured for 21 days as pellets in a serum-free expansion medium containing dexamethasone, L-ascorbate phosphate, L-proline, sodium pyruvate, ITS-Premix, and TGF-β3. Control pellet cultures were maintained without the addition of TGF-β3.

4.2.4 Porous silicon scaffolds preparation

P++ type boron-doped crystalline silicon wafers with 0.0008 - 0.0012 Ωcm resistivity were obtained from Siltronix®. Wafers were etched in a custom-made Teflon cell at a constant current density of 300 mA/cm^2 for 2 min 15 s, in a hydrofluoric acid (HF) solution in ethanol (3:1 HF:ethanol solution, volume ratio). Etched wafers were oxidized at 800°C for 1 hour. The wafers were cut into 0.5 cm^2 pieces. We also worked with pSi presenting a gradient of porosity: these pSi gradients were prepared by anodization of highly doped p^{++} type silicon wafers (0.0005-0.001 Ω cm, <100>, boron doped, obtained from Siltronix®) using a 1:1 HF:ethanol solution in a custom-built Teflon etching cell. A current density of 115 mA/cm^2 was applied for 60 s using a. For surface gradient preparation, the platinum electrode was placed perpendicular to the substrate and at one end of the etching cell (Clements *et al.*, 2012) (Collins *et al.*, 2002). For a more precise description of the set-up, see chapter 5 (*Figure 5.1*). PSi gradients were thermally oxidized for 1 h at 800 °C, and silanized with aminopropyltriethoxysilane (APTES) 4 % in dry toluene at room for 1 h with gentle shaking. For use in cell culture, all the wafers were sterilized with 70% (vol/vol) ethanol for 10 min before drying under sterile air flow.

4.2.5 Surface characterization

The topography of surface modified pSi samples was analyzed by scanning electron microscopy (Analytic FEI Quanta FEG 200) to determine pore size, with an acceleration voltage of 20 kV, in a pressure of 0.5 Torr.

To determine surface tension, sessile drop contact angle measurements were conducted in a custom-made set-up consisting of a syringe dispenser, a sample stage, a macro lens and a CCD camera connected to a video-acquisition card. At room temperature, 3µl of MilliQ water was spotted onto the surface. Images of the drop profiles were captured and ImageJ® software was used to measure contact angles on both sides of the droplet.

4.2.6 Cell adhesion and viability

DPSC attachment and viability were monitored by fluorescence microscopy. DPSC were seeded onto pSi at a cell density of $5x10^4$ cell/ml. Cell culture plates and flat unetched silicon wafers were used as controls. Cultures were incubated for 4 h, 24 h and 48 h at 37°C with 5% CO_2, in a humidified incubator. To determine cellular morphology and viability on the surfaces, cells were stained with 25 µg/ml of fluorescein diacetate (FDA) and 50 µg/ml of propidium iodide (PI) for 3 min at 37°C. Samples were subsequently washed with PBS to remove non-adherent cells and unbounded dye, before being observed under fluorescence microscopy at excitation wavelengths of 480 nm for FDA and 630 nm for PI. Images were captured on a Nikon TE2000-E microscope equipped with a Nikon digital camera. For cell counts, samples were fixed with 2.5% glutaraldehyde for 1 hour, and stained with 100 ng/ml 4,6-diamidino-2-phenylindole (DAPI) for 30 min to stain nuclei. Samples were then washed with PBS to remove any non-adherent cells and unbounded dye, and observed under fluorescence microscopy at an excitation wavelength of 360 nm. Cell counts were conducted at five different locations on the surface of each sample (four peripheral and one central) in areas measuring 1200x780 µm. All experiments were made in triplicate and statistical differences along the gradients were determined using the Student's t-test with $p < 0.05$ deemed as statistically significant.

4.2.7 Quantification of Silicic acid release: ICP-MS analysis

DPSC were cultured on pSi or flat Si, in osteogenic medium (OM) or in basal medium (MEM). The culture media were changed twice a week. The Si content in all the culture media after cell incubation was measured by means of inductively coupled plasma mass spectrometry (ICP-MS). ICP-MS analysis was performed by introducing extract aliquots into a mass spectrometer (Element XR ICP-MS, Thermo Scientific™). Solutions were sprayed through a high solid type nebulizer as plasma into a thermoelectrically controlled spray chamber. The results of the analysis were then compared with a standard for identification and quantification of Si concentration. The average and standard deviation of the Si concentrations per set of samples were reported as absolute concentrations, expressed in ppm. The Si concentrations were then calculated as mg/ml.

4.2.8 Osteodifferentiation onto pSi

DPSC were seeded at a density of 10^5 cells/cm_2 on porous silicon scaffolds and on oxidized unetched flat silicon wafers, and maintained in αMEM supplemented with 10% FBS for 5 days. Osteogenic induction was done as described in chapter 2, for 21 days. Flat silicon and culture plates were used as control. All experiments were conducted either in osteogenic medium (OM) or in basal medium (MEM). The osteogenic differentiation of DPSC was followed by the quantification of alkaline phosphatase (ALP) after 3 days, 7 days, 10 days and 14 days. Mineralization was assessed by the quantification of calcium deposits with Alizarin Red staining and by energy dispersive X-ray spectroscopy (EDX) after 21 days. The same experiments were conducted with bare pSi scaffolds, incubated without cells in culture medium (osteogenic medium or basal medium) at 37°C to reflect surface chemical reactions that occur *in vivo*.

4.2.9 Quantification of alkaline phosphatase (ALP) activity

ALP is a widely used marker, mainly expressed in differentiated cells producing mineralized matrix. After 3, 7, 10 and 14 days in differentiation medium, DPSC layers were rinsed with PBS, and scraped off into a 0.1% Triton X-100 solution. ALP activity was determined by the hydrolysis of p-nitrophenyl phosphate in 2-amino-2-methyl-1-propanolbuffer, pH 10.4, at 37°C for 30 min. Absorbance was measured at 504 nm with a microplate reader. Total protein was quantified with the Bio-Rad protein assay kit. ALP activity was expressed as nanomole of paranitrophenol per microgram of protein. The experiments were performed in triplicate. The results were normalized according to the total protein contents. Statistical analyses were performed using a parametric Student t-test, and a p-value of <0.05 was considered to be significant.

4.2.10 Mineralization assays

After 21 days in differentiation medium, DPSC layers were rinsed with PBS. Calcium deposits were stained with 40 mM pH 4.2 Alizarin red (AR) solution. Cells were rinsed three times with PBS and then fixed in 3.7% formaldehyde for 15 min. Alizarin red was added to the wells for 1 h and rinsed five times to avoid non-specific staining. Cells were treated with 10% (w/v) cetylpyridinium chloride in 10 mM sodium phosphate pH 7.0 for 15 min at room temperature to remove the bound dye. The calcium concentration was determined by absorbance measurements at 562 nm with a spectrophotometer. Values were normalized to the total protein content of DPSC cultured under the same conditions, in a parallel assay. Results were presented as optical densities (OD) per microgram of total cellular proteins. Statistical analyses were performed using a parametric Student t-test, and a p-value of <0.05 was considered to be significant.

Calcium deposits within bone nodule-like colonies were assessed by calcein blue (CB) staining. This experiment was conducted for DPSC incubated on pSi gradients after 3 weeks of incubation in either osteogenic medium (OM) or basal medium (MEM). Samples were stained using a 30 μM calcein blue solution overnight in the dark. After staining, samples were rinsed with PBS, followed by fixation with 3.7% formaldehyde for 15 min. Cells were then counterstained with 50 μg/ml propidium iodide (PI) for 3 min at 37°C. The percentage of CB-positive colony area was defined by the area of CB-positive colony area divided by the total colony area in each image. Images were taken by fluorescence microscopy, with excitation wavelength The colony area and CB-positive colony area were calculated using ImageJ software. Statistical analyses were performed using a parametric Student t-test, and a p-value of <0.05 was considered to be significant.

4.2.11 Scanning electron microscopy and energy dispersive X ray analysis

After 21 days, cells were fixed in 2.5% glutaraldehyde in 0.1 M phosphate buffer, dehydrated with increasing concentration of ethanol bath and post fixed in 0.1% OsO_4 in the same buffered solution. After chemical critical point drying with hexamethyldisilazane (HDMS) and platinum coating, samples were observed under a FEI Quanta 200 FEG scanning electron microscope (ESEM, FEI Company), coupled with an energy dispersive X-ray (EDX) analysis detector. The samples were placed on an adhesive carbon tape, fixed to a copper plate, and observed at an accelerating voltage of 15 kV. EDX microanalysis was employed to detect the presence of calcium and phosphorous on the samples, with EDX spectra collected at 2500x magnification. For EDX analysis, cells were only fixed in 2.5% glutaraldehyde, dehydrated in ethanol and dried with HDMS.

4.3 Results

4.3.1 Dental pulp stem cells characterization

A complete characterization of the recovered dental pulp cells is presented in chapter 2 (section *2.3 Results*). Briefly, the cells that were extracted from human dental pulp matched all the criteria to be defined as mesenchymal stem cells. Thus, we could assume that we conducted our experiments with Dental Pulp Stem Cells (DPSC), as preciously named (Gronthos *et al.*, 2000). Indeed, the recovered DPSC were plastic adherent cells, clonogenic and able to proliferate and differentiate into osteoblast, adipocyte and chondroblast. And they expressed, with various degrees of positivity, the cell surface markers CD90, CD117 and CD90, and they were negative for CD45 antigen (Figure 4.2).

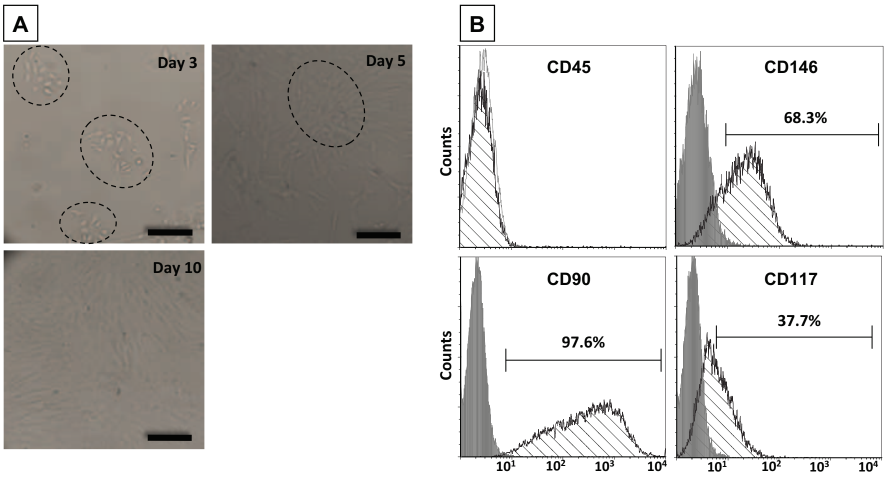

Figure 4.2: Characterization of DPSC. (A) Optical microscopy of adherent dental pulp cells forming colonies at 3 and 6 days, and reaching confluence 10 days after recovery. Scale bar = 100 μm. (B) Flow cytometry analysis of subconfluent dental pulp cells. Single-parameter histograms showing the expression of markers CD 90, CD 146, CD 117 and CD 45.

4.3.2 pSi scaffolds characterization

PSi scaffolds were generated from bulk p-type silicon wafers (resistivity of 0.0008 - 0.0012 Ωcm) by applying a constant current density of 300 mA/cm^2. SEM examination showed that the porous substrates had an average pore diameter of 36 ± 4 nm, and were quite uniformly porosified. The surface porosity (ratio between total area of the pores and the area of the considered region of interest) was 45 ± 6%. SEM images of the pSi surface are shown in Figure 4.3, with top view and cross section.

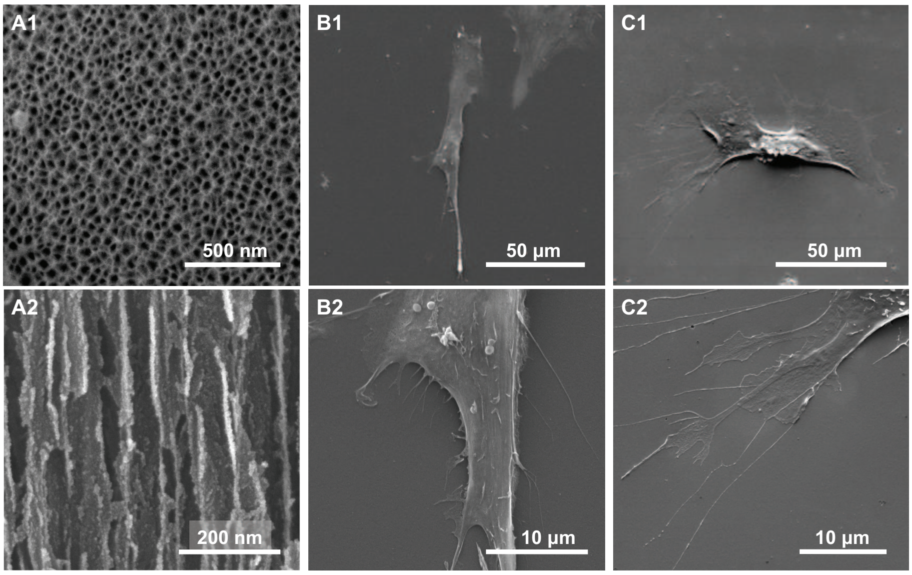

Figure 4.3: Scanning electron microscopy of pSi scaffold and DPSC adhesion after 24 h in culture medium. (A) Top view and cross section of pSi scaffold (A1 and A2, respectively). (B) DPSC on pSi scaffold at magnification x2000 and x10000 (B1 and B2, respectively). (C) DPSC on flat Si at magnification x2000 and x8000 (C1 and C2, respectively).

PSi gradients were prepared from highly boron-doped p^{++} type silicon wafers (resistivity of 0.0005-0.001 Ωcm) by applying a constant current density of 115 mA/cm^2 was applied for 60s in a custom-built Teflon etching cell, with the platinum electrode placed perpendicular to the substrate, at one end of the set-up. SEM evaluation showed that the pore diameters were different along the scaffold, with largest pores under the electrode (electropolished area) and the smallest pores at the other extremity of the scaffold, in continuity with the flat silicon (unetched bulk wafer). The pore diameters were measured along the gradient, every 2 mm, starting from the electropolished area. The pore diameter measurements are presented in Table 4.1.

Distance to Electrode (mm)	18	16	14	12	10	8	6	4	2
Pore Diameter (nm)	**8**	**14**	**18**	**24**	**37**	**70**	**120**	**248**	**500**
Standard Error	*5*	*7*	*8*	*11*	*18*	*28*	*44*	*92*	*209*

Table 4.1: Pore diameters (nm) measured along pSi gradients

4.3.3 DPSC adhesion and viability on pSi

Cells adhesion and viability were assessed using vital FDA/PI staining. FDA enters into viable cells and stains their cytoplasm in bright green. PI interacts with RNA and DNA of dead cells, producing a red color (Cao *et al.*, 2011). Thus we could observe cell adherence, cytoplasmic spreading and vitality. As already developed in chapter 3, we showed that DPSC could adhere and spread on oxidized pSi scaffolds, with initial cell adhesion and growth very similar compared to the controls on flat Si. Morphologies of DPSC on pSi scaffolds are presented in Figure 4.3 (SEM after 24 h of incubation) and in Figure 4.4 (Fluorescence microscopy of stained living cells, after 4 h, 24 h and 48 h of incubation). The absence of red staining (PI) confirmed cell-compatibility of the substrate.

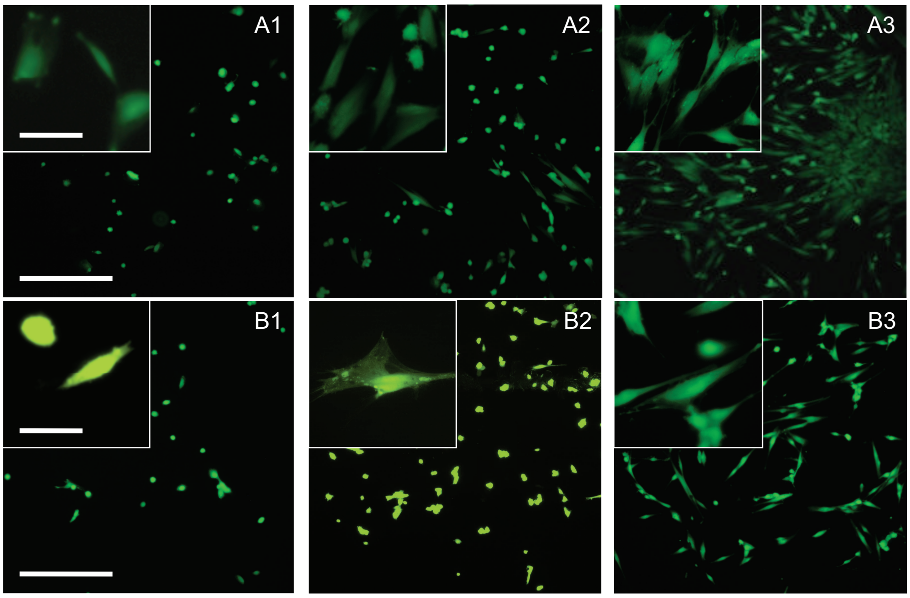

Figure 4.4: Vital fluorescence microscopy of DPSC on pSi and flat Si. (A) DPSC on flat Si after 4 h, 24 h and 48 h of incubation (A1, A2 and A3, respectively). (B) DPSC on pSi after 4 h, 24 h and 48 h of incubation (B1, B2 and B3, respectively). Cells are stained with fluorescein diacetate (vital cells, green staining) and propidium iodide (dead cells, red staining). Scale bar: main image = 200 µm; inset = 30 µm.

The cell counts after 4 h, 24 h and 48 h confirmed that DPSC could attach and grow on oxidized pSi surfaces, as well as on flat Si. Initial cell adhesion on pSi was slightly lower compared to flat Si and the number of DPSC counted on pSi was significantly lower after 24 h and 48 h, compared to flat Si (p=0.025 and p=0.002, respectively). However, DPSC started to proliferate on pSi after 24 h following the same growth pattern as the one observed on flat Si (Figure 4.5). More information and investigations about DPSC adhesion, spreading and proliferation on pSi are presented in chapter 3.

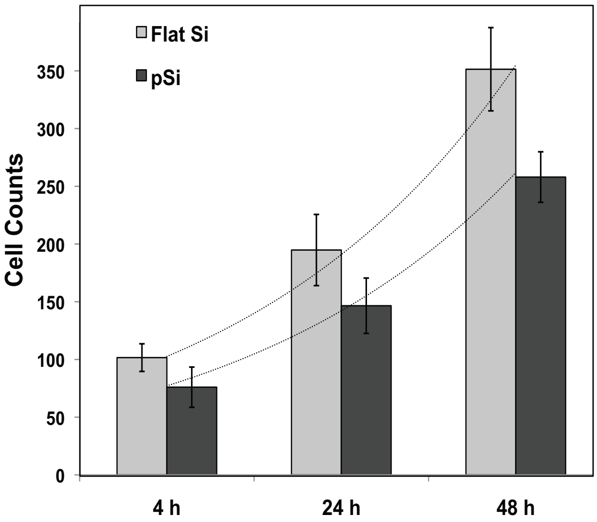

Figure 4.5: Cell counts after 4 h, 24 h and 48 h incubation. DPSC seeded on flat Si and pSi at a density of $5x10^5$ cells/ml. After incubation, cells were fixed with 2.5% glutaraldehyde and stained with DAPI (nuclei blue staining). Cells counted on areas measuring 1200x780 µm. Experiment made in triplicate, with 5 measurements per sample. Results presented as mean ± standard deviation, with error bar representing standard deviation. Dotted line to guide eyes.

4.3.4 Si content of the culture media

Culture media were changed twice a week. The concentration of Si content in each discarded medium was analyzed. Si concentrations in the culture media varied as a result of pSi dissolution *in vitro*. ICP-MS results showed significantly increased concentrations of Si in culture media incubated with pSi scaffolds, compared to culture media incubated with flat Si. We could not determine any significant difference between the media (OM and MEM) incubated with pSi. Overall, the Si concentration slightly decreased during the 3 weeks of experiment, with or without DPSC on the pSi scaffolds. This reflected a slight reduction of pSi dissolution, but could not be attributed to the presence or absence of DPSC on pSi (Figure 4.6).

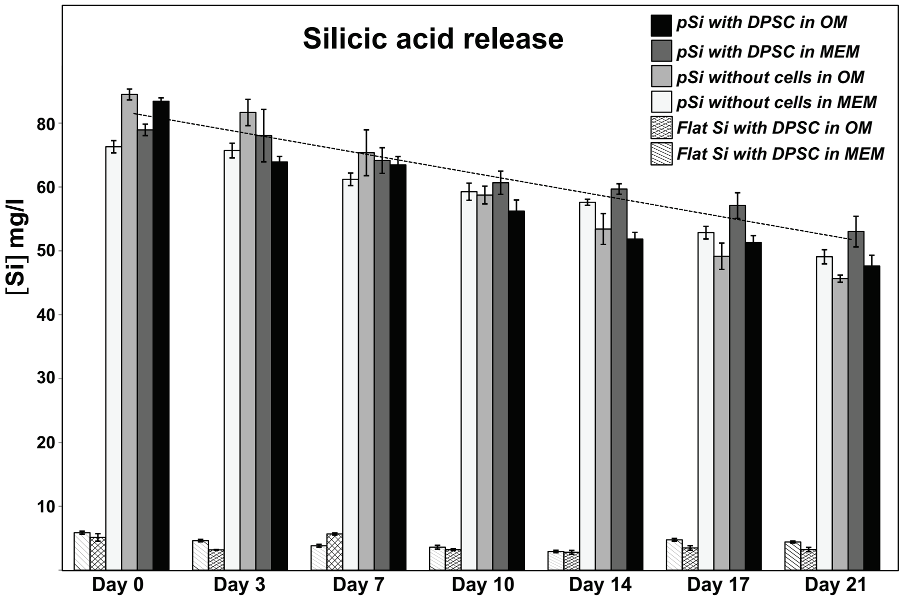

Figure 4.6: Si concentration in culture media (OM or MEM) after incubation with pSi or flat Si during DPSC osteodifferentiation.

4.3.5 DPSC osteodifferentiation on pSi

To investigate the kinetics of DPSC osteoblastic differentiation on pSi scaffolds compared to flat Si, we assessed alkaline phosphatase (ALP) activity during the 2 first weeks of osteogenic induction. After only 3 days in osteogenic medium (OM), ALP activity of DPSC on pSi was slightly increased compared to cultures on flat Si. At day 7, ALP activity was again greater on pSi than values obtained for cells on flat Si. After 10 days, and even more after 14 days, ALP activity was significantly greater on pSi than on flat Si. These data are presented as histograms in Figure 4.7. It is interesting to note that DPSC differentiation was greater on pSi, while their original adhesion and proliferation was delayed compared to flat Si. This experiment was also conducted without osteogenic induction, in basal medium (MEM). A low ALP activity was detectable after 3, 7 and 10 days and ALP activity was slightly greater on pSi than on flat Si. After 14 days, this increased ALP activity of DPSC on pSi (in MEM) was statistically significant (Figure 4.7).

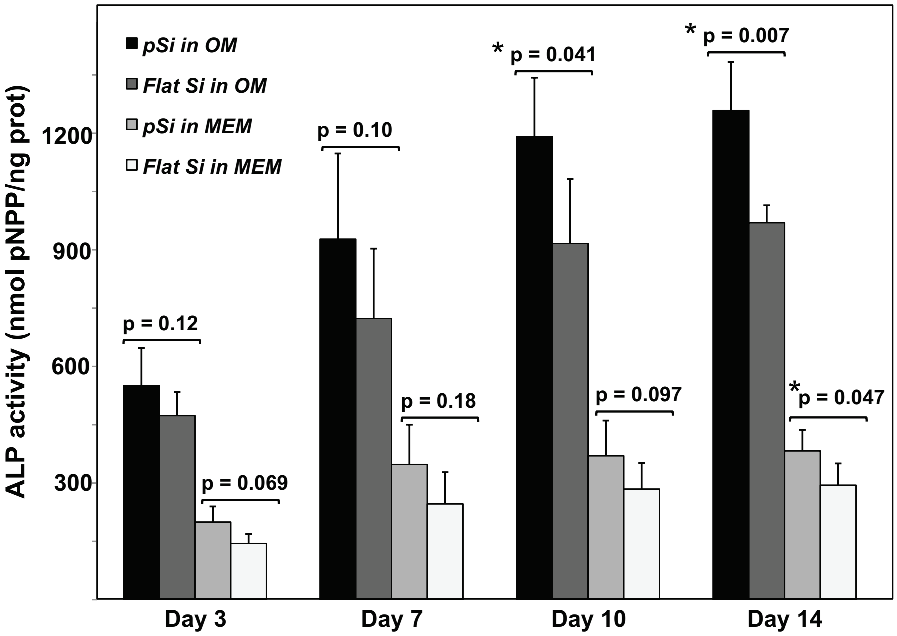

Figure 4.7: DPSC osteodifferentiation during the 2 first weeks of experiment, assessed by alkaline phosphatase (ALP) quantification. Results were normalized to the total quantity of proteins. Experiments were performed in triplicate. (*) indicates a statistical difference between groups, with significance determined by using the Student t test ($p < 0.05$).

4.3.6 Mineralization assays and Ca deposits

4.3.6.1 Alizarin red staining

After 3 weeks of osteogenic induction, DPSC gradually became bone-like cells and formed bone-like nodule colonies. The calcium deposits on pSi scaffolds and flat Si were stained with Alizarin red (AR). The differentiated DPSC produced more Ca deposits on pSi than on flat Si when incubated in OM (p=0.003). The same phenomenon was observed even without osteogenic induction, in basal medium, where the Ca deposits produced by DPSC were more abundant on pSi than on flat Si (p=0.004). These results were consistent with the increased DPSC osteodifferentiation on pSi scaffolds. We also investigated the formation of calcium deposits in the absence of cells, by incubating pSi scaffolds and flat Si without cells in culture medium (OM and MEM) for 3 weeks. We found the presence of a significant amount of Ca deposits on bare pSi when it was incubated in OM, while no Ca deposits was noticeable on bare flat Si in OM. Similarly, Ca deposits were detectable on bare pSi in MEM while no Ca deposits were found on bare flat Si. These data are summarized in Figure 4.8.

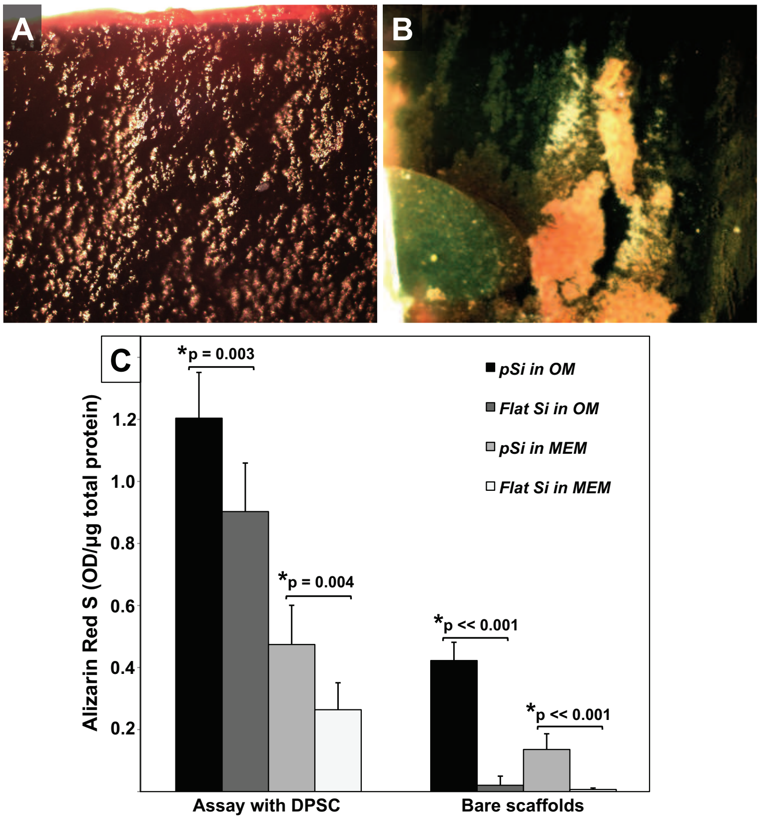

Figure 4.8: Calcium deposits stained with Alizarin red: (A) DPSC on pSi after 3 weeks in OM and (B) DPSC on pSi after 3 weeks in MEM. (C) Quantification of calcium deposits after 21 days of differentiation, assessed by Alizarin red staining. Calcium concentration was determined by absorbance at 562 nm. Optical density (OD) values were normalized to the total protein content of DPSC cultured under the same condition. Experiments were performed in triplicate. (*) indicates a statistical difference between groups, with significance determined by using the Student's t test ($p < 0.05$).

4.3.6.2 Calcein blue staining

In order to evaluate the influence of pore diameter on DPSC differentiation and on Ca deposits, DPSC were incubated on pSi gradients for 3 weeks, in OM. Calcein blue was chosen instead of alizarin red to be able to follow the fluorescence on the Psi gradients. Calcein blue staining indicated the extent of the mineralization at each stage of the gradient. Some CB-positive colonies were found along the whole gradient. However, we demonstrated that there was a gradual increase in frequency and colony size along the gradient as the pore diameters decreased, with an exception on the area of 37 nm pores where CB-positive colonies (46 %) were more abundant than on areas of 24 nm (36 %) and 18 nm pores (44 %). The fraction of CB-stained cells was 40.3 ± 8.7 % on the flat Si, which value was comparable with that on the areas with 24 nm pore diameter and 70 nm pore diameter. The percentage of CB-positive colonies is presented in Table 4.2, and a summary of these results is shown in Figure 4.9.

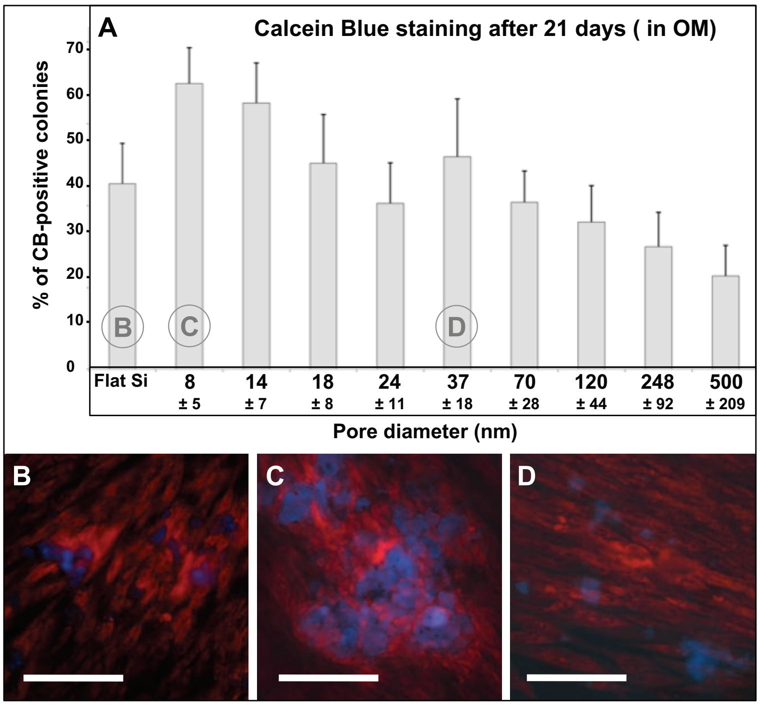

Figure 4.9: (A) Representative histograms of the percentage of CB-positive colonies along the pSi gradient. Abscissa indicates the corresponding pore diameters. (B)-(D) Representative fluorescence microscopy images of DPSC after 3 weeks in OM (red fluorescence) and Ca deposits stained by Calcein Blue (blue fluorescence), on flat Si, 8 nm pores and 37 nm pores (B, C and D, respectively). Scale bar = 100 µm.

Pore Diameter (nm)	Flat Si	8	14	18	24	37	70	120	248	500
% of CB-positive colonies	**40.3**	**62.1**	**57.8**	**44.8**	**36.1**	**46.2**	**36.3**	**32.0**	**26.6**	**20.3**
Standard Error	*8.7*	*7.7*	*8.7*	*10.5*	*8.7*	*12.5*	*6.7*	*7.8*	*7.4*	*6.6*

Table 4.2: Percentage of CB-positive colonies along the pSi gradient, with the corresponding pore diameters.

4.3.6.3 SEM images and EDX spectroscopy

DPSC were incubated for 3 weeks on pSi or flat Si, in either osteogenic medium (OM) or basal medium (MEM). After the 3 weeks, samples were fixed and dehydrated, then observed under SEM and analyzed with EDX spectroscopy. EDX analyses were realized on the whole corresponding SEM images (Figure 4.10). We demonstrated that there were significantly more Ca and P on pSi, compared to flat Si, with DPSC cultured in OM. The same tendency was observed with DPSC cultured in MEM, where some Ca and P were found on pSi and not on flat Si. To get some information about the CaP structure, we consider the ratio Ca/P: the values are presented in Table 4.3 (next page).

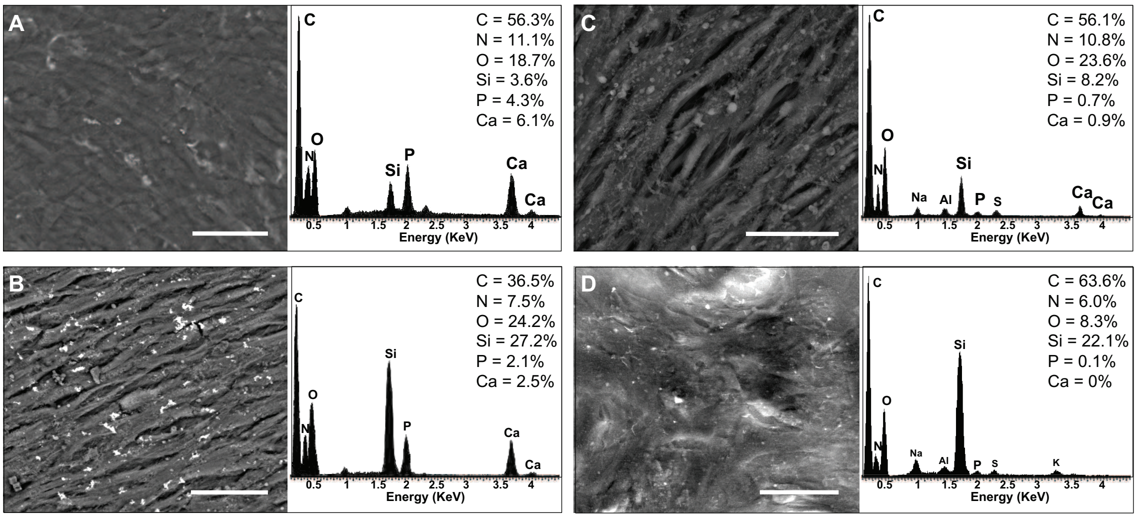

Figure 4.10: SEM images of DPSC after 3 weeks of *in vitro* growth and differentiation, and corresponding EDX spectra. (A) DPSC cultured on pSi, in OM. (B) DPSC cultured on flat Si, in OM. (C) DPSC cultured on pSi, in MEM. (D) DPSC cultured on flat Si, in MEM. Scale bar = 50 µm. EDX analysis results are in atomic %.

	P	*Ca*	*Ratio Ca/P*
pSi: DPSC in OM+	4.295	6.09	1.418
Flat Si: DPSC in OM+	2.11	2.48	1.175
pSi: DPSC in MEM	0.71	0.91	1.281
Flat Si: DPSC in MEM	0.06	0	N/A
Bare pSi in OM+	4.14	5.55	1.341
Bare Flat Si in OM+	0.06	0.09	N/A
Bare pSi in MEM	0.01	0.01	N/A
Bare Flat Si in MEM	0.04	0.04	N/A

Table 4.3: Ca/P ratio of the mineralized structures recovered on pSi and flat Si after 3 weeks of incubation with or without cells, in OM or MEM.

The same experiments were conducted without cells, on bare scaffolds incubated in either OM or MEM. Some mineralized structures were clearly observable, but only on pSi incubated in OM. EDX spectroscopy confirmed the Ca-P composition of these structures (Figure 4.11).

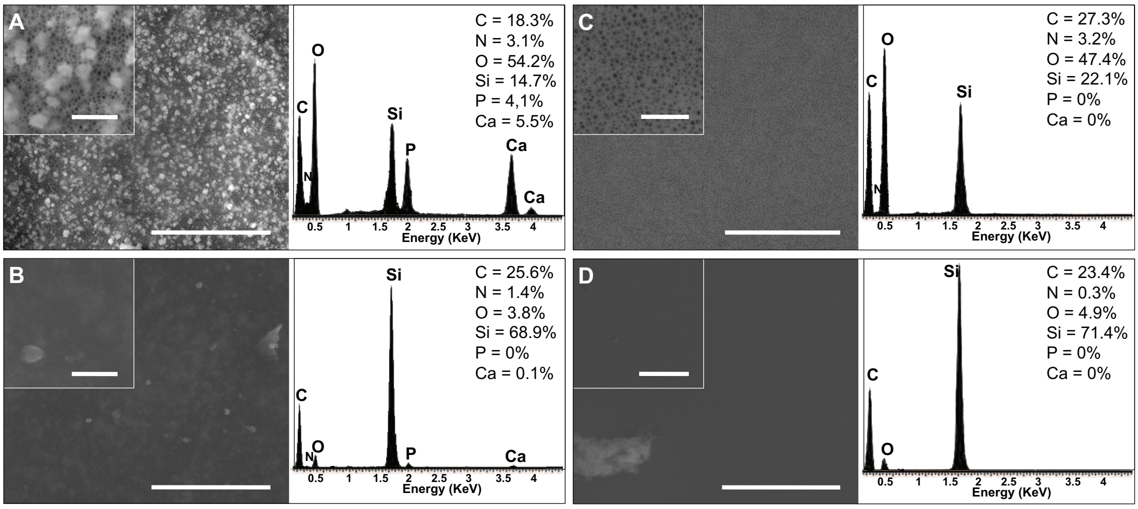

Figure 4.11: SEM images of bare scaffolds after 3 weeks of *in vitro* incubation, and corresponding EDX spectra. (A) pSi in OM. (B) flat Si in OM. (C) pSi in MEM. (D) flat Si in MEM. Main image scale bar = 5 µm. Inset image scale bar = 1 µm. EDX analysis results are in atomic %.

To investigate the influence of pore diameter on DPSC differentiation and mineralization process, we used pSi gradients as scaffolds for DPSC growth and further osteodifferentiation. As described above, DPSC were incubated for 3 weeks on pSi gradients, in either osteogenic medium (OM) or basal medium (MEM). After the 3 weeks, samples were fixed and dehydrated, then observed under SEM and analyzed with EDX spectroscopy. EDX analyses were realized on the whole corresponding SEM images (Figure 4.12). We discovered that Ca and P distribution were not homogeneous along the gradient: there was a gradual increase in amount of Ca and P (in atomic %) along the gradient as the pore diameters decreased, except on 37 nm pores where Ca and P deposits were more abundant than on 24 nm and 18 nm pores. The lowest deposits were found on flat Si. The results were normalized according to the quantity of cells at each stage of the gradient, represented by the amount of nitrogen (N from the proteins, in atomic %). Figure 4.11 presents a summary of these data, with representative SEM images at different stage of the gradient.

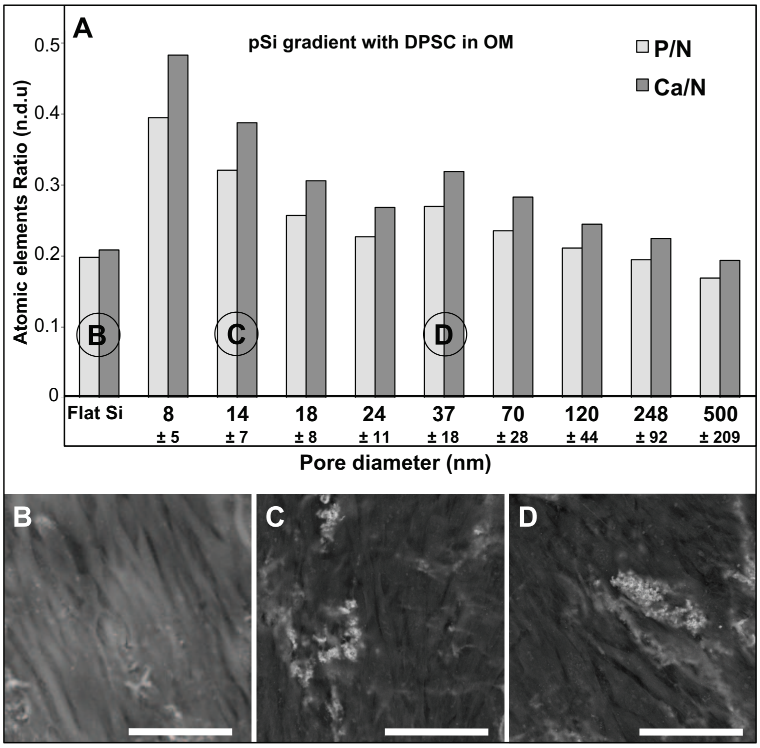

Figure 4.12: (A) Representative histograms of the EDX analysis along the pSi gradient, with results expressed in Atomic %. Abscissa indicates the corresponding pore diameters. (B)-(D) Representative SEM images of DPSC after 3 weeks in OM. Brighter spots correspond to Ca deposits. (B) flat Si. (C) 14 nm pores. (D) 37 nm pores. Scale bar = 50 µm.

The same experiments were reproduced without cells, on bare pSi gradients incubated in OM, in order to investigate the influence of pore size on Ca-P deposits. As observed on bare pSi scaffolds (with 36 nm pore diameter), some mineralized structures were observable on pSi gradients. EDX spectroscopy confirmed the Ca-P composition of these structures. Ca and P distributions were not homogeneous along the gradient: as observed with DPSC on pSi gradient, there was a gradual increase in amount of Ca and P (in atomic %) along the gradient, as the pore diameters decreased (Figure 4.13). But unlike the previous experiment with DPSC on pSi gradients, CaP deposits were not more abundant on 37 nm pores than on 24 nm and 18 nm pores.

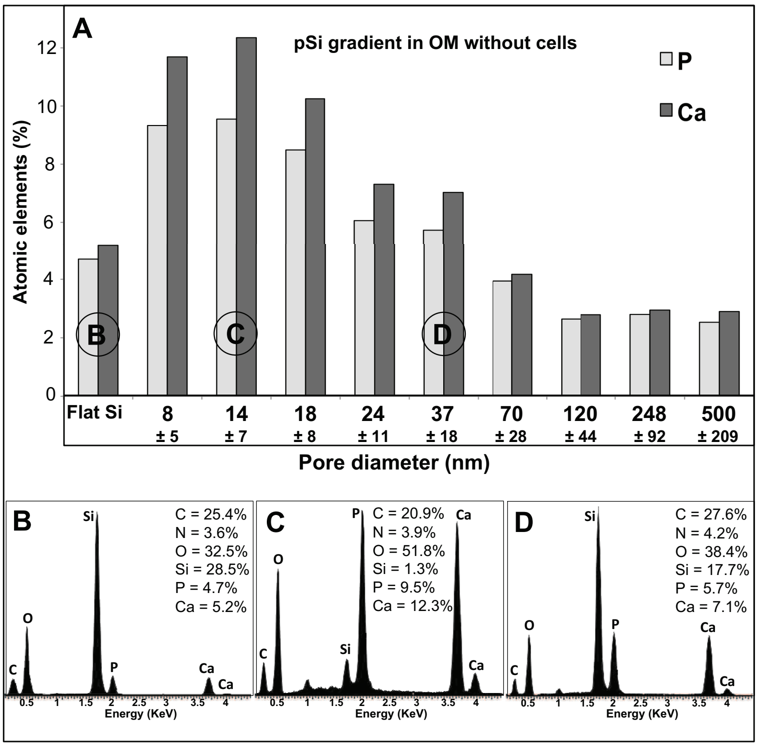

Figure 4.13: (A) Representative histograms of the EDX analysis along the bare pSi gradient incubated in OM for 3 weeks, with results expressed in Atomic %. Abscissa indicates the corresponding pore diameters. (B)-(D) Representative EDX spectra at different stage of the pSi gradient surface, after 3 weeks in OM. (B) flat Si. (C) 14 nm pores. (D) 37 nm pores.

4.4 Discussion

4.4.1 Porous silicon stability and DPSC growth

In this work, we managed to grow DPSC for up to 3 weeks showing that oxidized pSi, without additional functionalization, was sufficiently stable for long-term cell growth, and could promote CaP precipitation. DPSC could attach and grow on oxidized pSi surfaces, as well as on flat Si, except that cell adhesion on pSi was lower compared to flat Si. However, DPSC started to proliferate on pSi after 24 h as they did on flat Si, with just a delayed growth (Figure 4.3 and Figure 4.4). As we wanted to explore pores influence on cell differentiation and mineralization, we didn't functionalize the pSi surface, except with thermal oxidation to stabilize the surface. Chemical functionalization could enhance cell adhesion and proliferation (Low *et al.*, 2006) (Alvarez *et al.*, 2009), and such functionalization strategies are presented in chapter 3. On pSi gradients, we silanized the surface with APTES because the scaffold was not stable enough to support cell growth for 3 weeks. After APTES treatment, pSi gradients were able to support cell adhesion and differentiation.

4.4.2 Si effects on DPSC osteodifferentiation

Cell differentiation was assessed in terms of ALP activity of DPSC cultured on pSi scaffolds at 3, 7, 10 and 14 days. ALP activity increased from day 3 to day 14 on pSi and flat Si in OM and after 10 days the ALP activity was significantly higher on pSi. At 10 and 14 days after induction, pSi scaffolds had significantly higher ALP activity compared to flat Si ($p < 0.05$). Even in MEM, we found a limited ALP activity for DPSC, with a significantly higher ALP activity on pSi after 14 days. PSi dissolution induced the presence of silicic acid (the soluble form of Si) in culture medium, while Si was hardly detectable when flat Si was incubated in culture medium. This is confirmed by the fact that ALP activity for flat silicon is of the same order than on plastic (data not shown). Previous studies have already shown that silicon-rich phase could provide guided cell adhesion and tissue growth (El-Ghannam *et al.*, 2006) and it was suggested that Si could enhance bone-cell differentiation (Gupta *et al.*, 2010). As alkaline phosphatase is a specific biomarker for mesenchymal stem cell differentiation, the levels of ALP expression and the correlated Si content recorded in our study demonstrate that pSi have the ability to enhance osteodifferentiation. The enhanced expression of ALP on pSi, even without osteogenic supplement (DPSC in MEM), confirmed that pSi dissolution was sufficient to stimulate osteodifferentiation in the absence of exogenous supplements. This finding is in accordance with a recent study that investigated and confirmed the ability of silicic acid to accelerate the differentiation of mouse stromal cells (Fan *et al.*, 2011).

Concerning the resorption rate of pSi, we didn't find any evidence that cells interfered with pSi dissolution. Indeed, there was no difference between bare pSi and psi incubated with DPSC when measuring the Si content of culture media after incubation. This finding confirm a previous observation where bone marrow cells did not significantly affected the dissolution behavior of silica-calcium phosphate composite *in vitro* (El-Ghannam *et al.*, 2006).

4.4.3 Mineralization and CaP structure

We postulate that high ALP activity related to DPSC osteodifferentiation could lead to early calcium incorporation. Indeed, it had been already reported that increased expression of ALP and osteocalcin led to earlier incorporation of calcium mineralized tissues (Varanasi *et al.*, 2011). Alizarin Red staining and EDX analysis demonstrate significantly more Ca and P deposits on pSi than on flat Si with or without OM. However, such a difference was also reported when the experiments were conducted without cells, on bare scaffolds: there were significant Ca deposits (as assessed by Alizarin Red staining) and CaP deposits (as assessed by EDX spectroscopy) on pSi incubated in osteogenic medium, while only few deposits were found on flat Si. Images taken with SEM showed abundant mineralized formations on pSi, and not on flat Si, confirming the CaP nucleation role of the porous surface. It had already been demonstrated that pSi, unlike flat Si, had the ability to promote CaP (and even hydroxyapatite) nucleation, without elucidating the calcification mechanisms involved (Canham, 1995) (Canham *et al.*, 1997). We confirmed here that mesoporous silicon could behave as nucleation sites for CaP minerals. The driving force of nucleation is the supersaturation representing the free energy gains (Kashchiev, 2000). The critical supersaturation for the heterogeneous nucleation of Ca/P on bare silica for hydroxyapatite is 7.6 mM (Ngankam *et al.*, 2000). Porous silicon is used as an effective nuleator for protein crystals (Chayen *et al.*, 2001). It is assumed that nucleation rate is dependent of relation between pore radius and protein 'stockes' radii (Chayen *et al.*, 2006). The presence of nanoscopic pores on certain polymer surfaces led to order-of-magnitude faster aspirin nucleation rates when compared with surfaces without pores (Diao *et al.*, 2011). Biocompatible polymer surfaces imprinted with nanopores were utilized as heteronucleants to influence the nucleation kinetics (Lopez-Mejias *et al.*, 2013). A deep investigation on of the effect of pores on nucleation of carbonated hydroxyapatite on porous silica demonstrated that pore diameter is critical and that the surface chemistry (silanol and hydroxyl surface groups) are not involved (Pereira *et al.*, 1996). This was confirmed by Canham *et al.*, who studied hydroxyapatite nucleation on pSi in simulate body fluid (Canham *et al.*, 1997). Even if this work was confirmed by phenomenological studies (Chadwick et al., 2010) (Pramatarova *et al.*, 2004), the influence of the length scale of the pore was never investigated as is was done for polymeric substraste (Diao et al., 2011) (Lopez-Mejias *et al.*, 2013).

We wanted to further investigate the nature of the CaP deposits, focusing at Ca/P molar ratio. We compared the Ca/P ratio with theoretical values of calcium phosphate. According to the Ca/P ratio, the calcium phosphate particles formed on pSi without cells were octacalcium phosphate (OCP) (Ca/P = 1.341), while on pSi with DPSC they were closer to tricalcium phosphate (Ca/P = 1.418) (Dorozhkin, 2010). Previous studies of calcium phosphate nucleation on Psi have used simulated body fluid with a different calcium phosphate ratio than the osteogenic media used.

4.4.4 Pore diameter effects on mineralization

After demonstrating the influence of Si content on differentiation and of pSi surface on mineralization, we wanted to assess the influence of pore diameter on mineralization. We reproduced the previously described experiments on pSi gradients, with pore diameters ranging from few nanometers to 500 nm and more. We seeded DPSC on pSi gradients (and flat Si as control) and followed differentiation and mineralization for up to 3 weeks. We assessed CaP deposits at each stage of the gradient by fluorescence microscopy (Calcein Blue staining) and SEM (EDX spectroscopy). With fluorescence microscopy, we observed that there was a gradual increase in frequency of CB-positive colonies along the gradient as the pore diameters decreased, with an exception on the area with 37 nm pores diameter (Figure 4.8). A very similar pattern was found with the mean of EDX spectroscopy: there was a gradual increase in amount of Ca and P (in atomic %) along the gradient as the pore diameters decreased, with an exception on the area with 37 nm pores diameter. The maximum amounts of Ca and P deposits, assessed by both techniques, were recovered on the areas with pores diameter ranging from 8 ± 5 nm to 14 ± 7 nm. Deposits were the lowest on flat Si and larger pores (assessed by EDX spectroscopy). And deposits were more abundant on 37 nm pores than on 18 nm and 24 nm pores, which is not consistent with the global tendency of gradual increase along the gradient as pores diameters decrease (Figure 4.11).

To further investigate the effect of pores and of cells, we reproduced the experiments without cells, by incubating bare pSi gradient in OM for 3 weeks. EDX spectroscopy revealed a gradual increase in amount of Ca and P (in atomic %) along the gradient as the pores diameters decreased. The maximum amounts of Ca and P deposits were recovered on the areas with pores diameter ranging from 8 ± 5 nm to 14 ± 7 nm (Figure 4.12).

The area with pores diameter of 37 ± 18 nm was of particular interest as it showed a specific behavior only when pSi gradients were incubated with DPSC. During the 3 weeks of osteogenic induction, DPSC differentiate into osteoblast-like cells, likely to produce collagen extra cellular matrix. The collagen fibrils form a scaffold for a highly organized arrangement of oriented apatite crystals (Orgel *et al.*, 2006). In the periodic 67 nm cross-striated pattern of the collagen fibrils, the less dense 40 nm long gap zone is implicated as the place where apatite crystals nucleate from an amorphous phase, and subsequently grow (Mahamid *et al.*, 2010). Thus, we hypothesize that pSi with 40 nm pores favor ACP transformation and crystal growth during extra cellular matrix formation, by mimicking the 40 nm gap zone of the collagen fibrils. Such hypothesis is reinforced by the results obtained with pSi scaffolds (36 nm pores diameter): bare scaffolds incubated in OM induced the nucleation of OCP while scaffolds with DPSC permitted to CaP closer to β-TCP or HA.

Investigation showed that ACP nucleation started with nanometer-sized CaP complexes, and these prenucleation clusters aggregated to form amorphous calcium phosphate, such as OCP (Cuisinier *et al.*, 1995) (Houllé *et al.*, 1997) (Habraken *et al.*, 2013). These works bring out that the nucleated clusters are of the nanometer-scale and nucleation rate is higher due to size similarities.

Chapter 5 Influence of pSi Pore Diameter on DPSC Differentiation

5.1 Introduction

Biomaterials used as scaffold in tissue engineering must be tolerated by the cells, but are also expected to promote physiological cell responses: by acting as analogs of the natural extracellular matrix (ECM), they can regulate cell adhesion and extent through the binding of cell surface molecules to the materials surface (Bacakova *et al.*, 2011). The cell extents and the strength of cell adhesion regulate the cell proliferation and the balance between proliferation and differentiation (Mann *et al.*, 2002) (See also Chapter 1, Figure 1.1). The proliferation capacity and migration speed are dependent of both cell spreading and cell adhesion strength. Maximum cell proliferation and cell migration is achieved at an intermediate stage of cell extents and adhesion strength. Indeed cells with large adhesion areas (focal adhesion plaques) containing increased levels of adhesion molecules (such as talin and vinculin) show usually less migration and proliferation and express more differentiation markers (Mann *et al.*, 2002). The extent and strength of cell adhesion (and subsequent cell proliferation and differentiation) depend on the physical and chemical properties of the biomaterial surface, such as surface morphology and micropatterning of the surface with cell-adhesive domains (Bacakova *et al.*, 2011). Substrate topography has been shown to be an important factor for the regulation of cellular responses (Tsai *et al.*, 2009), and cell attachment, migration, proliferation and differentiation have been demonstrated to be effectively regulated by topographic features (Wang *et al.*, 2011), including pore diameter (Wang *et al.*, 2012), with dimensions ranging from the nano to the microscale (Lim *et al.*, 2007).

Cellular responses to nanostructured pSi have been investigated both *in vitro* and *in vivo* (Low *et al.*, 2006) (Sapelkin *et al.*, 2006) (Whitehead *et al.*, 2008) (Alvarez *et al.*, 2009) (Fan *et al.*, 2011). Porosity and pore size can be tuned by varying the etching conditions to generate surfaces with pore size ranging from a few nanometers to micrometer (Sailor, 2011) and pSi surface can be modified by oxidation or various chemical treatments, such as silanization or hydrosilylation (surface functionalizations are described in Chapter 1 and Chapter 3). We investigated the effect of pore diameter on DSPC adhesion, proliferation and further differentiation. As proliferation and differentiation are related, we aimed to determine optimal pores diameter for DPSC proliferation and for osteodifferentiation. For this purpose, we used pSi gradients with pore diameters ranging from <10 nm to >500 nm. These pSi films, containing a controlled distribution of pore sizes, are produced by using an inhomogeneous etching technique (Collins *et al.*, 2002). These pSi gradients have been used to assess cell attachment, with various cell types, such as neuroblastoma cell lines, for which attachment and morphology were shown to critically depend on pore size (Khung *et al.*, 2008) and rat mesenchymal stem cells, for which pore size of 20-30 nm enhanced cell attachment (Clements *et al.*, 2011) (Clements *et al.*, 2012). However, different cell types respond differently to topographical features (Low *et al.*, 2006). In addition, nanotopography influence cell proliferation through conformation of adhesive proteins and cell focal adhesion (Popat *et al.*, 2007), and human mesenchymal stem cell differentiation (Dalby et al., 2007). Therefore we investigated primary human stem cells adhesion, proliferation and differentiation on such pSi gradients.

5.2 Materials and Methods

5.2.1 Human Dental Pulp Stem Cells (DPSC)

Mesenchymal stem cells derived from human teeth (dental pulp stem cells) were recovered from discarded normal human impacted third molars, collected with informed consent of patients undergoing routine extractions at the Dental Clinic of the University of Adelaide, under approved guidelines set by the University of Adelaide and Institute of Medical and Veterinary Science (IMVS) Human Subjects Research Committees. DPSC were isolated as previously described (Gronthos *et al.*, 2002). Briefly, tooth surfaces were cleaned and cracked open to reveal the pulp chamber. The pulp tissue was gently separated from the crown and root and then digested in a solution of 3 mg/mL collagenase type I and 4 mg/ml dispase for 1 hour at 37 °C. Single-cell suspensions were obtained by passing the cells through a 70 μm strainer. Cultures were established by seeding single-cell suspensions (1 - 2 x 10^5) of dental pulp into T-25 flasks in growth media, (αMEM supplemented with 10% fetal calf serum, 100μM L-ascorbic acid, 2 mM L-glutamine, 100 IU/ml penicillin, and 100 μg/mL streptomycin), then incubated at 37°C in 5 % CO_2.

5.2.2 Porous Silicon Gradients

Porous silicon (pSi) gradients were prepared by anodization of highly doped p^{++} type silicon wafers (0.0005-0.001 Ω cm, <100>, boron doped, obtained from Siltronix®) using a 1:1 HF:ethanol solution in a custom-built Teflon etching cell using aluminium foil to contact the back of the silicon wafer and a Pt mesh as the counter electrode. A current density of 115 $mA.cm^{-2}$ was applied for 60 s using a Keithley 2425 sourcemeter. For surface gradient preparation, the platinum electrode (1 mm diameter, Sigma-Aldrich) was placed perpendicular to the substrate and at one end of the etching cell (Clements *et al.*, 2012) (Collins *et al.*, 2002); the etching set up is presented in Figure 5.1. In order to stabilize the scaffolds surface, pSi gradients were thermally oxidized for 1 h at 800 °C, and silanized with aminopropyltriethoxysilane (APTES) 4 % in dry toluene at room for 1 h with gentle shaking. For use in cell culture, the wafers were sterilised with 70% (vol/vol) ethanol for 10 min before drying under sterile airflow.

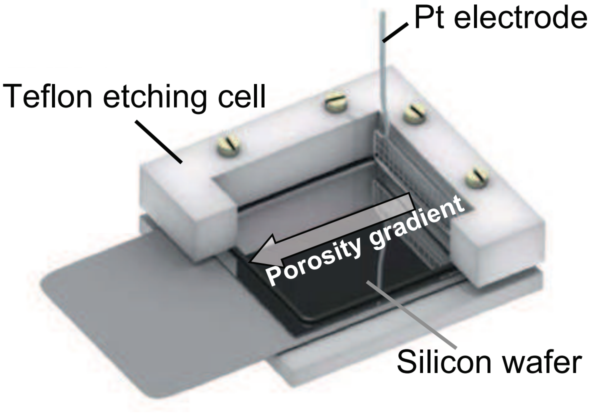

Figure 5.1: Etching set up, with platinum electrode placed perpendicular to the surface, at one and of the pSi wafer. Adapted from Clements *et al.* (2012).

5.2.3 Surface characterization

Gradient pSi surfaces were characterized by means of scanning electron microscopy (SEM) and interferometric reflectance spectroscopy (IRS), to determine the pore diameter and the porosity of the layer along the surface of the gradient. Samples were observed after preparation, before any cell experiment, and after 21 days in culture medium (αMEM) to assess their stability in aqueous solution. The SEM analysis was conducted using a FEI Helios SEM (10 kV accelerating voltage, under a pressure of 1.3 x 10^{-3} Pa). For IRS, a bifurcated optical cable was used to direct white light from a tungsten lamp source to the pSi gradient at normal incidence and the reflected light was collected and transmitted through the other arm of the bifurcated fiber optic cable to a CCD spectrometer.

5.2.4 Atomic Force Microscopy (AFM)

For atomic force microscopy (AFM) cell imaging, we used an Asylum MFP-3D AFM system, mounted on an Olympus inverted microscope. Gold-coated silicon nitride rectangular cantilevers were used with a typical spring constant of 30 pN/nm^{-1}, tip radius ~30 nm. The spring constant for each cantilever was determined by thermal noise method within the supplied software. DPSC were examined after 24 h of *in vitro* incubation on pSi with pores diameter of 36 ± 4 nm or on flat Si. Cells were fixed in 2.5 % glutaraldehyde for 1 h, and then rinsed 3 times in PBS. AFM topographic images were obtained in contact or tapping mode in liquid (PBS) at an average temperature of 30°C.

5.2.5 Cell adhesion

DPSC attachment was monitored by fluorescence microscopy. Cells were seeded onto the surface of sterilized pSi at a cell density of 5 x 10^4 cell/mL. Flat silicon (non etched silicon wafers) was used as control. Cells were incubated for 4 h, 24 h, 48 h and 72 h at 37 °C with 5 % CO_2, in a humidified incubator. For cell counts, samples were fixed with 2.5 % glutaraldehyde for 1 h, and stained with 50 µg/ml of Hoechst 33342 for 30 min to stain nuclei. Samples were then washed with PBS buffer to remove any non-adherent cells and unbounded dye, and observed under fluorescence microscopy at an excitation wavelength of 360 nm. Cell counts were conducted every 2 mm along the pSi gradients, starting from the area under the electrode (electropolished area). Three measurements were conducted in each region over an area of 1400 µm x 1050 µm. All experiments were performed in triplicate, and statistical differences along the gradients were determined using the Student t-test with $p < 0.05$ deemed as statistically significant.

5.2.6 Cell morphology and spreading

To evaluate cell morphology and spreading, DPSC were incubated at a density of $1x10^5$ cell/mL for 24 h on pSi gradients, and stained for actin, nuclei, and vinculin. After 24 h of incubation, cells were rinsed three times with PBS, fixed with 4 % paraformaldehyde for 20 min, then washed three more times to remove excess paraformaldehyde. DPSC were permeabilized with 0.5 % Triton X-100 in PBS at 4 °C for 15 min. In order to reduce non-specific background, samples were blocked with PBS/BSA 1 % for 10 min at 37 °C. After blocking, PBS/BSA was aspirated and the samples were first incubated for 1 h with TRITC-labeled phalloidin (1:200) at 37 °C in the dark. Mouse anti-vinculin antibody, at a dilution of 1:100 in 1 % BSA/PBS, was added to each sample for 1 h at 37 °C in the dark, then the samples were incubated for 30 min with secondary rabbit anti-mouse antibody at a dilution of 1:200 at room temperature. Finally, samples were incubated with Hoechst 33342 for 10 min at room temperature, and washed twice with deionized water. Samples were observed under fluorescence microscopy at an excitation wavelength of 360 nm for Hoechst staining (nucleus staining), 490 nm for vinculin and 630 nm for phalloidin (actin staining).

After staining the actin, vinculin and nuclei, fluorescent images were analyzed using imageJ software. Actin staining was used for identification of cell shapes into either round, branched or spindle cell morphology. The circularity of the cells was determined by using the length/width ratio. Round cells were defined to have a length/width ration of > 0.8, while spindle cells had length/width ratio below 0.8. Branched cells were characterized by more than two branches in their morphology. Cell areas were also measured for each type of cell morphology, giving insights into the spreading of cells on surfaces. The number of focal points was counted per cell for each type of cell morphology and normalized by the cell area for each cell morphology.

5.2.7 Proliferation assays

The proliferation rate of DPSCs on pSi gradients was assessed by bromodeoxyuridine (BrdU) incorporation for 24 h, 48 h and 72 h. BrdU incorporation is used as a marker for mitotically active cells. BrdU is a synthetic nucleotide analogue of thymidine, incorporated into the newly synthesized DNA of replicating cells (during the S phase of the cell cycle), substituting for thymidine during DNA replication (Horner *et al.*, 2000). DPSC were seeded on the scaffolds at a density of 1x 10^5 cells/mL in αMEM supplemented with 10 % FBS with 1:100 diluted BrdU labeling (Invitrogen). After 24 h, 48 h and 72 h incubation at 37 °C, samples were rinsed 3 times in PBS, fixed in 4 % paraformaldehyde, rinsed again 3 times in PBS and put in 1.5 M HCl (Sigma) for 30 min at room temperature to dissociate DNA strands. Samples were washed with PBS, incubated in PBS with 0.1 % Triton X-100 and 1 % BSA for 1 h at room temperature, then incubated with mouse anti-BrdU primary antibody overnight at 4 °C. After immunostaining, cells were washed with PBS/1 % BSA, incubated with FITC conjugated rabbit anti-mouse secondary antibody for 30 min and counterstained with 2 µg/ml Hoeschst 33342 for nucleus staining. Samples were observed under fluorescence microscopy at an excitation wavelength of 290 nm for nuclei (blue staining) and 490 nm for BrdU (green staining). All experiments were performed at least in triplicate and the number of BrdU-positive cells was expressed as a percentage of the total number of cells.

5.2.8 Cell differentiation

DPSCs were seeded at a density of 1 x 10^5 cells/cm^2 on pSi gradients and maintained in αMEM supplemented with 10 % FBS for 72 h, until they reached confluence. Osteogenic differentiation was then induced by culture in osteogenic medium (αMEM supplemented with 15 % FBS, dexamethasone, L-ascorbate phosphate, and β-glycerophosphate) for 21 days. Control cultures were maintained without osteogenic supplements and flat silicon was used as control. The osteoblastic differentiation of DPSC was followed, after 7 days, by the quantification of alkaline phosphatase (ALP) and osteocalcin (OC) by immunostaining. After 21 days, the osteodifferentiation was assessed by type I collagen immunostaining and by infrared spectroscopy (FTIR).

5.2.9 Immunofluorescence: ALP and type 1 Collagen

Cell differentiation was assessed after 7 days by ALP staining and after 21 days by type I collagen staining. Samples were washed with PBS and fixed with 4 % paraformaldehyde for 20 min at room temperature. Cells were permealized with 0.5% Triton X-100 in PBS for 15 min at 4 °C then blocked with 1 % BSA in PBS for 1 hour at room temperature. Samples were incubated with either rabbit anti-ALP or goat anti-collagen antibodies (1:100 in 1 % BSA) at 4 °C overnight. After three times of rinsing with PBS, samples were incubated with either PerCP-conjugated donkey anti-rabbit or FITC-conjugated donkey anti-goat secondary antibodies (1:200 in 1 % BSA) for 1 hour at room temperature. Finally, cell nuclei were stained with 50 µg/ml Hoechst 33342 for 30 min at room temperature. Samples were observed under confocal fluorescence microscopy at an excitation wavelength of 360 nm for Hoechst, 488 nm for type I collagen and 633 nm for ALP staining.

5.2.10 FTIR microscopy

After 21 days in osteogenic medium, pSi gradients were characterized with infrared microscopy (FTIR), to assess DPSC osteodifferentiation along the gradients. FTIR studies were performed with a Bruker Hyperion 1000 IR microscope operating with a Bruker Vertex 80 IR spectrometer. Along the whole gradient, reflectance spectra were collected over 64 scans, fram 650 to 4000 cm^{-1}, with a resolution of 4 cm^{-1}. All spectra were background corrected with an unetched silicon wafer of the same type. Spectra were recovered with OPUS 6.5 software and analyzed with Matlab software for averaging spectra and MagicPlotPro software for deconvolution.

5.2.11 Data analysis

Data was reported as the mean ± standard error. All post-acquisition image processing was conducted with ImageJ software. Statistical analysis was performed using SigmaStat. All data were checked for normalization. Data were analyzed using parametric Student t-test, and for ANOVA, non-parametric Tukey test was performed. For all tests, significance was determined to be $p < 0.05$

5.3 Results

5.3.1 Surface characterization

The pSi gradients were fabricated by anodization at a current density of 115 mA.cm^{-2}, using an asymmetric electrode configuration and a 1:1 HF/ethanol electrolyte solution, as previously described (Clements *et al.*, 2012). Electropolishing was observed near the Pt electrode and a conspicuous color change occurred towards the other extreme of the surface, indicating a change in pore architecture (Figure 5.2).

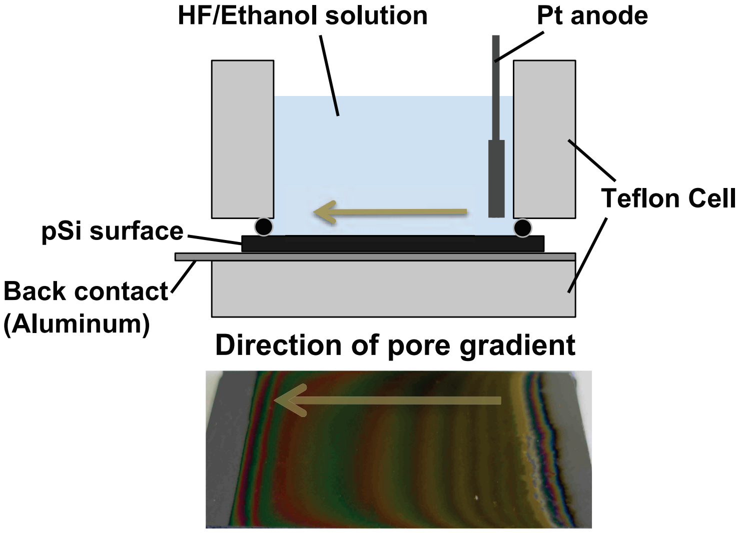

Figure 5.2: Asymmetric configuration of the etching set-up, and photograph of a freshly etched pSi gradient. Color changes are visible along the gradient. The samples are 20 mm long. Schematic set-up adapted from Clements *et al.* (2011)

The topography and the average pore size along the pSi gradients were characterized by means of scanning electron microscopy (Figure 5.3). The average pore size measured at 2 mm intervals decreased with a logarithmic profile from the region near the electrode to the other end of the surface. The non-linear nature of this profile was attributed to the non-linear decrease in current density across the substrate, in accordance with previous studies (Clements *et al.*, 2012)(Collins *et al.*, 2002). The pore sizes along the gradients are presented in Table 5.1: in the region closest to the Pt electrode, the largest pores were observed with a pore size of 1022 ± 353 nm. The pore size decreased to 500 ± 208 nm at a position 2 mm from the electrode, 119 ± 44 nm at a position 6 mm and 37 ± 18 nm at a position 10 mm from the electrode. At the extreme end of the sample furthest away from the electrode (18 mm from the electrode), a pore size of 8 ± 5 nm was determined. Pore size gradients were reproducible and showed little sample-to-sample variation.

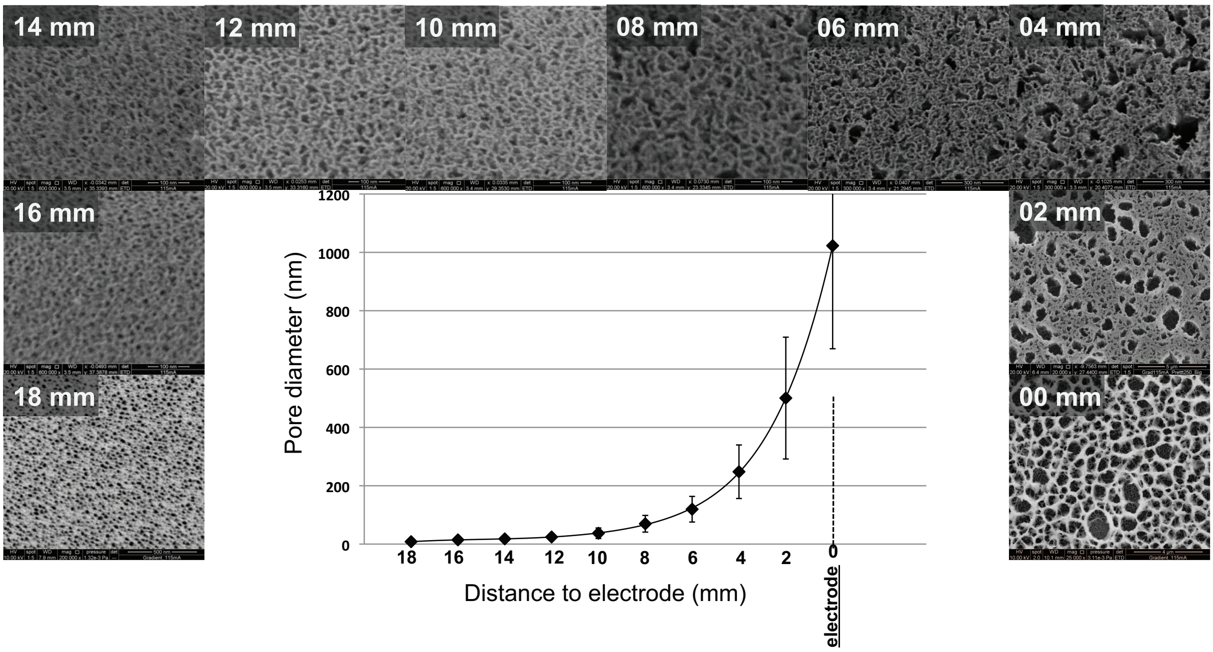

Figure 5.3: Graph of the average pore size along the pSi gradients, according to the distance to the electrode. Images are representative SEM top view of the pSi at different stages of the gradient; the value on each image indicates the distance to the electrode.

Porosity and pore depth, determined by Interferometric Reflectance Spectroscopy (IRS), are shown in Figure 5.4, with detailed values presented in Table 5.1 (next page). Both porosity and pore depth decreased with increasing distance from the electrode.

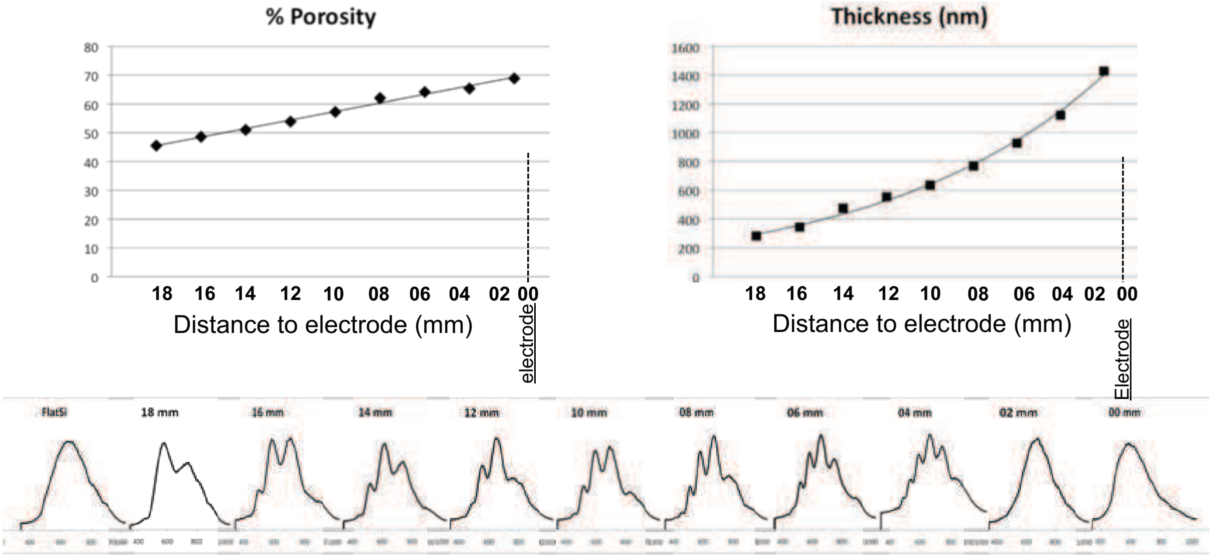

Figure 5.4: Porosity and thickness of the porous layer, assessed by IRS. The thickness corresponds to the pore depth. On the bottom of the figure are shown optical reflectance spectra showing the variation in the fringes along the length of a pSi gradient.

Distance to electrode (mm)	*18*	*16*	*14*	*12*	*10*	*8*	*6*	*4*	*2*	*0*
Pore diameter (nm)	8.24	14.49	17.91	24.31	37.18	69.64	119.51	248.00	500.49	1022.91
Standard Deviation	5.42	6.87	8.52	11.32	17.98	28.60	43.95	91.79	208.79	353.26
% porosity	45.5	48.58	51	53.87	57.25	62.03	64.13	65.33	68.85	72.22
Thickness (nm)	281.8	343.2	474.5	553.5	634.7	767.5	926.2	1121.7	1427.9	1744.7

Table 5.1: Pore diameter (Mean values and standard deviation of the mean), porosity and thickness of the porous layer at each stage of the pSi gradient.

After 21 days in αMEM, pores were still visible on pSi gradients, demonstrating the stability of the porous layer for up to 3 weeks, in the conditions of the *in vitro* experiments (Figure 5.5).

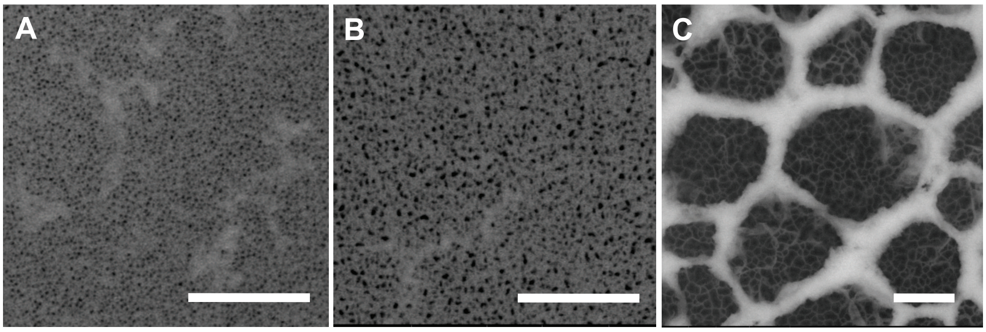

Figure 5.5: Representative SEM images of pSi gradient after 21 days in culture medium, showing the persistency of pores. (A) image at 14 mm from the electrode. (B) image at 6 mm from the electrode. (C) image under the electrode. Scale bar = 1 μm.

5.3.2 Cell adhesion and spreading

5.3.2.1 Cell counts

Adhesion assays were performed to quantify DPSC attachment along the pSi gradients (Figure 5.6, next page). DPSC adhesion to porous surfaces presented along the pSi gradient was at a level similar to that on flat Si after 4 h and 24 h of incubation. After 48 h, adhesion was similar on flat Si and porous surfaces located at 8 mm and above from the electrode (pore diameter ≤ 70 nm); there was significantly less cells attached on pores with diameter ≥ 120 nm compared to flat Si ($p = 0.013$). After 72 h, the cell counts were similar for flat Si and porous surfaces located at 10 mm and above from the electrode (pore diameter ≤ 37 nm); there was significantly less cells attached on pores with diameter ≥ 70 nm compared to flat Si ($p = 0.034$).

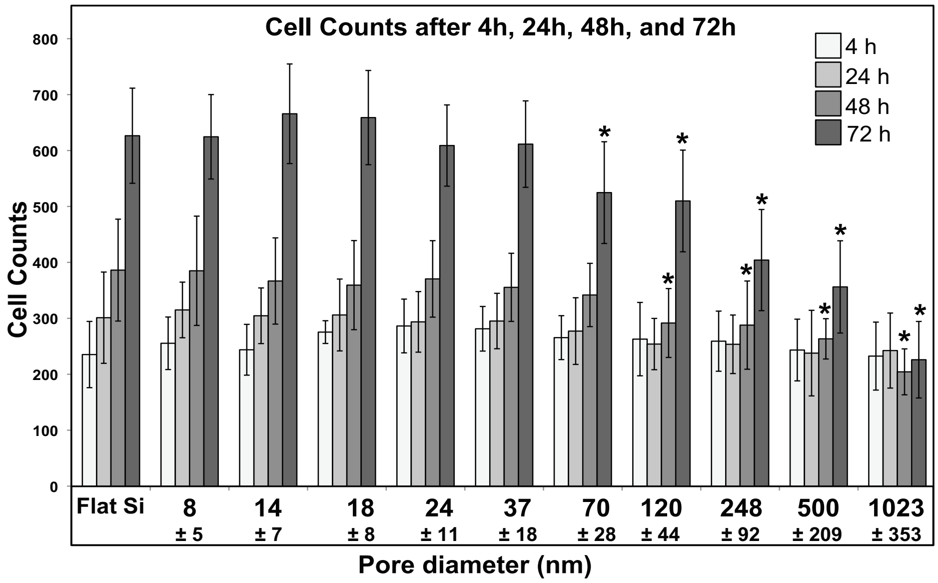

Figure 5.6: Cell counts per area 1700 x 1300 μm, at each stage of the pSi gradient. Experiments made in triplicate, with 3 measurements per area (each distance to electrode). Error bar = standard deviation of the mean. (*) indicates a significant difference ($p < 0.05$) compared to flat Si, after either 48 h or 72 h.

5.3.2.2 Cell spreading

Cell spreading *in vitro* is composed of morphogenetic processes by which cultured cells acquire non-spherical shapes and become attached to the substratum. Cell spreading evaluation is a simple and physiologically relevant method for studying cytoskeletal organization and regulation (Dubin-Thaler *et al.*, 2008). We observed and evaluated cell spreading after a 24 h incubation period. DPSC spreading varied from round cells to dendritic and polarized cells, according to their location on the gradients (Figure 5.7).

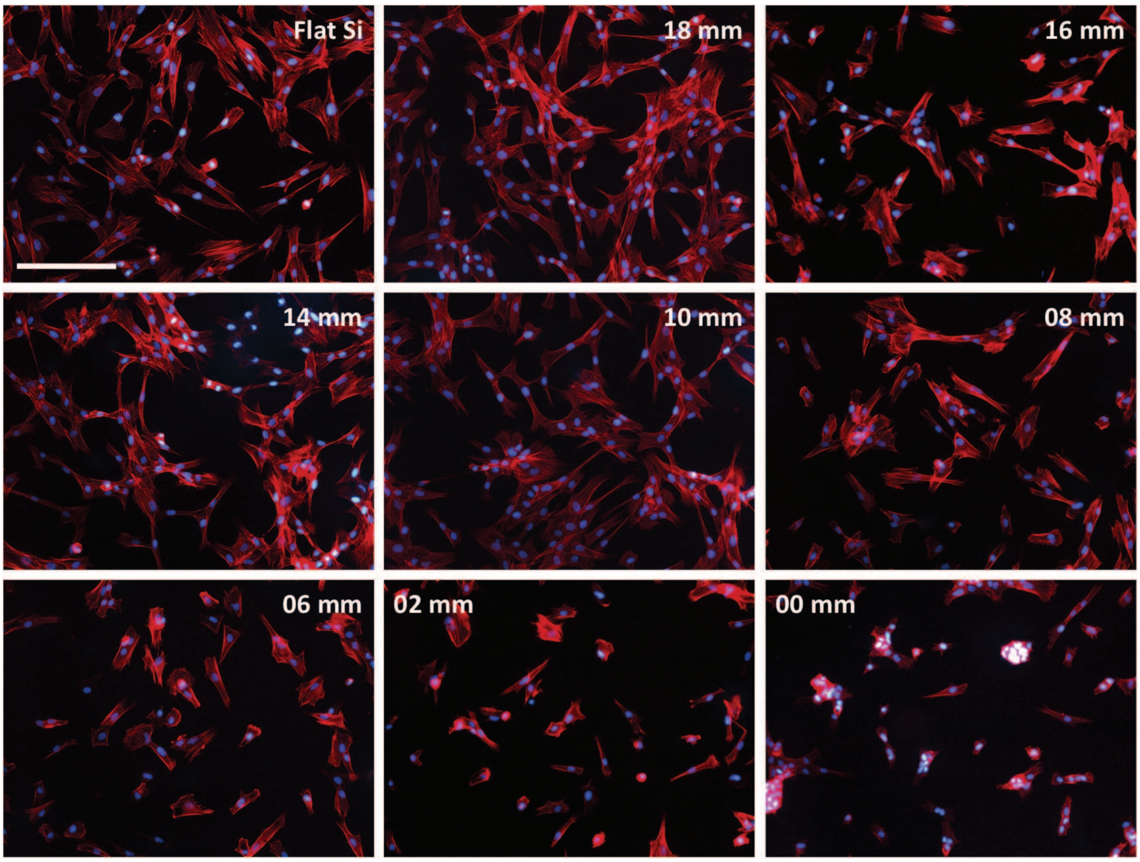

Figure 5.7: Fluorescence microscopy images of DPSC seeded on pSi grad, after 24 h of incubation. Cytoskeleton is stained in red (actin) and nuclei are stained in blue. The distance on each image indicates the distance to the electrode. Scale bar = 100 μm

From the fluorescence images, we assessed cell spreading by considering the cell surface area (area covered by the cell, in µm^2) and the cell circularity (ratio between the shorter and the longer axis of the cell, between 0 for elongated cells and 1.00 for round cells). As observed with fluorescence images, cell surface area dramatically decreased on large pores (pores diameter ≥ 120 µm) and cell circularity was significantly higher on these large pores. It was interesting to note that cell surface area gradually increased while pores diameter decreased and cell circularity gradually decreased while pores diameter increased; with an important exception in the middle of the gradient, at 10 mm from the electrode (pores diameter = 37 ± 18 nm). On this specific area, with pores diameter roughly ranging from 20 to 50 nm, cell spreading was enhanced compared to other regions with smaller or larger pores (Figure 5.8).

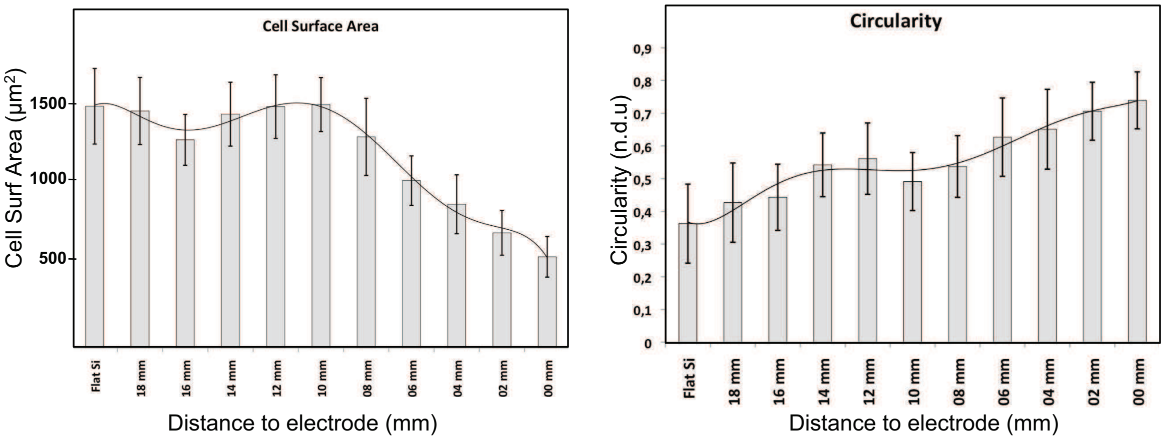

Figure 5.8: Graphical representation of cell surface area and cell circularity, assessed from fluorescence microscope images.

5.3.2.3 Focal adhesions

Integrin-mediated cell spreading and adhesion were assessed for DPSC cultivated on pSi gradients, by cytoskeleton (actin) and focal adhesion (vinculin) staining. Adhesion-mediated cell spreading and focal adhesion was monitored after 24 h of incubation via immunostaining of F-actin (phalloidin staining) and vinculin (Figure 5.9). On flat Si and pSi with pores ≤ 70 nm, development of stress fibers and vinculin could clearly be seen, indicating well spread cells with mature focal adhesion. On large pores (pores diameter ≥120 µm), minimal cell spreading was observed, with actin observed only around the nuclei, and less organized focal adhesion.

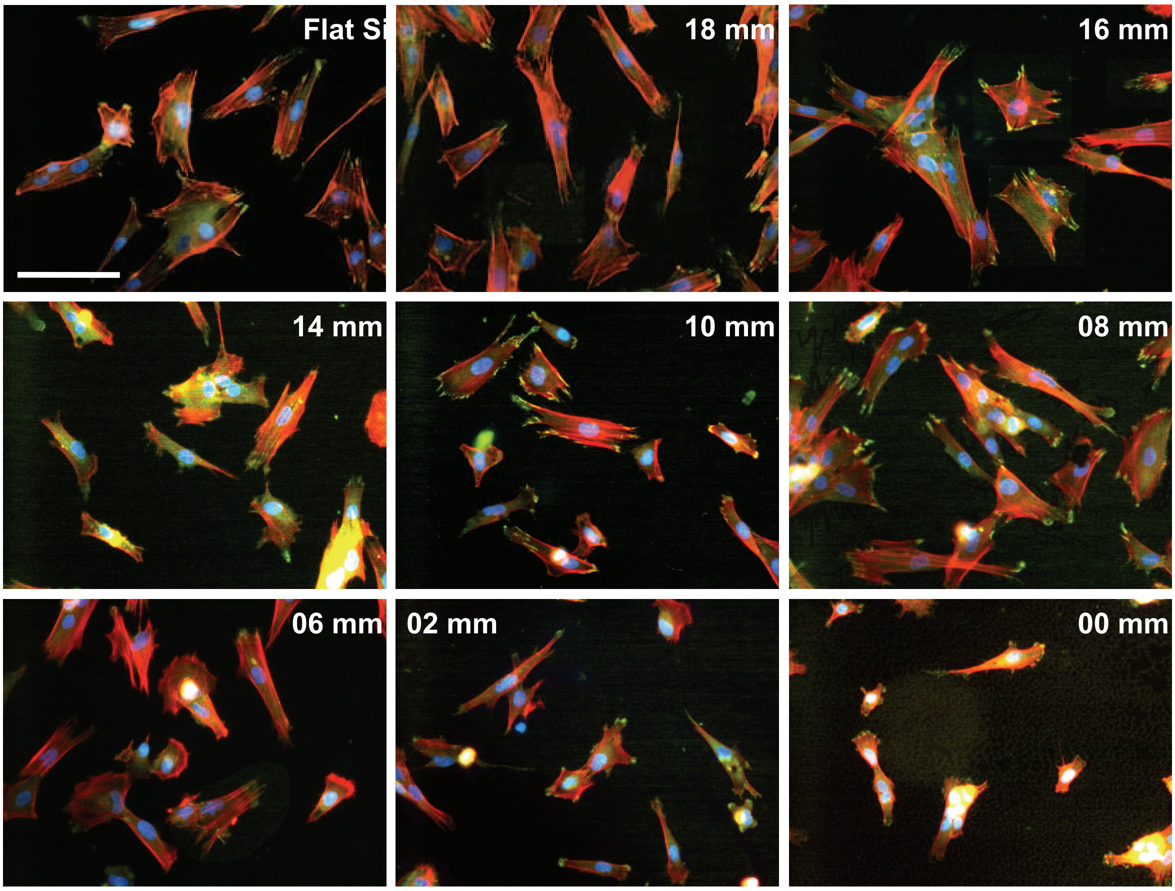

Figure 5.9: Fluorescence microscopy images of DPSC seeded on pSi grad, after 24 h of incubation, showing focal adhesion distribution. Cytoskeleton is stained in red (actin), nuclei are stained in blue and vinculin is stained in green. Focal adhesion (green staining) are fairly well organized on flat Si and pSi at 8 to18 mm from the electrode, and less organized (even not visible) on regions closer to the electrode. Scale bar = 100 µm

5.3.2.4 AFM: Filopodia and lamellipodia formation

We were interested in filopodia formation for DPSC growing on pSi samples, as this gives information about cell behavior since these cellular projections contribute to intercellular communication, cell adhesion and motility (Mattila *et al.*, 2008). After 24 h on flat Si, DPSC developed short filopodia at their apical pole, spreading from lamellipodia. After 24 h on pSi samples, DPSC developed such filopodia spreading from lamellipodia, but they also developed long and thin protrusions, growing directly from the cellular body. These findings were controlled by fluorescence microscopy with actin staining; the long and thin protrusions were formed by actin, confirming them as filopodia. These results are presented in Figure 5.10 (next page).

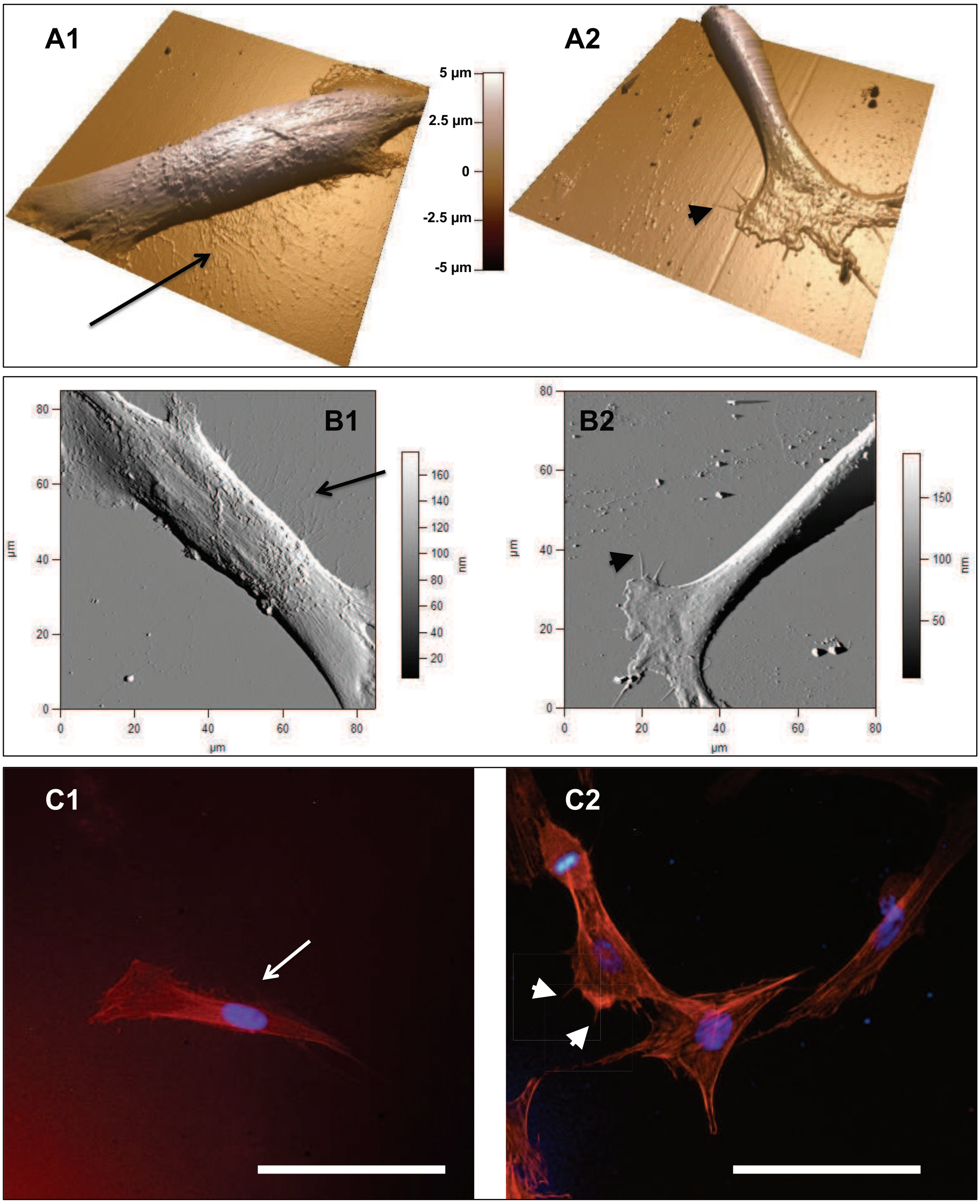

Figure 5.10: AFM and fluorescence microscopy examination of DPSC after 24 h of incubation on pSi (pores 36 ± 4 nm) and flat Si. Representative AFM 3D reconstruction of DPSC on pSi (A1) or flat Si (A2) and corresponding deflection images (B1: pSi. B2: flat Si). (C) Fluorescence microscopy images of DPSC on pSi (C1) or flat Si (C2) with actin staining (red staining) showing the filopodia formations. Scale bar = 50 µm. The arrows highlight the long thin filopodia growing from the main cell body while the arrowheads show filopodia growing from lamellipodia.

For DPSC incubated on pSi scaffolds, we measured height and width of the filopodia growing from the main cell body by AFM: the size of these actin finger-like structures ranged from 30 to 70 nm of height and from 50 to 200 nm of width, with a length that could be of several micrometers (Figure 5.11).

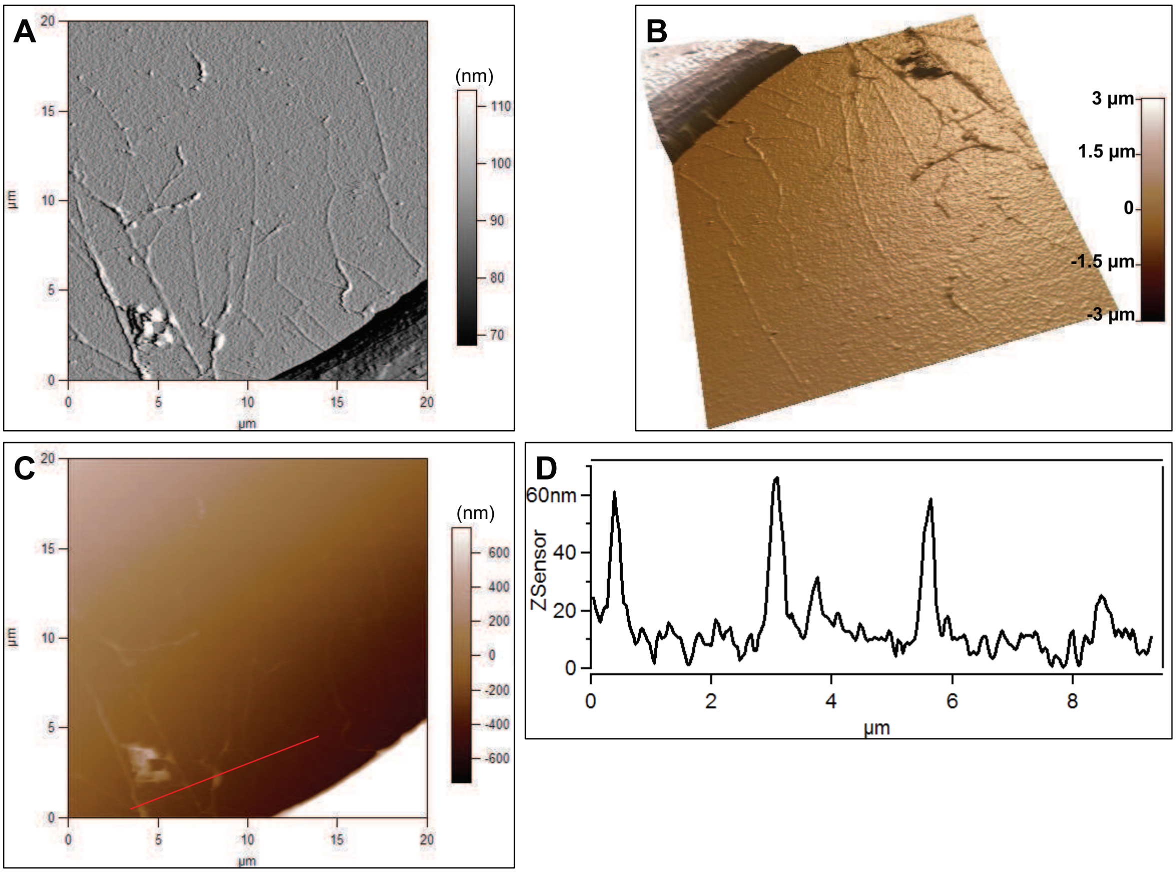

Figure 5.11: AFM images in contact mode of a DPSC cultured on pSi. (A) Deflection image; (B) Corresponding 3D reconstruction image; (C) Topography image; (D) Cross section along the line indicated in C.

5.3.3 Cell proliferation

To assess the proliferation rate of DPSC seeded on pSi gradients, incorporation of bromodeoxyuridine (BrdU) for 24 to 72 h was performed, in order to label dividing cells. All cell nuclei were stained in blue with Hoechst 33342, and dividing cells nuclei were, in addition, stained in green (Alexa 488 conjugated secondary antibody). The proliferation rate corresponds to the number of BrdU stained cells over the total number of cells (Figure 5.12).

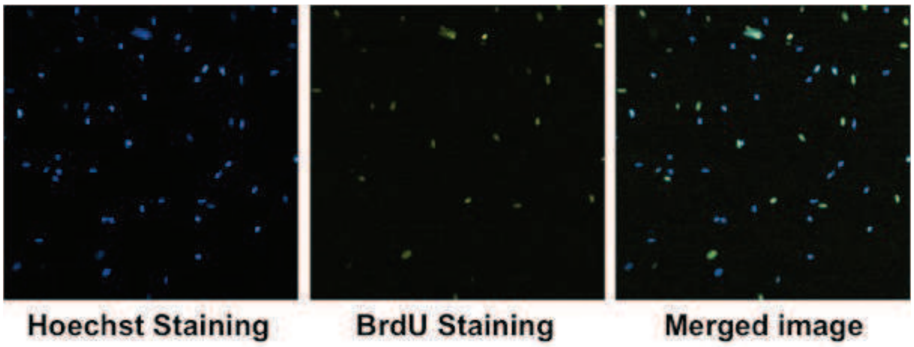

Figure 5.12: Fluorescence microscopy images of DPSC stained with Hoechst and anti-BrdU antibody. The percentage of BrdU positive cells is the ratio between BrdU stained cells (green nucleus) and total cells (blue nuclei).

BrdU assay revealed an increased proliferation rate on areas with pores diameter ranging from 18 to 70 nm. These areas (18 to 70 nm) were only partially matching with the areas where we counted the more cells after 72 h (flat Si and pores ≤ 37 nm) (Figure 5.13, next page). This apparent contradiction is quite difficult to interpret, but reinforce the fact that cells are influenced by the pores diameter at the nanometer scale, for early attachment, adhesion process and proliferation. On large pores (diameter ≥ 250 nm), adhesion and proliferation were clearly disadvantaged, compared to smaller pores.

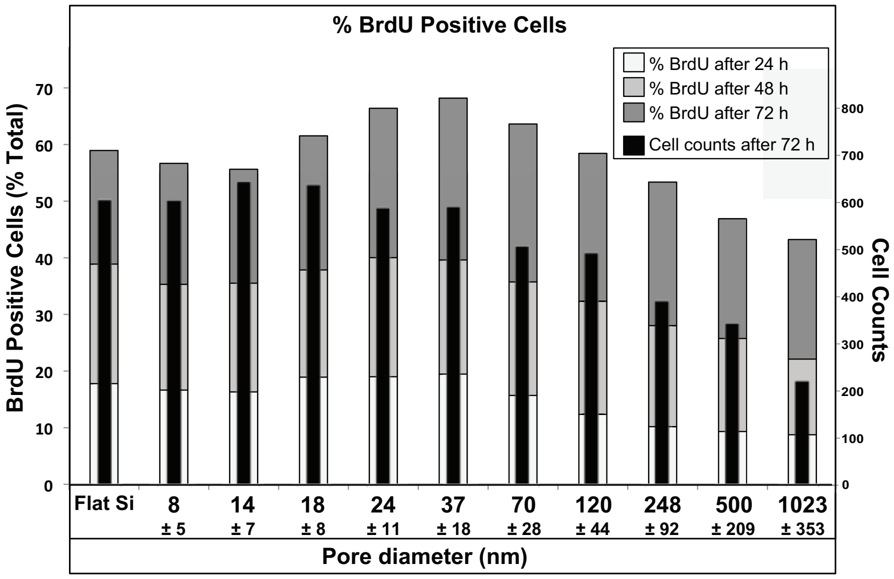

Figure 5.13: Percentage of BrdU positive cells along pSi gradients, assessed for up to 72 h after cell seeding. The black histograms show the total number of cells after 72 h.

5.3.4 DPSC osteodifferentiation

5.3.4.1 ALP staining after 7 days

Cell osteodifferentiation was determined at each stage of the pSi gradients by immunofluorescence, for the expression of ALP after 7 days. DPSC expressed differently ALP, as seen by immunofluorescence staining (Figure 5.14).

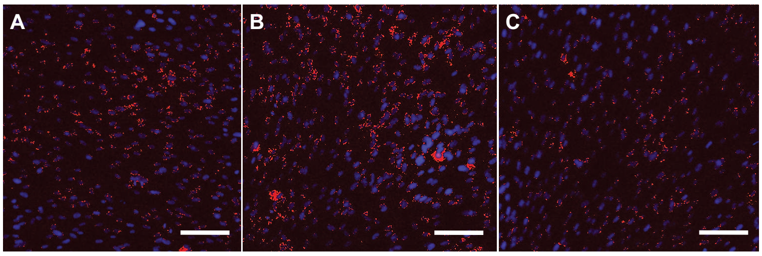

Figure 5.14: Representative confocal microscopy images of DPSC after 7 days in osteogenic medium. Nuclei are stained with Hoechst 33342 (blue staining) and ALP is stained with PE-conjugated antibodies (red staining). Images are treated by ImageJ software to enhance readability. (A) image at 18 mm from the electrode. (B) image at 10 mm from the electrode. (C) image at 2 mm from the electrode. Scale bar = 200 μm.

After 7 days of differentiation, DPSC were covering the pSi surface completely. Whole immunofluorescence staining analysis showed a distribution of ALP with 2 maxima: one on flat Si and one in the central zone of the gradients (corresponding to pores diameter = 37 ± 18 nm), as shown in Figure 5.15.

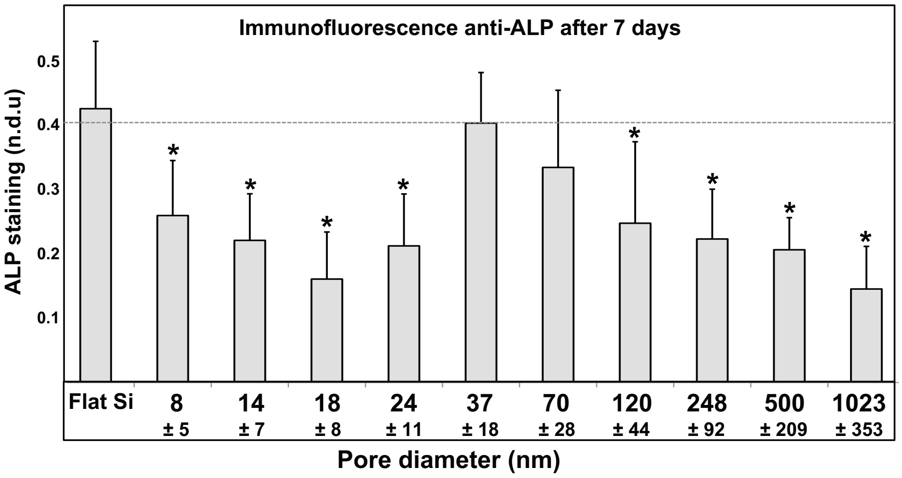

Figure 5.15: Quantification of ALP expression, assessed by Immunofluorescence. Data were normalized to the cell number on each area. (*) indicates a statistically significant difference compared to the ALP staining for the 37 nm pores ($p < 0.05$).

5.3.4.2 Type 1 Collagen staining after 21 days

After 3 weeks of cell culture in osteogenic medium, we assessed cell differentiation and corresponding collagen extra cellular matrix formation by immunofluorescence. Representative images of immunofluorescence staining for type 1 Collagen are shown in Figure 5.16.

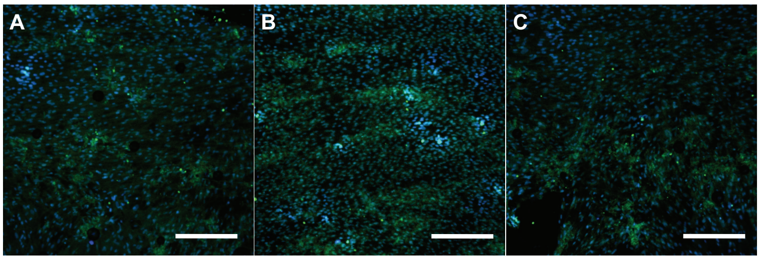

Figure 5.16: Representative confocal microscopy images of DPSC after 21 days in osteogenic medium. Nuclei are stained with Hoechst 33342 (blue staining) and type 1 Collagen is stained with FITC-conjugated antibodies (green staining). Distance from electrode: (A) 18 mm, (B) 10 mm, (C) 2 mm. Scale bar = 400 µm.

After 3 weeks, cells were still covering completely the surface of the pSi gradients. The analysis of immunofluorescence staining showed again 2 maxima for collagen expression: one on flat Si and one in the central zone of the gradients (pores diameter ranging from 24 to 120 nm). These results are presented in Figure 5.17.

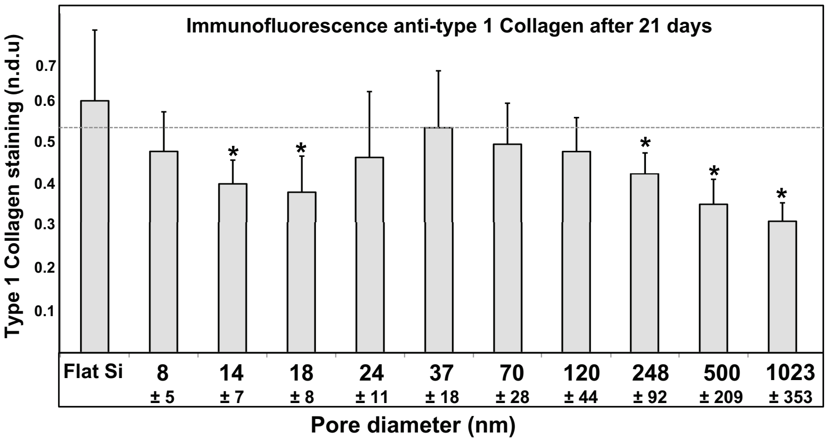

Figure 5.17: Quantification of type 1 Collagen expression, assessed by Immunofluorescence. Data were normalized to the cell number on each area. (*) indicates a statistically significant difference compared to the type 1 Collagen staining for the 37 nm pores ($p < 0.05$).

5.3.4.3 FTIR microscopy: PO_4 quantification

After 21 days in osteogenic medium, DPSC osteodifferentiation along the pSi gradients was assessed with infrared spectroscopy (FTIR). Spectra acquisitions were performed with a microscope that scanned the whole surface of the pSi gradients, permitting to create a mapping of the surface. Figure 5.18 shows single representative FTIR spectra corresponding to various stages of the pSi gradients (freshly prepared scaffold). On bare scaffolds (pSi gradients before any cell experiment), we described 3 main peaks. The major one (between 1070 to 1090 cm^{-1}) corresponds to asymetric stretching of Si-O-Si groups. Its usual wavenumber have been described between 1000 to 1100 cm^{-1}, according to the crystal phase of silicon dioxide (Pisciella *et al.*, 2005), and as pSi is a crystalline material, this peaks was found here to be closer to 1100 cm^{-1}. The second peak, at 810 cm^{-1}, corresponds to symetric stretching of Si-O-Si groups. The third peak, at 1250 cm^{-1}, represents C-N stretching that corresponds to APTES grafting on the pSi surface.

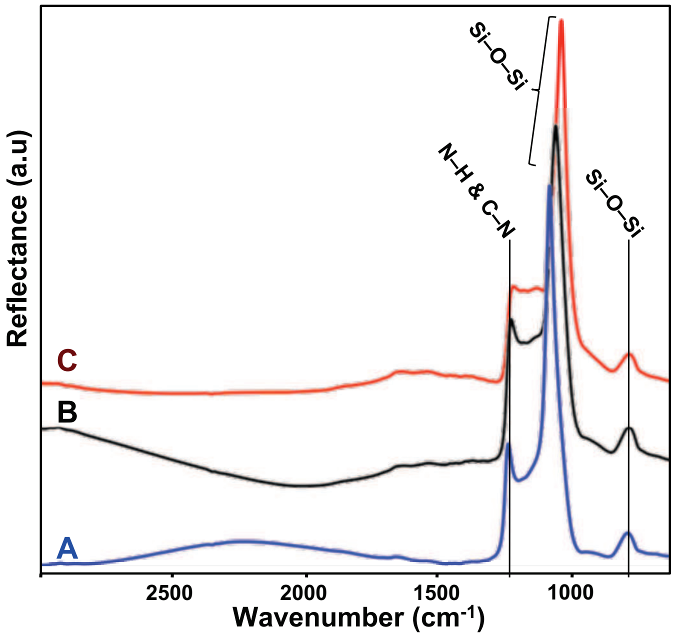

Figure 5.18: Typical FTIR spectra of bare pSi from various positions on the gradients. (A) Spectrum on smaller pores (18 mm from the electrode). (B) Spectrum in the middle of the gradient (10 mm from the electrode). (C) Spectrum on larger pores (4 mm from the electrode). Si-O-Si bands come from the pSi scaffold and the siloxane bound to APTES. C-N band comes from APTES.

Figure 5.19 shows single representative FTIR spectra corresponding to various stages of the pSi gradients after 3 weeks of cell differentiation. The spectra obtained portrayed two phosphate (P–O) peaks: one band at 960 cm^{-1} and one well-defined intense band at 1025 cm^{-1}, corresponding to symetric and asymetric P–O stretching, respectively. The Si–O–Si band at 1070 cm^{-1} is hardly distinguished from the P–O band. Concerning proteins peaks, several absorption bands were present, corresponding to carbonate bands (at 870 cm^{-1}, 1420 cm^{-1} and 1445 cm^{-1}) and amide bands (C–N and C=O vibrations at 1250 cm^{-1}, 1420 cm^{-1}, 1445 cm^{-1}, 1540 cm^{-1} and 1650 cm^{-1}) with the most intense peak at 1650 cm^{-1} (Figueiredo *et al.*, 2012) (Collart Dutilleul *et al.*, 2013). Vibration bands and corresponding molecules are presented in table 5.2.

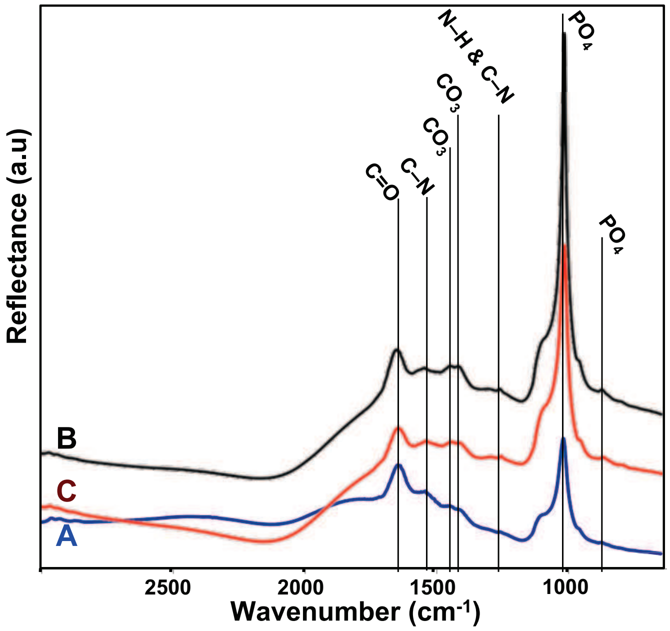

Figure 5.19: Typical FTIR spectra of bare pSi from various positions on the gradients, showing the vibrational assignments of the most significant bands. (A) Spectrum on smaller pores (18 mm from the electrode). (B) Spectrum in the middle of the gradient (10 mm from the electrode). (C) Spectrum on larger pores (4 mm from the electrode).

Wavenumber	*Vibration modes*
1650 cm^{-1}	C = O stretching (Amide I)
1540 cm^{-1}	C – N stretching (Amide II)
1445 cm^{-1}	CO_3 asym. stretching
1420 cm^{-1}	CO_3 sym. stretching
1250 cm^{-1}	N – H bending C – N stretching (Amide III)
1100 – 1070 cm^{-1}	Si – O – Si asym. stretching
1025 cm^{-1}	PO_4 asym. stretching
960 cm^{-1}	PO_4 sym. stretching
870 cm^{-1}	CO_3 bending
810 cm^{-1}	Si – O – Si sym. stretching

Table 5.2: Band assignments for the FTIR spectra recovered for pSi, with or without DPSC. Data collected from Pisciella *et al.* (2005), Toworfe *et al.* (2006), Low *et al.* (2010), Figueiredo *et al.* (2012) and Collart Dutilleul *et al.* (2013).

Because most of the bands of the spectra are composed of several spectral components, we used deconvolution methods and curve fitting for specific protein and phosphate bands. Thus, from the recorded spectra, we are able to discriminate which part was due to proteins, pSi scaffold or phosphate. We could focus on specific region of interest to compare the amount of protein and phosphate at each stage of the gradients, as FTIR data are most commonly used for comparison purposes (between areas of the same sample) rather than in absolute terms. Representative spectra with deconvolution are shown in figure 5.20 (next page). To assess cell differentiation, and we selected the area ranging from 960 to 1025 cm^{-1} for phosphate, to discriminate the Si-O-Si bands, and the area ranging from 1250 to 1650 cm^{-1} for proteins.

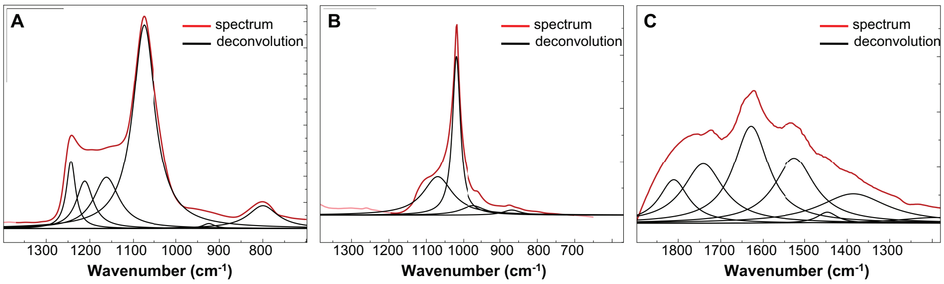

Figure 5.20: FTIR spectra and deconvolution. (A) Bare pSi spectrum, with a major peak at 1070 cm-1. (B) Region corresponding to phosphate; pSi scaffold with cells after 21 days of incubation; the major peak is at 1025 cm-1. (C) Region corresponding to proteins; pSi scaffold with cells after 21 days of incubation.

To assess the amount of proteins and phosphate on the pSi gradients surface, we scanned the whole surface of the gradients with the microscope, and acquired FTIR spectra at 96 different spots (Figure 5.21).

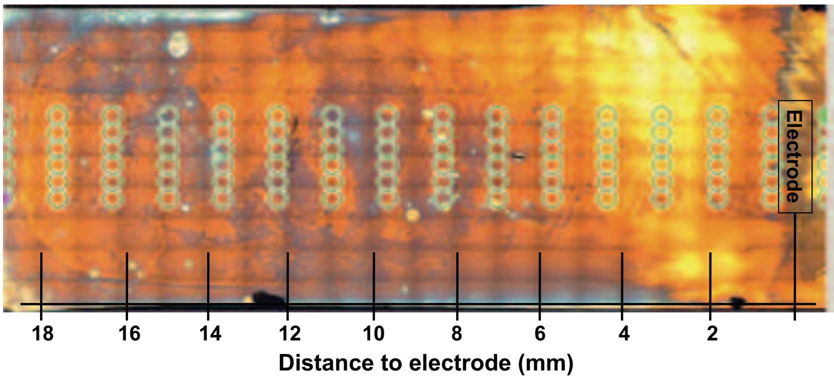

Figure 5.21: Top view of a pSi gradient after 3 weeks in OM: screening of the surface along the pSi gradients. Each circle represents a spot where FTIR spectra were acquired.

From the FTIR spectra, we selected the area ranging from 960 to 1025 cm^{-1} for phosphate and from 1250 to 1650 cm^{-1} for proteins, and we created a 3D graph representing the amount of proteins and the amount of phosphate on the different regions of the gradients. The proteins distribution was quite homogeneous on the whole gradients, indicating that we had a regular cell density along the gradient after 21 days, with cells covering all surface (Figure 5.22). The phosphate distribution revealed a maximum in the middle of the gradients, in the area at 8 to 10 mm from the electrode (pores diameter ranging from 37 to 70 nm) (Figure 5.23).

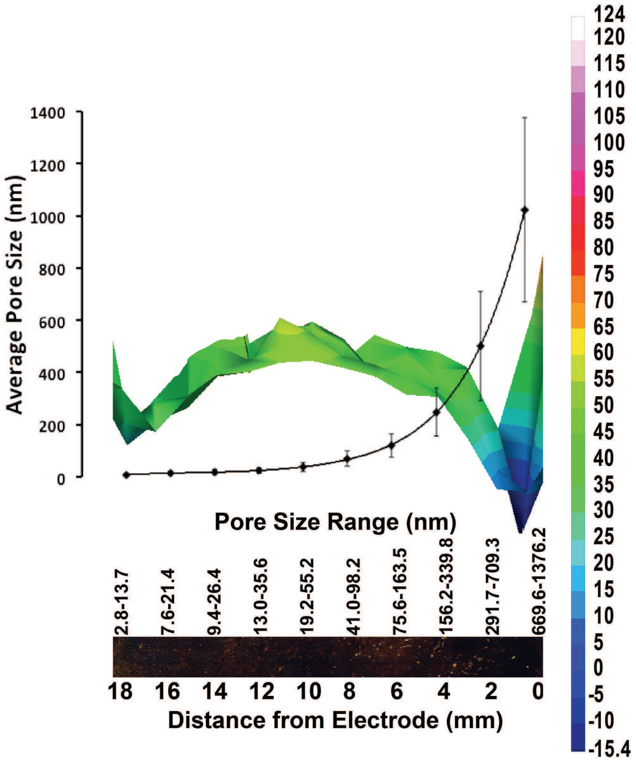

Figure 5.22: Reconstructed 3D image of the 1250 to 1650 cm^{-1} peaks distribution: presence of proteins along the gradient, indicating that cells were covering the whole gradient.

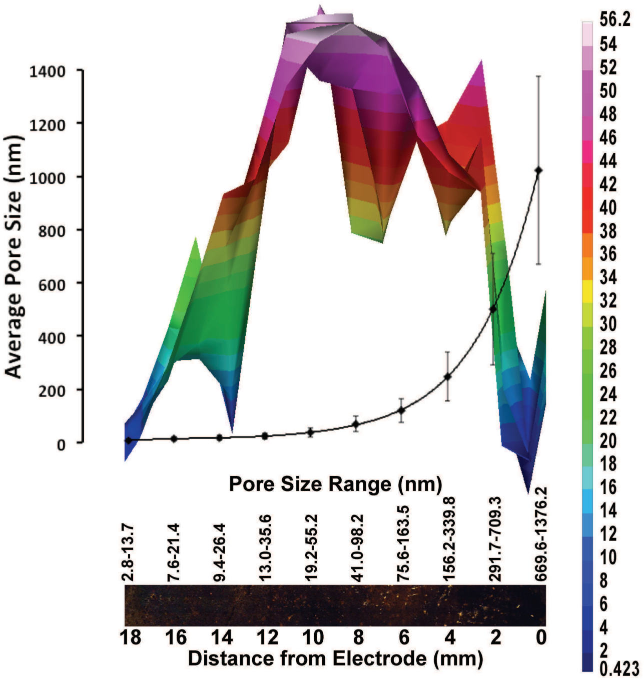

Figure 5.23: Reconstructed 3D image of the 960 to 1025 cm^{-1} peaks distribution, showing that the amount of phosphate deposition is maximized on the middle of the gradient.

5.4 Discussion

In this work asymmetric anodization give gradient of porosity used to study the influence of topography (pores diameter) on cell behavior. The dispersion of pore sizes, was consistent with other published studies (Collins *et al.*, 2002) (Clements *et al.*, 2012) from few nanometer to 1 µm. Upon thermal oxidation, the surface chemistry of the pSi is similar to the chemistry of glass, and glass is a common surface for cell culture studies (Khung *et al.*, 2008). However, after thermal oxidation, pSi gradients were not stable enough to support cell growth for more than 3 to 5 days. Surface treatment by silanization (grafting of APTES) stabilized the scaffolds and allowed long-term cell growth.

5.4.1 DPSC adhesion and spreading according to pores diameter

It has been described that porosity played a regulatory role in determining cell spreading and migration by changing the access to the binding sites on the substrate (Miron-Mendoza *et al.*, 2010). Cytoskeleton staining and fluorescence microscopy showed that DPSC adhered and spread well on smaller pores while they were round or less spread on larger pores. In the middle of the gradient (pores diameter = 37 ± 18 nm) cell spreading was enhanced compared to regions with smaller or larger pores. This pores diameter increase cell organization as assessed by cell spreading and corresponds to biological structures in human body, such as the pore size recovered in glomerular basement membrane (Gagliardini *et al.*, 2010) or the gap region between collagen fibrils in type 1 collagen (Shoulders *et al.*, 2009).

To evaluate the role of adhesion molecules in nanopores-induced cell attachment and further focal adhesion formation, immunostaining specific to vinculin was performed. Vinculin is an integrin that supports adhesion to the ECM, stabilizes protrusions through structural connections by bridging focal adhesions to the cytoskeleton, and activate migration-related signaling molecules (Huttenlocher *et al.*, 2011). Mature focal adhesions were recovered on flat Si and pSi with pores diameters $\leq$ 70 nm, while they were hardly visible on larger pores (Figure 5.9). These findings are in accordance with a recently published study investigating the effects of pores on the growth and function of fibroblasts (Pan *et al.*, 2013). They evaluated fibroblast growth on a stainless steel porous material with pores ranging from 40 to 210 nm: vinculin was widely distributed within cells grown on flat surfaces and the on 40 and 75 nm nanopores surfaces and decreased in cells grown on 185 and 210 nm nanopores surfaces. Focal adhesion, cell spreading and subsequent proliferation are closely related to the surface characteristics, even though the detailed mechanics through which the geometry and size of pores enhance cell attachment and proliferation are still unclear (Zhu *et al.*, 2004). We hypothesize that nanopores may affect cell adhesion by promoting an interaction between vinculin/integrin anchoring sites and the edges of pores for cell attachment. Thus, focal adhesions that were formed on pSi with pores >70 nm were aberrant, whereas we recovered mature focal adhesions on pores $\leq$ 70 nm. This hypothesis is supported by previous studies reporting that focal adhesions were enhanced when cells were cultured on pore surfaces with critical feature sizes smaller than 50 nm (Hu *et al.*, 2011) and the negative cellular response on larger pores up to 70 nm was ascribed to a lack of effective integrin clustering, which therefore inhibits the formation of focal adhesions and actin fibre networks (Huang *et al.*, 2009).

As we clearly demonstrated higher adhesion and spreading on pores ranging from 20 to 50 nm, we investigated cell spreading on this specific region by AFM. Long and thin filopodia growing from the cell body were observed, with size related to pores diameter. Cells attach to and pull on the matrix through focal adhesion and cytoskeleton during migration and filopodia act as cellular tentacles (Mattila *et al.*, 2008). It has been found that actin-dependent retraction of the filopodia occurred with discrete steps with an average size of 36 ± 13 nm with a myosin motor involved (Kress *et al.*, 2007). Therefore we could hypothesize that cell adhesion and spreading was more efficient on 20-50 nm pores than on smaller pores due to the correspondence with filopodia retraction steps: at each retraction step, the integrin-binding complexes are displaced from a pore edge to the next edge, to form more easily a mature focal adhesion.

5.4.2 DPSC proliferation

The highest rate of proliferative cells (BrdU positive cells) was recovered in the middle of the gradient, on the region with 37 ± 18 nm. The correlation of the switch between the proliferation and differentiation programs and the maturation of the focal adhesion remains to be fully elucidated (Bacakova *et al.*, 2011). Considering the important role of integrin-mediated focal adhesion and intracellular signaling in anchorage-dependent cell function, a previous study evaluated the influence of nanoscale pit texture. This study suggested that nanostructured physical signals could regulate cell function (Lim *et al.*, 2007). Thus, we assume that the mature focal adhesions and higher cell spreading recovered for pores ranging from 20 to 50 nm led to a higher cell proliferation in this region, by favoring cell function.

5.4.3 DPSC osteodifferentiation on pSi gradients

After 3 weeks in osteogenic medium, DPSC gradually differentiated into osteoblast-like cells. ALP staining revealed that DPSC differentiated earlier on 37 ± 18 nm pores. High cell density might increase the availability of secreted bioactive molecules and result in higher differentiation potential (Tang *et al.*, 2010) and this is in this region that higher spreading and cell density was noted (see previous sections). However initial cell density was similar after 3 days on flat Si and pSi with pores diameter < 70 nm and this shows that differences of osteodifferentiation are due to pore diameter. Collagen immunostaining and calcium phosphate accumulation confirmed the enhanced osteodifferentiation on the 37 ± 18 nm pores.

Chapter 6 General discussion and perspectives

6.1 General discussion

Regenerative medicine, and more specifically tissue engineering, is based on the use of cells preferably stem cells, bioactive molecules and scaffolds. Designing a material that induces a favorable response for stem cells is important in biomaterials research. In the thesis, short-term and long-term performances of human MSC from the dental pulp on porous silicon fabricated by electrochemical etching were investigated. Dental Pulp Stem Cells have been extensively studied *in vitro* and *in vivo* and they represent a promising source of stem cells. This is because they are easily accessible when a tooth is extracted, without any supplementary invasive procedures or ethical issues. We developed an efficient stem cell recovery system where porous silicon scaffolds supported DPSC adhesion, proliferation, and viability while at the same time functionalization with APTES and semicarbazide allowed for enhanced cell adhesion and early proliferation. Semicarbazide treatment led to a highly resorbable scaffold while APTES-treated pSi was stable for long-term culture. Stem cell based tissue engineering is considered according to two strategies: *in vitro* expansion and differentiation before grafting, or immediate grafting of the cell-scaffold complex. The two-studied functionalization permitted to address the two strategies.

In addition, we cultured DPSC on pSi surfaces for a period of 3 weeks to investigate the long-term effect of silicon nano-architecture on their osteogenic potential. Cells cultured on pSi surfaces demonstrated higher ALP activity, suggesting a faster osteodifferentiation compared to flat Si. Furthermore, the calcium and phosphorous concentrations were higher compared to flat Si, confirming that DPSC differentiated faster and produced more mineralized matrix. This enhanced differentiation was attributed to silicic acid release and porous structure: silicic acid induced a faster cell differentiation and the porous surface enhanced CaP nucleation compared to flat surface (higher CaP deposits even without cells).

In order to demonstrate the influence of pore size, we used pSi gradients as a screening tool. We investigated short-term DPSC attachment, spreading, proliferation and further differentiation on these gradients of porosity. This investigation aimed to design biomaterials with optimal porosity, able to enhance DPSC adhesion and guide their differentiation. We demonstrated that pSi with pores ranging from 20 to 50 nm enhanced cell adhesion, proliferation and osteodifferentiation. Unlike the belief that biological mineralization is mainly cell mediated, we demonstrated that nanoporosity was of primary importance for CaP nucleation, with or without osteoblast-like cells. Without cells, the maximum amounts of Ca and P deposits were recovered on the areas with pores diameter ranging from 8 ± 5 nm to 14 ± 7 nm. With DPSC, the pores diameter of 37 ± 18 nm led to the highest osteodifferentiation and mineralized matrix formation. ACP nucleation started with nanometer-sized CaP complexes, and these prenucleation clusters aggregated to form amorphous calcium phosphate, such as OCP. We hypothesized that pSi with 37 ± 18 nm pores favor ACP transformation and crystal growth during extra cellular matrix formation.

This research showed that tuned pSi scaffolds had a significant influence on the DPSC differentiation into mature osteoblast-like cells and on the kinetics of mineralization. Stem cell performance could be significantly improved using controlled nano-topography. These pSi scaffolds showed interesting potential applications in biomedicine: the nanoscale pore surfaces were able to influence the expression of integrin molecules and directed cell behaviors such as spreading, proliferation and focal adhesion formation. Silicic acid release and nano-patterned surfaces enhanced DPSC differentiation and induced calcium phosphate deposits to nucleate *in vitro*, thus promoting biomineralization process.

The complex mechanisms of calcification remain partially unknown but our results suggest that pSi could improve bonding between grafted biomaterial and tissue *in vivo*. However, the *in vivo* situation is probably much more complex than suggested by the *in vitro* experiments. The problem of Ca and PO_4 delivery to the mineralization front, the grafted stem cell survival, the scaffolds degradation kinetics and the possibility to use pSi as a drug delivery carrier are all issues that should be studied in *in vivo* models.

6.2 Perspectives

Stem cell therapies represent a new approach for the treatment of various diseases. Mesenchymal stem cells can operate through many different mechanisms and have generated great therapeutic expectations. However, their use is limited by the way to bring cells to the site of interest. When directly injected to the injured site, it is difficult to evaluate if cells remain in the correct site. When injected intravenously, cells cannot be followed and directed to their target site, with the risk of being stuck in pulmonary capillary vessels. Thus, it is admitted that tissue engineering requires a scaffold to carry cells to the injured site. The principle of bone tissue engineering is the fabrication of a complex (scaffold and stem cells) that matches the physical and biological properties of the natural bone tissue, without the disadvantages of autologous or allogenic bone grafts. Mesenchymal stem cells represent an advantageous source of stem cells for tissue regeneration, due to their favorable properties (regeneration of damaged tissues, minimal donor-site morbidity and low risk of autoimmune rejection). As biomaterial, pSi has been successfully investigated *in vitro* and hold promises for biomedical applications. Its compatibility and degradation have been already assessed *in vivo*. This biomaterial has now to be tested *in vivo* to carry stem cells for regenerative medicine, as chips, microparticles or nanoparticles. The porous structure allows the loading of the scaffold with bioactive molecules, and the optical properties permit to follow the grafted complex *in vivo*. Further loading with iron nanoparticles could even permit live tissue imaging of the grafted complex with magnetic resonance imaging or confocal Raman microscopy.

. References

1. Agrawal AA, BJ Nehilla, KV Reisig, TR Gaborski, DZ Fang, CC Striemer, PM Fauchet and JL McGrath (2010). Porous nanocrystalline silicon membranes as highly permeable and molecularly thin substrates for cell culture. Biomaterials 31: 5408–5417.

2. Ainslie KM, SL Tao, KC Popat and TA Desai (2008). In vitro immunogenicity of silicon-based micro- and nanostructured surfaces. ACS Nano 2: 1076–1084.

3. Alge DL, D Zhou, LL Adams, BK Wyss, MD Shadday, EJ Woods, TM Gabriel Chu and WS Goebel (2010). Donor-matched comparison of dental pulp stem cells and bone marrow-derived mesenchymal stem cells in a rat model. J Tissue Eng Regen Med 4: 73–81.

4. Alvarez SD, AM Derfus, MP Schwartz, SN Bhatia and MJ Sailor (2009). The compatibility of hepatocytes with chemically modified porous silicon with reference to in vitro biosensors. Biomaterials 30: 26–34.

5. Anglin E, L Cheng, WR Freeman and MJ Sailor (2008). Porous silicon in drug delivery devices and materials. Adv Drug Deliv Rev 60: 1266–1277.

6. Arthur A, G Rychkov, S Shi, SA Koblar and S Gronthos (2008). Adult human dental pulp stem cells differentiate toward functionally active neurons under appropriate environmental cues. Stem Cells 26: 1787–1795.

7. Arvidson K, BM Abdallah, LA Applegate, N Baldini, E Cenni, E Gomez-Barrena, D Granchi, M Kassem, YT Konttinen, K Mustafa, DP Pioletti, T Sillat and A Finne-

Wistrand (2011). Bone regeneration and stem cells. J Cell Mol Med 15: 718–746.

8. Atari M, C Gil-Recio, M Fabregat, D García-Fernández, M Barajas, MA Carrasco, H-S Jung, FH Alfaro, N Casals, F Prosper, E Ferrés-Padró and L Giner (2012). Dental pulp of the third molar: a new source of pluripotent-like stem cells. J Cell Sci 125: 3343–3356.

9. Bacakova L, E Filova, M Parizek, T Ruml and V Svorcik (2011). Modulation of cell adhesion, proliferation and differentiation on materials designed for body implants. Biotechnol Adv 29: 739–767.

10. Bakopoulou A, G Leyhausen, J Volk, A Tsiftsoglou, P Garefis, P Koidis and W Geurtsen (2011). Assessment of the impact of two different isolation methods on the osteo/odontogenic differentiation potential of human dental stem cells derived from deciduous teeth. Calcif Tissue Int 88: 130–141.

11. Bakopoulou A, G Leyhausen, J Volk, A Tsiftsoglou, P Garefis, P Koidis and W Geurtsen (2011). Comparative analysis of in vitro osteo/odontogenic differentiation potential of human dental pulp stem cells (DPSCs) and stem cells from the apical papilla (SCAP). Arch Oral Biol.

12. Barbara Z, B Eriberto, S Stefano, B Giulia, G Chiara, N Ferrarese, F Letizia and S Edoardo (2011). Dental Pulp Stem Cells and Tissue Engineering Strategies for Clinical Application on Odontoiatric Field. In Biomaterials Science and Engineering, Pignatello, R, ed. (InTech).

13. Beniash E, RA Metzler, RSK Lam and PUPA Gilbert (2009). Transient amorphous calcium phosphate in forming enamel. J Struct Biol 166: 133–143.

14. Bessa PC, M Casal and RL Reis (2008). Bone morphogenetic proteins in tissue engineering: the road from laboratory to clinic, part II (BMP delivery). J Tissue Eng Regen Med 2: 81–96.

15. Bianco P, M Riminucci, S Gronthos and PG Robey (2001). Bone marrow stromal stem cells: nature, biology, and potential applications. Stem Cells 19: 180–192.

16. Biggs MJP, RG Richards and MJ Dalby (2010). Nanotopographical modification: a regulator of cellular function through focal adhesions. Nanomedicine 6: 619–633.

17. Buxboim A, IL Ivanovska and DE Discher (2010). Matrix elasticity, cytoskeletal forces and physics of the nucleus: how deeply do cells "feel" outside and in? J Cell Sci 123: 297–308.

18. Campion CR, SL Ball, DL Clarke and KA Hing (2013). Microstructure and chemistry affects apatite nucleation on calcium phosphate bone graft substitutes. J Mater Sci Mater Med 24: 597–610.

19. Canham LT (1995). Bioactive silicon structure fabrication through nanoetching techniques. Adv Mater 7: 1033–1037.

20. Canham LT and CL Reeves (1995). Apatite Nucleation on Low Porosity Silicon in Acellular Simulated Body Fluids. MRS Proc 414: 189.

21. Canham LT, CL Reeves, A Loni, MR Houlton, JP Newey, AJ Simons and TI Cox (1997). Calcium phosphate nucleation on porous silicon: factors influencing kinetics in acellular simulated body fluids. Thin Solid Films 297: 304–307.

22. Canham LT, CL Reeves, DO King, PJ Branfield, JG Crabb and MCL Ward (1996). Bioactive polycrystalline silicon. Adv Mater 8: 850–852.

23. Cao D, Y-P Wu, Z-F Fu, Y Tian, C-J Li, C-Y Gao, Z-L Chen and X-Z Feng (2011). Cell adhesive and growth behavior on electrospun nanofibrous scaffolds by designed multifunctional composites. Colloids Surf B Biointerfaces 84: 26–34.

24. Carlisle EM (1972). Silicon: an essential element for the chick. Science 178: 619–621.

25. Carlisle EM (1988). Silicon as a trace nutrient. Sci Total Environ 73: 95–106.

26. Cavalcanti-Adam EA, T Volberg, A Micoulet, H Kessler, B Geiger and JP Spatz (2007). Cell spreading and focal adhesion dynamics are regulated by spacing of integrin ligands. Biophys J 92: 2964–2974.

27. Chadwick EG, OM Clarkin and DA Tanner (2010). Hydroxyapatite formation on metallurgical grade nanoporous silicon particles. J Mater Sci 45: 6562–6568.

28. Chayen NE, E Saridakis and RP Sear (2006). Experiment and theory for heterogeneous nucleation of protein crystals in a porous medium. Proc Natl Acad Sci USA 103: 597–601.

29. Chayen NE, E Saridakis, R El-Bahar and Y Nemirovsky (2001). Porous silicon: an effective nucleation-inducing material for protein crystallization. J Mol Biol 312: 591–595.

30. Cheng L, E Anglin, F Cunin, D Kim, MJ Sailor, I Falkenstein, A Tammewar and WR Freeman (2008). Intravitreal properties of porous silicon photonic crystals: a potential self-reporting intraocular drug-delivery vehicle. Br J Ophthalmol 92: 705–711.

31. Clements LR, P-Y Wang, W-B Tsai, H Thissen and NH Voelcker (2012). Electrochemistry-enabled fabrication of orthogonal nanotopography and surface chemistry gradients for high-throughput screening. Lab Chip 12: 1480–1486.

32. Coffer J, M Whitehead and D Nagesha (2005). Porous silicon-based scaffolds for tissue engineering and other biomedical applications. Phys Stat Sol (a) 202: 1451–1455.

33. Coffinier Y, C Olivier, A Perzyna, B Grandidier, X Wallart, JO Durand, O Melnyk and D Stiévenard (2005). Semicarbazide-Functionalized Si(111) Surfaces for the Site-Specific Immobilization of Peptides. Langmuir 21: 1489–1496.

34. Collart Dutilleul P-Y, D Deville de Périère, FJ Cuisinier, F Cunin and C Gergely (2014). Porous Silicon for Biomedical Applications. In H Santos, Woodhead Pub Limited, Cambridge, UK. 486-506.

35. Collart Dutilleul P-Y, C Thonat, P Jacquemart, F Cuisinier, B Levallois and F Chaubron (2012). [Dental pulp stem cells: characteristics, cryopreservation and therapeutic potentialities]. Orthod Fr 83: 209–216.

36. Collart Dutilleul P-Y, CG Fonseca, L Zimányi, O Romieu, AJ Pozos-Guillén, V Semetey, F Cuisinier, E Pérez and B Levallois (2013). Root canal hydrophobization by dentinal silanization: Improvement of silicon-based endodontic treatment tightness. J Biomed Mater Res Part B Appl Biomater 101: 721–728.

37. Collart-Dutilleul PY, E Secret, I Panayotov, C Gergely, F Cunin and FJG Cuisinier (2012). Human Dental Pulp Stem Cells Growth And Osteodifferentiation On Porous Resorbable Scaffolds. Bull Group Int Rech Sci Stomatol Odontol 51: e03–e04.

38. Collins BE, K Dancil, G Abbi and MJ Sailor (2002). Determining Protein Size Using an Electrochemically Machined Pore Gradient in Silicon. Adv Func Mater 12: 187–191.

39. Connolly JF, R Guse, J Tiedeman and R Dehne (1991). Autologous marrow injection as a substitute for operative grafting of tibial nonunions. Clin Orthop Relat Res 259–270.

40. Coppe C, Y Zhang and PK Den Besten (2009). Characterization of primary dental pulp cells in vitro. Pediatr Dent 31: 467–471.

41. Cölfen H (2010). Biomineralization: A crystal-clear view. Nat Mater 9: 960–961.

42. Cuisinier FJG, P Steuer, A Brisson and J-C Voegel (1995). High resolution electron microscopy study of crystal growth mechanisms in chicken bone composites. J Cryst Growth 156: 443–453.

43. d'Aquino R, A De Rosa, G Laino, F Caruso, L Guida, R Rullo, V Checchi, L Laino, V Tirino and G Papaccio (2009). Human dental pulp stem cells: from biology to clinical applications. J Exp Zool B Mol Dev Evol 312B: 408–415.

44. d'Aquino R, A De Rosa, V Lanza, V Tirino, L Laino, A Graziano, V Desiderio, G Laino and G Papaccio (2009). Human mandible bone defect repair by the grafting of dental pulp stem/progenitor cells and collagen sponge biocomplexes. Eur Cell Mater 18: 75–83.

45. d'Aquino R, A Graziano, M Sampaolesi, G Laino, G Pirozzi, A De Rosa and G Papaccio (2007). Human postnatal dental pulp cells co-differentiate into osteoblasts and endotheliocytes: a pivotal synergy leading to adult bone tissue formation. Cell Death Differ 14: 1162–1171.

46. Dalby MJ, MO Riehle, SJ Yarwood, CDW Wilkinson and ASG Curtis (2003). Nucleus alignment and cell signaling in fibroblasts: response to a micro-grooved topography. Exp Cell Res 284: 274–282.

47. Dalby MJ, N Gadegaard, R Tare, A Andar, MO Riehle, P Herzyk, CDW Wilkinson and ROC Oreffo (2007). The control of human mesenchymal cell differentiation using nanoscale symmetry and disorder. Nat Mater 6: 997–1003.

48. Dey A, PHH Bomans, FA Müller, J Will, PM Frederik, G de With and NAJM Sommerdijk (2010). The role of prenucleation clusters in surface-induced calcium phosphate crystallization. Nat Mater 9: 1010–1014.

49. Diao Y, AS Myerson, TA Hatton and BL Trout (2011). Surface design for controlled crystallization: the role of surface chemistry and nanoscale pores in heterogeneous nucleation. Langmuir 27: 5324–5334.

50. Dominici M, K Le Blanc, I Mueller, I Slaper-Cortenbach, F Marini, D Krause, R Deans, A Keating, D Prockop and E Horwitz (2006). Minimal criteria for defining multipotent mesenchymal stromal cells. The International Society for Cellular

Therapy position statement. Cytotherapy 8: 315–317.

51. Dorozhkin SV (2010). Amorphous calcium (ortho)phosphates. Acta Biomaterialia 6: 4457–4475.

52. El-Ghannam A and CQ Ning (2006). Effect of bioactive ceramic dissolution on the mechanism of bone mineralization and guided tissue growth in vitro. J Biomed Mater Res A 76: 386–397.

53. Engler AJ, S Sen, HL Sweeney and DE Discher (2006). Matrix elasticity directs stem cell lineage specification. Cell 126: 677–689.

54. Fan D, GR Akkaraju, EF Couch, LT Canham and JL Coffer (2011). The role of nanostructured mesoporous silicon in discriminating in vitro calcification for electrospun composite tissue engineering scaffolds. Nanoscale 3: 354–361.

55. Faucheux N, R Schweiss, K Lützow, C Werner and T Groth (2004). Self-assembled monolayers with different terminating groups as model substrates for cell adhesion studies. Biomaterials 25: 2721–2730.

56. Fawzy El-Sayed KM, S Paris, ST Becker, M Neuschl, W De Buhr, S Sälzer, A Wulff, M Elrefai, MS Darhous, M El-Masry, J Wiltfang and CE Dörfer (2012). Periodontal regeneration employing gingival margin-derived stem/progenitor cells: an animal study. J Clin Periodontol 39: 861–870.

57. Figueiredo MM and J Gamelas (2012). Characterization of Bone and Bone-Based Graft Materials Using FTIR Spectroscopy. Infrared Spectroscopy- ….

58. Forraz N and CP McGuckin (2011). The umbilical cord: a rich and ethical stem cell source to advance regenerative medicine. Cell Prolif 44 Suppl 1: 60–69.

59. Frith JE, RJ Mills and JJ Cooper-White (2012). Lateral spacing of adhesion peptides influences human mesenchymal stem cell behaviour. J Cell Sci 125: 317–327.

60. Gagari E, MK Rand, L Tayari, H Vastardis, P Sharma, PV Hauschka and PD Damoulis (2006). Expression of stem cell factor and its receptor, c-kit, in human oral mesenchymal cells. Eur J Oral Sci 114: 409–415.

61. Gagliardini E, S Conti, A Benigni, G Remuzzi and A Remuzzi (2010). Imaging of the porous ultrastructure of the glomerular epithelial filtration slit. J Am Soc Nephrol 21: 2081–2089.

62. Gandía C, A Armiñán, JM García-Verdugo, E Lledó, A Ruiz, MD Miñana, J Sanchez-Torrijos, R Payá, V Mirabet, F Carbonell-Uberos, M Llop, JA Montero and P Sepúlveda (2008). Human dental pulp stem cells improve left ventricular function, induce angiogenesis, and reduce infarct size in rats with acute myocardial infarction. Stem Cells 26: 638–645.

63. Gebauer D, A Völkel and H Cölfen (2008). Stable prenucleation calcium carbonate clusters. Science 322: 1819–1822.

64. Gentile F, R La Rocca, G Marinaro, A Nicastri, A Toma, F Paonessa, G Cojoc, C Liberale, F Benfenati, E di Fabrizio and P Decuzzi (2012). Differential Cell Adhesion on Mesoporous Silicon Substrates. ACS Appl Mater Interfaces 4: 2903–2911.

65. Giuliani A, A Manescu, M Langer, F Rustichelli, V Desiderio, F Paino, A De Rosa, L Laino, R d'Aquino, V Tirino and G Papaccio (2013). Three years after transplants in human mandibles, histological and in-line holotomography revealed that stem cells regenerated a compact rather than a spongy bone: biological and clinical implications. Stem Cells Transl Med 2: 316–324.

66. González-Muñoz MJ, A Peña and I Meseguer (2008). Role of beer as a possible protective factor in preventing Alzheimer's disease. Food Chem Toxicol 46: 49–56.

67. Gordon MY, N Levicar, M Pai, P Bachellier, I Dimarakis, F Al-Allaf, H M'Hamdi, T Thalji, JP Welsh, SB Marley, J Davies, F Dazzi, F Marelli-Berg, P Tait, R Playford, L Jiao, S Jensen, JP Nicholls, A Ayav, M Nohandani, F Farzaneh, J Gaken,

R Dodge, M Alison, JF Apperley, R Lechler and NA Habib (2006). Characterization and clinical application of human CD34+ stem/progenitor cell populations mobilized into the blood by granulocyte colony-stimulating factor. Stem Cells 24: 1822–1830.

68. Graziano A, R d'Aquino, G Laino, A Proto, MT Giuliano, G Pirozzi, A De Rosa, D Di Napoli and G Papaccio (2008). Human CD34+ stem cells produce bone nodules in vivo. Cell Prolif 41: 1–11.

69. Gronthos S, J Brahim, W Li, LW Fisher, N Cherman, A Boyde, P DenBesten, PG Robey and S Shi (2002). Stem cell properties of human dental pulp stem cells. J Dent Res 81: 531–535.

70. Gronthos S, M Mankani, J Brahim, PG Robey and S Shi (2000). Postnatal human dental pulp stem cells (DPSCs) in vitro and in vivo. Proc Natl Acad Sci USA 97: 13625–13630.

71. Gronthos S, SO Akintoye, C-Y Wang and S Shi (2006). Bone marrow stromal stem cells for tissue engineering. Periodontol 2000 41: 188–195.

72. Gupta G, S Kirakodu and A El-Ghannam (2010). Effects of exogenous phosphorus and silicon on osteoblast differentiation at the interface with bioactive ceramics. J Biomed Mater Res A 95: 882–890.

73. Habraken WJEM, J Tao, LJ Brylka, H Friedrich, L Bertinetti, AS Schenk, A Verch, V Dmitrovic, PHH Bomans, PM Frederik, J Laven, P van der Schoot, B Aichmayer, G de With, JJ DeYoreo and NAJM Sommerdijk (2013). Ion-association complexes unite classical and non-classical theories for the biomimetic nucleation of calcium phosphate. Nat Commun 4: 1507.

74. Hajj-Hassan M, M Khayyat-Kholghi, H Wang, V Chodavarapu and JE Henderson (2011). Response of murine bone marrow-derived mesenchymal stromal cells to dry-etched porous silicon scaffolds. J Biomed Mater Res A 99: 269–274.

75. Handschel J, C Naujoks, R Depprich, L Lammers, N Kubler, U Meyer and H-P Wiesmann (2011). Embryonic stem cells in scaffold-free three-dimensional cell culture: osteogenic differentiation and bone generation. Head & Face Medicine 7: 12.

76. Hing KA, PA Revell, N Smith and T Buckland (2006). Effect of silicon level on rate, quality and progression of bone healing within silicate-substituted porous hydroxyapatite scaffolds. Biomaterials 27: 5014–5026.

77. Horner PJ, AE Power, G Kempermann, HG Kuhn, TD Palmer, J Winkler, LJ Thal and FH Gage (2000). Proliferation and differentiation of progenitor cells throughout the intact adult rat spinal cord. J Neurosci 20: 2218–2228.

78. Houllé P, J-C Voegel, P Schultz, P Steuer and FJ Cuisinier (1997). High resolution electron microscopy: structure and growth mechanisms of human dentin crystals. J Dent Res 76: 895–904.

79. Hu J, JH Tian, J Shi, F Zhang, DL He, L Liu, DJ Jung, JB Bai and Y Chen (2011). Cell culture on AAO nanoporous substrates with and without geometry constrains. Microelectronic Engineering 88: 1714–1717.

80. Hu Y, SR Winn, I Krajbich and JO Hollinger (2003). Porous polymer scaffolds surface-modified with arginine-glycine-aspartic acid enhance bone cell attachment and differentiation in vitro. J Biomed Mater Res A 64: 583–590.

81. Huang AH-C, BR Snyder, P-H Cheng and AWS Chan (2008). Putative dental pulp-derived stem/stromal cells promote proliferation and differentiation of endogenous neural cells in the hippocampus of mice. Stem Cells 26: 2654–2663.

82. Huang GT-J, S Gronthos and S Shi (2009). Mesenchymal stem cells derived from dental tissues vs. those from other sources: their biology and role in regenerative medicine. J Dent Res 88: 792–806.

83. Huang J, SV Grater, F Corbellini, S Rinck, E Bock, R Kemkemer, H Kessler, J Ding and JP Spatz (2009). Impact of order and disorder in RGD nanopatterns on cell

adhesion. Nano Lett 9: 1111–1116.

84. Huitema LF and AB Vaandrager (2007). What triggers cell-mediated mineralization. Front Biosci 12: 2631–2645.

85. Hung C-N, K Mar, H-C Chang, Y-L Chiang, H-Y Hu, C-C Lai, R-M Chu and CM Ma (2011). A comparison between adipose tissue and dental pulp as sources of MSCs for tooth regeneration. Biomaterials 32: 6995–7005.

86. Hutmacher DW, JT Schantz, CXF Lam, KC Tan and TC Lim (2007). State of the art and future directions of scaffold-based bone engineering from a biomaterials perspective. J Tissue Eng Regen Med 1: 245–260.

87. Huttenlocher A and AR Horwitz (2011). Integrins in Cell Migration.

88. Ikeda E, K Yagi, M Kojima, T Yagyuu, A Ohshima, S Sobajima, M Tadokoro, Y Katsube, K Isoda, M Kondoh, M Kawase, MJ Go, H Adachi, Y Yokota, T Kirita and H Ohgushi (2008). Multipotent cells from the human third molar: feasibility of cell-based therapy for liver disease. Differentiation 76: 495–505.

89. Jugdaohsingh R, SHC Anderson, KL Tucker, H Elliott, DP Kiel, RPH Thompson and JJ Powell (2002). Dietary silicon intake and absorption. Am J Clin Nutr 75: 887–893.

90. Kashchiev D (2000). Nucleation Basic Theory with Applications. Butterworth Heinemann 544.

91. Kern S, H Eichler, J Stoeve, H Klüter and K Bieback (2006). Comparative Analysis of Mesenchymal Stem Cells from Bone Marrow, Umbilical Cord Blood, or Adipose Tissue. Stem Cells 24: 1294–1301.

92. Kémoun P, S Gronthos, ML Snead, J Rue, B Courtois, F Vaysse, J-P Salles and G Brunel (2011). The role of cell surface markers and enamel matrix derivatives on human periodontal ligament mesenchymal progenitor responses in vitro.

Biomaterials 32: 7375–7388.

93. Kémoun P, S Laurencin-Dalicieux, J Rue, J-C Farges, I Gennero, F Conte-Auriol, F Briand-Mesange, M Gadelorge, H Arzate, AS Narayanan, G Brunel and J-P Salles (2007). Human dental follicle cells acquire cementoblast features under stimulation by BMP-2/-7 and enamel matrix derivatives (EMD) in vitro. Cell Tissue Res 329: 283–294.

94. Khung YL, G Barritt and NH Voelcker (2008). Using continuous porous silicon gradients to study the influence of surface topography on the behaviour of neuroblastoma cells. Exp Cell Res 314: 789–800.

95. Király M, B Porcsalmy, A Pataki, K Kádár, M Jelitai, B Molnár, P Hermann, I Gera, W-D Grimm, B Ganss, A Zsembery and G Varga (2009). Simultaneous PKC and cAMP activation induces differentiation of human dental pulp stem cells into functionally active neurons. Neurochem Int 55: 323–332.

96. Kratchmarova I, B Blagoev, M Haack-Sorensen, M Kassem and M Mann (2005). Mechanism of divergent growth factor effects in mesenchymal stem cell differentiation. Science 308: 1472–1477.

97. Kress H, EHK Stelzer, D Holzer, F Buss, G Griffiths and A Rohrbach (2007). Filopodia act as phagocytic tentacles and pull with discrete steps and a load-dependent velocity. Proc Natl Acad Sci USA 104: 11633–11638.

98. Krishna OD, AK Jha, X Jia and KL Kiick (2011). Integrin-mediated adhesion and proliferation of human MSCs elicited by a hydroxyproline-lacking, collagen-like peptide. Biomaterials 32: 6412–6424.

99. Lagunas A, J Comelles, E Martínez, E Prats-Alfonso, GA Acosta, F Albericio and J Samitier (2012). Cell adhesion and focal contact formation on linear RGD molecular gradients: study of non-linear concentration dependence effects. Nanomedicine 8: 432–439.

100. Laino G, R d'Aquino, A Graziano, V Lanza, F Carinci, F Naro, G Pirozzi and G Papaccio (2005). A new population of human adult dental pulp stem cells: a useful source of living autologous fibrous bone tissue (LAB). J Bone Miner Res 20: 1394–1402.

101. Li T-S, K Hamano, M Nishida, M Hayashi, H Ito, A Mikamo and M Matsuzaki (2003). CD117+ stem cells play a key role in therapeutic angiogenesis induced by bone marrow cell implantation. Am J Physiol Heart Circ Physiol 285: H931–H937.

102. Li X, H Wang, E Touma, E Rousseau, RJ Quigg and JT Ryaby (2007). Genetic network and pathway analysis of differentially expressed proteins during critical cellular events in fracture repair. Journal of Cellular Biochemistry 100: 527–543.

103. Lim JY and HJ Donahue (2007). Cell sensing and response to micro- and nanostructured surfaces produced by chemical and topographic patterning. Tissue Eng 13: 1879–1891.

104. Lim JY, AD Dreiss, Z Zhou, JC Hansen, CA Siedlecki, RW Hengstebeck, J Cheng, N Winograd and HJ Donahue (2007). The regulation of integrin-mediated osteoblast focal adhesion and focal adhesion kinase expression by nanoscale topography. Biomaterials 28: 1787–1797.

105. Liu J, TC Jin, S Chang, A Czajka-Jakubowska and BH Clarkson (2011). Adhesion and growth of dental pulp stem cells on enamel-like fluorapatite surfaces. J Biomed Mater Res A 96: 528–534.

106. Low SP, KA Williams, LT Canham and NH Voelcker (2006). Evaluation of mammalian cell adhesion on surface-modified porous silicon. Biomaterials 27: 4538–4546.

107. Low SP, KA Williams, LT Canham and NH Voelcker (2010). Generation of reactive oxygen species from porous silicon microparticles in cell culture medium. J Biomed Mater Res A 93: 1124–1131.

108. Low SP, NH Voelcker, LT Canham and KA Williams (2009). The biocompatibility of porous silicon in tissues of the eye. Biomaterials 30: 2873–2880.

109. López-Mejías V, AS Myerson and BL Trout (2013). Geometric Design of Heterogeneous Nucleation Sites on Biocompatible Surfaces. Crystal Growth & Design 13: 3835–3841.

110. Ma T (2010). Mesenchymal stem cells: From bench to bedside. World J Stem Cells 2: 13–17.

111. Mahamid J, A Sharir, L Addadi and S Weiner (2008). Amorphous calcium phosphate is a major component of the forming fin bones of zebrafish: Indications for an amorphous precursor phase. Proc Natl Acad Sci USA 105: 12748–12753.

112. Mahamid J, B Aichmayer, E Shimoni, R Ziblat, C Li, S Siegel, O Paris, P Fratzl, S Weiner and L Addadi (2010). Mapping amorphous calcium phosphate transformation into crystalline mineral from the cell to the bone in zebrafish fin rays. Proc Natl Acad Sci USA 107: 6316–6321.

113. Mangano C, A De Rosa, V Desiderio, R d'Aquino, A Piattelli, F De Francesco, V Tirino, F Mangano and G Papaccio (2010). The osteoblastic differentiation of dental pulp stem cells and bone formation on different titanium surface textures. Biomaterials 31: 3543–3551.

114. Mann BK and JL West (2002). Cell adhesion peptides alter smooth muscle cell adhesion, proliferation, migration, and matrix protein synthesis on modified surfaces and in polymer scaffolds. J Biomed Mater Res 60: 86–93.

115. Marolt D, M Knezevic and GV Novakovic (2010). Bone tissue engineering with human stem cells. Stem Cell Res Ther 1: 10.

116. Mattila PK and P Lappalainen (2008). Filopodia: molecular architecture and cellular functions. Nat Rev Mol Cell Biol 9: 446–454.

117. Mayne A, S Bayliss and P Barr (2000). Biologically interfaced porous silicon devices. Phys Stat Sol (a) 182: 505–513.

118. Mercati F, L Pascucci, P Ceccarelli, C Dall'Aglio, V Pedini and AM Gargiulo (2009). Expression of mesenchymal stem cell marker CD90 on dermal sheath cells of the anagen hair follicle in canine species. Eur J Histochem 53: 159–166.

119. Miron-Mendoza M, J Seemann and F Grinnell (2010). The differential regulation of cell motile activity through matrix stiffness and porosity in three dimensional collagen matrices. Biomaterials 31: 6425–6435.

120. Miura M, S Gronthos, M Zhao, B Lu, LW Fisher, PG Robey and S Shi (2003). SHED: stem cells from human exfoliated deciduous teeth. Proc Natl Acad Sci USA 100: 5807–5812.

121. Monteiro BG, RC Serafim, GB Melo, MCP Silva, NF Lizier, CMC Maranduba, RL Smith, A Kerkis, H Cerruti, JAP Gomes and I Kerkis (2009). Human immature dental pulp stem cells share key characteristic features with limbal stem cells. Cell Prolif 42: 587–594.

122. Morsczeck C, W Götz, J Schierholz, F Zeilhofer, U Kühn, C Möhl, C Sippel and KH Hoffmann (2005). Isolation of precursor cells (PCs) from human dental follicle of wisdom teeth. Matrix Biol 24: 155–165.

123. Muñoz Noval A, R García, D Ruiz Casas, D Losada Bayo, V Sánchez Vaquero, V Torres Costa, RJ Martín Palma, MA García, JP García Ruiz, JJ Serrano Olmedo, JF Muñoz Negrete, F del Pozo Guerrero and M Manso Silván (2013). Design and characterization of biofunctional magnetic porous silicon flakes. Acta Biomaterialia 9: 6169–6176.

124. Ngankam PA, P Lavalle, L Szyk, G Decher, P Schaaf and FJG Cuisinier (2000). Influence of Polyelectrolyte Multilayer Films on Calcium Phosphate Nucleation. J Am Chem Soc 122: 8998–9005.

125. Noval AM, VS Vaquero, EP Quijorna, VT Costa, DG Pérez, LG Méndez, I Montero, RJM Palma, AC Font, JPG Ruiz and MM Silván (2012). Aging of porous silicon in physiological conditions: cell adhesion modes on scaled 1D micropatterns. J Biomed Mater Res A 100: 1615–1622.

126. Nudelman F, K Pieterse, A George, PHH Bomans, H Friedrich, LJ Brylka, PAJ Hilbers, G de With and NAJM Sommerdijk (2010). The role of collagen in bone apatite formation in the presence of hydroxyapatite nucleation inhibitors. Nat Mater 9: 1004–1009.

127. Orgel JPRO, TC Irving, A Miller and TJ Wess (2006). Microfibrillar structure of type I collagen in situ. Proc Natl Acad Sci USA 103: 9001–9005.

128. Pan H-A, J-Y Liang, Y-C Hung, C-H Lee, J-C Chiou and GS Huang (2013). The spatial and temporal control of cell migration by nanoporous surfaces through the regulation of ERK and integrins in fibroblasts. Biomaterials 34: 841–853.

129. Park J-H, L Gu, G von Maltzahn, E Ruoslahti, SN Bhatia and MJ Sailor (2009). Biodegradable luminescent porous silicon nanoparticles for in vivo applications. Nat Mater 8: 331–336.

130. Patla I, T Volberg, N Elad, V Hirschfeld-Warneken, C Grashoff, R Fässler, JP Spatz, B Geiger and O Medalia (2010). Dissecting the molecular architecture of integrin adhesion sites by cryo-electron tomography. Nat Cell Biol 12: 909–915.

131. Pereira MM and LL Hench (1996). Mechanisms of hydroxyapatite formation on porous gel-silica substrates. J Sol-Gel Sci Technol 7: 59–68.

132. Pisciella P and M Pelino (2005). FTIR spectroscopy investigation of the crystallisation process in an iron rich glass. Journal of the European Ceramic Society 25: 1855–1861.

133. Popat KC, K-I Chatvanichkul, GL Barnes, TJ Latempa, CA Grimes and TA Desai (2007). Osteogenic differentiation of marrow stromal cells cultured on nanoporous

alumina surfaces. J Biomed Mater Res A 80: 955–964.

134. Popplewell JF, SJ King, JP Day, P Ackrill, LK Fifield, RG Cresswell, ML di Tada and K Liu (1998). Kinetics of uptake and elimination of silicic acid by a human subject: a novel application of 32Si and accelerator mass spectrometry. J Inorg Biochem 69: 177–180.

135. Porter AE (2006). Nanoscale characterization of the interface between bone and hydroxyapatite implants and the effect of silicon on bone apposition. Micron 37: 681–688.

136. Pramatarova L, E Pecheva and D Dimova-Malinovska (2004). Porous silicon as a substrate for hydroxyapatite growth. Vacuum.

137. Reffitt DM, N Ogston, R Jugdaohsingh, HFJ Cheung, BAJ Evans, RPH Thompson, JJ Powell and GN Hampson (2003). Orthosilicic acid stimulates collagen type 1 synthesis and osteoblastic differentiation in human osteoblast-like cells in vitro. Bone 32: 127–135.

138. Robey PG and P Bianco (2006). The use of adult stem cells in rebuilding the human face. J Am Dent Assoc 137: 961–972.

139. Sailor MJ (2012). Porous Silicon in Practice: Preparation, Characterization and Applications (Weinheim, Germany: John Wiley & Sons).

140. Sakai K, A Yamamoto, K Matsubara, S Nakamura, M Naruse, M Yamagata, K Sakamoto, R Tauchi, N Wakao, S Imagama, H Hibi, K Kadomatsu, N Ishiguro and M Ueda (2012). Human dental pulp-derived stem cells promote locomotor recovery after complete transection of the rat spinal cord by multiple neuro-regenerative mechanisms. J Clin Invest 122: 80–90.

141. Sapelkin AV, SC Bayliss, B Unal and A Charalambou (2006). Interaction of B50 rat hippocampal cells with stain-etched porous silicon. Biomaterials 27: 842–846.

142. Schwarz K and DB Milne (1972). Growth-promoting effects of silicon in rats. Nature 239: 333–334.

143. Seaborn CD and FH Nielsen (1994). Effects of germanium and silicon on bone mineralization. Biol Trace Elem Res 42: 151–164.

144. Secret E, K Smith, V Dubljevic, E Moore, P Macardle, B Delalat, M-L Rogers, TG Johns, J-O Durand, F Cunin and NH Voelcker (2013). Antibody-functionalized porous silicon nanoparticles for vectorization of hydrophobic drugs. Adv Healthc Mater 2: 718–727.

145. Seo B-M, M Miura, S Gronthos, PM Bartold, S Batouli, J Brahim, M Young, PG Robey, C-Y Wang and S Shi (2004). Investigation of multipotent postnatal stem cells from human periodontal ligament. Lancet 364: 149–155.

146. Shi S and S Gronthos (2003). Perivascular niche of postnatal mesenchymal stem cells in human bone marrow and dental pulp. J Bone Miner Res 18: 696–704.

147. Shi S, PG Robey and S Gronthos (2001). Comparison of human dental pulp and bone marrow stromal stem cells by cDNA microarray analysis. Bone 29: 532–539.

148. Shoulders MD and RT Raines (2009). Collagen Structure and Stability. Annu Rev Biochem 78: 929–958.

149. Simmons PJ and B Torok-Storb (1991). CD34 expression by stromal precursors in normal human adult bone marrow. Blood 78: 2848–2853.

150. Sonoyama W, T Yamaza, S Gronthos and S Shi (2007). Multipotent Stem Cells in Dental Pulp. Culture of Human Stem Cells 187–206.

151. Sonoyama W, Y Liu, D Fang, T Yamaza, B-M Seo, C Zhang, H Liu, S Gronthos, C-Y Wang, S Wang and S Shi (2006). Mesenchymal stem cell-mediated functional tooth regeneration in swine. PLoS ONE 1: e79.

152. Tang J, R Peng and J Ding (2010). The regulation of stem cell differentiation by cell-cell contact on micropatterned material surfaces. Biomaterials 31: 2470–2476.

153. Torres-Costa VV, GG Martínez-Muñoz, VV Sánchez-Vaquero, ÁÁ Muñoz-Noval, LL González-Méndez, EE Punzón-Quijorna, DD Gallach-Pérez, MM Manso-Silván, AA Climent-Font, JPJ García-Ruiz and RJR Martín-Palma (2012). Engineering of silicon surfaces at the micro- and nanoscales for cell adhesion and migration control. Int J Nanomedicine 7: 623–630.

154. Toworfe GK, RJ Composto, IM Shapiro and P Ducheyne (2006). Nucleation and growth of calcium phosphate on amine-, carboxyl- and hydroxyl-silane self-assembled monolayers. Biomaterials 27: 631–642.

155. Tran-Hung L, S Mathieu and I About (2006). Role of human pulp fibroblasts in angiogenesis. J Dent Res 85: 819–823.

156. Tsai W-B and J-H Lin (2009). Modulation of morphology and functions of human hepatoblastoma cells by nano-grooved substrata. Acta Biomaterialia 5: 1442–1454.

157. Varanasi VG, JB Owyoung, E Saiz, SJ Marshall, GW Marshall and PM Loomer (2011). The ionic products of bioactive glass particle dissolution enhance periodontal ligament fibroblast osteocalcin expression and enhance early mineralized tissue development. J Biomed Mater Res A 98: 177–184.

158. Veis A (2003). Mineralization in Organic Matrix Frameworks. Reviews in Mineralogy and Geochemistry 54: 249–289.

159. Veis A and JR Dorvee (2013). Biomineralization Mechanisms: A New Paradigm for Crystal Nucleation in Organic Matrices. Calcif Tissue Int 93: 307–315.

160. Wang P, L Clements, H Thissen, A Jane, W-B Tsai and NH Voelcker (2012). Screening Mesenchymal Stem Cell Attachment and Differentiation on Porous Silicon Gradients. Adv Func Mater 22: 3414–3423.

161. Wang P-Y, J Yu, J-H Lin and W-B Tsai (2011). Modulation of alignment, elongation and contraction of cardiomyocytes through a combination of nanotopography and rigidity of substrates. Acta Biomaterialia 7: 3285–3293.

162. Wang Y, HJ Kim, G Vunjak-Novakovic and DL Kaplan (2006). Stem cell-based tissue engineering with silk biomaterials. Biomaterials 27: 6064–6082.

163. Werner S, O Huck, B Frisch, D Vautier, R Elkaim, J-C Voegel, G Brunel and H Tenenbaum (2009). The effect of microstructured surfaces and laminin-derived peptide coatings on soft tissue interactions with titanium dental implants. Biomaterials 30: 2291–2301.

164. Whitehead MA, D Fan, P Mukherjee, GR Akkaraju, LT Canham and JL Coffer (2008). High-porosity poly(epsilon-caprolactone)/mesoporous silicon scaffolds: calcium phosphate deposition and biological response to bone precursor cells. Tissue Engineering Part A 14: 195–206.

165. Yamada Y, K Ito, S Nakamura, M Ueda and T Nagasaka (2011). Promising cell-based therapy for bone regeneration using stem cells from deciduous teeth, dental pulp, and bone marrow. Cell Transplantation 20: 1003–1013.

166. Yang C, L Huang, T Shen and JA Yeh (2010). Cell adhesion, morphology and biochemistry on nano-topographic oxidized silicon surfaces. Eur Cell Mater 20: 415–430.

167. Yang C-Y, T-C Liao, H-H Shuai, T-L Shen, JA Yeh and C-M Cheng (2012). Micropatterning of mammalian cells on inorganic-based nanosponges. Biomaterials 33: 4988–4997.

168. Yim EKF, EM Darling, K Kulangara, F Guilak and KW Leong (2010). Nanotopography-induced changes in focal adhesions, cytoskeletal organization, and mechanical properties of human mesenchymal stem cells. Biomaterials 31: 1299–1306.

169. Yoo CH, H-J Na, D-S Lee, SC Heo, Y An, J Cha, C Choi, JH Kim, J-C Park and YS Cho (2013). Endothelial progenitor cells from human dental pulp-derived iPS cells as a therapeutic target for ischemic vascular diseases. Biomaterials.

170. Zemel A, F Rehfeldt, AEX Brown, DE Discher and SA Safran (2010). Optimal matrix rigidity for stress-fibre polarization in stem cells. Nature Physics 6: 468–473.

171. Zhu X, J Chen, L Scheideler, R Reichl and J Geis-Gerstorfer (2004). Effects of topography and composition of titanium surface oxides on osteoblast responses. Biomaterials 25: 4087–4103.

172. Zreiqat H, Y Ramaswamy, C Wu, A Paschalidis, Z Lu, B James, O Birke, M McDonald, D Little and CR Dunstan (2010). The incorporation of strontium and zinc into a calcium-silicon ceramic for bone tissue engineering. Biomaterials 31: 3175–3184.

173. Zuk PA, M Zhu, P Ashjian, DA De Ugarte, JI Huang, H Mizuno, ZC Alfonso, JK Fraser, P Benhaim and MH Hedrick (2002). Human adipose tissue is a source of multipotent stem cells. Mol Biol Cell 13: 4279–4295.

Appendix

- **Formulaire de consentement éclairé**
  Written informed consent

- **Porous silicon scaffolds for stem cells growth and osteodifferentiation**

P-Y. Collart Dutilleul, D. Deville de Périère, F.J. Cuisinier, F. Cunin and C. Gergely. (2014) Porous silicon scaffolds for stem cells growth and osteodifferentiation. In H. Santos, Woodhead Pub Limited, Cambridge, UK. 486-506.
DOI: 10.1533/9780857097156.3.486

- **Human mesenchymal stem cells from dental pulp behavior onto bioresorbable porous silicon scaffolds**

Submitted to *ACS Applied Materials & Interfaces*, on 21 October 2013
Manuscript ID: am-2013-046316

Formulaire de consentement, pour recherche sur les cellules souches de la pulpe dentaire, à partir de dents de sagesse extraites

Je soussigné(e)…………………………………………………..…..déclare avoir été informé(e) par le Dr. *Pierre-Yves COLLART DUTILLEUL* de la possibilité d'intégrer les déchets opératoires (dents) faisant suite aux avulsions effectuées au cours de mon hospitalisation, dans une collection biologique destinée à la recherche scientifique.

Je sais que ces prélèvements pourront être utilisés par des chercheurs du Centre Hospitalier Régional et Universitaire de Montpellier ou des chercheurs travaillant en dehors du CHRU, pour des travaux de recherche entrepris dans le cadre du programme suivant :
Recherche de cellules souches dans la pulpe dentaire : isolation et mise en évidence de leur potentiel de prolifération et différenciation.
Investigations menées ***au Laboratoire Biosanté et Nanoscience (EA 4203, Université Montpellier1)*** *par le Dr Pierre-Yves COLLART DUTILLEUL, sous la responsabilité du Professeur Frédéric CUISINIER (PU-PH).*

Considérant disposer des informations qui me permettent de prendre ma décision,

☐ **je donne mon accord** pour que les dents extraites lors des avulsions soient utilisées à des fins de recherche scientifique.

☐ **je m'oppose** à ce que les dents extraites lors des avulsions soient utilisées à des fins de recherche scientifique et demande qu'elles soient détruites.

Ces prélèvements seront conservés anonymement dans la structure suivante :
Laboratoire Biosanté et Nanoscience EA 4203, UFR Odontologie, 545 Av Pr. JL Viala, 34193 MONTPELLIER Cedex 5, sous la responsabilité du Pr. Cuisinier (Tél : 04 11 75 92 25)

J'autorise le Dr *Collart Dutilleul*, à effectuer ou faire effectuer les études qui peuvent contribuer à la compréhension des mécanismes moléculaires impliqués dans la physio-pathologie de la prolifération/différenciation des tissus d'origine pulpaire, avec comme objectif futur l'utilisation de cellules souches pulpaires en médecine régénérative.

Je sais que **ma décision est révocable à tout moment**, sans justification et sans que cela ne porte aucunement préjudice à la qualité des soins qui me seront prodigués.

J'ai également été informé(e) que des données médicales me concernant peuvent être transmises au responsable de ces recherches scientifiques, dans le strict respect du secret médical.

Si je le souhaite, les données me concernant, pourront m'être communiquées directement ou par l'intermédiaire d'un médecin de mon choix.
Je dispose également du droit d'être informé(e) des résultats globaux de cette recherche.

Fait à Montpellier le…………………………, après information donnée par le Dr. Pierre-Yves Collart Dutilleul.

Signature du patient

20

Porous silicon scaffolds for stem cells growth and osteodifferentiation

P. Y. COLLART DUTILLEUL, D. DEVILLE
DE PÉRIÈRE and F. J. CUISINIER, UFR Odontologie, France,
F. CUNIN, Institut Charles Gerhardt Montpellier, France and
C. GERGELY, Montpellier 2 University, France

DOI:10.1533/9780857097156.3.486

Abstract: Stem cells constitute the source of differentiated cells for the generation of tissues during development and for regeneration of tissues that are diseased or injured postnatally. Stem cell-based therapy often requires a scaffold to carry cells and/or growth factor to the injured site. Porous silicon (PSi) is a promising biomaterial for tissue engineering, as it is both non-toxic and bioresorbable. Surface modification can offer control over the degradation rate of PSi and can also impart properties to promote cell adhesion. Thus, coupling the good proliferation and differentiation capacities of either adult mesenchymal stem cells (MSC) or embryonic stem cells (ESC) with the textural and chemical properties of the PSi substrates provides an interesting approach for therapeutic use. Moreover, the PSi nanostructure and the release of silicic acid have positive effect on precursor cell osteodifferentiation and mineralized matrix formation.

Key words: porous silicon, mesenchymal stem cells, cell adhesion, osteodifferentiation, mineralization.

20.1 Introduction

Numerous studies have been carried out to verify that stem cells could become a source of stable differentiated cells capable of inducing tissue formation, including mineralized hard tissue. Stem cells for hard tissue formation have received considerably increased attention from researchers, as these cells can be an interesting source of stable differentiated cells, capable of inducing bone formation and control hydroxyapatite crystal growth. Stem cells of various origins are able to produce *in vitro* calcified nodules and to form a mineralized tissue after transplantation *in vivo*. Supporting scaffolds for bone tissue engineering are often required to lead cell implantation, growth and differentiation (D'Aquino *et al.*, 2007; Graziano *et al.*, 2008).

These scaffolds can be inductive or instructive to direct stem cells down specific lineage pathways and increase the therapeutic effect. Thus, directed stem cells have the potential for rapid bone regeneration and repair. Since the advent of tissue engineering, bone has received particular interest, since it is one of the tissues with most regenerative abilities in the human body.

Porous silicon (PSi) is a promising biomaterial for bone tissue engineering, as it is non-toxic, bioresorbable, and can be inductive for osteodifferentiation. It has the ability to degrade in aqueous solutions into non-toxic silicic acid and surface modifications offer control over the degradation rate of PSi (Low *et al.*, 2006). Moreover, this tunable, biocompatible and resorbable material has been reported for the growth of hydroxyapatite, inferring the possible bone implantability of the material (Canham, 1995).

20.2 Stem cells for bone tissue engineering: adult, neonatal and embryonic stem cells (ESCs)

The first cell-based strategy for bone repair was autologous connective tissue progenitors from the iliac crest. This autograft procedure was accomplished without any *in vitro* manipulation, and was thus considered part of the surgical procedure (Connolly *et al.*, 1991). However, bone grafting is not always possible, as it injures the donor site, and the success of graft is entirely dependent on the transfer of sufficient numbers of progenitor cells. In addition, this approach may be least applicable in situations where it is most needed, such as in the case of ageing or disease with a reduction of osteogenic progenitors. Stem cell therapy involves *in vitro* sorting and expansion before cell grafting. Cells can be of autologous or allogenic origin. Autologous grafts offer the optimal compatibility, but require available cells from the patients. Therefore, allogenic grafts with cells from alternative allogenic source are of great interest, as they could provide ‘ready for use’ products for bone treatments.

20.2.1 Adult mesenchymal stem cells: bone marrow, adipose tissue and dental pulp-derived stem cells

It has been shown that plastic-adherent human cells derived from bone marrow were able to differentiate into a number of mesenchymal cell types including osteoblasts, chondrocytes and adipocytes. These cells were called ‘MSCs’ in reference to their high self-renewing properties, clonogenicity, and ability to form cartilage and bone (Fig. 20.1). They were suggested to be responsible for the normal turnover and maintenance of adult mesenchymal tissues. These MSCs have been defined to

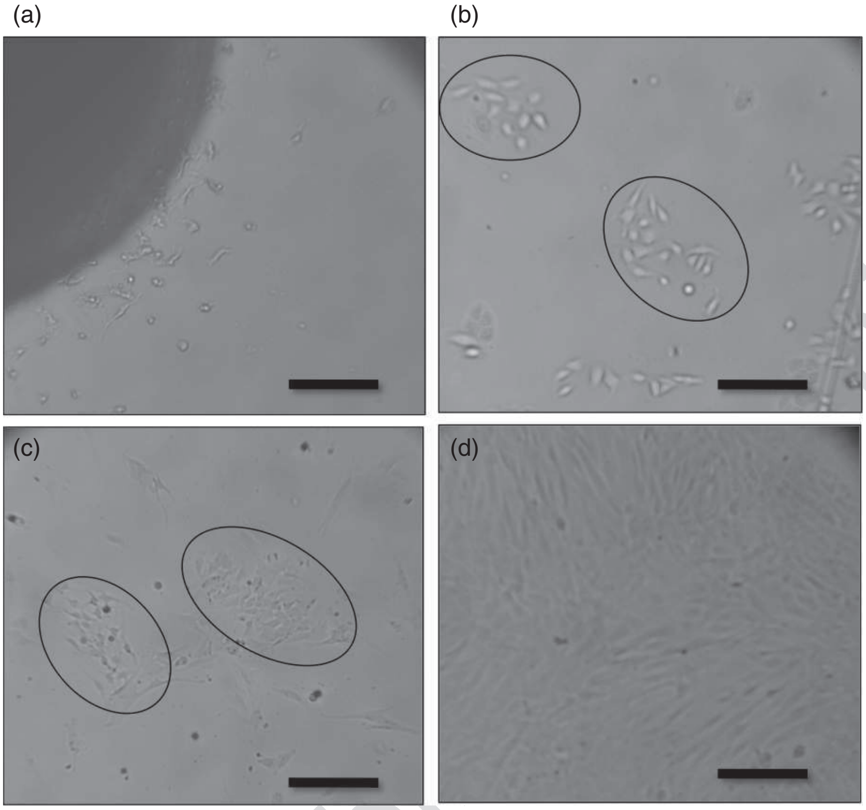

20.1 Human MSCs from dental pulp. (a): Stem cells outgrow from pulp tissue explants. (b, c, d): Stem cells colonies formed after digestion and being plated in culture dishes. Colonies formed in 3 and 5 days (a and b, respectively), cells reaching confluence after 10 days (d). Scale bar: 300 μm.

be plastic-adherent when maintained in standard culture conditions; they must express CD105, CD73 and CD90, and lack expression of CD45 and CD34 (haematopoietic markers) surface molecules; and they must also differentiate to osteoblasts, adipocytes and chondroblasts *in vitro* (Dominici *et al.*, 2006). MSCs' therapeutic potential has generated significant excitement in the field of regenerative medicine, as they can be found in various niches within human body. The ability of these cells to self-renew and differentiate into multiple tissues makes them an attractive cell source for cellbased regenerative therapies. MSCs have considerable potential for the treatment of musculoskeletal disorders owing to their expansion capacity, immunosuppressive properties and ability to differentiate into bone and cartilage (Ma, 2010).

The most studied source of adult MSCs has been the bone marrow, as it was recognized early that its stroma contained stem cells capable of forming bone and cartilage. Later, other sources of adult stem cells have been described, such as adipose tissue, dental pulp, skeletal muscle, umbilical cord blood and others (Marolt *et al.*, 2010).

Bone marrow mesenchymal stem cells (BMSCs)

BMSCs are commonly recovered from pure bone marrow aspirates and isolated according to their adherence and culture on tissue culture plastics. They can be also selected using specific cell surface markers, and then expanded in culture. The number of stem cells varies between different patients. Age and marrow aspiration volume influence also the number of isolated stem cells. BMSCs can, however, be expanded *in vitro* to large numbers and keep their osteogenic potential even in older patients (Bianco *et al.*, 2001).

Adipose-derived stem cells (ADSC)

Zuk *et al.* (2002) have been the first to describe and characterize ADSCs from human lipoaspirates. They showed that a multi-lineage stem cell population could be isolated from the stromo-vascular fraction of adipose tissue. These ADSCs are able to differentiate into osteoblasts, can be recovered from raw lipoaspirates consecutive through liposuction under anaesthesia, and represent an important niche of adult stem cells. They have been extensively studied *in vitro* for their ability to form various tissues, including bone-like tissue.

Dental pulp stem cells (DPSC)

Stem cells within the dental pulp have been first described by Gronthos *et al.* (2000). They have then been studied and characterized as an adult stem cell population that possesses the properties of high proliferative potential, the capacity of self-renewal and multi-lineage differentiation. Dental pulp can be easily collected from adult DPSC or deciduous teeth (stem cells from human exfoliated deciduous teeth) after dental extraction, when teeth have to be removed. The most frequent case is the collection of normal human third molar extracted for orthodontic reasons (Gronthos *et al.*, 2002).

20.2.2 Embryonic stem cells

ESCs from rat or other animal origin are widely used in research. But for biomedical applications, ESCs have to be of human origin, which leads to technical and ethical issues. Human ESCs are harvested from pre-implanted embryos from the inner-cell mass within the first 2 weeks of development. These cells are obtained from extra embryos developed by *in vitro* fertilization techniques, or from embryos derived from voluntary interruption of pregnancy. They proliferate *in vitro* while maintaining an undifferentiated state, and are capable of differentiating into many somatic cell types. Although they show great capacities for cell therapy and tissue engineering, these particular cells create a delicate ethical debate, as they induce destruction of human embryos.

20.2.3 Neonatal stem cells from the umbilical cord

Neonatal tissues constitute a stem cell source that can be accessed in a non-invasive and rapid manner during and just after birth. The main source is the umbilical cord, covered by an amniotic epithelium that protects a gelatinous matrix called 'Wharton's jelly'. Stem cells can be recovered during birth, *in utero* or *ex utero*, from both cord blood and cord matrix (Wharton's jelly) (Forraz and McGuckin, 2011). Cord blood can be collected using a collecting needle connected to an anticoagulant-containing bag. Wharton's jelly is obtained by collecting the whole umbilical cord. With the average umbilical cord measuring 50 cm, this source of MSCs might become more and more clinically relevant.

20.3 Stem cells osteogenic differentiation and bone formation

Bone tissue is composed of matrix and cells: bone matrix is mainly built of type I collagen (90%), with non-collagenous proteins (such as osteocalcin (OCN), osteonectin, and bone sialoproteins). These scarce non-collagenous proteins participate in matrix maturation and mineralization. Osteoblasts and osteoclasts are responsible for bone formation and bone resorption. With progenitor cells, they mediate the mechanism of bone remodelling. During bone formation phase, the osteoblasts are recruited from MSC in bone marrow, since osteoclasts are derived from haematopoietic cells. Thus, stem cell therapy for bone regeneration will focus on MSC for osteoblastic differentiation, since host cells will provide osteoclasts during vascularization process.

20.3.1 Molecular control of osteogenesis

Bone repair consists in inflammation, intra membranous ossification, chondrogenesis, endochondral ossification and remodelling. Li *et al.* (2007) have described molecular events that regulate osteogenesis: they observed an upregulation of genes related to cell cycle and cell-to-cell signalling, confirming the fact that both cell division and communication are essential to initiate bone healing. MSCs proliferate and differentiate under the influence of a number of molecular pathways, but mitogen-activated protein kinase (MAPK) signalling plays a pivotal role in osteogenic induction. MAPK pathway is activated by a variety of growth factors such as fibroblast growth factors (FGF), platelet derived growth factors (PDGF), transforming growth factor beta (TGFβ), bone morphogenic proteins (BMP) and insulin-like growth factors (IGF). These extracellular signals activate a signalling cascade of MAP kinase inside the cell, resulting in cell proliferation and osteodifferentiation. Another pathway involved in osteodifferentiation is the Wnt signalling pathway: Wnt represents a family of secreted molecules which are involved in various aspects of cellular biology, including cell growth, differentiation and death. The binding of Wnt proteins permits the translocation of β-catenin into the nucleus, resulting in an enhanced expression and activity of the osteogenic promoter Runx2. Wnt signalling and hedgehog signalling cooperate in controlling bone formation, especially at the early stage of osteoblast formation, initiating cellular differentiation. Cell–cell interactions are also required for activating some signalling cascade: notch signalling and ephrin signalling are the main cell–cell interaction pathways. Notch receptors and ligands are membrane proteins able to up-regulate bone related genes to favour the proliferation of immature osteoblasts, while limiting osteoblast maturation by inhibiting the Runx2 transactivation function. Ephrin ligands and receptors are also membrane proteins. They are constituted by two classes of ephrins: the B class ephrin ligands and receptors (EphB-Tyrosine Kinase receptor) induce osteogenic transcription factors, and inhibit osteoclast differentiation, leading to bone formation. EphrinA/EphA receptor interaction facilitates bone remodelling by suppressing osteoblast differentiation and activating osteoclast differentiation (Fig. 20.2).

Osteoblastic differentiation in vitro and in vivo

MSCs are capable of osteodifferentiation *in vitro* under appropriate conditions. This differentiation is induced through addition of various molecules and chemicals, such as dexamethasone, ascorbic acid and β-glycerophosphate. Osteoblast-specific genes expression and proteins demonstrate this *in vitro* differentiation. However, *in vitro* assays have limitations and there is always a need to verify osteoblast differentiation potential *in vivo*. Thus, it has been shown that osteoprogenitor cells can only form bone tissue when transplanted *in vivo*, while MSCs can form both bone and bone-microenvironment supporting haematopoiesis *in vivo*. Moreover, MSCs demonstrate self-renewal and maintenance of stemness capacity during *in vivo* implantation (Arvidson *et al.*, 2011).

Stem cells potential for scaffold-based bone tissue engineering applications

ESCs and adult (or neonatal) MSCs are the main types of stem cells usable for scaffold-based tissue engineering. However, ESCs have a limited applicability to human cell therapy due to ethical concerns, but also to immunological

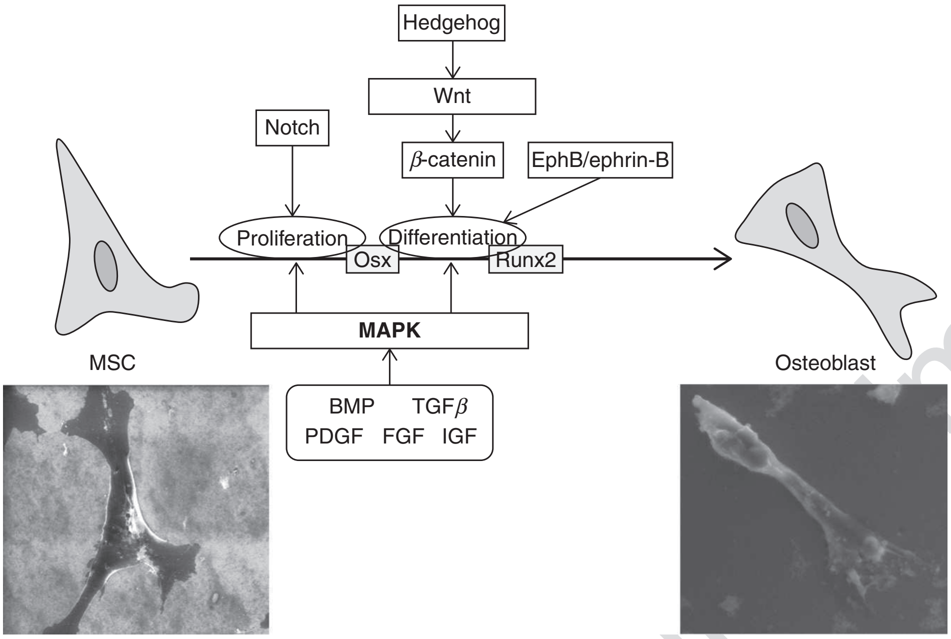

20.2 Schematic representation of the principal signalling networks and transcription factors regulating osteoblast differentiation and osteogenesis. Scanning electron microscopy (SEM) of an MSC, original magnification × 2000) and of an osteoblast differentiated *in vitro* from MSC (original magnification × 2000). BMP: bone morphogenic protein, TGFβ: transforming growth factor, PDGF: platelet derived growth factor, FGF: fibroblast growth factors, IGF: insulin-like growth factor, MAPK: mitogen-activated protein kinase, Osx: Osterix transcription factor.

incompatibilities, potential for malignant tumour growth, and insufficient understanding and control over differentiation. Thus, adult MSCs seem to be the cell type of choice for scaffold-based therapeutic applications. MSC delivery to the site of bone tissue defects requires scaffolds adapted to cell culture and activity in endogenous osteogenesis, including correct biochemical and mechanical stimuli.

20.3.2 Stem cells and mineralization process

Biomineralization is a general process by which inorganic calcium phosphate crystals are produced in biological environments. For bone formation, deposition of calcium phosphate salts occurs on an extracellular organic matrix by means of a heterogeneous nucleation process, which constitutes the first stage of hard tissue mineralization (Ngankam *et al.*, 2000).

Biomineralization process: ions and nucleation sites

Bone biominerals are composed of complex structures, having precise architectural order over several length scales. They rely on their biological constituents for regulation of mineralization, forming an organic–inorganic hybrid structure. The formation mechanisms of biomineralization involving several possible pathways remain unclear. Biomineralization has been described to start with matrix vesicle-mediated mineral initiation. It also involves heterogeneous nucleation of mineral crystals with an important role played by non-collagenous glycoproteins that bind calcium and collagen. Calcium phosphate crystals can be formed via stable pre-nucleation clusters, with aggregation into an amorphous precursor phase, then transformation of this phase into a crystal (Cölfen, 2010). Nudelman *et al.* (2010) demonstrated that collagen forms the structural matrix and has an active role in the mineralization of apatite for bone formation. Indeed, collagen fibrils have positively charged regions, and these nanosized regions can be used for mineral infiltration and charge–charge attractions. This initial mineral deposition leads to a dense network of pre-nucleation clusters, to transformation into amorphous calcium phosphate and to oriented crystalline hydroxyapatite inside the fibrils. Even though the biomineralization process has been mainly studied in *in vitro* models and *in vivo* bone formation may follow different rules, observations in small animals and tooth formation suggest that at least part of the mineralization mechanism of the collagen model is relevant for *in vivo* systems (Beniash *et al.*, 2009).

Collagen and calcium phosphate deposition during osteodifferentiation

Calcium and inorganic phosphate are the two main constituents of hydroxyapatite, the bone mineral that gives mechanical resistance to the organic matrix. The Ca/P mass ratio in bone is 2.2, and the initial step of Ca–P crystal nucleation takes place within matrix vesicles that appear from the plasma membrane of osteogenic cells, and migrates into the extracellular skeletal compartment. Phosphate accumulates inside these matrix vesicles by a transport system, followed by an influx of calcium ions. This process permits the formation of hydroxyapatite crystal, associated with organic matrix collagen fibrils. Collagen is synthesized and assembled by osteoprogenitors, following a classical pathway for a secreted protein. The collagen chains are synthesized as precursors, and undergo a series of maturation reactions, such as glycosylation and hydroxylation in the endoplasmic reticulum and Golgi complex. They are then assembled to form a triple helix. After processing and assembly, this type I procollagen is secreted into the extracellular space, where it will mature and polymerize into normal fibrils. Thus, collagen, calcium and phosphate are provided to the extracellular space through osteoprogenitors. During osteodifferentiation, MSCs will turn into progenitor cells, then osteoblasts, expressing collagen type I genes.

20.4 Influence of pore size, nanoroughness and chemical surface treatment

To mimic the *in vivo* cell behaviour for *in vitro* culture, one should consider scaffold chemistry, mechanical properties and architecture (Yang *et al.*, 2012). An extracellular matrix is composed of various proteins within a 3D network. Thus, a scaffold for tissue engineering should provide optimal mechanical properties and environment for cell culture. PSi can be designed to mimic the properties of bone tissue, and coatings can impart proper surface chemistry, adapting various pore sizes, porosity and nanoroughness. Indeed, nanotopography can affect protein adsorption, cytoskeletal arrangement, and cell adhesion and spreading.

20.4.1 Influence of PSi pore size on MSC adhesion

The effect of pore size and porosity on cell growth is of particular relevance, as it will direct the fabrication of a porous biomaterial. Additionally, its biocompatibility depends on its porosity and pore size. These pore dimensions can be precisely controlled and are highly tunable during PSi electrochemical anodization or etching. A variety of pore sizes can be produced: from micropores (<5 nm), mesopores (5–50 nm) to macropores (>50 nm) depending on the preparation conditions (Sailor, 2011). Although microscale topography modulates cellular behaviour *in vitro*, it is important to consider that cells *in vivo* make contact with nanoscale as well as microscale topographical features. Even if cells are typically tens of microns in diameter, the dimensions of subcellular structures tend to the nanometre scale. Furthermore, extracellular supporting tissues present an intricate network of cues at the nanoscale composed of a complex mixture of nanometre-size (5–200 nm) pits, pores, protrusions, and fibres (Biggs *et al.*, 2010). The main means to evaluate the influence of pore size on MSCs adhesion and proliferation is PSi gradients, allowing cells growth on surface with a pore range from few nanometres to few micrometres: this method involves electrochemical etching of crystalline Si in a hydrofluoric acid (HF) solution to fabricate PSi films displaying a

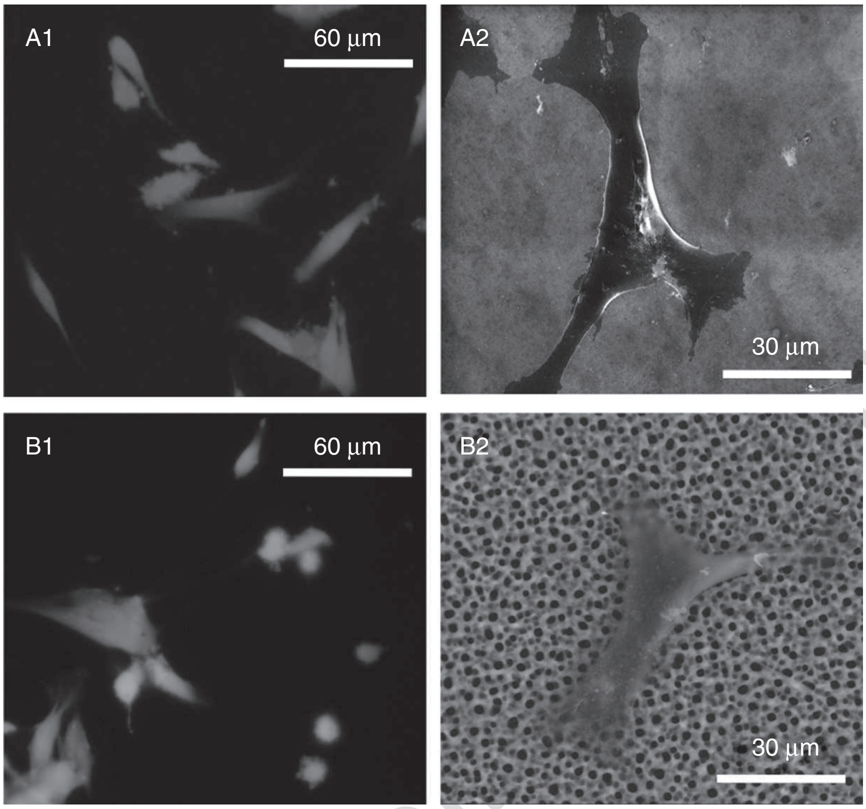

20.3 Epifluorescence microscopy and SEM of MSC culture on PSi, after 24H of culture. A: mean pore size = 30 nm. A1 and A2: epifluorescence microscopy and SEM, respectively. B: mean pore size = 1 µm. B1 and B2: epifluorescence microscopy and SEM, respectively. Cells present a better adhesion on PSi with small pore size, compared to PSi with large pores: cells recover a more physiological shape (A1) and spread more (A2) on 30 nm-PSi, while cells are more bulging and spread less on 1 µm-PSi (B1 and B2). (*Source*: Adapted from Collart Dutilleul (non-published data.)

gradient of pore sizes in an asymmetrical arrangement. The size range of these pores can be controlled by modifying the applied current and the HF (Collins *et al.*, 2002; Clements *et al.*, 2012). Different cell types respond differently to topographical features, such as nanoscale pores, and studies have demonstrated that MSCs show better attachment to PSi with pore size of 20–30 nm in diameter (Wang *et al.*, 2012). Pore size in this range is similar to the pore size of biological systems, such as pores in basement membranes, and corresponds to the size of biological pits, pores, protrusions and fibres (Fig. 20.3). While producing PSi, pore depth can also vary. However, cells are not sensitive to changes in pore depth in the range observed with various type of PSi (Low *et al.*, 2006).

20.4.2 Optimal surface treatment and coating for cell adhesion

MSCs were shown to respond to both topographical and chemical characteristics. However, chemical surface treatment and grafting of proteins seem to have a higher impact than changes in pore size during short-term culture (Clements *et al.*, 2012). PSi surface treatment is necessary not only to improve cell adhesion, but also to permit accessible and stable pores: the inner walls of the porous matrix must be protected from excessive degradation in the aqueous cell culture environment without eliciting any undesirable effects on the cells. Moreover, surface modification by turning PSi from hydrophobic to hydrophilic promotes cell adhesion and growth. The most common and simple treatment is oxidation, which can be done by ozone, ageing, or thermal or chemical treatment. PSi biocompatibility has been extensively studied with various cell lines cultured on chemically modified PSi samples. Few studies have been done with primary MSC cultures to determine an optimal surface treatment (Hajj-Hassan *et al.*, 2011; Clements *et al.*, 2012). Moreover, it has been shown that stem cell growth can be modulated by factors mimicking extracellular matrix, such as amino or arginine-glycine-aspartate (RGD) residues. Cell behaviour is influenced by changing the integrin and focal adhesion assembly, leading to changes in cytoskeletal organization and cell mechanical properties (Yim *et al.*, 2010). Thus, amine-terminated samples are expected to enhance MSC adhesion and proliferation as it does for other cell lines: silanization with aminopropyl trimethoxysilane and triethoxysilane improves PSi stability and enhances cell adhesion in comparison to oxidized PSi. The chemistry greatly improves the stability of PSi in contact with cultured cells while allowing cell coverage levels comparable to standard culture preparations on tissue culture polystyrene (Low *et al.*, 2006). Thermal hydrosilylation is also used to graft chemical species to generate a stable substrate for cell adhesion and proliferation. Among these species are dodecene, undecylenic acid and oligoethylene glycol (Alvarez *et al.*, 2009).

In addition to chemical surface treatment, a coating of proteins can be realized onto the PSi surface to mimic cell adhesion and relative responses in an *in vivo* condition with a surface presenting biocompatible contact sites in a nanoscale dimension (topographic scale of adhesive proteins such as collagen fibres, laminin and fibronectin is present on the order of nanometres). The cell adhesion process depends upon cell surface receptors interacting with proteins belonging to the extracellular matrix. Several proteins have been considered for PSi coating: collagen, foetal calf serum and the tripeptide RGD. Collagen is a component of the extracellular matrix and can be used to coat surfaces to stimulate cell adhesion, as well as foetal calf serum, which contains several cell adhesive proteins. Collagen and foetal calf serum have been successfully used to promote cell attachment and cell spreading (Low *et al.*, 2006). The tripeptide RGD is an integrin-binding domain present within many matrix proteins including fibronectin and vitronectin. Clements *et al.* (2012) showed that RGD immobilized on PSi is still a bioactive peptide and that cells adhere more when the concentration of RGD grafted increases.

Composite materials, such as poly(ε-caprolactone)/PSi, are also used for cell culture and tissue engineering. Highly porous scaffolds composed of mesoporous Si and commonly-used biopolymers, such as polycaprolactone, are electrically conductive composite materials exhibiting an interfacial behaviour that promotes calcification and sustains the *in vitro* stability and proliferation of connective tissue cells in implant surfaces. Poly(ε-caprolactone) has been shown to have a biocompatible and biodegradable character that is widely exploited in guided bone regeneration and drug delivery, and the resorbable PSi component sensitively accelerates the necessary calcification process. This type of composite presents a relevant material to orthopaedic tissue engineering, with such tunable properties as mechanical strength, controlled release of molecules, and rate of resorption of the composite to the host surroundings (Coffer *et al.*, 2005). This PSi-containing polymer scaffold enhances calcification, can be considered non-toxic to cells, and supports the proliferation, viability, attachment, and differentiation of bone precursor cells, suggesting that materials of this type of composition have potential merit as biomaterials (Whitehead *et al.*, 2008).

Another type of PSi membrane has also been described using porous nanocrystalline Si, a new type of Si nanomaterial with potential applications in cell culture and tissue engineering. This PSi material is a 15 nm thick nanoporous membrane made with scalable Si manufacturing, permeable to small solutes. This nanoporous and ultrathin material can serve as a cell culture substrate, and is of interest to separate tissues during surgical grafting, such as bone tissue, bone substitute, periosteum or epithelium (Agrawal *et al.*, 2010).

20.4.3 Roughness and surface energy

Several molecular mechanisms by which cells perceive and respond to their surrounding environments have been studied, including integrin–ligand interactions, contact surface hydrophilicity and extracellular matrix topography and architecture. The *in vitro* control of the cellular environment is a challenge for manipulating both cell development and scaffold substitute function in the field of bioengineering. However, the differences existing between natural and experimental surface characteristics may confer some of the discrepancies reported between *in vivo* and *in vitro* results. Several approaches have been used to generate biomimetic *in vitro* environments. These experiments explore cell interaction, either with the substrate's topography (physical domain) or with the substrate's chemical nature (chemical domain). The effects of nanotopographic features on cell behaviours have been investigated using a variety of nanoscale patterns, such as columns, sharp tips, pores and dots. Therefore, to biomimic cell adhesion and relative responses in an *in vivo* condition, cell adhesion surfaces are required to present biocompatible contact sites in a nanoscale dimension with periodicity matching with cell surface proteins. Nonetheless, the physical nature of the interactions between the cell and the surfaces in controlling specific cell behaviour remains unclear. Several results suggest that nanometre-sized topographical biocompatible substrates potentially provide a distinct *in vitro* environment for cells, resembling the *in vivo* conditions (Yang *et al.*, 2010). However, the nanotopography plays a relevant role in the final wettability properties of surfaces, where hydrophobic surfaces prevent cell adhesion. PSi can be arranged with nanoscale patterns, but freshly formed nanostructured PSi shows hydrophobic properties. Surface oxidation turns hydrophobic surfaces into hydrophilic: freshly etched PSi is hydrophobic, and controlled ozone or thermal oxidation can drop the water contact angle to below 5°. This is attributed to the formation of a polar Si–OH capped surface after oxidation (Low *et al.*, 2006).

20.4.4 Influence of pore size, stiffness and surface treatment on osteodifferentiation

Cell attachment on PSi substrate has been extensively studied, but few studies evaluated the influence of topography on cell differentiation. Recently, Wang *et al.* (2012) explored the influence of nanoscale surface topography on cell behaviour. Using rat MSCs, they found that surface topography influences cell differentiation, but not proliferation. Osteogenesis was enhanced by porous topography with a ridge roughness lower than 10 nm with an increase in osteodifferentiation when pore sizes decreased. Thus, osteodifferentiation was comparable between flat Si and PSi with 100–200 nm, and was clearly enhanced when pore sizes decreased to 10–30 nm. This impact of pore size on osteodifferentiation is of high importance for the development of scaffold materials that can stimulate stem cell differentiation into osteoblasts in absence of chemical treatment without compromising material properties. Dalby *et al.* (2007) had already demonstrated the use of nanoscale disorder to stimulate human MSCs to produce bone mineral *in vitro* in the absence of osteogenic supplements. Their approach had similar efficiency to that of cells cultured with osteogenic media. Nanocues, such as PSi pores, may prove to be important in tissue-specific stem cell differentiation.

These findings are supported by various observations of chemical stimulation, chemical patterning and material hardness having roles in stem cell differentiation (Zemel *et al.*, 2010). The effect of surface treatment of PSi on stem cells has been investigated mainly for cell adhesion; however, several studies have shown that the immobilization of RGD on the substrate not only enhanced cell adhesion but also modulated the intercellular mechanisms of cell proliferation and differentiation (Hu *et al*., 2003; Cavalcanti-Adam *et al.*, 2007; Lagunas *et al.*, 2012). Thus, RGD peptide coated surfaces enhance osteogenic differentiation when present in sufficient concentration (Frith *et al.*, 2012). Finally, the mechanical properties of the underlying substratum have previously been shown to affect a number of cellular processes including locomotion, proliferation and differentiation. Microenvironments appear important in stem cell lineage specification, but can be difficult to control with PSi. MSCs are shown to specify lineage and commit to phenotypes with extreme sensitivity to tissue-level elasticity. Soft matrices that mimic brain are neurogenic, stiffer matrices that mimic muscle are myogenic, and comparatively rigid matrices that mimic collagenous bone, such as PSi, prove to be osteogenic. After several weeks in culture, cells commit to the lineage specified by matrix elasticity (Engler *et al.*, 2006).

20.5 Growth factors delivery and Si effects on osteodifferentiation

Stem cells grown in biomaterials with bone growth factors constitute a source of transplantable material. Indeed, mesenchymal stem cells differentiation into elements of the skeleton can be enhanced by the addition of bone growth factors. PSi is a potential carrier scaffold to deliver growth factors to the site of defect, where regeneration is needed.

Moreover, controlled release of ionic products from PSi dissolution can stimulate and enhance bone-cell function: dissolved Si has been shown to enhance osteoblast differentiation (Gupta *et al.*, 2010).

20.5.1 Drug delivery devices for osteogenic induction

Tissue engineering combines precursor cells from the patient with scaffolding matrices and the stimulus of growth factors. BMPs are probably the most important growth factors in bone formation and healing. These cytokines have been extensively studied during recent decades and, nowadays, recombinant human BMPs (rhBMP) are widely used in several tissue engineering products that might serve for the complete regeneration of bone or cartilage. Current applications include rhBMPs loaded in delivery systems made of synthetic or natural polymers and the differentiation of transplanted stem cells from the patient with rhBMPs for later body implantation. BMPs have a strong effect on bone and cartilage growth during early skeletal formation, and thus have promising potential for clinical bone and cartilage repair, working as powerful bone-inducing components in diverse tissue engineering products. PSi may also be used as carrier for the delivery of BMPs. BMP-2 and BMP-7 have received approval from the US Food and Drug Administration for specific clinical cases (Bessa *et al.*, 2008). Indeed, PSi also exhibits a number of properties that make it an attractive material for controlled drug delivery applications. Its high surface area, coupled with the ability to control pore sizes, allows PSi to be loaded with a range of bioactive species. Tuneable properties of surface area, porous volume, and pore size allow controlling the amount and *in vivo* release rate of molecule payloads (Anglin *et al.*, 2008). By promoting osteogenic development of MSCs, the association of PSi and BMPs offers an interesting perspective for bone reparation and regeneration.

20.5.2 Silicic acid and Si effects on bone formation

Since the discovery that bioactive ceramics bond to bone without fibrous encapsulation, many studies have focused on the mechanism of bioactivity *in vitro* and *in vivo*. These studies have indicated that controlled dissolution of bioactive ceramics was of prime importance for stimulation of bone cell function and tissue regeneration (El-Ghannam *et al.*, 2006). The main advantage of PSi over other biomaterials is its ability to degrade, in aqueous solutions, into non-toxic silicic acid [$Si(OH)_4$], which is the biologically significant form of Si that is in blood plasma. Silicic acid is vital for normal bone and connective tissue homeostasis. *In vivo*, PSi releases $Si(OH)_4$ with a negligible inflammatory response before being excreted in the urine (Popplewell *et al.*, 1998; Park *et al.*, 2009). The release of $Si(OH)_4$ due to the corrosion of PSi in plasma stimulates calcification and collagen growth, which could ideally accelerate new bone regeneration. Cell differentiation assays and ultrastructural measurements transmission electron microscope (TEM) have been carried out to explore the influence of Si on stem cell osteodifferentiation. It has been demonstrated that Si plays an important role in the expression of alkaline phosphatase, a specific biomarker for MSC differentiation (Fan *et al.*, 2011). OCN and bone sialoprotein (BSP) (non-collagenic proteins produced by osteoblast and involved in Ca–P crystal formation) are significantly more expressed by stem cells cultured in Si-rich medium, confirming that Si enhances stem cell differentiation into osteoblast, and that Si may directly be involved in OCN and BSP-mediated mechanisms (Gupta *et al.*, 2010). Histological evaluation and histomorphometric quantification of bone ingrowth and mineral apposition

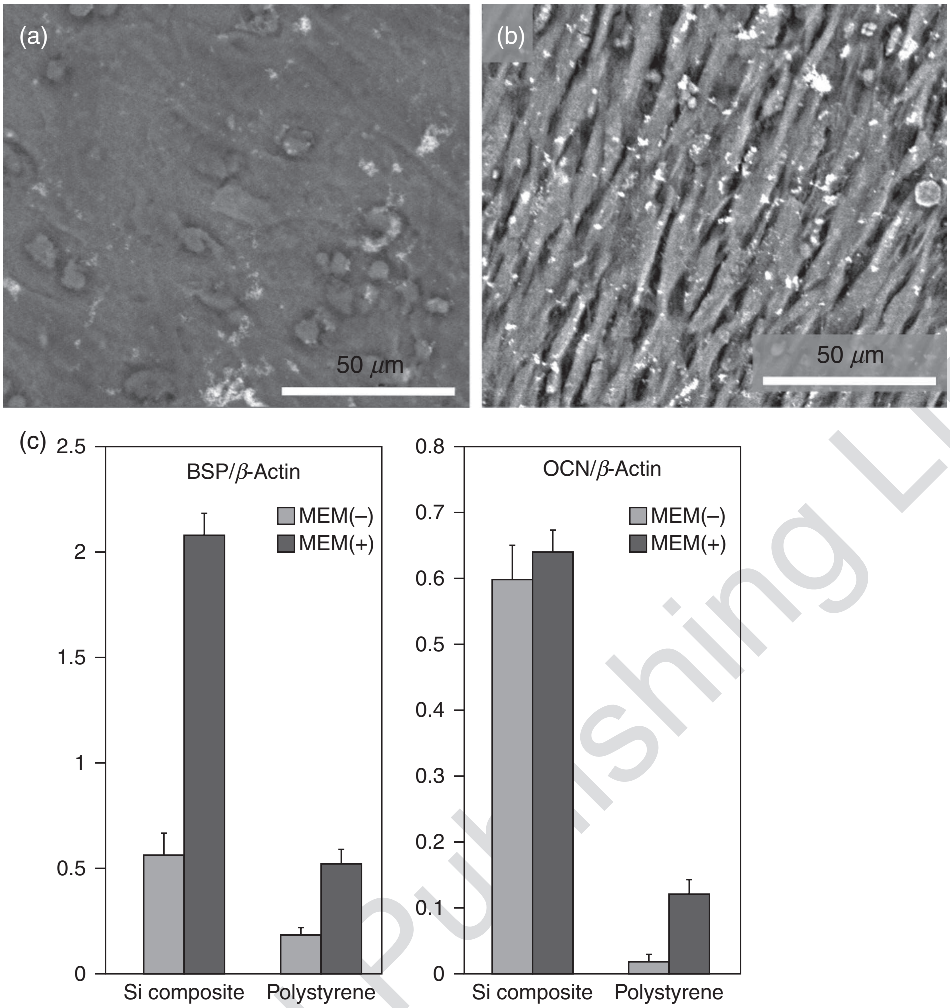

20.4 a and b: SEM of MSC osteodifferentiation and mineralized matrix deposits. (a) on PSi membrane (pore diameter = 30 nm); (b) on culture plate (polystyrene). On PSi, osteoblast-like cells are embedded in a mineralized matrix, while cells are more clearly visible on polystyrene, with a less abundant extracellular matrix. (c) quantity of mRNA bone sialoprotein (BSP) and osteocalcin (OCN) expressed by osteoblast-like cells on Si composite and on culture plate (polystyrene), after 2 days of culture in basal medium mimimum essential medium (MEM(–)) or in osteogenic medium (MEM(+)). Mean concentration of [Si] in culture medium containing Si composite is 6.5 mg/L. mRNA concentration is normalized to the concentration of β-Actin. Cells express more of osteogenic marker when cultured in the presence of [Si]. (*Source*: a and b: adapted from Collart Dutilleul (non-published data). c: adapted, with permission, from Gupta *et al.* (2010).)

in vivo demonstrated the benefits to bone ingrowth and repair through incorporation of Si (Hing *et al.*, 2006). These results show that PSi, by its degradation, plays a significant role in both stem cell osteodifferentiation and mineralization (Fig. 20.4). If it is clear that the dissolution of PSi in the form of $Si(OH)_4$ is a powerful mechanistic force behind the nucleation and growth of calcium phosphate, it also seems that Si surfaces provide nucleation sites for the formation of apatite deposits. This conclusion is based on mechanistic observations concerning surfaces formed of CaO-rich silica, noting that Si in these materials is responsible for directing the formation of apatite deposits in simulated plasma. Si intermediates as a nucleation site in directing the formation of calcium phosphate spherulites and growth of apatite on the scaffold (Whitehead *et al.*, 2008). Bone cells attached onto a surface containing high Si content absorb significantly higher concentrations of calcium than cells attached onto a surface containing low Si content. In conjunction with the absorption of high calcium concentration, attached bone marrow stem cells produce calcified nodules and mineralized extracellular matrix, indicating osteoblastic differentiation (El-Ghannam *et al.*, 2006). Thus, the mechanism of bone mineralization at the interface with bioactive surfaces is mainly cell mediated: an Si-rich phase provides a guided cell adhesion and tissue growth *in vitro*. The addition of Si to a scaffold affects surface topography, dissolution–reprecipitation rates and the bone apposition process (Porter, 2006).

20.6 Conclusions and future trends

In tissue engineering, developing synthetic grafts with sufficient combined mechanical strength, bioactivity and biodegradability for bone–tissue regeneration applications therefore remains an important challenge. A material that combines high bioactivity and porous structure (for good tissue growth) with high levels of mechanical strength (for load-bearing applications) will improve clinical outcomes and enable a significantly wider application of restorative materials (Zreiqat *et al.*, 2010). Most materials currently used in medical implants are bioinert and, as such, do not interact with living systems.

PSi has the property to be used as a scaffold, which could be well vascularized and integrated within the host skeleton, to stimulate the formation of new living bone. It provides a controlled biophysical and biochemical microenvironment, possibly directing the differentiation of stem cells into a specific lineage. Its porous, tunable and loadable structure allows cell adhesion and maintenance of cell function.

MSCs have a great potential for cell replacement, relying on their capacities to differentiate into several cell lineages, to modulate immune response and to secrete biological soluble factors. They have been assessed *in vivo* by direct transplantation to injured sites. However, new strategies involve the generation of an engineered construct combining biocompatible scaffolds with MSCs. Several pilot clinical trials are currently in process (http://www.clinicaltrials.gov).

PSi has been extensively studied *in vitro* for its capacity to support cell growth and differentiation, and *in vivo* for drug delivery applications. Its efficiency in bone tissue engineering has now to be confirmed in experimental research *in vivo* and in clinical trials.

20.7 References

Agrawal, A.A., Nehilla, B.J., Reisig, K.V., Gaborski, T.R., Fang, D.Z., Striemer, C.C., Fauchet, P.M. and McGrath, J.L. (2010) ‘Porous nanocrystalline silicon membranes as highly permeable and molecularly thin substrates for cell culture’, *Biomaterials*, **31**(20), 5408–5417.

Alvarez, S.D., Derfus, A.M., Schwartz, M.P., Bhatia, S.N. and Sailor M.J. (2009) ‘The compatibility of hepatocytes with chemically modified porous silicon with reference to in vitro biosensors’, *Biomaterials*, **30**, 26–34.

Anglin, E.J., Cheng, L., Freeman, W.R. and Sailor M.J. (2008) ‘Porous silicon in drug delivery devices and materials’, *Adv Drug Deliv Rev*, **60**(11), 1266–1277.

Arvidson, K., Abdallah, B.M., Applegate, L.A., Baldini, N., Cenni, E., Gomez-Barrena, E., Granchi, D., Kassem, M., Konttinen, Y.T., Mustafa, K., Pioletti, D.P., Sillat, T. and Finne-Wistrand, A. (2011) ‘Bone regeneration and stem cells’, *J Cell Mol Med*, **15**(4), 718–746.

Beniash, E., Metzler, R.A., Lam, R.S.K. and Gilbert, P. (2009) ‘Transient amorphous calcium phosphate in forming enamel’, *J Struct Biol*, **166**, 133–143.

Bessa, P.C., Casal, M. and Reis, R.L. (2008) ‘Bone morphogenetic proteins in tissue engineering: the road from laboratory to clinic, part II (BMP delivery)’, *J Tissue Eng Regen Med*, **2**, 81–96.

Bianco, P., Riminucci, M., Gronthos, S. and Robey, P.G. (2001) ‘Bone marrow stromal stem cells: nature, biology, and potential applications’, *Stem Cells*, **19**, 180–192.

Biggs, M.J.P., Richards, R.G. and Dalby, M.J. (2010) ‘Nanotopographical modification: a regulator of cellular function through focal adhesions’, *Nanomedicine: NBM*, **6**, 619–633.

Canham, L.T. (1995) ‘Bioactive silicon structure fabrication through nanoetching techniques’. *Adv Mater*, **7**(12), 1033–1037.

Cavalcanti-Adam, E.A., Volberg, T., Micoulet, A., Kessler, H., Geiger, B. and Spatz, J.P. (2007) ‘Cell spreading and focal adhesion dynamics are regulated by spacing of integrin ligands’, *Biophys J*, **92**(8), 2964–2974.

Clements, L.R., Wang, PY., Tasi, WB., Thissen, H. and Voelcker N.H. (2012) ‘Electrochemistry-enabled fabrication of orthogonal nanotopography and surface chemistry gradients for high-throughput screening’, *Lab Chip*, **12**, 1480–1486.

Coffer, J., Whitehead, M. and Nagesha, D. (2005) ‘Porous silicon-based scaffolds for tissue engineering and other biomedical applications’, *Phys Stat Sol A*, **202**(8), 1451–1455.

Cölfen, H. (2010) ‘Biomineralization: a crystal clear view’, *Nat Mater*, **9**(12), 960–961.

Connolly, J.F., Guse, R., Tiedeman, J. and Dehne, R. (1991) 'Autologous marrow injection as a substitute for operative grafting of tibial nonunions', *Clin Orthop Relat Res*, **266**, 259–270.

Collins, B.E., Dancil, K., Abbi, G. and Sailor, M.J. (2002) 'Determining protein size using an electrochemically machined pore gradient in silicon', *Adv Funct Mater*, **12**(3), 187–191.

Dalby, M.J., Gadegaard, N., Tare, R., Andar, A., Riehle, M.O., Herzyk, P. and Wilkinson, C.D.W. (2007) 'The control of human mesenchymal cell differentiation using nanoscale symmetry and disorder', *Nat Mater*, **6**(12), 997–1003.

d'Aquino, R., Graziano, A., Sampaolesi, M., Laino, G., Pirozzi, G., De Rosa, A. and Papaccio, G. (2007) 'Human postnatal dental pulp cells co-differentiate into osteoblasts and endotheliocytes: a pivotal synergy leading to adult bone tissue formation', *Cell Death Differ*, **14**(6), 1162–1171.

Dominici, M., Le Blanc, K., Mueller, I., Slaper-Cortenbach, I., Marini, F.C., Krause, D.S., Deans, R.J., Keating, A., Prockop, D.J. and Horwitz, E.M. (2006) 'Minimal criteria for defining multipotent mesenchymal stromal cells. The International Society for Cellular Therapy position statement', *Cytotherapy*, **8**(4), 315–317.

El-Ghannam, A. and Ning, C.Q. (2006) 'Effect of bioactive ceramic dissolution on the mechanism of bone mineralization and guided tissue growth *in vitro*', *J Biomed Mater Res A*, **76**(2), 386–397.

Engler, A.J., Sen, S., Sweeney, H.L. and Discher, D.E. (2006) 'Matrix elasticity directs stem cell lineage specification', *Cell*, **126**(4), 677–689.

Fan, D., Akkaraju, G.R., Couch, E.F., Canham, L.T. and Coffer, J.L. (2011) 'The role of nanostructured mesoporous silicon in discriminating in vitro calcification for electrospun composite tissue engineering scaffolds', *Nanoscale*, **3**(2), 354–361.

Forraz, N. and McGuckin, C.P. (2011) 'The umbilical cord: a rich and ethical stem cell source to advance regenerative medicine', *Cell Prolif*, **44**(1), 60–69.

Frith, J.E., Mills, R.J. and Cooper-White, J.J. (2012) 'Lateral spacing of adhesion peptides influences human mesenchymal stem cell behaviour', *J Cell Sci*, **125**(2), 317–327.

Gronthos, S., Mankani, M., Brahim, J., Robey, P.G. and Shi, S. (2000) 'Postnatal human dental pulp stem cells (DPSCs) in vitro and in vivo', *Proc Natl Acad Sci USA*, **97**(25), 13625–13630.

Graziano, A., d'Aquino, R., Laino, G., Proto, A., Giuliano, M.T., Pirozzi, G., De Rosa, A., Di Napoli, D. and Papaccio, G. (2008) 'Human CD34+ stem cells produce bone nodules *in vivo*', *Cell Prolif*, **41**(1), 1–11.

Gronthos, S., Brahim, J., Li, W., Fisher, L.W., Cherman, N., Boyde, A., DenBesten, P., Robey, P.G. and Shi, S. (2002) 'Stem cell properties of human dental pulp stem cells', *J Dent Res*, **81**(8), 531–535.

Gupta, G., Kirakodu, S. and El-Ghannam, A. (2010) 'Effects of exogenous phosphorus and silicon on osteoblast differentiation at the interface with bioactive ceramics', *J Biomed Mater Res A*, **95**(3), 882–890.

Hajj-Hassan, M., Khayyat-Kholghi, M., Wang, H., Chodavarapu, V. and Henderson, J. E. (2011) 'Response of murine bone marrow-derived mesenchymal stromal cells to dry-etched porous silicon scaffolds', *J Biomed Mater Res A*, **99**(2), 269–274.

Hing, K.A., Revell, P.A., Smith, N. and Buckland, T. (2006) 'Effect of silicon level on rate, quality and progression of bone healing within silicate-substituted porous hydroxyapatite scaffolds', *Biomaterials*, **27**(29), 5014–5026.

Hu, Y., Winn, S.R., Krajbich, I. and Hollinger, J.O. (2003) ‘Porous polymer scaffolds surface-modified with arginine-glycine-aspartic acid enhance bone cell attachment and differentiation in vitro’, *J Biomed Mater Res A*, **64**(3), 583–590.

Lagunas, A., Comelles, J., Martínez, E., Prats-Alfonso, E., Acosta, G. A., Albericio, F. and Samitier, J. (2012) ‘Cell adhesion and focal contact formation on linear RGD molecular gradients: study of non-linear concentration dependence effects’, *Nanomedicine: NBM*, **8**(4), 432–439.

Li, X., Wang, H., Touma, E., Rousseau, E., Quigg, R.J. and Ryaby, J.T. (2007) ‘Genetic network and pathway analysis of differentially expressed proteins during critical cellular events in fracture repair’, *J Cell Bioch*, **100**(2), 527–543.

Low, S.P., Williams, K.A., Canham, L.T. and Voelcker, N.H. (2006) ‘Evaluation of mammalian cell adhesion on surface-modified porous silicon’, *Biomaterials*, **27**(26), 4538–4546.

Ma, T. (2010) ‘Mesenchymal stem cells: from bench to bedside’, *World J Stem Cell*, **2**(2), 13–17.

Marolt, D., Knezevic, M. and Novakovic, G.V. (2010) ‘Bone tissue engineering with human stem cells’, *Stem Cell Research & Therapy*, **1**, 10–20.

Ngankam, P.A., Lavalle, P., Voegel, J.C., Szyk, L., Decher, G., Schaaf, P. and Cuisinier, F.J.G. (2000) ‘Influence of polyelectrolyte multilayer films on calcium phosphate nucleation’, *J Am Chem Soc*, **122**, 8998–9005.

Nudelman, F., Pieterse, K., George, A., Bomans, P.H.H., Friedrich, H., Brylka, L.J., Hilbers, P.A.J., de With, G. and Sommerdijk, N.A.J.M. (2010) ‘The role of collagen in bone apatite formation in the presence of hydroxyapatite nucleation inhibitors’, *Nat Mater*, **9**, 1004–1009.

Park, J-H., Gu, L., Maltzahn, von, G., Ruoslahti, E., Bhatia, S. N. and Sailor, M. J. (2009) ‘Biodegradable luminescent porous silicon nanoparticles for in vivo applications’, *Nat Mater*, **8**(4), 331–336.

Popplewell, J. F., King, S. J., Day, J. P., Ackrill, P., Fifield, L. K., Cresswell, R. G., di Tada, M.T. and Liu, K. (1998) ‘Kinetics of uptake and elimination of silicic acid by a human subject: a novel application of ^{32}Si and accelerator mass spectrometry’, *J Inorg Biochem*, **69**(3), 177–180.

Porter, A.E. (2006) ‘Nanoscale characterization of the interface between bone and hydroxyapatite implants and the effect of silicon on bone apposition’, *Micron*, **37**(8), 681–688.

Sailor, M.J. (2011) *Porous Silicon in Practice*, Weinheim, Wiley-VCH.

Wang, P-Y., Clements, L.R., Thissen, H., Jane, A., Tsai, W-B. and Voelcker, N. (2012) ‘Screening mesenchymal stem cell attachment and differentiation on porous silicon gradients’, *Adv Funct Mater*, **22**(16), 3414–3423.

Whitehead, M.A., Fan, D., Mukherjee, P., Akkaraju, G.R., Canham, L.T. and Coffer, J.L. (2008) ‘High-porosity poly(epsilon-caprolactone)/mesoporous silicon scaffolds: calcium phosphate deposition and biological response to bone precursor cells’, *Tissue Eng*, **14**(1), 195–206.

Yang, C.Y., Huang, L-Y., Shen, T-L. and Yeh, J.A. (2010) ‘Cell adhesion, morphology and biochemistry on nano-topographic oxidized silicon surfaces’, *Eur Cell Mater*, **20**, 415–430.

Yang, C.Y., Liao, T.C., Shuai, H.H., Shen, T.L., Yeh, J.A. and Cheng, C.M. (2012) ‘Micropatterning of mammalian cells on inorganic-based nanosponges’, *Biomaterials*, **33**(20), 4988–4997.

Yim, E.K.F., Darling, E.M., Kulangara, K., Guilak, F. and Leong, K.M. (2010) ‘Nanotopography-induced changes in focal adhesions, cytoskeletal organization, and mechanical properties of human mesenchymal stem cells’, *Biomaterials*, **31**, 1299–2306.

Zemel, A., Rehfeldt, F., Brown, A.E.X., Discher, D. E. and Safran, S.A. (2010) ‘Optimal matrix rigidity for stress fiber polarization in stem cells’, *Nat Phys*, **6**(6), 468–473.

Zreiqat, H., Ramaswamy, Y., Wu, C., Paschalidis, A., Lu, Z., James, B., Birke, O., McDonald, M., Little, D. and Dunstan, C.R. (2010) ‘The incorporation of strontium and zinc into a calcium-silicon ceramic for bone tissue engineering’, *Biomaterials*, **31**(12), 3175–3184.

Zuk, P. A., Zhu, M., Ashjian, P., De Ugarte, D.A., Huang, J.I., Mizuno, H., Alfonso, Z.C., Fraser, J.K., Benhaim, P. and Hedrick, M.H. (2002) ‘Human adipose tissue is a source of multipotent stem cells’, *Mol Biol Cell*, **13**, 4279–4295.

Human mesenchymal stem cells from dental pulp behavior onto bioresorbable porous silicon scaffolds

Pierre-Yves Collart-Dutilleul[1], *Emilie Secret*[2], *Ivan Panayotov*[1], *Dominique Deville de Périère*[1], *Raúl J. Martín-Palma*[3], *Vicente Torres-Costa*[3], *Marta Martin*[4], *Csilla Gergely*[4], *Jean-Olivier Durand*[2], *Frédérique Cunin*[2] *and Frédéric J. Cuisinier*[1]

[1]BioNano Laboratory EA 4203, Montpellier 1 University, Montpellier, France

[2]Matériaux Avancés Catalyse Santé, Institut Charles Gerhardt, UMR 5253 CNRS, Montpellier, France

[3]Departamento de Física Aplicada, Universidad Autónoma de Madrid, 28049 Cantoblanco, Madrid, Spain

[4]Laboratoire Charles Coulomb, Université Montpellier 2, UMR 5221 CNRS, Montpellier, France

KEYWORDS

Porous silicon, dental pulp stem cells, cell adhesion, surface functionalization, tissue engineering.

ABSTRACT

In regenerative medicine, stem cell-based therapy often requires a scaffold to deliver cells and/or growth factors to the injured site. Porous silicon (pSi) is a promising biomaterial for tissue engineering as it is both non-toxic and bioresorbable. Moreover, surface modification can offer control over the degradation rate of pSi and can also promote cell adhesion. Dental pulp stem cells (DPSC) are pluripotent mesenchymal stem cells found within the teeth and constitute a readily source of stem cells. Thus, coupling the good proliferation and differentiation capacities of DPSC with the textural and chemical properties of the pSi substrates provides an interesting approach for therapeutic use. In this study, the behavior of human DPSC is analyzed on pSi substrates presenting pore of various sizes, 10 ± 2 nm, 36 ± 4 nm and 1.0 ± 0.1 μm, and undergoing different chemical treatments: thermal oxidation, silanization with aminopropyltriethoxysilane (APTES), and hydrosilylation with undecenoic acid or semicarbazide. DPSC adhesion and proliferation were followed for up to 72 h by fluorescence microscopy, scanning electron microscopy (SEM), enzymatic activity assay, and BrdU assay for mitotic activity. Porous Silicon with 36 nm pore size was found to offer the best adhesion and the fastest growth rate for DPSC compared to pSi comporting smaller pore size (10 nm) or larger pore size (1 μm), especially after silanization with APTES. Hydrosilylation with semicarbazide favored cell adhesion and proliferation, especially mitosis after cell adhesion, but such chemical modification has been found to led to a scaffold that is stable for only 24 to 48 h in culture medium. Thus, semicarbazide-treated pSi appeared to be an appropriate scaffold for stem cell adhesion and immediate *in vivo* transplantation, while APTES-treated pSi was found to be more suitable for long term *in vitro* culture, for stem cells proliferation and differentiation.

INTRODUCTION

In regenerative medicine, tissue engineering applications are based on the development of biological substitutes that can restore, maintain or even improve tissue functions: tissue engineering combines cells and bioactive factors in a defined microenvironment created by a biomaterial scaffold. A key component for tissue engineering is the biomaterial scaffold that, ideally, should support cell attachment, proliferation and differentiation, and be biocompatible and biodegradable at a controlled rate.[1] Stem cell-based therapy often requires a scaffold to carry cells to the injured site. Porous silicon (pSi) appears to be a promising biomaterial for tissue engineering as it is both non-toxic and bioresorbable under physiological conditions, and it dissolves progressively into nontoxic silicic acid.[2] Its dissolution rate is dependent on the pore geometry and surface chemical properties, and these two factors influence cell adhesion.[3,4] Moreover, this tunable, biocompatible, and resorbable material has been reported to favor the growth of hydroxyapatite, suggesting the possible bone implantability of the material.[5] Its biocompatibility and immunogenicity has already been demonstrated under different conditions and it additionally offers useful photoluminescence properties.[6] Furthermore, pSi-based scaffolds have been investigated for orthopedic[7] and ophtalmic implants,[8] for controlling the adhesion and proliferation of different cell types,[3,9,10] and even as intravenously injectable particles for imaging tumors *in vivo*[11] or retina pressure actuators.[12]

Surface treatment resulting in accessible porosity with chemically stable inner surface is a key step to prevent rapid hydrolysis and degradation of the porous matrix in aqueous cell culture environments, without eliciting any undesirable effects on the cells. Moreover, surface chemical modification by turning pSi from hydrophobic to hydrophilic promotes cell adhesion and growth.[3,13] The most common and simple surface treatment is oxidation, which can be performed by either ozone, aging, thermal or chemical treatments. Amine-terminated modifications as silanization with aminopropyl trimethoxysilane or triethoxysilane improve pSi chemical stability and enhance cell adhesion in comparison to oxidized pSi.[3] Thermal hydrosilylation was also used to graft chemical species to generate a substrate for cell adhesion and proliferation, such as dodecene, undecenoic acid or oligoethylene glycol.[9]

Substrate topography has been known for a long time to affect crucial cell functions, namely adhesion, proliferation, migration,and differentiation. Moreover, material surface morphology has strong effects on cell cytoskeleton and morphology.[14] Furthermore cellular organization requires that a cell assess its relative location, taking in multiple cues from its microenvironment i.e. the extracellular matrix *in vivo*, and the supporting scaffold *in vitro*.[15] Cells respond to topographic surfaces in a wide variety of ways, which depend upon cell type, pore size, as well as the physicochemical properties of the substrate material. The effect of pore size and porosity of pSi on cell growth is of particular relevance. Indeed, its pore dimensions can be precisely controlled and are highly tunable during pSi electrochemical anodization. A variety of pore sizes can be produced: from micropores (< 2 nm), mesopores (2–50 nm) to macropores (> 50 nm) depending on the preparation conditions.[16] Although microscale topography modulates cellular behaviour *in vitro*, it is important to consider that cells *in vivo* make contact with microscale as well as nanoscale topographical features. Diverse topographical features have been assessed for different cell types, at the micrometer and submicrometer scale, and some recent studies on pSi have focused specifically on pore geometry influence on cell adhesion and proliferation.[17-20] Pore geometry was clearly shown to affect the cellular response, but each cell type responded differently. Rat hippocampal neurons were observed to preferentially adhere on macroporous surfaces, with a pore size ranging between 50 and 100 nm, rather than on flat silicon surfaces.[17]

Neuroblastoma cells cultured over continuous porous gradient substrates were more likely to develop on surface topography with feature sizes of <20 nm, and substrates with an average pore size of a few hundreds of nanometers restricted cell adhesion and proliferation.[4] Primary human endothelial cells, mouse fibroblasts, mouse neuroblastoma cells, and human cortical neuron cell lines adhered and proliferated more on mesoporous silicon than on flat silicon, with a tendency to proliferate more on pSi with an average pore size of ≈5 nm, rather than ≈20 nm.[20] It is of interest to note that this was, so far, the only study assessing primary human cells. Rat mesenchymal stem cells (rMSC) adhesion was enhanced as pore size decreased, with a maximum proliferation for an average pore size of ≈20 nm but responded more strongly to surface chemical changes during short-term culture[19] and had a high proliferation rate also on flat silicon.[18]

Coupling the auspicious capacities of human adult mesenchymal stem cells (hMSC) with the unique properties of pSi substrates provides a promising approach for therapeutic application in regenerative medicine. Indeed, mesenchymal stem cells therapeutic potential has generated significant excitement in the field of regenerative medicine, as they can be found in various niches within human body. The ability of these cells to self-renew and differentiate into multiple tissues makes them an attractive cell source for cell-based regenerative therapies. MSCs have considerable potential for the treatment of musculoskeletal disorders owing to their expansion capacity, immunosuppressive properties and ability to differentiate into bone and cartilage.[21] Adult stem cells constitute the source of differentiated cells for the regeneration of tissues that are diseased or injured. In adults, these cells are accessible from different origins, such as bone marrow, adipose tissue or dental pulp.[22]

In this manuscript, we investigated for the first time the behavior of primary culture of hMSC on pSi scaffolds. Mesenchymal stem cells from the dental pulp, named Human Dental Pulp Stem Cells (DPSC),[23] were studied for adhesion and proliferation on oxidized mesoporous and macroporous pSi substrates, presenting pore size of 10 ± 2 nm, 36 ± 4 nm and 1.0 ± 0.1 µm. We also evaluated the influence of pSi substrate surface modification with CO_2H, NH_2 or $NHCONHNH_2$ groups on the cell behaviour. After characterization of the silicon substrates, cell adhesion and proliferation behavior were studied using fluorescence and electron microscopy, enzymatic proliferation assays and bromodeoxyuridine (BrdU) incorporation for the detection of proliferating cells.

MATERIALS AND METHODS

Human Dental Pulp Stem Cells (DPSC)

Human impacted third molar extracted for orthodontic reasons were recovered from healthy patients (15-18 years of age). Written informed consent was obtained from the parents of the patients. This protocol was approved by the local ethical committee (*Comité de Protection des Personnes*, Montpellier hospital, France). Tooth surfaces were cleaned using 2% chlorhexidine and cut around the cementum-enamel junction by using sterilized disc. The teeth were then broken into 2 pieces to reveal the pulp chamber. The pulp tissue was gently separated from the crown and root and then digested in a solution of 3 mg/mL collagenase type I and 4 mg/mL dispase (BD Biosciences, Bedford, MA) for 1 hour at 37°C. The solution was then filtered through 70 µm Falcon strainers and immersed in αMEM supplemented with 10% fetal bovine serum (FBS), 100 U/mL penicillin, 100 µg/mL streptomycin (all from Invitrogen, Carlsbad, CA, USA) and placed in 75 ml flasks. Cells were incubated for 1 week at 37°C with 5% CO_2. Non-adherent cells were removed by a change of medium 24 h after cell seeding.

DPSC characterization

After 1 week, sub-confluent cells were collected and analyzed for minimal criteria to define human mesenchymal stem cells, such as adherence to plastic, expression of cell surface antigens and ability to differentiate into osteoblasts, adipocytes and chondroblasts *in vitro*.[24] The antigen profiles of cultured DPSCs were analyzed by detecting the expression of the cell surface markers CD90, CD146, CD117 and CD45 using flow cytometry (all antibodies from Miltenyi Biotec, Paris, France). CD90 is a widely accepted marker for mesenchymal stem cells, CD146 is a marker expressed in perivascular mesenchymal stem cells, CD117 is the receptor of stem cell factor, and CD45 is a marker of hematopoietic cells, mainly myeloid progenitors.[25,26] The latter has been used to demonstrate the absence of contamination by CD45+ hematopoietic progenitors. Cells were controlled for pluripotency with *in vitro* osteogenic, adipogenic and chondrogenic differentiation following a previously described protocol.[27] Briefly, for osteogenic and adipogenic differentiation, dental pulp cells were seeded at a density of 10^5 cells/cm^2 and maintained in αMEM supplemented with 10% FBS until confluence. Cells were then cultured in osteogenic medium (αMEM supplemented with 15% FBS, dexamethasone, L-ascorbate phosphate, and β-glycerophosphate) or in adipogenic medium (αMEM supplemented with 10% FBS, dexamethasone, insulin, and isobutylmethylxanthine) for 21 days (all products from Invitrogen, Carlsbad, CA, USA, except L-ascorbate phosphate and β-glycerophosphate from Sigma, St Louis, MO, USA). Control cultures were maintained without osteogenic or adipogenic supplements. To induce chondrogenic differentiation, cells were cultured for 21 days as pellets in a serum-free expansion medium containing dexamethasone, L-ascorbate phosphate, L-proline, sodium pyruvate, ITS-Premix, and TGF-β3 (all products from Invitrogen, Carlsbad, CA, USA, except L-ascorbate phosphate and sodium pyruvate from Sigma, St Louis, MO, USA). Control pellet cultures were maintained in basal medium.

Porous silicon (pSi) scaffolds preparation

Silicon wafers were obtained from Siltronix (Siltronix, Archamps, France). P++ type boron-doped crystalline silicon wafers with 0.0008 - 0.0012 Ωcm resistivity were obtained from Siltronix®. Wafers were etched in a custom-made Teflon cell at a constant current density of either 30 mA/cm^2 for 10 min or 300 mA/cm^2 for 2 min 15 s, in a hydrofluoric acid (HF) solution in ethanol (3:1 HF:ethanol solution, volume ratio). To create pSi with larger pores (1 µm), p-type <100> wafers with 7 - 21 Ωcm resistivity were etched at a constant current density of 4.5 mA/cm2 for 10 min, in a 50% HF solution in dimethylformamide (DMF, Sigma, St Louis, MO, USA). Etched wafers were oxidized at 800°C for 1 hour. The wafers were cut into 0.5 cm^2 pieces. Some of the samples etched in a 300 mA/cm^2 current were also submitted to various chemical treatments: silanization with aminopropyltriethoxysilane (APTES) after thermal oxidation (as described above), hydrosilylation with undecenoic acid without pre-oxidation treatment, and hydrosilylation with semicarbazide without pre-oxidation treatment (all reagents from Sigma, St Louis, MO, USA). PSi surface modifications with APTES, and with undecenoic acid were described elsewhere.[3,9] The covalent attachment of the semicarbazide to hydrogen-terminated pSi surfaces by thermal hydrosilylation was realized according to recently published procedure using tert-Butyl-2[(allylamino)carbonyl]hydrazine carboxylate.[28] The removal of the protecting group yields a semicarbazide-terminated monolayer.[29] For use in cell culture, the wafers were sterilized with 70% ethanol (volume ratio) for 10 min before drying under sterile airflow.

Surface characterization

The topography of the surface modified pSi samples was analyzed by environmental scanning electron microscopy (SEM) (Analytic FEI Quanta FEG 200) to determine the pore size, and by atomic force microscopy (AFM) (Asylum MFP-3D, Asylum Research, Santa Barbara, CA) to determine the surface roughness. For SEM, an acceleration voltage of 20.00 kV was used in a pressure of 0.5 Torr. For AFM, gold-coated silicon nitride rectangular cantilevers were used with a typical spring constant of 30 pN/nm^{-1}, tip radius ~30 nm (BL-RC150 VB-C1: Bio- Lever A, Olympus Optical Co., Ltd., Tokyo, Japan). The spring constant for each cantilever was determined by thermal noise method within the supplied software. Height images were recorded in tapping mode in liquid at room temperature. Typically, 512 x 512 point scans were taken at a scan rate of 1 Hz per line.

Surface tension was determined using sessile drop contact angle measurements, conducted in a custom-made set-up consisting of a syringe dispenser, a sample stage, a macro lens and a CCD camera. 5µl of MilliQ water was spotted onto the surface at room temperature. Images of the drop profiles were captured and ImageJ® software was used to measure contact angles on both sides of the droplet. A minimum of four replications was conducted for each sample surface.

Cell adhesion

DPSC attachment was monitored by fluorescence microscopy. Cells were seeded onto the surface of sterilized pSi at a cell density of 5x10^4 cell/ml. Flat silicon (non etched silicon wafers) and glass coverslip were used as controls. Cells were incubated for 4h, 24h, 48h and 72h at 37°C with 5% CO_2, in a humidified incubator, in ultra low adherence 24 well plates (Corning, NY, USA) which inhibit cell attachment on the tissue culture plate, allowing DPSC to attach only to the pSi. After the incubation time, the cells were fixed with 2.5% glutaraldehyde and stained with 50 µg/mL of 4,6-diamidino-2-phenylindole (DAPI, Sigma, St Louis, MO, USA) for 30 min before being washed with phosphte buffer saline (PBS; Invitrogen, Carlsbad, CA, USA) to remove any non-adherent cells. Cells were observed under fluorescence microscopy at an excitation wavelength of 290 nm. Controls were cells cultured on glass coverslip and flat silicon, cut into 0.5 cm^2 squares. Cell counts were conducted at five different locations on the surface of each sample (four peripheral and one central) in areas of 1400 µm x 1050 µm.

Proliferation assays

Cell proliferation was first measured via quantification of acid phosphatase activity using paranitrophenylphosphate phosphatase test (pNPP).[30] DPSC proliferation was assessed after 4 h, 24 h, 48 h and 72 h incubation. At the end of each experimental time, the cells were washed three times with PBS and lysed with 500 mL of the acid phosphatase lysis buffer (0.1 M sodium acetate, 0.1% Triton X-100, pH 5.5), supplemented with 1 mg/mL of pNPP (all products from Sigma, St Louis, MO, USA). After 1 h incubation at 37 °C, the reaction was stopped by the addition of 10 µL of 1 N NaOH (Sigma, St Louis, MO, USA). The supernatent was removed, placed in a new 24 wells plate and the yellow colorimetric reaction was measured by a microtiter plate reader at 405 nm. All proliferation experiments were performed at least in triplicate and results were normalized according to the glass coverslip control at 72 h, for which 100% of proliferation was attributed.

The proliferation rate of DPSCs on pSi was also assessed by bromodeoxyuridine (BrdU, Invitrogen, Carlsbad, CA, USA) incorporation for 24 h.[31] DPSC were seeded on the various pSi scaffolds at a density of 10^5 cells/ml in αMEM supplemented with 10% FBS with 1:100 diluted

BrdU labeling (Invitrogen, Carlsbad, CA, USA). After 24 h incubation at 37°C, samples were rinsed 3 times in PBS, fixed in 4% paraformaldehyde, rinsed again 3 times in PBS and put in 1.5M HCl (Sigma, St Louis, MO, USA) for 30 min at room temperature to dissociate DNA strands. Samples were washed with PBS, incubated in PBS with 0.1% Triton X-100 and 1% BSA for 1 h at room temperature, then incubated with mouse anti-BrdU primary antibody (Milteny) overnight at 4°C. After immunostaining, cells were washed with PBS/1% BSA, incubated with FITC conjugated rabbit anti-mouse secondary antibody for 30 min and counterstained with 2μg/ml Hoeschst 33342 (Sigma, St Louis, MO, USA) for nucleus staining. Samples were observed under fluorescence microscopy at an excitation wavelength of 290 nm for nuclei (blue staining) and 490 nm for BrdU (green staining). All experiments were performed at least in triplicate and the number of BrdU-positive cells was expressed as a percentage of the total number of cells, counted at 5 different points per sample.

Cellular morphology and viability

Fluorescein diacetate (FDA) and propidium iodide (PI) staining was used to observe cell morphology and to distinguish viable and dead cells (both products from Invitrogen, Carlsbad, CA, USA). FDA, which enters viable cells by energy-dependent endocytosis, yield a bright green color; while PI, which interacts with RNA and DNA of cells having disrupted cytoplasmic and nuclear membranes, produces a red color.[32] Living cells were stained with 25 μg/mL of fluorescein diacetate (FDA) and 20 μg/ml of propidium iodide (PI), and incubated for 3 min at 37°C. After staining, samples were washed with PBS before being observed under a Nikon TE2000-E microscop equipped with a Nikon digital camera at an excitation wavelengths of 480 nm for FDA and 630 nm for PI. Observations were conducted at five different locations on the surface of each sample (four peripheral and one central) at magnifications x20 and x40. All experiments were made in triplicate.

SEM evaluation of DPSC morphology and spreading

The cells were cultured on the various pSi scaffolds and control for 24 h under normal conditions, as described above. After 24 h incubation the cells were washed twice with PBS buffer and fixed with 2.5% glutaraldehyde for 1 h at room temperature. After washing the specimens were dehydrated in graded ethanol solutions from 50% to 100%, and in hexamethyldisilazane (HMDS, Ted Pella, Redding, CA, USA). The samples were then sputter-coated with platinum. Scanning electron microscopy (SEM) was performed on an Analytic FEI Quanta FEG 200 microscope with an acceleration voltage of 15 kV in a pressure of 10^{-5} Torr. From the SEM images, two parameters for characterizing the cell morphology were considered: the cell area (in μm^2), defined as the area covered by the cell projected over the substrate and the cell circularity, defined as the ratio between the shorter and the longer axis of the cell (value between 0 for elongated cells and 1.00 for round cells). All experiments were made in triplicate.

Statistical analysis

All data were evaluated with a Shapiro-Wilk normality test. The cell attachment evaluations (cell counts) were plotted as mean ± standard error of the mean and statistical analyses were performed using a parametric Student t-test. The results of proliferation experiments with pNPP enzymatic assays were normalized according to the glass coverslip control at 72 h, for which 100% of proliferation was attributed. The data were plotted as mean ± standard error of the mean and statistical analyses were performed using a parametric Student t-test. The results of BrdU proliferation assay, cell surface area and cell circularity were analyzed with a non-parametric one-way Tukey ANOVA test (SigmaStats, SPSS Inc., Chicago, IL, USA). A p-value of <0.05 was considered to be significant.

RESULTS

pSi samples

PSi substrates were generated from bulk boron-doped p-type silicon wafers via anodization.[16] Substrates with various pore sizes were obtained by modulating the etching conditions and the doping level of the silicon wafer. Figure 1 shows representative SEM and AFM images of the pSi substrates; distinct textural features are depicted when comparing the different pSi substrates.

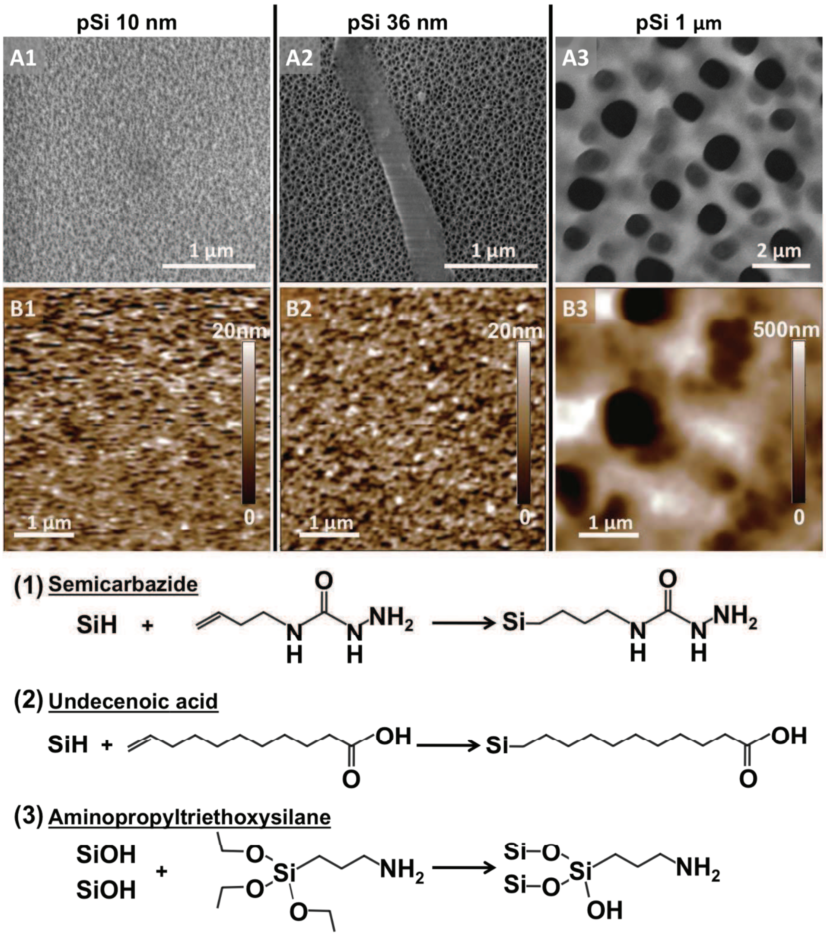

Figure 1: Characterization of the porous silicon scaffolds. Surface topography of the silicon substrates imaged with (A) scanning electron microscopy and (B) atomic force microscopy. Porous silicon with mean pore diameter of 10 ± 2 nm, 36 ± 4 nm and 1.0 ± 0.1 µm are shown as A1-B1, A2-B2 and A3-B3 respectively. Surface chemical treatments are presented as: (1) Non oxidized pSi hydrosililated with semicarbazide. (2) Non oxidized pSi hydrosililated with undecenoic acid. (3) Oxidized pSi silanized with APTES.

PSi substrates obtained from silicon wafers with a resistivity of 0.0008 - 0.0012 Ωcm by applying a constant current density of 30 mA/cm^2 and 300 mA/cm^2 had an average pore diameter of 10 ± 2 nm (pSi 10 nm) and 36 ± 4 nm (pSi 36 nm), respectively. The pSi layers produced from silicon wafers with 7 - 21 Ωcm resistivity, by applying a current density of 4.5 mA/cm^2, had an average pore diameter of 1020 ±100 nm (pSi 1 µm). The pSi substrates were quite uniformly porosified. Topographic images of pSi were obtained using AFM, and the calculated statistical roughness (RMS) of the substrate were found at 1.9 ± 0.7 nm for “pSi 10 nm”, 7 ± 2 nm for “pSi 36 nm” and 54 ± 20 nm for “pSi 1 µm”.

Surface chemical treatments realized on “pSi 36 nm” substrates are hydrosilylation with undecenoic acid or semicarbazide, and silanization (after thermal oxidation) with APTES. The reaction schemes of the chemical treatments are presented in Figure 1. The sample pSi 36 nm was chosen because it displayed the best results in term of cell adhesion, compared to pSi 10 nm and pSi 1 µm (Figure 2). Water contact angle measurements performed after surface functionalization revealed that all the substrates were hydrophilic (Table 1). Oxidized pSi hydrophilicity was attributed to the formation of a polar Si-OH capped surface after oxidation. By analyzing SEM micrographs, the surface porosities (ratio between total area of the pores and the area of the considered region of interest) were found to be as follows: 40 ± 4% for pSi 10nm, 45 ± 6% for pSi 36nm and 24 ± 4% for pSi 1µm.

	Flat Si	pSi 10 nm	pSi 36 nm	pSi 1 µm
Oxidized	26° ± 4	16° ± 2	15° ± 3	33° ± 5
Undecenoic acid			35° ± 5	
APTES			37° ± 6	
Semicarbazide			12° ± 3	

Table 1: Water contact angle of the various scaffolds (Flat Si and pSi)

Cell adhesion and growth

We examined DPSC attachment to various surface-modified pSi layers and compared the results with those of DPSCs cultured on glass coverslips and on flat silicon wafers after a period of 4 h, 24 h, 48 h and 72 h. The results are shown in Figure 2.

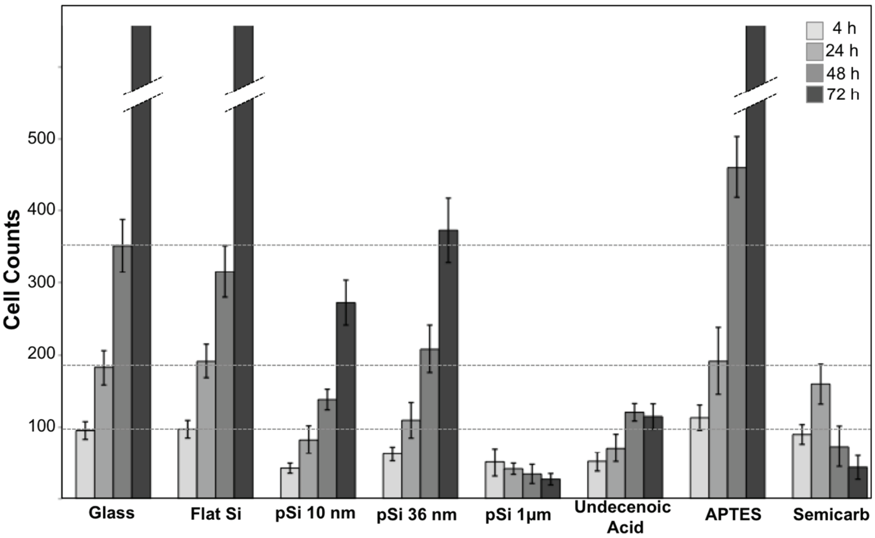

Figure 2: DPSC attached on various type of pSi, after 4h, 24h, 48h and 72h of incubation. Glass coverslip and (non-porous) flat silicon were used as controls. Cells were counted per 1400 μm x 1050 μm area, in five areas per samples. The bars protruding from the frame correspond to cells reaching confluence.

The experimental results showed that initial cell adhesion and growth were very similar on glass coverslip, Flat Si, APTES-treated pSi and semicarbazide-treated pSi, after 4 h and 24 h. Initial cell adhesion on oxidized pSi (pSi 10nm, pSi 36nm and pSi 1μm) and undecenoic acid-treated pSi were significantly lower compared to glass coverslip ($p<0.001$, $p=0.003$, $p<0.001$, and $p<0.001$ respectively). However, DPSC started to proliferate on pSi 10 nm and pSi 36 nm after 24 h following the same growth pattern observed on glass coverslip, while the number of cells slightly decreased on pSi 1 μm and on undecenoic acid-treated pSi after 24h and 48 h respectively. After 48 h, the numbers of cells were similar on glass coverslip and on flat Si, significantly higher on APTES-treated pSi ($p<0.001$) and significantly lower on semicarbazide-treated pSi ($p<0.001$), pSi 10 nm ($p<0.001$) and pSi 36 nm ($p<0.001$). It is remarkable that there were significantly more cells on pSi 36 nm than on pSi 10 nm after 48 h and 72 h ($p=0.006$ and $p=0.004$, respectively), and that the number of cells on semicarbazide-treated pSi increased during 24 h and decreased abruptly after 48 h. After 72 h, DPSC reached confluence on glass coverslip, flat Si and APTES-treated pSi.

Cells were stained with the vital dye FDA to observe cell adherence and cytoplasmic spreading. The morphologies of DPSC on surface modified pSi at early attachment stage (after 4 h) are shown in Figure 3.

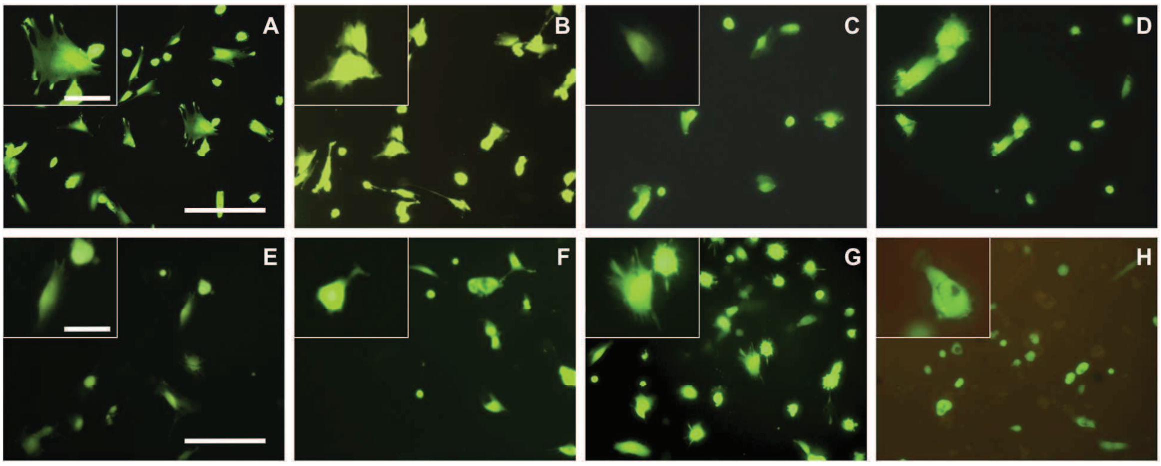

Figure 3: Fluorescence microscopy of DPSC on the various scaffolds after 4 h incubation. Cells are stained with vital FDA staining (cytoplasma: green staining). A: glass coverslip, B: Flat Si, C: pSi 10nm, D: pSi 36nm, E: pSi 1µm, F: undecenoic acid-treated pSi, G: APTES-treated pSi, H: semicarbazide-treated pSi. Main pictures: x20, scale bar = 100 µm. Inserts: magnification x40, scale bar = 40 µm.

From Figure 3 it is obvious that cells attached on all surfaces, with various shapes from normal fibroblastic morphology (Fig 3A, 3B and 3G) to less-spread cells with protrusions (FIG 3C and 3D), and even round cells (Fig 3E, 3F and 3H). Fibroblastic morphologies were found mainly on glass coverslip, flat Si and APTES-treated pSi. Cells with protrusions were mainly found on pSi 10 nm and pSi 36 nm, while round cells with few protrusions were recovered on pSi 1 µm, undecenoic acid-treated pSi and semicarbazide-treated pSi. These results correlate well with the results on cell adhesion described from Figure 2.

Cell proliferation

DPSC proliferation over a 3-day-time period, assessed by acid phosphatase activity, was evaluated for the various pSi scaffolds, and compared to that of glass coverslip and Flat Si. In order to normalize the results, 100% cell enzymatic activity was attributed to the value found for glass coverslip after 72 h of cell incubation (Fig. 4).

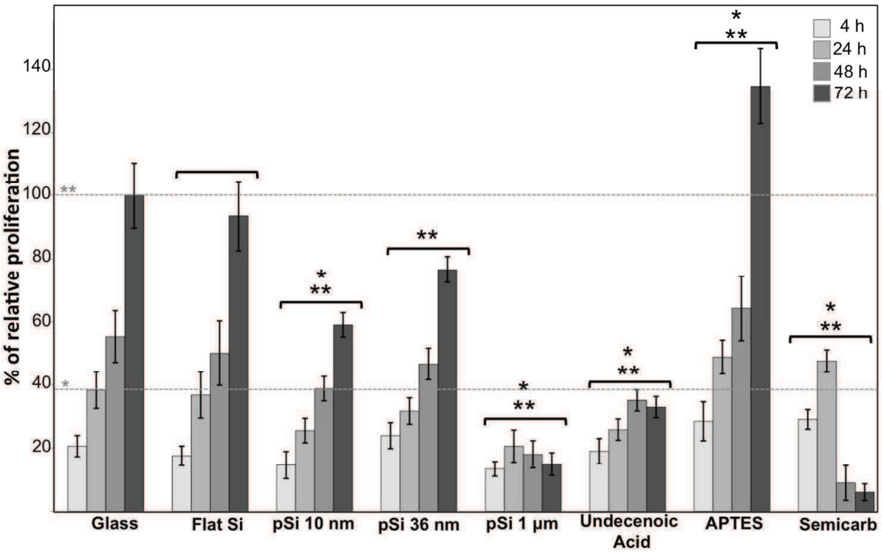

Figure 4: DPSC proliferation at 4 h, 24 h, 48 h and 72 h on various pSi surfaces, assessed by acid phosphatase activity determination. Glass coverslip and oxidized non-porous silicon (flat Si) were used as control. In order to normalize the results, 100% adhesion was attributed to cells attached on glass coverslip after 72 h of cell seeding. All experiments were performed in triplicate. Statistical significance was determined by using the Student's t test ($P < 0.05$) for comparison with glass coverslip: (*)Statistical difference at 24 h. (**)Statistical difference at 72 h.

The experiments showed that DPSCs clearly proliferated at all time points on glass coverslip, flat Si, pSi 10 nm, pSi 36 nm and APTES-treated pSi, while the proliferation was limited on pSi 1 µm and undecenoic acid-treated pSi. For semicarbazide-treated pSi, the proliferation rate was higher compared to glass coverslip until 24 h, and dropped dramatically after 48 h. After 24 h of incubation, the proliferation rate was equivalent on glass coverslip and on flat Si. At 24 h, APTES-treated pSi and semicarbazide-treated pSi improved DPSC proliferation of 27 % and 24 % (p=0.042 and p=0.039, respectively). The proliferation rate was lower on pSi 10 nm, pSi 1 µm and undecenoic acid-treated pSi (p=0.012, p=0.004 and p=0.011, respectively). On pSi 36 nm, this rate was slightly lower compared to glass coverslip and slightly higher compared to pSi 10 nm, but without statistical significance (p=0.106 and p=0.094, respectively). Interestingly, we found that, after 48 h and 72 h, the proliferation rate on pSi 36 nm was significantly higher than the rate on pSi 10 nm (p=0.006 at 48 h and p=0.003 at 72 h), revealing the tendency for DPSC to attach and proliferate more on pores of about 36 nm than on pores of about 10 nm. After 72 h of incubation, the proliferation rate was equivalent on flat Si and glass coverslip, higher for 34 % on APTES-treated (p=0.005), and lower on pSi 10 nm, and pSi 36 nm.

To confirm the proliferation capacities of DPSC on pSi, we investigated their mitotic activity just after cell seeding, by BrdU incorporation for 24 h. The percentages of BrdU positive cells, corresponding to mitotically active cells, are shown in Figure 5.

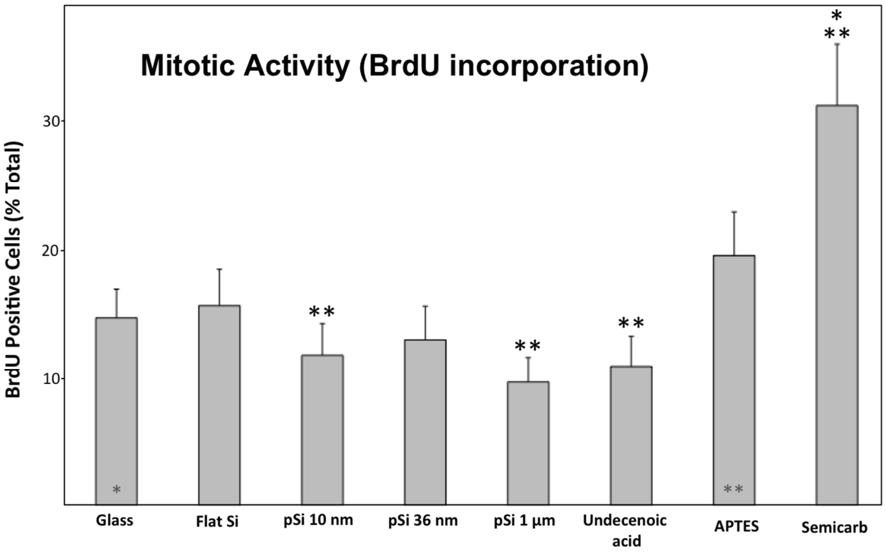

Figure 5: Number of BrdU-positive cells after 24 h of incubation, expressed as a percentage of the total number of DPSCs counted on the various pSi surfaces. Glass coverslip and oxidized non-porous silicon (Flat Si) were used as controls. All experiments were performed in triplicate. Statistical significance was determined by one-way ANOVA Tukey test ($P < 0.05$): (*) Comparison with glass coverslip. (**) Comparison with APTES

The ratios of BrdU-positive cells were remarkably enhanced on semicarbazide-treated pSi (29.2 ± 6%) compared to glass coverslip (14.7 ± 4%, $p<0.001$), Flat Si (15.6 ± 6%, $p<0.001$) and APTES-treated pSi (19.5 ± 7%, p=0.011). The BrdU-positive cells rate was 14.7 ± 4% on glass coverslip. In comparison, this rate was similar on flat Si (15.6 ± 6%, p=0.756), slightly higher on APTES-treated pSi (19.5 ± 7%, p=0.142), and slightly lower on pSi 10 nm (11.8 ± 5%, p=0.331), on pSi 36 nm (13.0 ± 5%, p=0.555), on pSi 1 µm (9.6 ± 4%, p=0.075) and on undecenoic acid-treated pSi (10.9 ± 4%, p=0.189).

Cell morphology

SEM was employed to study the effects of porosity and chemical surface treatments on the morphology of single adhering cells, and to determine cell circularity and cell surface area. Figure 6 shows representative images of DPSC growing on the different pSi substrates, on glass coverslip and flat silicon as controls, after 24 h of incubation.

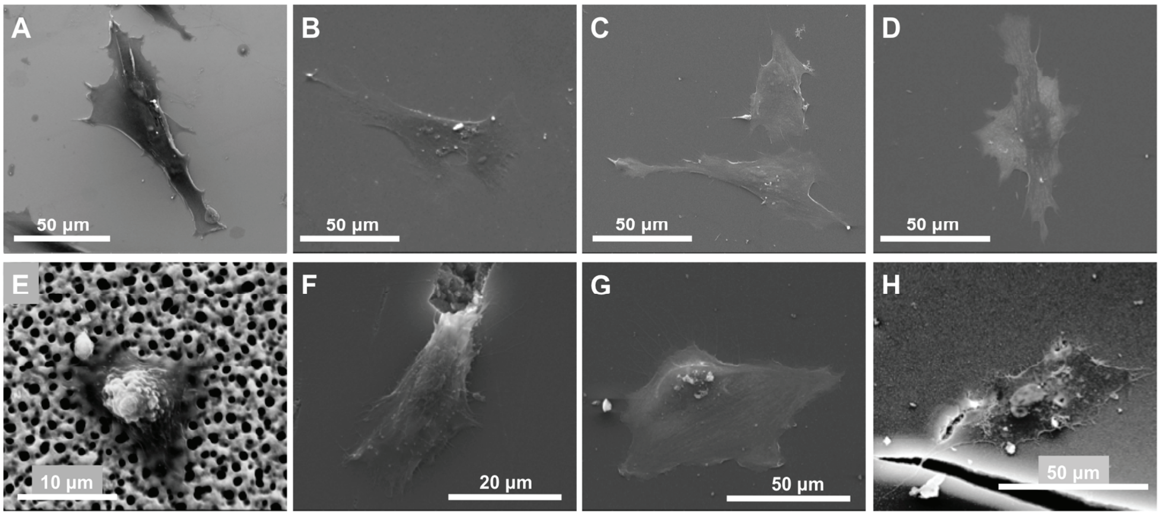

Figure 6: Scanning electron microscopy of DPSC after 24 h incubation. A: glass coverslip, B: flat Si, C: pSi 10nm, D: pSi 36nm, E: pSi 1µm, F: undecenoic acid-treated pSi, G: APTES-treated pSi, H: semicarbazide-treated pSi.

On pSi 10 nm and pSi 36 nm substrates, cells appeared elongated and well spread with the formation of long protrusions out of the cell membrane (Figure 6 C, D). The same shapes were recovered on both glass coverslip and flat Si, even though fewer protrusions were visible (Figure 6A and 6B). DPSC on APTES-treated and semicarbazide-treated pSi appeared less elongated, but well spread with many long protrusions (Figure 6G and 6H). Differently, on the pSi 1 µm and undecenoic acid-treated pSi substrates, cells appeared more rounded with a few short and squat protrusions (Figure 6E and 6F). Similar images are presented in Figure S1 in the Supporting Information, showing cell protrusions at higher magnification, highlighting the relationship between cells and porous scaffolds at the nanometer scale.

To gain a more quantitative understanding of cell surface adhesion, the cell surface area and circularity were determined on the different substrates (Figure 7).

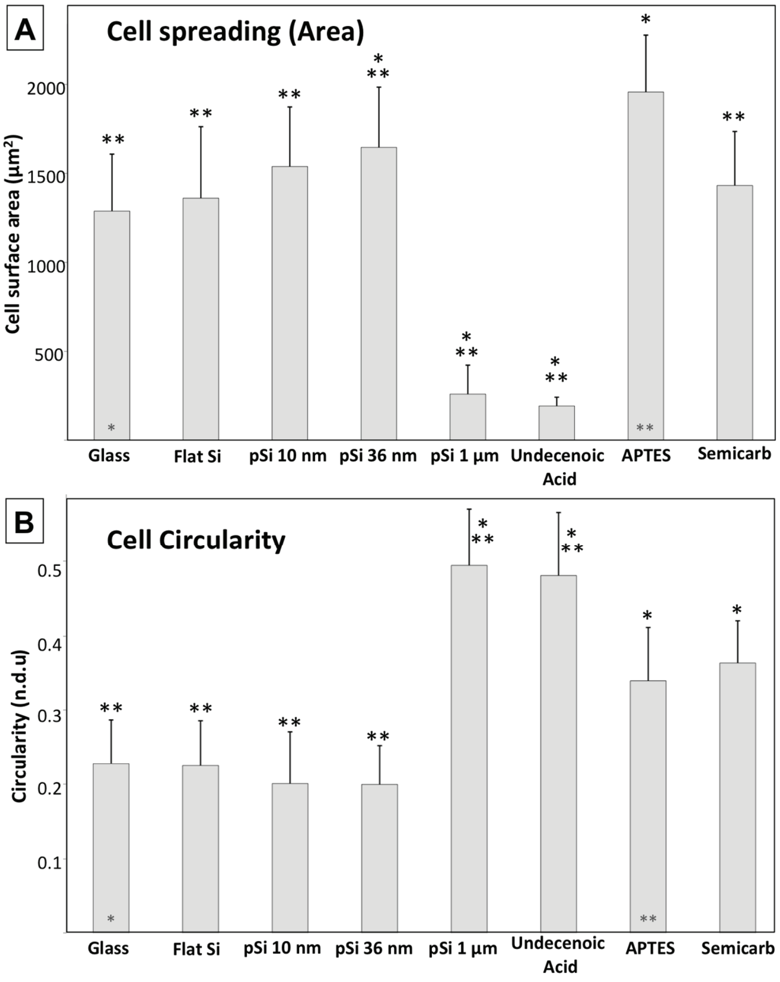

Figure 7: A: Mean cell surface area calculated from SEM images after 24 h (in µm^2). B: Mean cell circularity, evaluated from the SEM images after 24 h. 0 represent a line and 1.0 a circle (non defined unit). Statistical significance was determined by one-way ANOVA Tukey test ($P < 0.05$): (*) Comparison with glass coverslip. (**) Comparison with APTES.

Compared to glass coverslip, the mean cell surface area was similar on flat Si, pSi 10 nm and semicarbazide-treated pSi; it was higher on pSi 36 nm (p=0.040) and APTES-treated pSi (p<0.001); and it was lower on pSi 1 µm (p<0.001) and undecenoic acid-treated pSi (p<0.001).

APTES-treated pSi had a significantly higher cell surface area compared to all other surfaces (Figure 7A). It is interesting to note that, on all surfaces except pSi 1 µm and undecenoic acid-treated, DPSC were spread and covered a very large area (between 1290 ± 316 μm^2 on glass coverslip and 1958 ± 314 μm^2 on APTES-treated pSi), which is consistent with the mesenchymal stem cells characteristics.[33] We also considered cell circularity which value varies between 0 (elongated cell) and 1.0 (perfect circle). Comparing directly circularity of cells on the various pSi substrates, morphology was found to vary significantly on 3 groups of substrates: DPSC had a similar circularity on glass coverslip (0.23 ± 0.06), flat Si (0.22 ± 0.06), pSi 10 nm (0.20 ± 0.07) and pSi 36 nm (0.20 ± 0.05). Cell circularity was similar on APTES-treated (0.34 ± 0.07) and semicarbazide-treated pSi (0.36 ± 0.06), and it was also similar on pSi 1 µm (0.49 ± 0.08) and undecenoic acid-treated pSi (0.48 ± 0.08) (Figure 7B).

Cell morphology after 72 h

We followed cell growth for 72 h, until they reached confluence on the control surfaces (glass coverslip and flat Si). Cells were stained with the vital dye FDA to observe cell adherence and cytoplasmic spreading. The morphologies of DPSC on surface modified pSi after 72 h are shown in Figure 8.

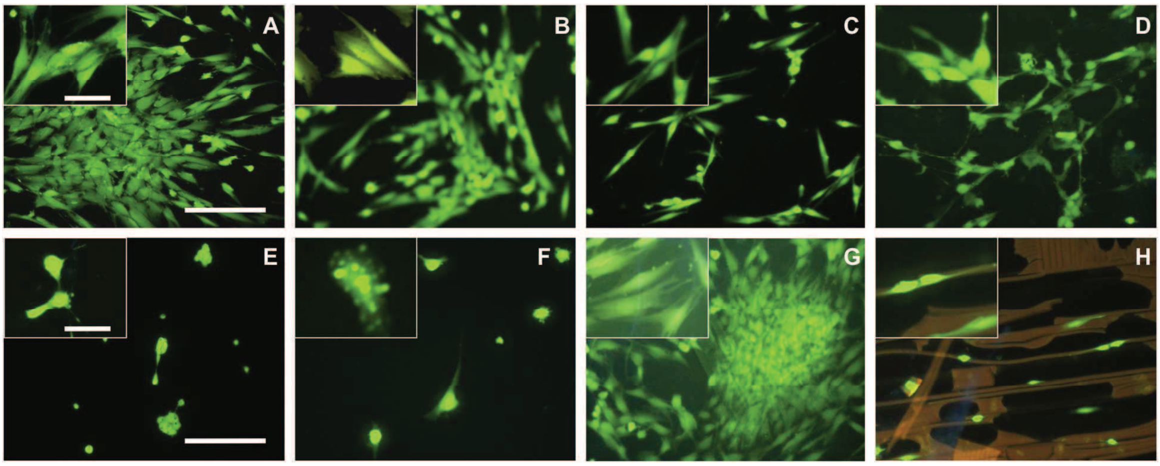

Figure 8: Fluorescence microscopy of DPSC after 72 h incubation. Cells are stained with vital FDA. A: glass coverslip, B: Flat Si, C: pSi 10 nm, D: pSi 36 nm, E: pSi 1 µm, F: undecenoic acid-treated pSi, G: APTES-treated pSi, H: semicarbazide-treated pSi. Main pictures: x20, scale bar = 100 µm. Inserts: x40, scale bar = 40 µm.

As expected according to results presented above, DPSC reached confluence on glass coverslip, flat Si and APTES-treated pSi, growing as clonogenic cell clusters (CFU-F: colony-forming units-fibroblastic) with a high proliferation rate. On pSi 10 nm and pSi 36 nm, DPSC were forming few CFU-F with a moderate proliferation rate, while DPSC were hardly growing on pSi 1 µm and undecenoic acid-treated pSi. The semicarbazide-treated pSi was clearly degraded, with DPSC attached only on the porous remaining substrate (Figure 8H), highlighting the fast resorbability of the pSi scaffold.

DISCUSSION

The aim of this work was to elucidate the influence of pore morphology and chemical status of different pSi substrates on immediate human mesenchymal stem cell adhesion and on their proliferation rate. Therefore we compared the attachment, spreading, morphology and proliferation of DPSC seeded on different porous surfaces. Our major finding was that pore geometry and surface chemical surface modification strongly influenced the subsequent behavior of DPSC that adhered and proliferated on pSi substrates. It was previously observed that cells could sense nanoscopic features on pSi substrates down to just a few nanometers (≈ 5 nm) and reacted differently to distinctive nanotopographical cues.[4,15,20]

Considering topographical influence, our results showed a higher adhesion and higher proliferation rate for DPSC on pSi substrates with typical pore sizes around 36 nm, as compared to the other pore sizes, at all the considered time points. In term of morphology and spreading, DPSC seemed to react in a similar way on pSi 10 nm and pSi 36 nm as on other substrates such as glass coverslips, and flat Si wafers, with a wider surface area on pSi 36 nm indicating an enhanced cell spreading. On pSi 1 µm, DPSC were not able to proliferate after adhesion and to cover the surface. Even if flat surfaces (glass and flat Si), used as controls in this work, allowed a better cell adhesion compared to porous surfaces, the same proliferation profile was obtained for simple oxidized pSi surface as for the flat surfaces, with the advantage for the porous surfaces to be bioresorbable (Figures 2 and 4). Recently, it has been demonstrated, for four distinct cell types (endothelial cells, mouse fibroblasts, mouse neuroblastoma cells, and human cortical neurons), a higher adhesion on pSi substrates with pore size of 10 nm, as compared to flat silicon or pSi with pore size of 20 nm.[20] Our results clearly portraited a different behavior for human mesenchymal stem cells and confirmed the fact that each cell line had different adhesion characteristics on various pSi surfaces at different time points.[3] As mesenchymal cells, DPSC are involved in structural and fibrous tissues, and their preferential adhesion and proliferation on 36 nm pores could be related to the formation of focal adhesion complex: it has been shown that focal adhesions exhibited a complex multiscale architecture where nanoscopic, doughnut-shaped complexes (≈25 nm in diameter and spaced at ≈45 nm intervals) were distributed within the adhesion area.[34] More recently, it has been reported that a 34 nm lateral spacing of adhesion peptides increased the formation of mature focal adhesions point.[35] Thus, we hypothesize that DPSC, as other hMSC, have the ability to form mature focal adhesion on pSi with pores around 36 nm, explaining the differences observed in their attachment onto pSi 36 nm, pSi 10 nm and pSi 1 µm.

After investigating the pore size influence, pSi with 36 nm pores were used to investigate the influence of various surface chemical treatments, including silanization (after thermal oxidation) and hydrosilylation. Hydrosilylation with undecenoic acid offered a limited adhesion and proliferation rate. As already reported in previous works, with other cell types,[3,9] we showed that silanization with APTES encouraged cell attachment, spreading and proliferation, with a significant number of DPSC attached to the pSi surface and a proliferation rate higher than on glass coverslip or flat Si. We also demonstrated here, for the first time, the efficiency of semicarbazide grafted by hydrosilylation for DPSC adhesion and early proliferation. Indeed, semicarbazide-treated pSi permitted cell adhesion, spreading and proliferation similar to those found on APTES-treated pSi, with an even higher rate of mitotically active cells after 24 h. These results are in accordance with studies showing that amine-capped surfaces promoted cell attachment.[36] However, after 48 h, semicarbazide-treated pSi degraded and only few cells remained attached on the surface. In contrast, thermal oxidation, by creating Si-OH bonds at the pSi surface, significantly stabilized pSi in aqueous solution and functionalization with APTES further reduced the rate of hydrolytic dissolution. Thus, the semicarbazide grafting approach on pSi appears not to be used for long-term cell culture *in vitro*, but offers promising perspectives for cell attraction and immediate transplantation *in vivo*, as stem cell therapy often requires a scaffold to carry stem cells to the injured site in the body.

CONCLUSION

Here, we have investigated three different pore sizes and three different chemical treatments to evaluate the use of pSi scaffolds for the adhesion and proliferation of primary culture of human mesenchymal stem cells from the dental pulp. We have identified, for the first time, two efficient amino-grafted pSi scaffolds for human mesenchymal stem cells adhesion and growth, with optimized pore diameter, for *in vitro* proliferation (and further differentiation), with an interesting potential for *in vivo* transplantation.

DPSC on pSi 36 nm were observed to have a better adhesion and a faster growth compared to pSi with smaller (10 nm) or larger (1 μm) pore size, in particular after silanization with APTES. Hydrosilylation with semicarbazide led to a new chemical modification favoring cell adhesion and proliferation, especially mitosis after cell adhesion. As this modified pSi surface was stable for only 24 to 48 h, it appeared to be potentially usable for stem cells adhesion and immediate *in vivo* transplantation, while APTES-treated pSi was more suitable for long term *in vitro* culture, for stem cells proliferation and differentiation.

More studies are on course to investigate: (1) the ability of APTES-treated pSi as scaffold for stem cells differentiation in different lineage, as pore size might also influence cell differentiation, (2) the optimization of surface stabilization with the semicarbazide treatment, (3) the efficiency of semicarbazide-treated pSi as an immediate cell carrier for *in vivo* transplantation. Further studies will also elucidate the role played by the porosity on focal adhesion formation, as well as the implication on the cytoskeleton organization.

for cell attraction and immediate transplantation *in vivo*, as stem cell therapy often requires a scaffold to carry stem cells to the injured site in the body.

CONCLUSION

Here, we have investigated three different pore sizes and three different chemical treatments to evaluate the use of pSi scaffolds for the adhesion and proliferation of primary culture of human mesenchymal stem cells from the dental pulp. We have identified, for the first time, two efficient amino-grafted pSi scaffolds for human mesenchymal stem cells adhesion and growth, with optimized pore diameter, for *in vitro* proliferation (and further differentiation), with an interesting potential for *in vivo* transplantation.

DPSC on pSi 36 nm were observed to have a better adhesion and a faster growth compared to pSi with smaller (10 nm) or larger (1 μm) pore size, in particular after silanization with APTES. Hydrosilylation with semicarbazide led to a new chemical modification favoring cell adhesion and proliferation, especially mitosis after cell adhesion. As this modified pSi surface was stable for only 24 to 48 h, it appeared to be potentially usable for stem cells adhesion and immediate *in vivo* transplantation, while APTES-treated pSi was more suitable for long term *in vitro* culture, for stem cells proliferation and differentiation.

More studies are on course to investigate: (1) the ability of APTES-treated pSi as scaffold for stem cells differentiation in different lineage, as pore size might also influence cell differentiation, (2) the optimization of surface stabilization with the semicarbazide treatment, (3) the efficiency of semicarbazide-treated pSi as an immediate cell carrier for *in vivo* transplantation. Further studies will also elucidate the role played by the porosity on focal adhesion formation, as well as the implication on the cytoskeleton organization.

FIGURES

Figure 1.

Characterization of the porous silicon scaffolds. Surface topography of the silicon substrates imaged with (A) scanning electron microscopy and (B) atomic force microscopy. Porous silicon with mean pore diameter of 10 nm, 36 nm and 1 µm are shown as A1-B1, A2-B2 and A3-B3, respectively. Schemas of surface chemical treatments are presented as: (1) Non oxidized pSi hydrosililation with semicarbazide. (2) Non oxidized pSi hydrosililation with undecenoic acid. (3) Oxidized pSi silanization with APTES.

Figure 2.

DPSC attached on various type of pSi, after 4h, 24h, 48h and 72h of incubation. Glass coverslip and non-porous flat silicon were used as control. Cells were counted per surface measuring 1400 µm x 1050 µm, in five areas per samples (the mean values are presented, with error bars corresponding to standard deviation). The bars protruding from the frame correspond to cells reaching confluence.

Figure 3.

Fluorescence microscopy of DPSC on various pSi scaffolds after 4 h incubation. Cells are stained with vital FDA staining (cytoplasma: green staining). A: glass coverslip, B: Flat Si, C: pSi 10nm, D: pSi 36nm, E: pSi 1µm, F: undecenoic acid-treated pSi, G: APTES-treated pSi, H: semicarbazide-treated pSi. Main pictures: x20, bar = 100 µm. Inserts: magnification x40, bar = 40 µm

Figure 4.

DPSC proliferation at 4 h, 24 h, 48 h and 72 h on various pSi surfaces, assessed by acid phosphatase activity determination. Glass coverslip and oxidized non-porous silicon (flat Si) were used as control. In order to normalize the results, 100% adhesion was attributed to cells attached on glass coverslip after 72 h of cell seeding. All experiments were performed in triplicate. Statistical significance was determined by using the Student's t test ($P < 0.05$) for comparison with glass coverslip : (*)Statistical difference at 24h. (**)Statistical difference at 72h.

Figure 5.

Number of BrdU-positive cells after 24H of incubation, expressed as a percentage of the total number of DPSCs counted on the various pSi surfaces. Glass coverslip and oxidized non-porous silicon (Flat Si) were used as control. All experiments were performed in triplicate. Statistical significance was determined by one-way ANOVA Tukey test ($P < 0.05$) : (*) Comparison with Glass Coverslip. (**) Comparison with APTES.

Figure 6.

Scanning electron microscopy of DPSC after 24 h incubation. A: glass coverslip, B: flat Si, C: pSi 10nm, D: pSi 36nm, E: pSi 1µm, F: undecenoic acid-treated pSi, G: APTES-treated pSi, H: semicarbazide-treated pSi.

Figure 7.

A: Mean cell surface area calculated from SEM images after 24 h. B: Mean cell circularity, evaluated from the SEM images 24 h. 0 represent a line and 1.0 a circle (non defined unit). Statistical significance was determined by one-way ANOVA Tukey test ($P < 0.05$) : (*) Comparison with glass coverslip. (**) Comparison with APTES.

Figure 8.

Fluorescence microscopy images of DPSC after 72 h incubation. Cells are stained with vital FDA. A: glass coverslip, B: Flat Si, C: pSi 10nm, D: pSi 36nm, E: pSi 1µm, F: undecenoic acid-treated pSi, G: APTES-treated pSi, H: semicarbazide-treated pSi. Main pictures: x20, bar = 100 µm. Inserts: x40, bar = 40 µm

TABLES.

Table 1.

Water contact angle measurements on the various scaffolds, after thermal oxidation and surface functionalization (for pSi 36 nm)

ASSOCIATED CONTENT

Supporting information.

Additional data showing cell protrusions with SEM at high magnification, highlighting the relationship between cells and porous scaffolds at the nanometer scale. This material is available free of charge via the Internet at http://pubs.acs.org.

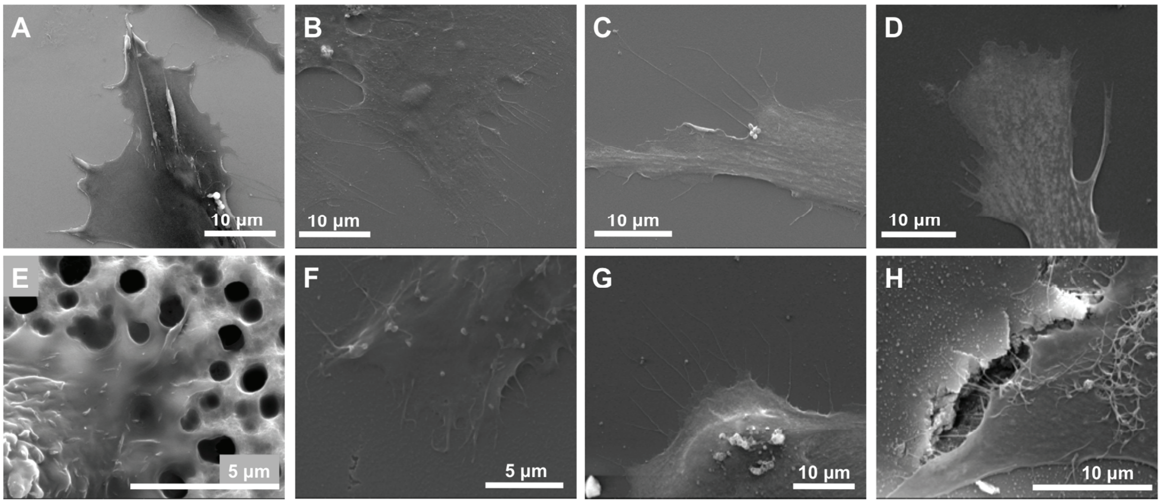

Figure S1. Scanning electron microscopy of DPSC after 24 h incubation at magnification x 8000 (image A, B, C D and G), x 15000 (image F and H) or x 30000 (image E). A: glass coverslip, B: flat Si, C: pSi 10nm, D: pSi 36nm, E: pSi 1µm, F: undecenoic acid-treated pSi, G: APTES-treated pSi, H: semicarbazide-treated pSi.

AUTHOR INFORMATION

Corresponding Author

*E-mail: frederic.cuisinier@univ-montp1.fr. Phone: +33 4 11 75 92 52

Author Contributions

The manuscript was written through contributions of all authors. All authors have given approval to the final version of the manuscript.

Notes

The authors declare competing no financial interest.

REFERENCES

(1) Wang, Y.; Kim, H. J.; Vunjak-Novakovic, G.; Kaplan, D. L. *Biomaterials* **2006**, *27*, 6064–6082.

(2) Collart-Dutilleul, P.Y.; Deville de Périère, D.; Cuisinier, F.J.; Gergely, C.; Cunin, F. In *Porous Silicon for Biomedical Applications*; Santos, H., Eds.; Woodhead Pub Limited, **2014**; in press.

(3) Low, S. P.; Williams, K. A.; Canham, L. T.; Voelcker, N. H. *Biomaterials* **2006**, *27*, 4538–4546.

(4) Khung, Y. L.; Barritt, G.; Voelcker, N. H. *Exp Cell Res* **2008**, *314*, 789–800.

(5) Canham, L. T. *Adv Mater* **1995**, *7*, 1033–1037.

(6) Ainslie, K. M.; Tao, S. L.; Popat, K. C.; Desai, T. A. *ACS Nano* **2008**, *2*, 1076–1084.

(7) Whitehead, M. A.; Fan, D.; Mukherjee, P.; Akkaraju, G. R.; Canham, L. T.; Coffer, J. L. *Tissue engineering Part A* **2008**, *14*, 195–206.

(8) Cheng, L.; Anglin, E.; Cunin, F.; Kim, D.; Sailor, M. J.; Falkenstein, I.; Tammewar, A.; Freeman, W. R. *Br J Ophthalmol* **2008**, *92*, 705–711.

(9) Alvarez, S. D.; Derfus, A. M.; Schwartz, M. P.; Bhatia, S. N.; Sailor, M. J. *Biomaterials* **2009**, *30*, 26–34.

(10) Torres-Costa, V. V.; Martínez-Muñoz, G. G.; Sánchez-Vaquero, V. V.; Muñoz-Noval, Á. Á.; González-Méndez, L. L.; Punzón-Quijorna, E. E.; Gallach-Pérez, D. D.; Manso-Silván, M. M.; Climent-Font, A. A.; García-Ruiz, J. P. J.; Martín-Palma, R. J. R. *Int J Nanomedicine* **2011**, *7*, 623–630.

(11) Park, J.-H.; Gu, L.; Maltzahn, von, G.; Ruoslahti, E.; Bhatia, S. N.; Sailor, M. J. *Nat Mater* **2009**, *8*, 331–336.

(12) Muñoz Noval, A.; García, R.; Ruiz Casas, D.; Losada Bayo, D.; Sánchez Vaquero, V.; Torres Costa, V.; Martín Palma, R. J.; García, M. A.; García Ruiz, J. P.; Serrano Olmedo, J. J.; Muñoz Negrete, J. F.; del Pozo Guerrero, F.; Manso Silván, M. *Acta biomaterialia* **2013**, *9*, 6169–6176.

(13) Noval, A. M.; Vaquero, V. S.; Quijorna, E. P.; Costa, V. T.; Pérez, D. G.; Méndez, L. G.; Montero, I.; Palma, R. J. M.; Font, A. C.; Ruiz, J. P. G.; Silván, M. M. *J Biomed Mater Res A* **2012**, *100*, 1615–1622.

(14) Dalby, M. J.; Riehle, M. O.; Yarwood, S. J.; Wilkinson, C. D. W.; Curtis, A. S. G. *Exp Cell Res* **2003**, *284*, 274–282.

(15) Buxboim, A.; Ivanovska, I. L.; Discher, D. E. *J Cell Sci* **2010**, *123*, 297–308.

(16) Sailor, M.J. In *Porous Silicon in Practice: Preparation, Characterization and Applications*; John Wiley & Sons, **2012**.

(17) Sapelkin, A. V.; Bayliss, S. C.; Unal, B.; Charalambou, A. *Biomaterials* **2006**, *27*, 842–846.

(18) Wang, P.; Clements, L.; Thissen, H.; Jane, A.; Tsai, W.-B.; Voelcker, N. H. *Adv Func Mater* **2012**, *22*, 3414–3423.

(19) Clements, L. R.; Wang, P.-Y.; Tsai, W.-B.; Thissen, H.; Voelcker, N. H. *Lab Chip* **2012**, *12*, 1480–1486.

(20) Gentile, F.; La Rocca, R.; Marinaro, G.; Nicastri, A.; Toma, A.; Paonessa, F.; Cojoc, G.; Liberale, C.; Benfenati, F.; di Fabrizio, E.; Decuzzi, P. *ACS Appl Mater Interfaces* **2012**, *4*, 2903–2911.

(21) Ma, T. *World J Stem Cells* **2010**, *2*, 13–17.

(22) Marolt, D.; Knezevic, M.; Novakovic, G. V. *Stem Cell Res Ther* **2010**, *1*, 10.

(23) Gronthos, S.; Mankani, M.; Brahim, J.; Robey, P. G.; Shi, S. *Proc Natl Acad Sci USA* **2000**, *97*, 13625–13630.

(24) Dominici, M.; Le Blanc, K.; Mueller, I.; Slaper-Cortenbach, I.; Marini, F.; Krause, D.; Deans, R.; Keating, A.; Prockop, D.; Horwitz, E. *Cytotherapy* **2006**, *8*, 315–317.

(25) Coppe, C.; Zhang, Y.; Besten, Den, P. K. *Pediatr Dent* **2009**, *31*, 467–471.

(26) Shi, S.; Gronthos, S. *J Bone Miner Res* **2003**, *18*, 696–704.

(27) Kémoun, P.; Laurencin-Dalicieux, S.; Rue, J.; Farges, J.-C.; Gennero, I.; Conte-Auriol, F.; Briand-Mesange, F.; Gadelorge, M.; Arzate, H.; Narayanan, A. S.; Brunel, G.; Salles, J.-P. *Cell Tissue Res* **2007**, *329*, 283–294.

(28) Secret, E.; Smith, K.; Dubljevic, V.; Moore, E.; Macardle, P.; Delalat, B.; Rogers, M.-L.; Johns, T. G.; Durand, J.-O.; Cunin, F.; Voelcker, N. H. *Adv Healthc Mater* **2013**, *2*, 718–727.

(29) Coffinier, Y.; Olivier, C.; Perzyna, A.; Grandidier, B.; Wallart, X.; Durand, J. O.; Melnyk, O.; Stiévenard, D. *Langmuir* **2005**, *21*, 1489–1496.

(30) Werner, S.; Huck, O.; Frisch, B.; Vautier, D.; Elkaim, R.; Voegel, J.-C.; Brunel, G.; Tenenbaum, H. *Biomaterials* **2009**, *30*, 2291–2301.

(31) Horner, P. J.; Power, A. E.; Kempermann, G.; Kuhn, H. G.; Palmer, T. D.; Winkler, J.; Thal, L. J.; Gage, F. H. *J. Neurosci.* **2000**, *20*, 2218–2228.

(32) Cao, D.; Wu, Y.-P.; Fu, Z.-F.; Tian, Y.; Li, C.-J.; Gao, C.-Y.; Chen, Z.-L.; Feng, X.-Z. *Colloids Surf B Biointerfaces* **2011**, *84*, 26–34.

(33) Krishna, O. D.; Jha, A. K.; Jia, X.; Kiick, K. L. *Biomaterials* **2011**, *32*, 6412–6424.

(34) Patla, I.; Volberg, T.; Elad, N.; Hirschfeld-Warneken, V.; Grashoff, C.; Fässler, R.; Spatz, J. P.; Geiger, B.; Medalia, O. *Nat. Cell Biol.* **2010**, *12*, 909–915.

(35) Frith, J. E.; Mills, R. J.; Cooper-White, J. J. *J Cell Sci* **2012**, *125*, 317–327.

(36) Faucheux, N.; Schweiss, R.; Lützow, K.; Werner, C.; Groth, T. *Biomaterials* **2004**, *25*, 2721–2730.

GRAPHIC FOR TABLE OF CONTENTS

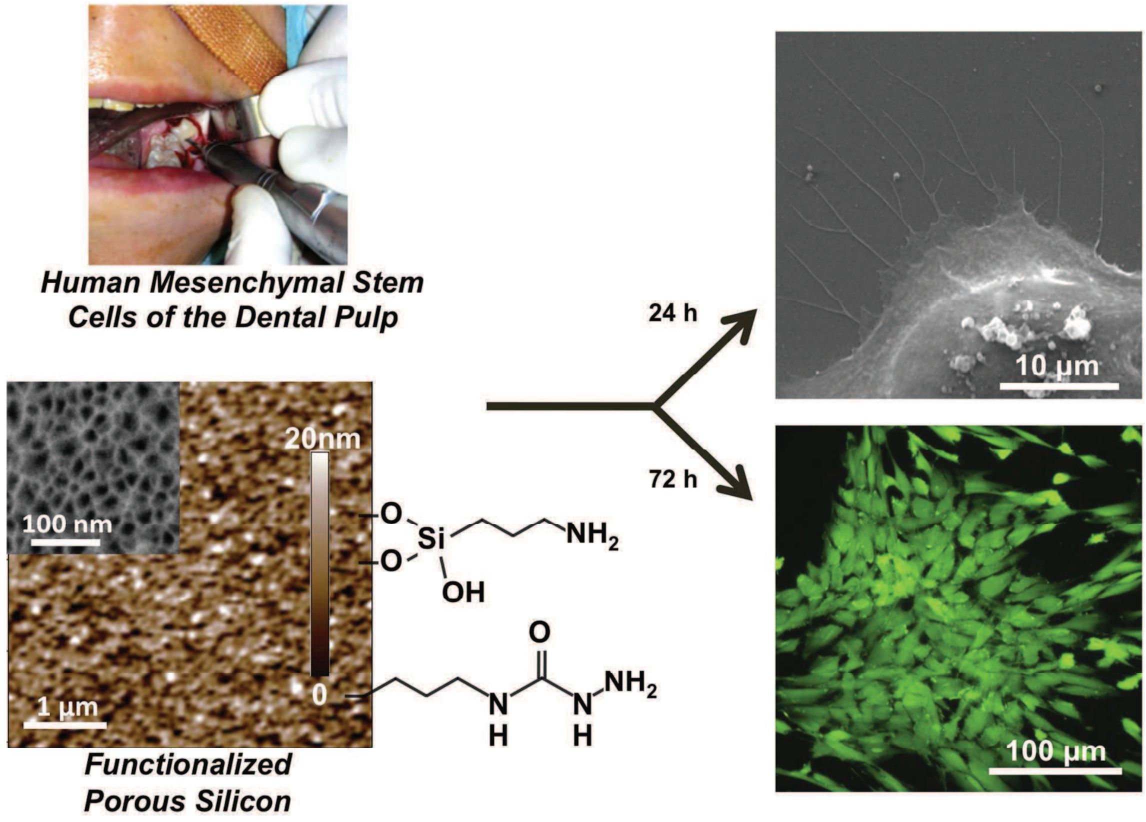

Pierre-Yves COLLART DUTILLEUL

Dental pulp stem cells growth and osteodifferentiation on porous silicon scaffolds

Résumé :

Le silicium poreux est un biomatériau prometteur pour l'ingénierie tissulaire car il est non toxique et biorésorbable. Des modifications de surface permettent de controler sa vitesse de dégradation et peuvent favoriser l'adhésion cellulaire. Les cellules souches de la pulpe dentaire (DPSC) sont des cellules souches mésenchymateuses retrouvées dans la pulpe dentaire, à l'intérieur des dents, et constituent une source accessible de cellules souches. Regrouper les capacités de prolifération et différenciation des DPSC avec les propriétés morphologiques et biochimiques du pSi représente une approche intéressante pour des applications thérapeutiques de médecine régénératrice. Dans cette thèse, nous avons étudié le comportement de DPSC humaines sur des supports de pSi, avec des pores variant de quelques nanomètres à plusieurs centaines de nanomètres. Nous avons travaillé sur différentes fonctionalisations chimiques afin d'optimiser l'adhésion cellulaire et de stabiliser le matériau: oxydation thermique, silanisation et hydrosilylation. L'adhésion, la prolifération et la différenciation osseuse ont été évaluées par microscopie à fluorescence, microscopie électronique à balayage, activité enzymatique, tests de prolifération (activité mitotique), immunofluorescence et spectroscopie FTIR. Le pSi avec des pores de 30 à 40 nm de diamètre s'est révélé être le plus approprié pour l'adhésion, la prolifération cellulaire et la différenciation ostéoblastique. De plus, la structure nanométrique et le relargage d'acide silicique par le pSi a démontré un effet positif sur l'induction osseuse et la formation d'une matrice minéralisée. Le pSi est donc apparu comme un matériau prometteur pour l'adhésion de cellules souches mésenchymateuses, que ce soit pour une transplantation immédiate *in vivo* ou pour expansion et différenciation *in vitro*.

Abstract:

Porous silicon (pSi) is a promising biomaterial for tissue engineering as it is both non-toxic and bioresorbable. Moreover, surface modification can offer control over the degradation rate of pSi and can also promote cell adhesion. Dental pulp stem cells (DPSC) are mesenchymal stem cells found within the teeth and constitute a readily source of stem cells. Coupling the good proliferation and differentiation capacities of DPSC with the textural and chemical properties of the pSi substrates provides an interesting approach for therapeutic use. In this thesis, the behavior of human DPSC is analyzed on pSi substrates presenting pore of various sizes, from few to hundreds nanometers. We investigated different chemical surface treatments, in order to enhance cell adhesion and stabilize the material: thermal oxidation, silanization and hydrosilylation. DPSC adhesion, proliferation and further osteodifferentiation were followed for up to 3 weeks by fluorescence microscopy, scanning electron microscopy (SEM), enzymatic activity assay, BrdU assay for mitotic activity, immunostaining and FTIR spectroscopy. Porous Silicon with pore size ranging from 30 to 40 nm was found to offer the best adhesion, the fastest growth rate for DPSC and the highest osteoinductive effect. Moreover, the pSi nanostructure and the release of silicic acid had a positive effect on precursor cells osteodifferentiation and mineralized matrix formation. Porous silicon appeared to be an appropriate biomaterial for mesenchymal stem cells adhesion and immediate *in vivo* transplantation, or for long term *in vitro* culture, for stem cells proliferation and differentiation.

Mots Clés :	**Key Words:**
Ingénierie Tissulaire	Tissue Engineering
Cellules Souches Mésenchymateuses	Mesenchymal Stem Cells
Silicium Poreux	Porous Silicon
Adhésion cellulaire	Cell Adhesion
Différenciation cellulaire	Cell Differentiation